Universidade de Aveiro Departamento Física
2006

Armandina Maria Lima Lopes

Estudos de distorções da rede e correlações electrónicas em manganites utilizando sondas locais

Local probe studies on lattice distortions and electronic correlations in manganites

Universidade de Aveiro Departamento Física
2006

Armandina Maria Lima Lopes

Local probe studies on lattice distortions and electronic correlations in CMR Manganites

Dissertação apresentada à Universidade de Aveiro para cumprimento dos requisitos necessários à obtenção do grau de Doutor em Física, realizada sob a orientação científica do Dr. Vítor Brás de Sequeira Amaral, Professor Associado do Departamento de Física da Universidade de Aveiro e do Dr. João Guilherme Martins Correia, Investigador Principal do Instituto Tecnológico Nuclear.

To the memory of my grandmother Ana Santos Meira e Silva
To my family

o júri

presidente

Prof. Dr. Manuel João Senos Matias
professor catedrático do Departamento de Geociências da Universidade de Aveiro

Prof. Dr. João António de Bessa Meneses e Sousa
professor catedrático do Departamento de Física da Faculdade de Ciências da Universidade do Porto

Prof. Dr. Reiner Vianden
professor do Helmholtz – Institut fur Strahlen – und Kernphysik da Universidade de Bona

Prof. Dr. José Fernando Ferreira Mendes
professor catedrático do Departamento de Física da Universidade de Aveiro

Dr. João Guilherme Martins Correia
investigador principal do Instituto Tecnológico Nuclear

Prof. Dr. Vítor Brás de Sequeira Amaral
professor associado do Departamento de Física da Universidade de Aveiro

agradecimentos

This manuscript reflects my research work developed during the last years, within a collaboration between the University of Aveiro, University of Porto, University of Trás-dos-Montes and Alto Douro and the ISOLDE-CERN facility. I am sincerely grateful to a countless number of people which helped me during these last years. Unfortunately, here, I can only name some.

I am sincerely grateful to my supervisors, Professor Vítor Amaral and Doctor João Guilherme Correia, for supporting my work in all terms, their constant advice and enthusiasm.

To my friend and mentor, João Pedro Araújo, I can only say that this work wouldn't be possible without him.

To the colleagues of Aveiro Univ., specially Rosário Soares, António Moreira, João Amaral, Mário Reis, Nuno João Oliveira and Sérgio Pereira for their help, advise and most of all their friendship during these last two years. A very special thank to Stanislav Ferdov not only for helping me with Fullproof program but essentially for his support in these last months.

To the members of IFIMUP-Porto for their help and support. I am specially indebt to Professor João Bessa Sousa who guided me in my first steps in research. I thank his constant support and care during these years.

To the members of the Chemistry Dep. of Trás-dos-Montes and Alto Douro Univ. who helped in the production of the bulk manganite samples. A special thank to Pedro Tavares for his supervision. More importantly, I thank him and his wife for their friendship and hospitality.

To all members of the ISOLDE Collaboration at CERN, specially Professors W. Tröger and T. Butz, whom I thank for providing the PAC spectrometer.

I thank my beam time co-workers especially my "companheira" Elisabete Rita, Tânia Mendonça, Ana Claudia, Frank Heinrich, Uli Wahl and ASPIC colleagues Andreas Weber and Kay Potzger. I will not forget their help and good humour while collecting data.

I have also to thank the Portuguese colleagues at CERN for the leisure times we passed together.

I am also obliged to A. Gomes, A.P. Guimarães and I. Oliveira, members of the Centro Brasileiro de Pesquisas Fisicas, for their help during my stay in that laboratory.

I also thank Carla Sotomaior and Robert Harlander for their support and friendship.

Fundação para a Ciência e a Tecnologia is acknowledge for awarding me a PhD scholarship.

palavras-chave

Manganites, distorções locais, ordem orbital e de carga, polarões, correlações electrónicas.

resumo

Nesta tese apresenta-se um estudo experimental das distorções locais e correlações electrónicas em óxidos magnéticos com magnetoresistência colossal. A técnica de sonda local – Correlação Angular Perturbada – é utilizada em amostras caracterizadas quanto às suas propriedades macroscópicas nomeadamente propriedades estruturais, magnéticas e eléctricas, tendo em vista a obtenção de informação microscópica relevante via gradiente de campo eléctrico e campo magnético hiperfino, focando em particular os seguintes aspectos:

-Distorções de rede e agregados de polarões no sistema $LaMnO_{3+\Delta}$.
É apresentado um estudo dos gradientes de campo eléctrica e campo magnético hiperfino em amostras representativas do sistema $LaMnO_{3+\Delta}$, correlacionando estas propriedades locais com a caracterização das propriedades macroscópicas, efectuada nas mesmas amostras.
Desta forma, foi possível estudar a natureza microscópica das distorções polarónicas. Foi dada especial atenção ao composto com composição $LaMnO_{3.12}$ uma vez que este é um sistema padrão de uma manganite ferromagnética-isoladora que apresenta uma transição estrutural romboédrica (R)-ortorrômbica (O) perto da temperatura ambiente.
O estudo revelou que agregados de distorções locais sobrevivem até 776 K, na fase de estrutura média mais simétrica (romboédrica), onde, por simetria, os octaedros MnO_6 deveriam ser regulares. Estas distorções são semelhantes às observadas no sistema $LaMnO_3$ onde os octaedros MnO_6 apresentam uma distorção Jahn-Teller colectiva. Com a diminuição da temperatura observa-se um aumento contínuo destes agregados. Abaixo de uma temperatura crítica estas distorções relaxam acomodando-se numa estrutura com reduzidas distorções Jahn-teller. Verificou-se também que a transição estrutural (macroscópica) pode ser entendida como uma transição de percolação dos ambientes microscópicos.

-Coexistência das ordens eléctrica e magnética no sistema $Pr_{1-x}Ca_xMnO_3$.
É apresentado o primeiro estudo de gradiente de campo eléctrico no sistema $Pr_{1-x}Ca_xMnO_3$. Este estudo foi efectuado numa larga gama de temperaturas permitindo estudar localmente as diversas transições que este sistema apresenta. Em particular, na região do diagrama de fases onde existe ordenamento de carga e orbital ($0.32<x<0.90$), a componente principal do gradiente de campo eléctrico apresenta uma descontinuidade perto desta transição. Esta anomalia no gradiente de campo eléctrico é relacionada com possiveis distorções da simetria local sugerindo a presença de uma polarização eléctrica espontânea a temperaturas inferiores às de ordenamento de carga.

keywords

Manganites, local distortions, charge and orbital order, polarons, electronic correlations.

abstract

This thesis presents an experimental study on lattice distortions and electronic correlations in colossal magnetoresistive magnetic oxides. The Perturbed Angular Correlation local probe technique is used to study selected manganite systems in order to obtain relevant insight into microscopic phenomena responsible for their macroscopic properties. Complementary structural, magnetic and electric characterization was performed. The work is focused on the following aspects:

- Lattice distortions and polaron clusters in $LaMnO_{3+\Delta}$ system.
A study of the electric field gradient and magnetic hyperfine field was performed in representative samples of the $LaMnO_{3+\Delta}$ system, and correlated with macroscopic information obtained in the same samples.
Particular attention was given to the $LaMnO_{3.12}$ sample since this compound is a prototype of a ferromagnetic-insulator manganite, presenting a rhombohedric-orthorhombic structural phase transition near room temperature. We found that random distributed polaron clusters survive in the undistorted Rhombohedric phase, up to temperatures as high as 776 K. These distortions are as strong as those observed in the orbital ordered $LaMnO_3$. Lowering temperature, the clusters continuously expand until a microscopic transition takes place. Below the transition, the distortions are accommodated into a weaker JT distorted phase. Additionally, the macroscopic structural phase transition can be viewed as a percolation transition of the microscopic environments.

- Coexistence of electric and magnetic order in the $Pr_{1-x}Ca_xMnO_3$ system.
The electrical field gradient (EFG) was studied for several compositions of the $Pr_{1-x}Ca_xMnO_3$ system. This local probe analysis was complemented with the study of the magnetic and structural properties. This allowed the determination of the electrical field gradient phase diagram for this system. The problematic of the charge/orbital order was also studied. Perturbed Angular Correlation studies were used to infer about atomic-scale distortions in a wide temperature range encompassing the charge/orbital and magnetic ordering transitions. The electrical-field gradient generated by the charge distribution around the probe shows strong anomalies when the system undergoes the charge-order (CO) transition. In particular, the principal component of the EFG presents a sharp discontinuity below the CO transition. The anomaly of EFG below T_{CO} was related with the displacements of the ions causing a distortion of the local symmetry and thus connected with the existence of a local electric polarization.

Contents

Introduction

Perovskite-type manganites of general chemical formula $R_{1-x}A_xMnO_3$, with R a trivalent rare-earth and A a divalent alkaline earth cation, have been the focus of intense scientific research over the past years in view of the variety of physical phenomena that they display as well as their potential applications in magnetic sensing and spin-polarized transport. The interest in such perovskite systems remounts already to the early fifties where first reports on the striking relation between the magnetization and resistivity were publish by Jonker and van Santen in lanthanum based compounds [1–3]. Soon after that discovery, Zener [4], Anderson and Hasegawa [5] explained successfully the connection between metallicity and ferromagnetism in terms of the double exchange (DE) interaction among Mn ions. This, together with the Goodenough theory of covalency bonding [6] has established in the 1950s the exchange rules among Mn ions in manganites providing a first understanding of the mechanisms driving the electric and magnetic properties of such compounds. The competition between antiferromagnetic charge-ordered (AF-CO) ground states favored by the super exchange interaction and a ferromagnetic (FM) coupling with consequent delocalization of the charge carriers appeared as a good systematization of one of the most interesting manganites properties. This apparent theoretical success seemed to lag the research on these perovskite materials in the subsequent years. In 1993, however, the finding of colossal magnetoresitance (CMR) in thin films of $La_{0.72}Sr_{0.25}MnO_3$ and $La_{0.66}Ba_{0.33}MnO_3$ by K. Chahara *et al.* and R. Von Helmholt and coauthors, respectively [7, 8], brought this topic to the forefront of today's theoretical and experimental research. The route to induce colossal magnetoresistance relies on the appropriate doping of the parent antiferromagnetic insulator compound being commonly performed by replacement of elements, incorporation of vacancies and/or oxygen. These processes create mixed manganese valence, Mn^{4+}/Mn^{3+}, favoring ferromagnetic interaction and dynamic electron transfer between Mn^{3+} and Mn^{4+} ions, *i.e.*, double exchange interaction, driving the material towards the metal insulator transition [4]. Although this description explains qualitatively the CMR effect, this framework is insufficient to explain the mechanism responsible for the large resistivity of the paramagnetic insulator (PI) phases, the ferromagnetic insulator (FMI) state observed in the phase diagrams of some manganites (*e.g.*, in the small bandwidth $Pr_{1-x}Ca_xMnO_3$ system [9]) or even the new ferromagnetic charge-ordered (CO) phase observed in $La_{0.5}Ca_{0.5}MnO_3$ [10]. Millis *et al.* [11,12] argued that

the physics of manganites is dominated by the interplay between a strong electron-phonon coupling and the large Hund coupling that optimizes the electronic kinetic energy by the generation of a ferromagnetic phase. Experimental evidences of charge localization via Jahn-Teller (JT) distortions due to the strong electron-lattice coupling were reported by [13–19] using different experimental techniques as pair distribution function (PDF) analysis of neutron diffraction patterns [13, 17] or through oxygen isotopic effect [16]. Also, large oxygen thermal factors in PI phases dropping rapidly near below T_C, observed by X-ray absorption fine structure (XAFS) [14, 15] and diffraction studies [18], were associated with the presence of JT distortion in the PI phase. Moreover, Bellinge *et al.* and Booth [13–15] also found that these distortions exist well below T_C indicating a coexisting of the localized phase in the metallic region. The dynamic character of the latices distortions, polarons, was probed by nuclear quadrupole resonance (NQR) studies reported by Allodi and co-authors [20].

Although early works tended to focus on compounds with large CMR effect, recently the attention has been shifted towards other hole doping compositions such as $x<0.2$ and $x\geq0.5$ and small bandwidth systems, where the competition between the several degrees of freedom in manganites can be better analyzed. Indeed, it is in the low doped manganites and small bandwidth systems that very unusual features, such as polaronic distortions, local inhomogeneities with phase separation and peculiar charge-order states, systematically appear [21,22]. It is known that at hole densities, such as $x = 0.5$, a charge/orbital/spin-ordered state can be stabilized leading to a phase diagram asymmetric with respect to half-doping [9]. Within the long-range charge-ordered phases the localization of carriers renders the material insulating. Accompanying this process, the Mn^{3+} orbitals (e_g) also exhibit long range ordering (orbital order OO) and as a consequence, a complex magnetic ordering (antiferromagnetic CE-type spin order) occurs in these structures at low temperatures.

Historically, the occurrence of charge ordering in manganites was first observed from neutron diffraction and x-ray data by Wollan and Koehler [23] in the fifties and later examined by Jirak *et al.* [24]. These findings appeared in agreement with former predictions of Goodenough [6] who interpreted the CE-type antiferromagnetic structure of $La_{0.5}Sr_{0.5}MnO_3$ as an evidence of charge ordering and suggested a possible orbital ordering pattern associated with it. Latter, a first clear evidence of charge ordering was ascertained by Chen and Cheong using electron microscopy [25]. Electron-diffraction images at low temperature exhibit superlattice peaks, which are thought to arise from the alternation of Mn^{3+} and Mn^{4+} ions. Right after P. G. Radaelli *et al.* [26] solved by neutron and x-ray diffraction the crystallographic superstructure arising from such ordering. In the last decade a quite large number of publications have been devoted to this phenomena, and signatures of charge-order such as anomalies in the resistivity, magnetic susceptibility and as well as in the heat capacity were observed. Moreover these investigations revealed an extraordinary sensitivity of CO to the average size of the A-site cations, pressure and magnetic field, as well as oxygen isotope and chemical substitutions [27–31]. Another manifestation of this sensitivity is found in the melting of the

charge ordered state through photo-irradiation [32] or X-ray irradiation [33]. In spite of the huge research activity around these CO states a great controversy still exists regarding the correct charge/orbital pattern. The Wollan and Koehler/Radaelli picture for charge-order with inequivalent Mn^{3+}/Mn^{4+} cations placed on specific lattice sites [23, 26] was proved to be oversimplified. Recently, several experimental and theoretical works have found that little charge contrast (ϵ) of the Mn ions exists (*i.e.* Mn should have valence $3.5 \pm \epsilon$ with $\epsilon = 0$ or $\epsilon \ll 0.5$) [34–40].

One realizes that at present the manganites are probably the outmost representative materials which show versatile unconventional physical phenomena. The intrinsic inhomogeneities conspicuous of these systems with clusters of competing phases and structural/charge/magnetic order at different scales, that can be modified by external parameters, present a great challenge for condensed matter physics. In particular local probe techniques can be valuable since atomic scale insight is crucial to better understand the physics of these compounds. The importance of local probe research in these materials is illustrated by a large number of available publications. X-ray and neutron diffraction can be extremely powerful techniques in providing structural related information. However, the quantities measured with these techniques reflect average values over the macroscopic sample volume and local features are usually difficult to resolve. On the other hand, nuclear hyperfine techniques, like nuclear magnetic resonance (NMR) and NQR, are extremely useful in providing atomic scale information on the probe-element interactions with the lattice host. In particular, the measurement of the electric field gradient (EFG) and/or the magnetic hyperfine fields (MHF) at specific site provides direct information on the local charge distribution and/or local spin density transfer. Unfortunately, NQR and NMR nuclear probes of the desired elements do not always exist. Furthermore the sensitivity of these techniques is temperature dependent, prohibiting measurement in a large temperature range. On the other hand, nuclear methods using nuclear excited states of radioactive elements, with appropriate nuclear spin, magnetic and quadrupole moments provide, in specific cases, the adequate probe elements. Particularly, the perturbed angular correlations (PAC) technique, can provide relevant information on the electronic environment. Furthermore PAC sensitivity is temperature independent allowing measurements in a wide range of temperatures.

This thesis is essentially based on the perturbed angular correlations experimental studies of low doped and small bandwidth CMR manganites. Production and bulk property characterization of samples is a mean to accomplish the latter goal. Combining local probe studies with macroscopic characterization, relevant information is extracted to achieve microscopic insight on the materials and corresponding relevance on the macroscopic properties.

As a final remark one can refer the very recent work of Dagotto [22] where he summarizes the state of affairs in manganite research and objectively lists a number of important challenges and open questions concerning these systems, some of which we shortly reproduce here:

- The evidence for CO nanoclusters above T_C should be further confirmed.

- The existence of the predicted new temperature scale T* above the Curie temperature should be further investigated.

- What is the nature of the FM insulating phases that appear in some phase diagrams?

- What is the nature of the CO states at $x<0.5$, such as those in $Pr_{1-x}Ca_xMnO_3$?

In this context, this manuscript presents the author's contribution for the experimental study of CMR magnetic oxides constituting an effort to provide additional insight into those aspects. The thesis is structured in five chapters which can be briefly summarized as follows:

General aspects on CMR magnetic oxides. This chapter briefly describes the relevant aspects of colossal magnetoresistive oxides necessary to understand the subsequent chapters of this thesis. The materials and their problematic are presented.

Experimental techniques. The experimental set-ups and procedures of the techniques used for sample characterization and the technique used for the synthesis of the materials are briefly introduced. Reference is given to the institutions and collaborators who prepared other samples used in this thesis. The ISOLDE-CERN facility, where the radioactive probe elements are produced and samples implanted and studied is presented.

Nuclear methods. Some aspects of hyperfine interactions are presented focusing on those that are related to the perturbed angular correlations technique. Also, the PAC technique is described stressing on the relevant parameters and formulae to be used in subsequent chapters.

Lattice distortions and polaron clusters in $LaMnO_{3+\Delta}$ system. After a bulk property characterization of the $LaMnO_{3+\Delta}$ system, the study of local distortions and their dynamics with the $\gamma-\gamma$ perturbed angular correlation spectroscopy is presented. We have undertaken a systematic study on the hyperfine fields on this system and correlated them with the macroscopic characteristics of each sample. Particular attention is given to the $LaMnO_{3.12}$ compound since it is a prototypical FMI manganite that undergoes a rhombohedral (R)-orthorhombic (O) structural transition around room temperature. A wide range of temperatures is explored allowing to follow the structural and magnetic phase transition and to study the microscopic nature/evolution of polaronic distortions. The results are discussed and compared with the ones from recent literature.

Coexistence of electric and magnetic order in $Pr_{1-x}Ca_xMnO_3$ system. The complex phase diagram of the $Pr_{1-x}Ca_xMnO_3$ system is studied by means of PAC spectroscopy. Firstly a macroscopic characterization of all samples under study is presented. Subsequently, a systematic study using PAC spectroscopy characterizing the $Pr_{1-x}Ca_xMnO_3$ local environments along its phase diagram and at different temperatures is obtained. In particular, much attention is devoted to the charge and orbital ordered phases. For these compositions, besides the study in a wide range of temperatures, detailed analysis close to the charge-order transition is presented and compared to compositions where charge ordering does not occur. Our atomic-scale view of the CO phenomena is discussed and positioned within the existing models.

Conclusions and perspectives. A general conclusion of this thesis is presented. The perspectives for future research work, following these studies are reviewed and highlighted.

List of articles Here we list all scientific articles published in international journals during this thesis.

Chapter 1

General aspects on CMR magnetic oxides

In this chapter the Colossal Magnetoresistive (CMR) magnetic oxides are presented, emphasizing the relevant aspects for the understanding of the work presented in this thesis.

1.1 Crystal structure

The crystallographic structure of the compounds studied in this thesis was first solved, through x-ray diffraction data, by Jonker and J.H. Van Santen in the fifties [1–3]. The designation *manganites* to the materials with chemical formula $R_{1-x}A_xMnO_3$, where R is a trivalent rare-earth and A a divalent alkaline cation, was then proposed by that authors. They found that these systems have a crystallographic structure derived from the ABO_3 cubic perovskite[1].

1.1.1 Ideal perovskite structure

The ABO_3 ideal perovskite structure crystalizes in the $Pm\bar{3}m$ space group and can be viewed as a cubic closed packed (fcc) array formed by the O^{2-} anions and the large cation A, with the small B cation sited in the center of the cube surrounded by the oxygen octahedra. An equivalent representation can be obtained through a displacement of the origin by (1/2, 1/2, 1/2). In this representation the A cation is located in the center of the cube surrounded by a oxygen octahedron, whereas the B cation is sited in the corners of the cube. These two structure representations are depicted in figure 1.1.

Chemically, the system can be characterized by a wide range of cations which can occupy the A and B sites in the perovskite structure (*e.g.*, $SrTiO_3$ at room temperature). The

[1]This name was firstly attributed to the $CaTiO_3$ compound in 1939 by Gustav Rose in reference to the mineralogist Lev Aleksevich von Perovski.

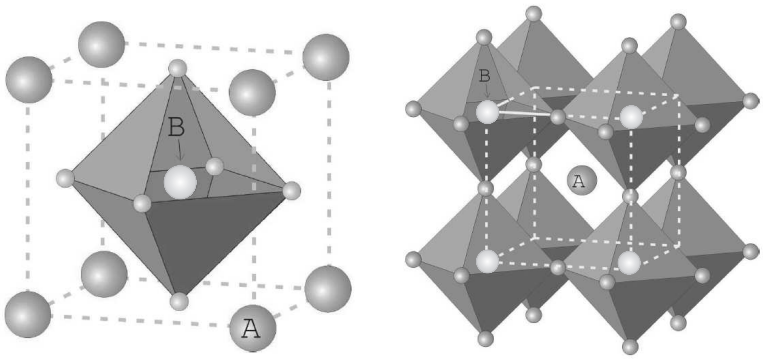

Figure 1.1: Schematic representation of the ideal perovskite structure. Left side, representation with the B cation sited in the center of the structure surrounded by the O_6 octahedron. Right side, equivalent representation but with the A cation in the center surrounded by twelve oxygen.

cations charge always sums 6 and the structure stabilization depends crucially on the A and B ionic radius, r_A, r_B. One can see that to stabilize an ideal cubic closed packed structure the ionic radius have to obey the relation

$$\sqrt{2}(\mathrm{r_A} + \mathrm{r_O}) = 2(\mathrm{r_B} + \mathrm{r_O}) \tag{1.1}$$

where r_O is the oxygen ionic radii. Commonly the ideal cubic structure is distorted by cation size mismatch and the Jahn-Teller effect (described in section 1.1.2) and thus manganites usually crystallize in a more complex perovskite related structure.

1.1.2 Distorted perovskite structure

Tolerance factor

The distorted cubic perovskite structures are frequently orthorhombic though other symmetries such as rhombohedric or tetragonal can be stabilized. These perovskite systems can accommodate considerably different cation sizes. Divalent cations which can occupy the A site include calcium, strontium, barium and lead; trivalent cations include lanthanum, praseodymium, neodymium, etc. Besides manganese, other 3d element such as iron, cobalt or nickel can be located on the B sites. Table 1.1 presents the ionic radii of some elements that can be accommodate in the perovskite structure. The deformation of the ideal cubic cell to accommodate the different cations sizes can be quantified by the tolerance factor introduced by Goldschmidt [41]

$$t = \frac{r_A + r_O}{\sqrt{2}(r_B + r_O)} \tag{1.2}$$

This factor, which is one for the ideal cubic structure, can also be expressed using the

interatomic distances between the oxygen and the ions at A and B sites (d_{A-O} and d_{B-O} respectively)

$$t = \frac{d_{A-O}}{\sqrt{2}d_{B-O}} \tag{1.3}$$

As the value of t departs from one internal stresses increases and the cubic lattice becomes unstable. In particular case of $t < 1$ the perovskite B-O bonds are under tension whereas A-O bonds are under compression and thus one observes a cooperative rotation of the BO_6 octahedra and a corresponding reduction of the B-O-B bond angle from φ=180°. When the tolerance factor is close to unity the rhombohedral structure is often found. This structure corresponds to a small rotation of the oxygen octahedra about a [111] axis of figure 1.1 (see also figure 1.2(a)). As t further deviates from $t = 1$ the the cation misfit is accommodated by a collective buckling of the oxygen octahedra corresponding to a rotation about the [110] axis. This structure is commonly called the O-type orthorhombic phase and the corresponding unit cell is depicted in figure 1.2(b)

Rhombohedral and orthorhombic deformation In general, the manganite crystalline structures differ from that of an ideal perovskite. In particular, the compounds studied in this work crystallize in the rhombohedral or orthorhombic phases, with the unit cell larger than that of figure 1.1 to take into account the lattice distortions. For example, to accommodate the orthorhombic distortion 4 unit formulas (Z=4) are needed and the cell parameters of the O-type orthorhombic structure (a_O, b_O and c_O) relates with the a_P cubic cell parameter as: $a_O \sim a_P\sqrt{2}$, $b_O \sim a_P\sqrt{2}$ and $c_O \sim 2a_P$. In figure 1.2(a) an illustration of the relation between the cubic, orthorhombic and rhombohedral lattices is depicted. A representation of a possible orthorhombic structure with the Mn(B) cation in the center of O_6 octahedra is presented in figure 1.2(b). In the orthorhombic structure and depending on the degree of distortion, different relations between the cell parameters occur and usually they obey to the inequality $a_O\sqrt{2} \leq c_O \leq b_O\sqrt{2}$ for the O-type orthorhombic distortion. For the so called

Table 1.1: Ionic radii (in Å) of some elements common in the perovskite structures.

O^{2-}	Mn^{3+}	Mn^{4+}			
1.40	0.645	0.530			
Ba^{2+}	Sr^{2+}	Ca^{2+}	Cd^{2+}		
1.61	1.44	1.34	1.31		
La^{3+}	Pr^{3+}	Nd^{3+}	Sm^{3+}	Eu^{3+}	Tb^{3+}
1.36	1.30	1.27	1.24	1.23	1.20

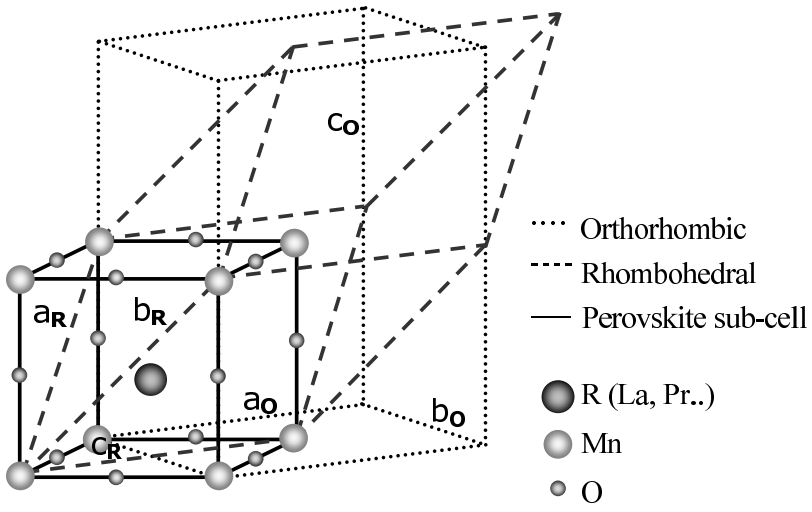

(a)

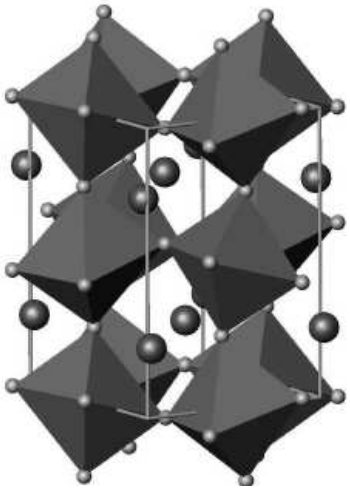

(b)

Figure 1.2: a) Comparison between the cubic and non-cubic (orthorhombic and rhombohedral) lattices (adapted from [42]). b) Schematic representation of the orthorhombic structure with the Mn(B site) cation in the center of O_6 octahedron.

O'-type orthorhombic structure (highly distorted phase due to Jahn-Teller effect, see below) a different inequality $c_O \leq a_O\sqrt{2} \leq b_O\sqrt{2}$ is found.

Jahn-Teller effect In addition to the cooperative octahedra rotation mentioned above, another deformation of the structure can occur. A cooperative oxygen displacement with the oxygens moving toward one near-neighbor Mn(B) atom and way from the others and thus deforming the regular MnO_6 octahedra. Consequently a more severe distorted crystallographic phase, the O'-type orthorhombic structure, is stabilized due to the superposition

of the octahedra rotation with the octahedra deformation. $LaMnO_3$ and $PrMnO_3$, for example, have O'-type orthorhombic structure with the octahedra stretched in one direction and compressed in the perpendicular plane due to the presence of the Mn^{3+} Jahn-Teller ion.

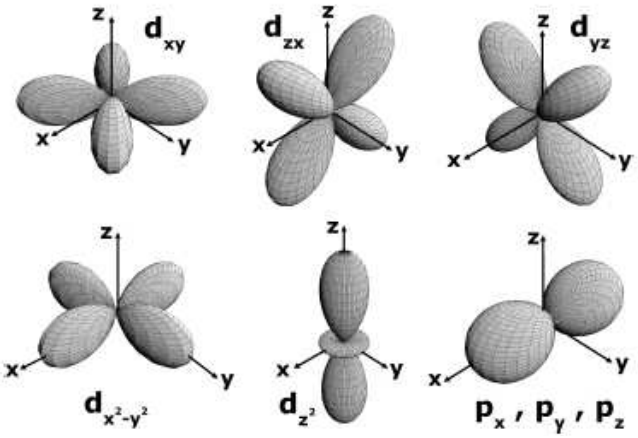

(a)

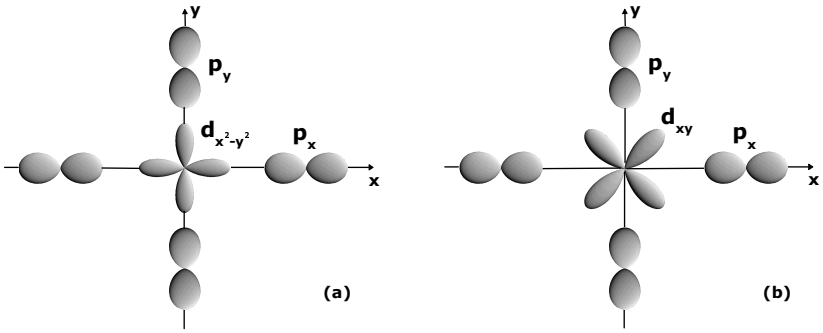

(b)

Figure 1.3: a) Schematic representation of the five d orbitals. In a cubic crystal field, the fivefold degeneracy is lifted in three t_{2g} orbitals [(xy), (yz), and (zx)](up) and two e_g orbitals [(x^2 - y^2) and z^2](down). The 2p oxygen orbitals are also shown (down right). b) Projection on the xy plane of the (x^2 - y^2) e_g(left) and xy t_{2g}(right) orbitals in the center of the four in-plane 2p oxygen (adapted from [43]).

These Jahn-Teller deformations manifest in the presence of certain ions (Mn^{3+}, Cr^{2+} or Cu^{2+}) due to a particular electronic configuration in a non linear molecular environment. If one considers a free transition-metal ion as Mn^{3+} ($3d^4$) or Mn^{4+} ($3d^3$) its d orbitals (d_{xy}, d_{zx}, d_{yz}, $d_{x^2-y^2}$ and d_{z^2} , see figure 1.3(a)) will be degenerated in energy. However if this atom is placed in the center of a O^{2-} ($2p^6$) oxygen[2] octahedra the crystal field potential blocks the free rotation of the electrons by introducing the crystal field splitting of the d orbitals. This partial removal of the orbital degeneracy splits the orbitals into two subgroups named e_g ($d_{x^2-y^2}$ and d_{z^2}) and t_{2g} (d_{xy}, d_{zx}, d_{yz}) orbitals. The former points toward O^{2-} ions and

[2]Oxygen have 2p orbitals, p_x, p_y and p_z also degenerated in energy.

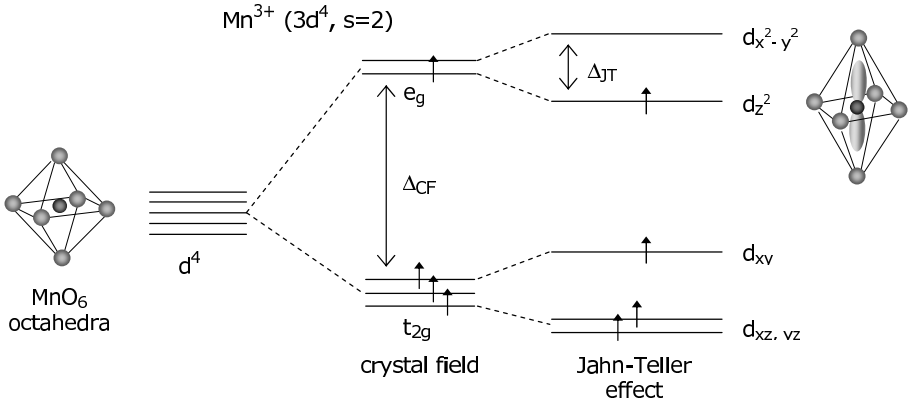

Figure 1.4: Schematic representation of the orbital energy splitting due to the crystal field and Jahn-Teller effect. An illustration of a regular and distorted octahedron is also shown.

consequently, due to the Coulombic repulsion, have higher energy then the latter that points between oxygens. In figure 1.3(b) a representative projection of this orbital configuration is shown. This leads to the crystal field splitting of the e_g and t_{2g} orbitals (see figure 1.4), which does not introduce any distortion in the MnO_6 octahedra, unless one of the e_g states is occupied. As an example, the Mn^{4+} ion, due to the Hund's rule (all the spins are aligned parallel) has its 3 electrons in each t_{2g} orbitals and in this case a octahedra MnO_6 is regular. When a electron is added into these d orbitals, as in Mn^{3+}, the extra electron has to occupy one of the high energy e_g orbitals. This occurs since the crystal field energy splitting is much lower ($\approx$1 eV [44, 45]) than the energy required for putting this extra electron (with antiparallel spin as required by the exclusion principle) in an already occupied t_{2g} orbital ($\approx$ 2 eV ([45, 46]). The electronic energy of the single occupied e_g state in Mn^{3+} can be lowered if the double degeneracy of the e_g orbitals is lifted through deformation of the MnO_6 octahedra, at cost of lattice energy. For example, when the two apical O atoms move away from the Mn ions, the energy of d_{z^2} becomes lower than the $d_{x^2-y^2}$, that moves toward the Mn ions, and the degeneracy is lifted (see figure 1.4). This electron-lattice coupling is generally termed Jahn-Teller distortion.

According to A. K. Bogush *et al.* [47] the MnO_6 octahedra different bond-lengths can be estimated using the unit cell parameters and writes as

$$m^2 = \frac{a^2 + b^2 + c^2}{32} \tag{1.4}$$

$$s^2 = \frac{c^2}{8} - m^2 \tag{1.5}$$

$$l^2 = \frac{b^2 s^2}{16s^2 - b^2} \tag{1.6}$$

where l, m and s are the long, medium and short distances. One should remark that the Mn-O bond lengths calculated from the unit cell parameters give an average value of the MnO_6 octahedra deformation. However, is known that Jahn-Teller local distortions can be present in manganites and the local Mn-O bond lengths cannot be obtained using these expressions.

It is generally agreed that the energy gain due to the Jahn-Teller distortion can bind a charge carrier to its site, creating a polaron[3]. Moreover this strong electron lattice coupling persists for other compositions than the undoped compounds. In fact, in the undoped limit, and at small doping, it is known that a robust structural distortion is present in manganite systems [6]. It is also believed that these polarons are essential to explain the insulating behavior in these compounds [45].

1.2 Magnetic Coupling

$R_{1-x}A_xMnO_3$ manganites can present a variety of magnetic states depending on doping, temperature and applied magnetic field. Commonly, at high temperatures a paramagnetic (PM) state is found and at low temperatures a ferromagnetic or antiferromagnetic order sets in below the transition temperature (Curie or Néel temperature, T_C or T_N respectively). For example, the $LaMnO_3$ and $PrMnO_3$ end-members are antiferromagnetic insulators due to the presence of only Mn^{3+} ions which couple antiferromagnetically via oxygen-mediated Mn^{3+}-Mn^{3+} super exchange interactions (see section 1.2.1). If the trivalent La/Pr ion is partially substituted by a divalent ion like Ca^{2+}, Sr^{2+} or Ba^{2+} a corresponding amount of Mn^{4+} will appear to compensate the charge deficit. The presence of the Mn^{4+} ions favors double exchange ferromagnetic interactions (see section 1.2.2) and a ferromagnetic order can develop below T_C. The temperature and doping level where the ferromagnetic order appears depend sensitively on the elements present in the manganite composition. It is known that exchange interaction depends critically on the interatomic distances and bond angles. In fact, a study by Hwang *et al.* [49] shows precisely the importance of these parameters on the magnetic and electric properties of the manganite systems. They studied several compounds as a function of the tolerance factor (or A site average ionic radius) and figure 1.5 depicts the magnetic and electronic phase diagram obtained in that study. A clear correlation was found between the tolerance factor (or average A site ionic radius) and the critical temperature of the studied compounds. It is commonly accepted that T_C decreases when the Mn-O-Mn bond angle decreases from the ideal φ=180° ($t \neq 1$) since the strength of double exchange depends on the overlap of the spatial wave functions of Mn and O ions.

It has been recognized that the competition between Mn^{3+}-Mn^{3+} antiferromagnetic super exchange and Mn^{4+}-Mn^{3+} ferromagnetic double exchange interactions together with strong

[3] In the context of manganites the term polaron [48] is usually associated with a local distortion of the lattice around the charge, sometimes also with a magnetic cloud or region with ferromagnetic correlations (magnetic polaron).

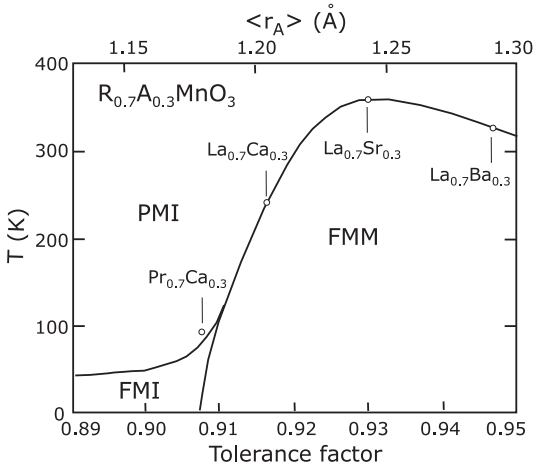

Figure 1.5: Magnetic and electronic phase diagrams of several manganite compounds as a function of the average tolerance factor (or A site ionic radius) (adapted from [49]).

electron lattice coupling dominates the properties of these systems and are responsible for the rich electrical and magnetic phase diagrams. In the following a brief introduction to these exchange interactions is given.

1.2.1 Super exchange

The spin-spin indirect exchange interactions (super exchange and double exchange) involve an electron transfer from an occupied state to an overlapping empty orbital through oxygen ions. If this electron transfer requires an excitation energy, the transfer is just virtual. If no energy is required, the electron transfer is real.

In the case of super exchange this transfer is just virtual. For example if one considers the interaction between two Mn^{3+} ions (one electron in the e_g orbital) no real electron transfer through oxygen occurs since that would require extra energy to accommodate a second electron in the e_g orbitals. The most favorable configuration is that where each e_g electron is antiferromagnetically coupled with an electron in the overlapping 2p oxygen orbitals[4]. This fulfills the Pauli exclusion principle and allows electron delocalization thus reducing the kinetic energy. In this way an antiferromagnetic coupling between the two Mn ions is the favored energetic state. Figure 1.6(a) helps to visualize this spin arrangement.

If one considers the interaction between two Mn^{4+} (empty e_g orbital) also no real charge transfer occurs. The two electrons with antiparallel spins occupying the 2p orbital, which overlaps with the empty e_g ones, can delocalize if each of the Mn^{4+} t_{2g} core spins align parallel with one oxygen electron spin (accordingly to the Hund rule). Consequently an

[4]The two oxygen spins are coupled antiferromagnetically since both electrons belong to the same 2p orbital.

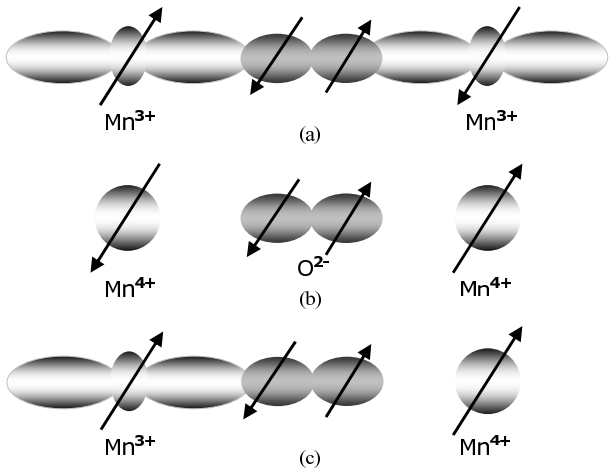

Figure 1.6: Schematic representation of indirect exchange interactions. a) Antiferromagnetic super exchange between Mn^{3+} ions. b) Antiferromagnetic super exchange between Mn^{4+} ions. c) Ferromagnetic double exchange between Mn^{3+}-Mn^{4+} ions.

antiferromagnetic arrangement between the Mn^{4+} is favored. In figure 1.6(b) a schematic representation of this magnetic coupling is shown.

1.2.2 Double exchange

Real charge transfer may occur in a mixed-valent system where the spin interaction between electrons is mediated by the double exchange mechanism. In this case, the exchange between Mn^{3+}-Mn^{4+} via an oxygen ion is achieved by simultaneous transfer of the e_g electron from the Mn^{3+} ion to the oxygen and from the oxygen to the adjacent Mn^{4+}. Due to the strong intra atomic Hund coupling and assuming that carriers do not change their spin when hopping from one ion to the next this mechanism is favored when the mobile electron spin is parallel to the localized atomic spins, *i.e.*, when the two Mn^{3+} and Mn^{4+} ions have a parallel spin arrangement (see figure 1.6(c)).

This mechanism was first introduced by C. Zener [4] and developed by Anderson and coworkers to explain the strong correlation between magnetic and electric properties found by J. Volger [50] who published the first magnetoresistance (MR) data for the Ca and Sr manganite compounds. Considering the interaction of magnetic ions with general spin directions the transfer integral writes [5][5].

$$t_{\mathrm{I}} = t_0 \cos\frac{\theta}{2} \tag{1.7}$$

Here t_0 is the transfer integral due to the spatial part of the wave functions, which decreases when the Mn-O-Mn bond angle decreases, and θ is the angle between the two spin

[5]The quantum version of this process has been described by Kubo and Ohata in 1972 [51]

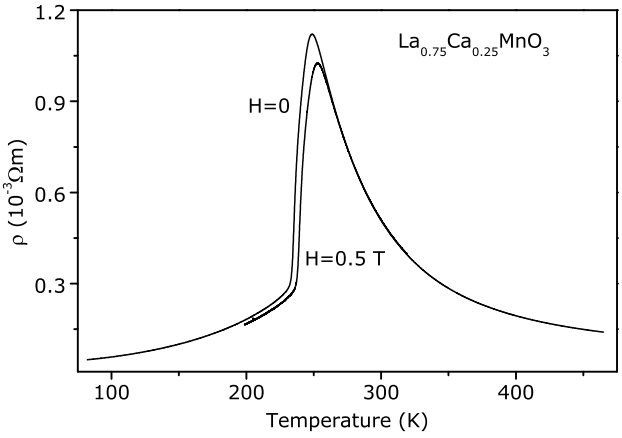

Figure 1.7: Representative manganite resistivity curve as a function of temperature with metal insulatot transition close to T_C (from [52]).

directions of the Mn ions. As one can see, the transfer integral is maximum when spins are parallel and is zero when spins are anti-parallel. Thus the charge carriers have their maximum mobility when the system orders ferromagnetically, *i.e.*, below T_C. Figure 1.7 where a representative resistivity curve obtained on the $La_{0.75}Ca_{0.25}MnO_3$ [52] compound is presented evidences exactly that effect. Below the ferromagnetic order and due to the increase of charge mobility the system presents an insulator to metal transition. By applying an external magnetic field the insulator to metal transition is shifted to higher temperatures.

This interaction, double exchange, explained in broad terms the connection between ferromagnetism and metallicity in the manganites but, as mentioned before, this description is insufficient to handle the very complex phase diagram of manganites.

1.2.3 Magnetic structures

The magnetic interactions between ions described above can give rise to various spin arrangements. Figure 1.8 summarizes the types of spin arrangements most commonly found.

From those one stresses the A and G type antiferromagnetic and B ferromagnetic arrangements as they are more often encountered in the manganites. As it can be seen in figure 1.8 in the A-type AF spin structure FM planes are coupled antiferromagnetically whereas the G type AF structure is characterized by an AF coupling in the three spatial directions. The manganite compounds $LaMnO_3$ and $CaMnO_3$ have the A and G spin structures, respectively. Additionally, a more complex spin structure is also observed in the manganites, the so-called CE-type ordering. This structure will be introduced later in this chapter (section 1.4).

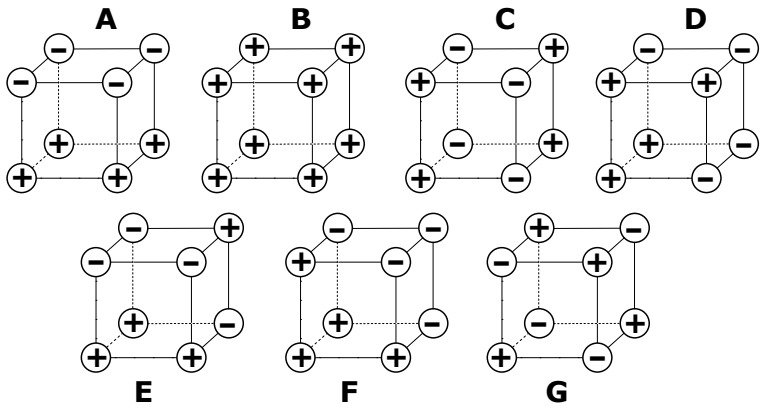

Figure 1.8: Schematic representation of possible magnetic spin arrangements in manganites. Positive and negative signs indicates different spin orientations (adapted from [43]).

1.3 Phase separation

The fact that double exchange is not enough to understand the physics of manganites was evidenced by Millis *et al.* [11, 12] that presented estimations of the critical Curie temperature and resistivity using the DE framework. This author argued that DE produces the wrong T_C by a large factor. Presently, it is widely accepted that the magnetic and electronic properties of manganites are determined by the competition between at least four independent energy scales namely the magnetic interaction between the Mn spins, electron-phonon coupling, Colombic (electronic) repulsion and the kinetic energy of the carriers. The energy scales of these effects are very similar and the delicate balance between them give rise to a ground state which is intrinsically inhomogeneous with strong tendencies toward phase separation. Nowadays studies suggest that tendencies toward phase separation involves typically ferromagnetic metallic and charge ordered (anti or ferromagnetic) insulating clusters. And, contrarily to early ideas based on single isolated polarons, *i.e.*, local distortion of the homogeneous background[6], more recent experimental works clearly illustrates the mixed-phase character of the manganites with substantially larger clusters of one phase embedded on the other [10, 53]. The existence of intrinsic inhomogeneities can occur not only above but also below the ordering temperatures, and also in the high hole-doping region [54]. Moreover, the presence of these nanoclusters in single crystals has been also established experimentally [55].

One of the most important aspect of these mixed-phase tendencies is its link with colossal

[6]initial reports of polarons employed techniques that obtained spatially averaged and not real-spatial information. In fact, using pair-distribution-function (PDF) analysis of neutron powder diffraction $La_{1-x}Ca_xMnO_3$ data, Billinge *et al.* (1996) [13] reported the presence of a mixture of short and long Mn-O bonds, implying distorted and undistorted Mn-O octahedra. Booth *et al.* [14, 14] reached to similar conclusions by using X-ray absorption measurements. These authors used a polaronic picture since from their data they could not distinguish whether the distorted octahedra are randomly distributed, isolated polarons, or spread over more than one atomic site (clusters), compatible with the phase separation scenario.

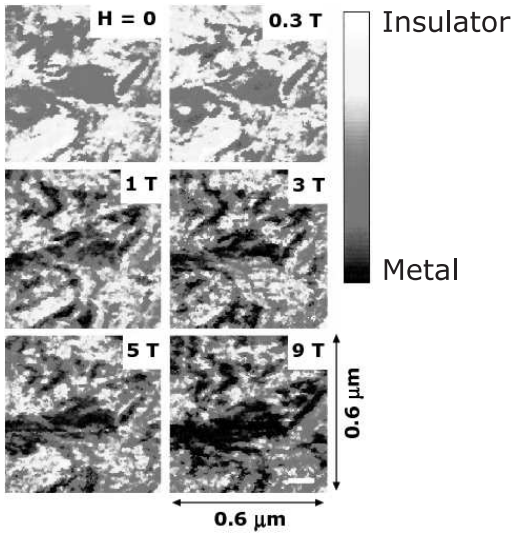

Figure 1.9: Observation of phase coexistence using scanning tunneling spectroscopy. Clusters of metallic and insulating states below T_C with cluster size depending on the applied magnetic field (From [53]).

magnetoresistance effect. These nanoscale inhomogeneities are believed to be crucial for the occurrence of CMR. The observation of clusters involving metallic and insulating states below T_C with a cluster size that depends on the applied magnetic field was associated to the magnetoresistance behavior caused by a percolation process of these two phases. This remarkable evidence of mixed-phase characteristics in CMR manganites was reported by Fath *et al.* [53] using scanning tunneling spectroscopy in the $La_{0.70}Ca_{0.30}MnO_3$. Figure 1.9 presents the result of Fath *et al.* evidencing the phase coexistence and the mentioned percolative process. Similar results were obtained by Uehara and coauthors [56] in their study of $La_{0.250}Pr_{0.375}Ca_{0.375}MnO_3$.

In the last five years an enormous number of experimental results using several techniques have convincingly showed the existence of mixed-phase tendencies in manganites. Among the most important results one can cite the scanning tunneling microscopy works in $(La/Pr)_{5/8}Ca_{3/8}MnO_3$ epitaxial thin film by J. X. Ma *et al.* [57] or the work in $La_{0.33}Ca_{0.67}MnO_3$ by J. Tao and J. M. Zuo [54]. Also, using photoemission spectroscopy (PES) in $(La/Pr)_{3/8}Ca_{3/8}MnO_3$ single crystals, D. D. Sarma and coauthors [55] visualized the formation of distinct insulating domains embedded in the metallic host at low temperatures. Neutron and x-ray scattering measurements provided additional information on this issue namely the works of Dai *et al.* and Kiryukhin and coauthors [58–60] showed the presence of local distortion (correlated/uncorrelated local distortions) in different crystallographic phases and through the metal insulator transition. Distorted local phases in an undistorted matrix were also reported by Mannella and coauthors using Raman spectroscopy [61].

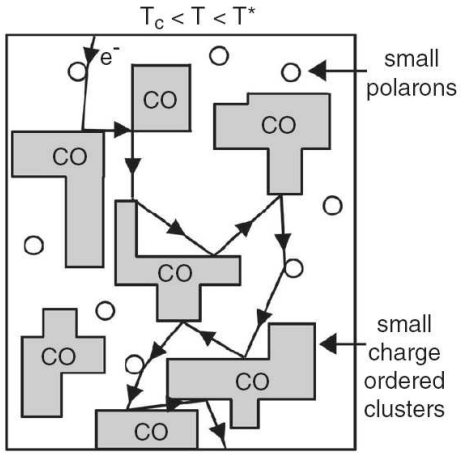

Figure 1.10: Representation of a cluster state in the regime between T_C and T*. Small polarons are represented by circles and electrons travelling across the sample, thick line. The grey areas are the CO clusters where scattering is more severe [22].

Related to these inhomogeneous states the existence of a new temperature scale (T*) well above the Curie temperature where clusters start forming upon cooling was predicted by E. Dagotto [21]. De Teresa and coauthors [19] reported the existence of such a scale and more recent results by Deisenhofer *et al.* [62] also report the existence of such temperature using electron spin resonance and magnetic susceptibility measurements. Figure 1.10 presents a picture of a cluster state between T_C and T*.

The coexistence of FM and AF phases was also found in the $La_{1-x}Ca_xMnO_3$ system at several small hole densities by Allodi *et al.* [63, 64] using nuclear magnetic resonance. Moreover, NMR reports by Savosta *et al.* showed the presence of two competing ferromagnetic phases (insulator and metallic) at low temperatures in $LaMnO_{3+\Delta}$ and $La_{1-x}Sr_xMnO_3$ [65]. Evidence for magnetic inhomogeneities (small magnetic clusters) above T_C was provided using small-angle neutron scattering by De Teresa *et al.* [19, 66]. In the $Pr_{1-x}Ca_xMnO_3$ system an interesting mixed-phase state with FM and charge-order-AF phases for $x \approx 0.33$ at low temperatures was reported by some authors [67–69] specially at high magnetic fields. Moreover in recent $Pr_{0.67}Ca_{0.33}MnO_3$ small-angle neutron scattering studies it is claimed that the ferromagnetic phase exists within the AF matrix in the form of thin layers [70] or ferromagnetic filaments of nanometric diameter [71].

In summary, the presence cluster states appears to be very common in manganites and thus these states should be considered as a new paradigm of the physics of these systems.

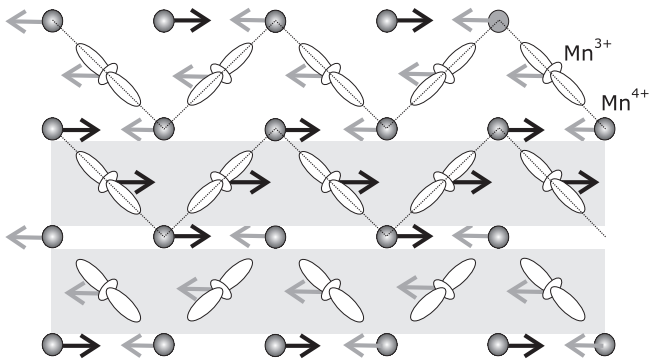

Figure 1.11: Schematic representation, according to the conventional Goodenough's model, of the charge, orbital (d_{z^2}) and CE-type antiferromagnetic ordering in half doped manganates. The figure shows the zig-zag ferromagnetic spin chains coupled antiferromagnetically in the a-b plane. The shadow region evidences charge-order.

1.4 Charge-order

The charge-orbital ordered state along with the so-called CE-type antiferromagnetic order was argued to be the ground state of half-doped manganites by Goodenough [6] in face to the neutron scattering $La_{0.5}Sr_{0.5}MnO_3$ data obtained by Wollan and Koehler (1955) [23]. In the early approach of Goodenough charge-order was assumed as constituting a checkerboard pattern of Mn^{3+}/Mn^{4+} ions, upon which spin and orbital order was found.

The charge-ordered phases in manganites arises from interactions between the charge carriers and phonons where the Jahn–Teller distortions play a significant role. This interaction promotes the charge localization at specific sites below a certain temperature, T_{CO}, giving rise to long-range order of the Mn^{3+}/Mn^{4+} ions throughout the crystal structure. This renders the material insulating. Associated to this charge-order the Mn^{3+} e_g ($3d_{z^2}$) also develop long-range order, promoting orbital ordering. Since the exchange interaction is ferromagnetic through a filled and an empty $3d_{z^2}$ orbital (super exchange between Mn^{3+}-Mn^{4+}), but antiferromagnetic through two empty or two filled $3d_{z^2}$ orbitals, the magnetic exchange interactions between the Mn ions become anisotropic. As a consequence, a complex magnetic ordering in these structures is observed. At low temperatures, charge ordered manganites are antiferromagnetically ordered with a CE-type ordering. Similar effects occur in the end-members where the presence of only one species of Mn ions (Mn^{3+}) gives rise to an orbital order with an A-type antiferromagnetic order. As previously mentioned, in the A-type spin ordering, the spins order ferromagnetically in the a-b plane and these planes pile antiferromagnetically along the c axis. In the CE-type spin ordering the a-b plane stacks also antiferromagnetically along the c axis but the order in the a-b planes is somewhat more complex. These a-b planes are composed of zigzag FM arrays which are coupled antiferromagnetically. Figure 1.11 where the CE-type AF ordering is presented helps to visualize this

carge, magnetic and orbital order arrangement. To accommodate this CE-type spin order the magnetic structure is thus characterized by a duplication of a and b cell parameters, while the crystallographic structure below T_{CO} have a doubled cell along b with respect to the high temperature Pbnm symmetry.

This charge order-orbital state was found not only in compositions with equal proportions of Mn^{3+}/Mn^{4+} (x=0.5) but in many other compositions depending on the A site cations. For example it occurs in the $0.50 \leq x \leq 0.85$ range for the $La_{1-x}Ca_xMnO_3$ series (see figure 1.14(a) [9, 25, 72] and for the x=1/8 and 1/2 in $La_{1-x}Sr_xMnO_3$ [9, 73]. The $Pr_{1-x}Ca_xMnO_3$ and $Sm_{1-x}Ca_xMnO_3$ systems exhibits a large charge ordered region with x extending from 0.30 to 0.90 (see figure 1.14(b)) and from 0.35 to 0.80, respectively [9, 24, 28]. In these latter systems the higher T_{CO} value is obtained for $x \approx 0.60$ while for the LaCa series this value is around $x \approx 0.75$. Generally, the charge ordering occurs in the paramagnetic state (with FM correlations), and the transition to the AF CE-state is accompanied by long-range orbital ordering.

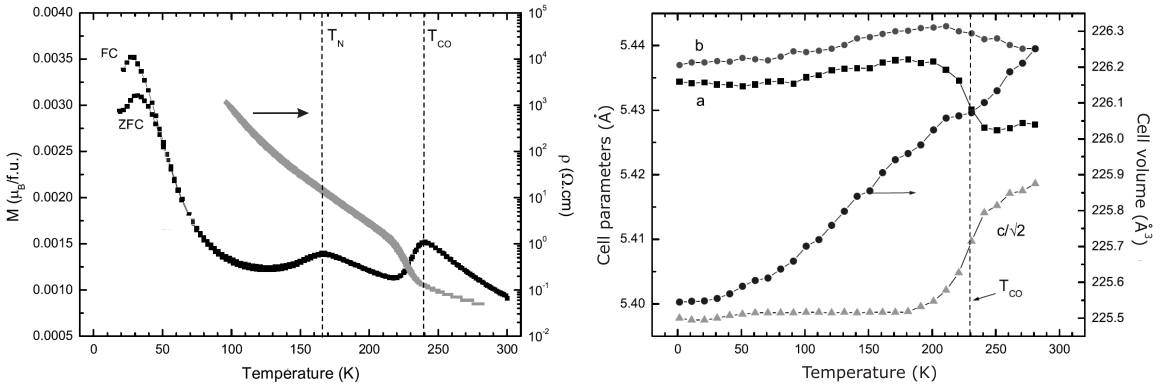

Figure 1.12: Temperature dependence of magnetization and resistivity, a) and lattice parameters, b) observed for $Pr_{0.63}Ca_{0.37}MnO_3$. The critical temperature of the charge/orbital ordering transition ($T_{CO} \approx 240$ K) is higher than the antiferromagnetic Néel temperature ($T_N \approx 167$ K) (from [74]).

Usually, anomalies in the magnetic susceptibility, as well as in the electric resistivity at the charge-order temperature are observed. Figure 1.12 depicts illustrative experimental data evidencing those anomalies as well as the changes in the lattice cell parameters through the CO transition. The increase in the electrical resistivity below T_{CO} due to charge localization, can be visualized in that figure. If one applies a strong magnetic field to these systems those anomalies are no longer visible due to charge-order melting [27]. A similar effect occurs through irradiation with x-rays [33] or pressure [29] application.

Finally one should mention that the famous CO picture with Mn^{3+} - Mn^{4+} checkerboard pattern proposed by Goodenough and latter confirmed by Chen and Cheong using electron

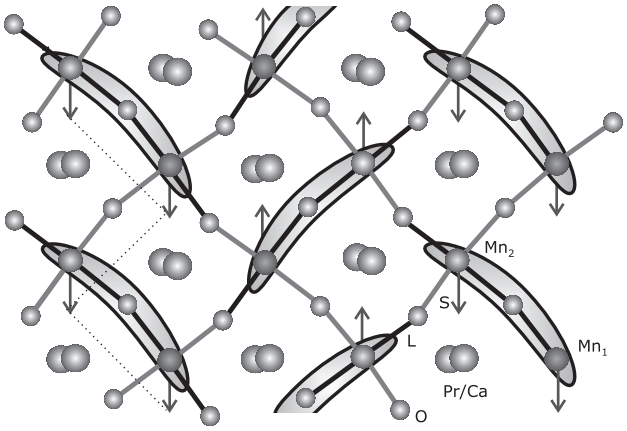

Figure 1.13: Schematic representation of the Zener polaron in manganites according to Aladine's model [36]. Mn ions in distinct crystallographic positions sharing one electron (no charge dispropornation). l and s stand for long and short Mn-O distances. Below T_{CO} the Mn spins in a dimer (Mn_1-O-Mn_2) couple ferromagnetically. Below T_N the CE-type antiferromagnetic order of such pre-formed pairs appears also as a zig-zag of ferromagnetic spin chains coupled antiferromagnetically.

microscopy [25] and Radaelli *et al.* [26] by neutron and x-ray diffraction as well by several other authors has been severely questioned since the works of Garcia and coworkers [34], Rodriguez Carvajal and Daoud Aladine [35, 36]. These authors argue that all Mn ions in the crystal are virtually identical and Daoud Aladine *et al.* proposed an electronic ground state where one e_g electron is shared by two Mn ions, the so-called Zener polaron [35,36]. A schematic representation of the Aladine's model is presented in figure 1.13. Meanwhile, in an attempt to solve this controversy much theoretical and experimental work [35–40] has been devoted to the charge-order state in manganites. In spite of such an effort an conciliatory picture was not so far achieved.

1.5 Magnetic and electric phase diagrams

As mentioned above the fine balance between the energy scales in manganite systems give rise to a series of different magnetic and electronic states with associated phase transitions as a function of temperature and doping. Usually manganite compounds are divided into three groups, namely large, intermediate and small bandwidth systems. This classification is based on the hopping amplitude for electrons in the e_g-band. The effective d-d hopping integral (t) between two Mn neighbors or the electron bandwidth (W) is regulated by the super-transfer process via 2p oxygen orbitals, *i.e.*, depends on the hybridization between the 3d e_g and 2p orbitals. Thus the bandwidth W decreases with the deviation of the Mn-O-Mn bond angle from φ=180°, in other words, when the compound shows a structural variation from the

undistorted perovskite (tolerance factor t≠1). In this way the $Pr_{1-x}Ca_xMnO_3$ is considered as a small bandwidth system as a consequence of its small cation sizes that induce a large deviation of the tolerance factor from unity. The tolerance factor or equivalently average A-site cation radius increases from (Pr, Ca) to (La, Sr) and the $La_{1-x}Sr_xMnO_3$ series represents a prototype for the large bandwidth manganites. One easily realizes that double exchange interactions and metallicity are favored in the latter case while electronic instabilities, such as the charge and orbital order may become dominant in some regions of the intermediate an small bandwidth phase diagram. Figure 1.14 shows the magnetic and electric phase diagram for the $La_{1-x}Ca_xMnO_3$ and $Pr_{1-x}Ca_xMnO_3$ systems.

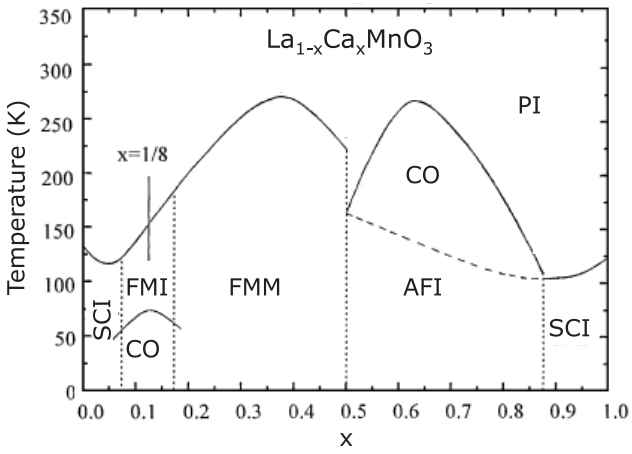

(a)

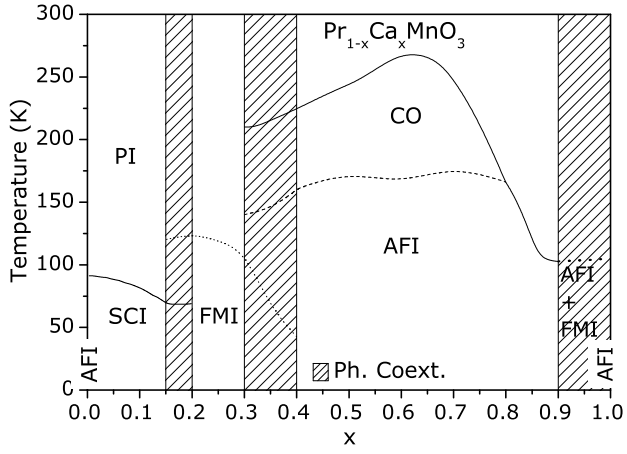

(b)

Figure 1.14: Magnetic and electric phase diagram for the $La_{1-x}Ca_xMnO_3$ system a) (from [75]) and for the $Pr_{1-x}Ca_xMnO_3$ series b) (from [69] [9]).

As one can observe in those phase diagrams the stoichiometric end-members, La/$PrMnO_3$ and $CaMnO_3$ are antiferromagnetic insulators (A-type and G-type respectively, as already

mentioned). For $LaMnO_3$ system a canting of the Mn spins is observed, and hence produces a weak ferromagnetism below T_N. Moreover the $LaMnO_3$ and $PrMnO_3$ endmembers present a collective Jahn–Teller distortion and orbital ordering [76–78]. This Jahn–Teller distorted and orbital-ordered state stabilizes for temperatures below 780 K [76, 77] in $LaMnO_3$ and 1050 K $PrMnO_3$ [78]. The antiferromagnetic insulator state found for the endmembers persists for small doping more precisely, a canting antiferromagnetic insulator state is found. Increasing doping in the $La_{1-x}Sr_xMnO_3$ and $La_{1-x}Ca_xMnO_3$ systems give rise to a ferromagnetic metallic (FMM) ground state for compositions within $0.15 \leq x \leq 0.50$, while this state is absent in the $Pr_{1-x}Ca_xMnO_3$ phase diagram. Instead a ferromagnetic insulator (FMI) state is found for composition ranging $0.20 \leq x \leq 0.30$ and as already mentioned a charge/orbital ordered ground-state extends over $0.30 < x < 0.90$. In the small region $0.90 < x < 1.0$ an antiferromagneic insulator state is again found. In this phase diagram the shadowed areas stand for phase coexistence. The extension of these areas is still controversial. In fact the phase diagram here presented from M. Reis *et al.* [69] presents broader coexistence regions than the original phase diagram from C. Martin and coauthors [9].

As mentioned, chemical substitutions in manganites lead to modifications in the bandwidth due to changes in the average A-site cation radius <r> and consequently changes in the physical properties. L. M. Rodriguez-Martinez and J.P. Attfield [79, 80] have experimentally shown that not only the A-site cation radius play a crucial role in determining the properties of manganites but also cation radius variance which is related with the disorder introduced by chemical substitution in the A-sites. Indeed these authors experimental show that the critical temperature T_C can be reduced by a large factor if the variance σ^2 of the ionic radii is modified, keeping <r> constant.

A different route to induce magnetic/electric and structural phase transitions in manganites relies on the incorporation of excess oxygen (Δ) in the $LaMnO_3$ parent compound. A remarkable property of this system is its wide range of oxidative non-stoichiometry ($0 < \Delta < 0.2$). In $LaMnO_{3+\Delta}$ the oxygen excess cannot be accommodated interstitially in the lattice but results in the creation of equivalent amounts of La and Mn vacancies[7] [81], inducing Mn^{3+} oxidation to Mn^{4+}. The hole content can be approximately given by the simple relation $Mn^{4+} = 2\Delta$ (from charge equilibria) [81]. The phase diagram of this system is presented in figure 1.15. As one can observe the variation of oxygen in $LaMnO_{3+\Delta}$ shifts the temperature of the rhombohedric to orthorhombic structural phase transition and for $\Delta < 0.10$ the system is rhombohedric at room temperature. For low values of Δ ($\Delta < 0.05$) the system stabilizes, at room temperature, in a highly distorted orthorhombic crystallographic structure, O'. The Jahn-Teller temperature defines the transition from the O' phase to the less distorted orthorhombic O phase.

As already mentioned the stoichiometric $LaMnO_3$ is an A-type antiferromagnetic insu-

[7] Accordingly one should write $La_{3/(3+\Delta)}Mn_{3/(3+\Delta)}O_3$.

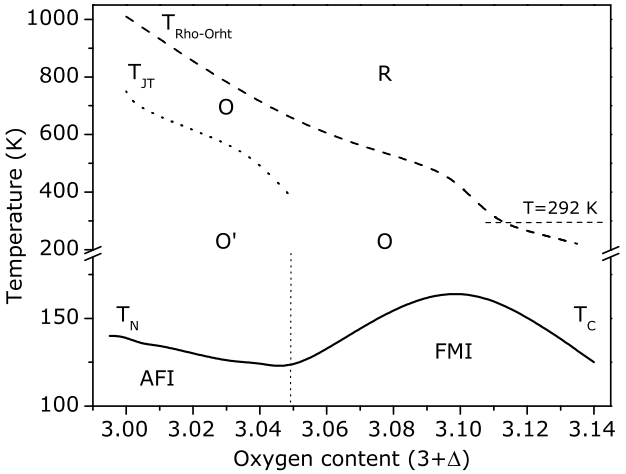

Figure 1.15: Structural, magnetic and electric phase diagram for the $LaMnO_{3+\Delta}$ system (data from [82–84]).

lator. With the introduction of holes, Mn^{4+}, the system evolves, as Δ increases, from the antiferromagnetism observed for $\Delta < 0.05$ towards a ferromagnetic ground state. Nevertheless, the insulator nature of this system persists till very high hole density, $\Delta < 0.15$ [85].

In this chapter we provided only general information about the most relevant aspects of manganite systems. More detailed descriptions about these systems can be found in several review articles [21, 22, 44, 45, 86–92].

Chapter 2

Experimental techniques

In this chapter an overview of the experimental techniques used in this work is presented. In the first part, the macroscopic sample characterization methods are shortly described, giving reference to previous works where these techniques are fully explained. In the second part, technical information on the local probe techniques is given.

2.1 Sample preparation

In the following we shortly describe the sol-gel method for sample preparation. Although some samples were prepared by collaborating groups ($Pr_{1-x}Ca_xMnO_3$ with x= 0.35, 0.40 and 0.50 [93], $Pr_{1-x}Ca_xMnO_3$ with x= 0.25 and 0.32 [94], $LaMnO_{3.12}$ [95] and $CaMnO_3$ [95]) efforts were made to produce bulk samples using the sol-gel method.

The sol-gel techniques has proven to be an adequate method to produce high density colossal magnetoresistance oxides at low sintering temperatures [96, 97]. These techniques has advantages over the other methods, such as solid state reaction, not only for achieving high purity and homogenous samples, but also for a good control of the stoichiometry and grain size of the produced samples [97]. An important aspect related with the work in this thesis is that the short annealing times allows the incorporation radioactive isotopes, as ^{111}In ($^{111}InCl_3$) during sample preparation allowing a homogenous mixing of the components on the atomic scale. This procedure can be used as a complementary method to ion implantation in the preparation of samples for perturbed angular correlation studies were isotopes have half-lives greater than a few hours/days. One also should stress that the low sinterization temperatures allows to prepare samples with high volatile elements that cannot be produced with other methods requiring high sinterization temperatures. In fact, good quality bulk samples, with the desired amount of cadmium, where produced using the sol-gel technic [98–100].

To prepare the manganite samples we followed the sol-gel method description reported by C. Vázquez-Vázquez and co-authors [96]. Stoichiometric amounts of $MnCO_3$, $CaCO_3$ and

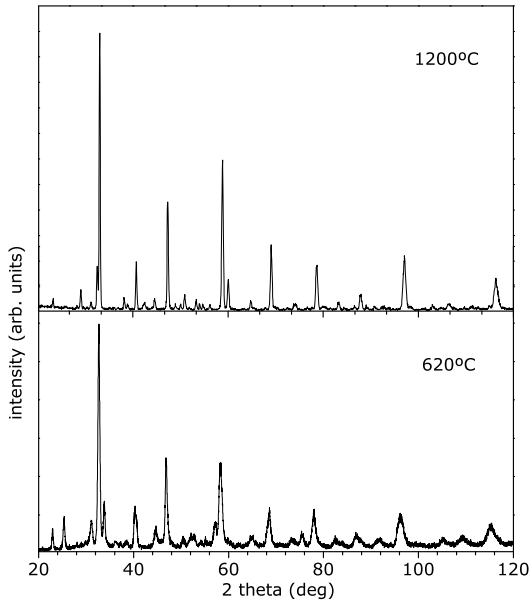

Figure 2.1: x-ray diffraction pattern performed in the $La_{0.65}Ca_{0.35}MnO_3$ test sample: after the annealing treatment at T=1200 °C for t=7 h (top); after calcination at 620 °C for t=3 h (bottom).

Pr_2O_3 (or La_2O_3) were used as starting materials[1]. To each oxide (carbonate) a aqueous solution of HNO_3 was added and the desired nitrates were obtained. These nitrates were mixed and the pH solution was adjusted to 5.2[2]. Urea was used as gelling agent and the optimal molar relationship [urea]/[salts] was found to be [urea]/[salts]=3. That solution was slowly stirred and the solvent evaporated in a hot plate at temperatures ranging from 75 to 137 °C. At T=137 °C urea started to decomposed yielding NH_3. After, a dried gel was formed and then decomposed by heating at 250 °C for ∼3h. The result was a black powder that was grounded in a mortar with a pestle yielding the precursor to prepare the final samples. This precursor was pelletized and calcinated at 620 °C for 3 h. Subsequent annealing treatments were performed to obtain the desired final samples. Between each heat treatment the samples were grounded in a mortar with a pestle and pressed into pellets.

Through x-ray diffraction we detected that at 620 °C the perovskite structure is already formed (see figure 2.1). Although a high crystallinity and absence of spurious phases is found only after subsequent a annealing at T≥1000°C. In figure 2.1 the x-ray diffraction pattern performed in a test sample $La_{0.65}Ca_{0.35}MnO_3$ is shown. To evaluate at the micrometer scale the sample quality, scanning electron microscope (SEM) measurements were performed. The sample composition was estimated by energy dispersive spectrometry. In figure 2.2 a scanning

[1] In reference [96] the starting materials were in the nitrates form. Since the nitrate are highly hygroscopic we opted to use the oxides or carbonates form of the desired elements.

[2] The pH of the solution was controled by adding diluted amonia (NH_3)/acid nitric (HNO_3) to the solution.

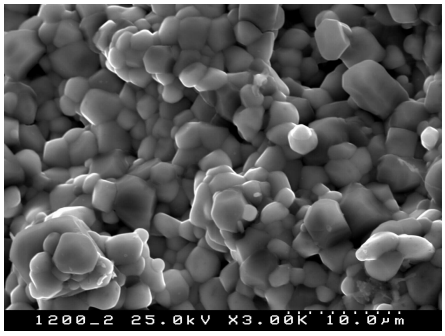

Figure 2.2: Scanning electron microscope photograph performed in the $La_{0.65}Ca_{0.35}MnO_3$ test sample after the annealing treatment at T=1200 °C for t=7 h.

electron microscopy photograph for the $La_{0.65}Ca_{0.35}MnO_3$ test sample, after the annealing treatment at T=1200 °C for t=7 h, is shown. The homogeneity of the sample is clearly visible through the narrow grain size distribution (typical size $\sim 3\mu$ m).

Several samples were prepared using this method [98–100] and in table 2.1 the ones used in this work are listed. In the same table the preparation conditions (final annealing treatment) and stoichiometry, obtained with electron dispersive spectroscopy, are presented. These samples went through the same set of heat treatments, after decomposition, namely a calcination at 700 °C during 3 h, a sinterization at 900 °C for 7 h followed by the final annealing treatment listed in table 2.1. These heat treatments were performed in air and followed by quenching.

Table 2.1: List of samples prepared by the sol-gel method with corresponding final annealing treatments and metal compositions obtained by electron dispersive spectroscopy (EDS).

Nominal composition	Annealing T(°C)/t(h)	EDS results
$PrMnO_3$	1300°C/40 h	$Pr_{0.98}Mn_1$
$Pr_{0.95}Ca_{0.05}MnO_3$	1300°C/40 h	$Pr_{0.93}Ca_{0.053}Mn_1$
$Pr_{0.86}Ca_{0.14}MnO_3$	1300°C/40 h	$Pr_{0.82}Ca_{0.13}Mn_1$
$Pr_{0.60}Ca_{0.40}MnO_3$	1200°C/40 h	$Pr_{0.60}Ca_{0.41}Mn_1$
$Pr_{0.50}Ca_{0.50}MnO_3$	1200°C/40 h	$Pr_{0.49}Ca_{0.51}Mn_1$
$Pr_{0.40}Ca_{0.60}MnO_3$	1300°C/40 h	$Pr_{0.41}Ca_{0.61}Mn_1$
$Pr_{0.35}Ca_{0.65}MnO_3$	1300°C/40 h	$Pr_{0.36}Ca_{0.64}Mn_1$
$Pr_{0.25}Ca_{0.75}MnO_3$	1300°C/40 h	$Pr_{0.21}Ca_{0.71}Mn_1$
$Pr_{0.15}Ca_{0.85}MnO_3$	1300°C/40 h	$Pr_{0.16}Ca_{0.81}Mn_1$
$Pr_{0.05}Ca_{0.95}MnO_3$	1300°C/40 h	$Pr_{0.05}Ca_{0.91}Mn_1$

As already mentioned some samples were prepared by collaborating groups and a description of the sample preparation method can be found in [43, 101].

2.2 Structural and chemical characterization

X-ray diffraction To check the quality of the produced samples and determine the average crystallographic structure $\theta - 2\theta$ x-ray measurements were performed at *Laboratório Central de Análise, Aveiro* (LCA). For this purpose a Philips X Pert - MPD x-ray diffractometer with Cu K_α radiation (λ=1.541 Å), primary and secondary monochromators and automatic slits was used. Also to make detailed studies of the temperature dependence of the crystallographic structure, this diffractometer is equipped with a system that allows to perform x-ray measurements in a 80 K to 550 K temperature range. For this work the diffractograms were obtained in a $10° < 2\theta < 110°$ range and depending on the desired precision of the measurement the 2θ steps ranged between 0.01° and 0.03°. For a more detailed explanation of this experimental technique and measurement procedures see [102, 103].

Scanning electron microscopy/energy dispersive spectrometry In order to evaluate, at the micrometer scale, the sample quality and to obtain the composition, a FEI scanning electron microscope (SEM) model Quanta 400 FEG, and equipped with an energy dispersive spectrometer available at the *Departamento de Química da Universidade de Trás-os-Montes e Alto Douro* was used. These studies were performed in collaboration with Professor Pedro Tavares.

A detailed description of the experimental apparatus, operating modes and technical specifications is available in [104]

2.3 Magnetic and electric characterization

SQUID magnetometer Most of the magnetization measurements necessary to this work were performed at *Instituto de Física de Materiais da Universidade do Porto* (IFIMUP) in a Quantum Design Superconducting Quantum Interference Device (SQUID) magnetometer. This magnetometer has a 10^{-7} emu resolution and is equipped with 5.5 Tesla superconducting coil. This system allows accurate magnetization measurements in low applied fields in a 4 to 380 K temperature range. Other magnetization measurements were performed in a similar SQUID magnetometer at *Centro Brasileiro de Pesquisas Fisícas* (CBPF), Rio de Janeiro.

To perform the necessary measurements samples with needle shape were used[3]. These samples were mounted in plastic straws either glued with a special low temperature tape or inside a gelatine capsule.

To obtain the sample magnetic parameters such as Curie (T_C), Néel (T_N) or charge-order (T_{CO}) temperature low field magnetization measurements were performed. For this purpose the thermal dependence of magnetization (in low fields) was acquired after the sample has been cooled without applied magnetic field (ZFC) and /or field cooled (ZFC), such that:

[3]Needle-like samples were used in order to reduce demagnetization effects.

-Zero field cooling, sample cooled with H=0 to the lowest temperature then, the magnetic field was applied and the subsequent magnetization measurements was performed while sweeping the temperature in a range of 10 K up to 380 K.

-Field cooling, sample cooled down to the desired temperature under an applied field. The measurement was performed, with constant applied field, while heating in the same range of temperatures.

Most of the samples were measured using only the field cooling sequence. Whenever it was possible the magnetization measurements were performed using both sequences and the magnetization irreversibility was checked. Ideally these measurements should be performed with a magnetically virgin superconducting coil to avoid remanent fields and inhomogeneities. When that was not possible and a remanent field was present, the sample magnetization in the paramagnetic phase was used to determine the correction to the applied field.

In the following chapters, to compare the magnetization curves at different fields, one approximates the susceptibility in the ordered phase as χ=M/H (low coercive fields and remanence).

Isothermal curves (M*vs.*H curves) were also obtained in order evaluate the saturation magnetization. In these cases measurements were performed while decreasing the applied magnetic field from 5 to 0 Tesla.

For a detailed description of the experimental apparatus, technical specifications and measurement principles see [103, 105, 106].

Resistivity and magnetoresistance To study the manganite compounds on their electrical and magnetoresistance properties, the set-ups available at IFIMUP, Porto and CBPF, Rio de Janeiro were used. Both systems allow measurements in a 10 to 300 K range of temperatures and a temperature controller insures a temperature stabilization better than 0.1 K. In the IFIMUP set-up a conventional bipolar electromagnet is able to apply an external magnetic field up to 1 Tesla. The sample is cooled in a closed cycle refrigerator. The CBPF set-up operates with a helium bath and is equipped with a Superconducting coil, allowing to perform resistivity measurements with an applied magnetic field up to 12 Tesla.

Resistance and magnetoresistance measurements were made using a standard experimental procedure. First the samples were glued with a varnish (G-varnish) to the copper sample-holder (this varnish provides a good thermal contact between the two elements). After, the electrical contacts were made with silver paste and 70μm diameter copper wires. In all measurements the standard four contact in line technique was used. The sample-holder is then mounted in the refrigerator cold finger.

To obtain the sample resistivity a Time Electronics DC current calibrator was used to impose a stabilized DC current ($\Delta I/I = 10^{-6}$) through the sample. The voltage was measured by a Keithley 181 nano-voltmeter (1 nV resolution). In this measurement current inversion was introduced to eliminate possible thermal induced voltages. In this way, the resistivity

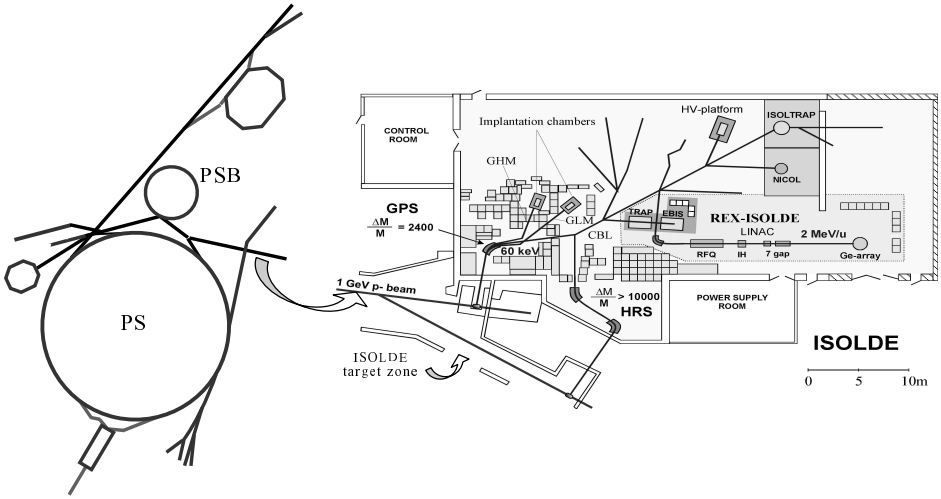

Figure 2.3: Overview of CERN accelerators and ISOLDE hall with general purpose separator (GPS) with it's three different beam lines (CBL, GLM and GHM). Implantation chambers in the end of the GLM and GHM beam lines.

data was acquired changing continuously the temperature with the desired rates (typically in the 0.2 to 1 K/min range). Details of the set-up description and measurement principles can be found in [105, 107, 108].

2.4 Local probe technique

Production of radioactive isotopes To perform our local probe measurements radioactive isotopes are needed. These isotopes can be introduced into the samples ether by diffusion of a solution containing the desired isotope or via ion implantation. A large number of nuclei are produced in Isotope Separators On-Line facilities as ISOLDE-CERN [109]. This infrastructure offers a wide variety of radioactive isotopes some of which are suitable for nuclear solid state physics techniques, as Mössbauer or perturbed angular correlations.

At ISOLDE, isotopes are produced by nuclear reactions via irradiation of an appropriated target placed in the external 1 GeV proton beam delivered by the CERN PS-Booster (PSB). This target under intense bombardment, supplies the radioactive beam, that after element selection and magnetic mass analysis, is steered to the experiments.

In detailed, the PS Booster is able to deliver a pulse of 3.2×10^{13} protons every 1.2 seconds in each super cycle. A super cycle is composed of 12 pulses that are distributed among CERN experiments. Usually, up to half of the pulses are brought to bombard the ISOLDE target, giving approximately a 2 μA proton beam. These beam conditions allows the production of short-lived isotopes at ISOLDE target. As shown in figure 2.3, where a scheme of the accelerators and ISOLDE hall is shown, protons from the PSB are delivered to the

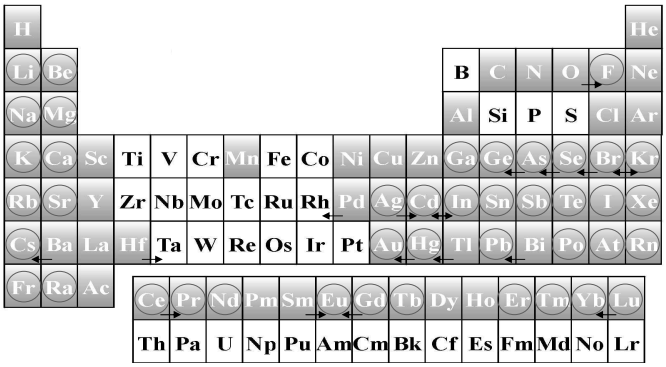

Figure 2.4: Periodic table showing the elements produced at ISOLDE (light gray). Circles represent elements for which suitable isotopes exist for solid state experiments. Arrows indicate possible feeding of the PAC element by a neighboring isobar elements during $\beta^{\pm}$ and EC decays.

ISOLDE target zone. Here two isotope separators are located: the high resolution separator (HRS) and the general purpose separator (GPS) with mass resolution $\Delta M/M<1/10000$ and $\Delta M/M=1/2400$, respectively. In this way, the two separators can run in parallel in a time-shared mode. The radioactive beam distribution system is done in such a way that all experiments can be fed by either isotope separators through a central beam line (see figure 2.3). Additionally, the beam arising from the general purpose separator can split into three different mass beams within a certain mass range (15% of the central mass) and delivered simultaneously into the experimental hall via three different beam lines (central mass (CBL), low mass (GLM) and high mass beam line(GHM)). In figure 2.3 one also can see a schema of the general purpose separator and the three different beams. The produced nuclei diffuse in the hot target and are ionized by an appropriate ion-source[4] being then accelerated to 60 kV into the separator beam-lines till the implantation chambers.

Actually ISOLDE can deliver more than 600 isotopes of 70 different elements. In figure 2.4 a periodic table showing those elements is presented. There the elements suitable for solid state experiment such as emission channeling (EC), mössbasuer or perturbed angular correlation (PAC) are referred.

Sample Implantation Usually the implantations for solid sate physics at ISOLDE are made in the GPS separator in one of the implantation chambers mounted at the GLM or GHM beam lines. The control systems of the separator beam lines are based on personal computers and PC-consoles via a local area network that allows to access the hardware for controls and measurements. In this way, users can easily operate the magnets, quadrupoles and vacuum system needed to steer the beam through the separator beam lines. After

[4] In the production of ^{111m}Cd isotope, the most used isotope in this thesis, a Sn target with plasma ion source was used.

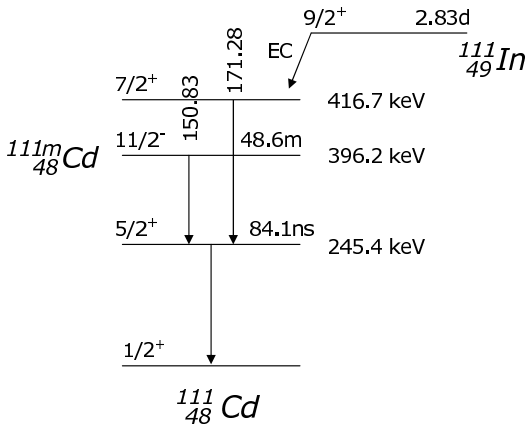

Figure 2.5: Simplified decay schemes for ^{111}In and ^{111m}Cd cascade. Intermediate PAC probe state with energy E=245.4 keV, half life $t_{1/2}$=84.1 ns and angular momentum I=5/2.

optimization of the beam current that arrives to the implantation chamber and selection of the desired isotope in the mass control set-up the system is ready to start the implantation process.

The solid state implantation chambers are equipped with beam collimators and a multi-sample holder allowing to implant several samples without breaking vacuum. The collimators and sample holder position are controlled by a step-motor that is operated from the control-room. In the course of sample implantation for PAC experiments the beam is swept to produce an homogeneous implanted area (usually 5×5 mm^2), so as to effectively achieve doses below 10^{13} at.cm^{-2}. During implantations the current arising to the samples is measured and integrated to perform dose control.

The implantation profiles of implanted samples can be calculated using the TRIM [110] code. The projected range, R_P,[5] and the straggling, σ, were calculated for manganite samples implanted with ^{111m}Cd [52]. The values obtained for cation doped manganite systems were R_P ∼188 Å and σ ∼76 Å and R_P ∼185 Å and σ ∼76 Å for $LaMnO_{3.12}$.

Table 2.2: Magnetic dipole, μ, and electrical quadropole, Q, moments for the 245.4 keV state (intermediate state of the ^{111}In → ^{111}Cd and ^{111m}Cd → ^{111}Cd cascade (from [111]).

μ (μ_N)	Q (b)
-0.766(3)	0.83(13)

Although several isotopes were tested (*e.g.*, ^{149}Gd, ^{172}Lu and ^{204m}Pb) showing promising results as probes for perturbed angular correlations experiments in manganite systems, in

[5]Usually the implanted ions depth profile is approximated by a gaussian function centered in R_P (projected range) and standard deviation σ (straggling).

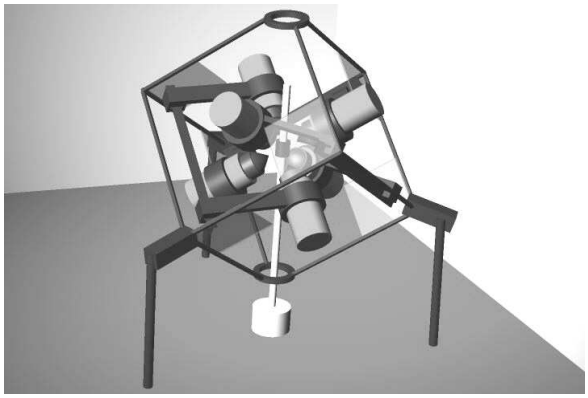

Figure 2.6: Schematic representation of the 6-Detector $\gamma - \gamma$ PAC spectrometer. The refrigerator/furnace can be mounted in the center of the detectors.

this work we have concentrated in ^{111m}Cd and ^{111}In. The nuclear probe characteristics as the decay scheme of the ^{111}In and ^{111m}Cd isotopes is presented in figure 2.5 and the dipole and quadropole moments of the intermediate state of the ^{111}In $\rightarrow$ ^{111}Cd and ^{111m}Cd $\rightarrow$ ^{111}Cd cascade are presented in table 2.2. Nuclear data parameters concerning these and other isotopes can be found in [111].

The facilities for sample preparation include a fully equipped radioisotopes laboratory and a tube furnace with capability of annealing samples in vacuum or in gaseous controlled pressure atmospheres. The temperature of the furnaces is electronically controlled and heat treatments can be performed up to 1500 °C.

Once samples are implanted an annealing is performed to remove the remaining implantation damage. Annealing at 700 °C for 20 minutes in oxygen flow is enough to remove the ^{111m}Cd implantation damages in manganite systems [52]. This is particularly convenient due to the short half-life (48 min.) of ^{111m}Cd, mostly used probe isotope in this work. Although in the $Pr_{1-x}Ca_xMnO_3$ system the annealing procedure was the same for all the samples (20 min. at 700 °C in oxygen flow), for $LaMnO_{3+\Delta}$ oxygen doped manganites, to preserve the samples oxygen content, the annealings were performed in controlled atmosphere according to the conditions depict in table 4.1.

In the particular case where the ^{111}In was incorporated into the sample via diffusion the sample was first wetted with a $^{111}InCl_3$ solution of 10 μ Ci activity and then, to remove the chloride and promote the isotope diffusion, a subsequent heat treatment was performed. In the $LaMnO_{3+\Delta}$ compound the best conditions for the annealing was 5 hours at 1000 °C in a $P_{O_2} = 2 \times 10^{-5}$ bar atmosphere.

Finally one should mention that according to the literature [112, 113] in manganites systems the ^{111m}Cd and ^{111}In probes occupy the A (La/Pr/Ca) site in the perovskite structure.

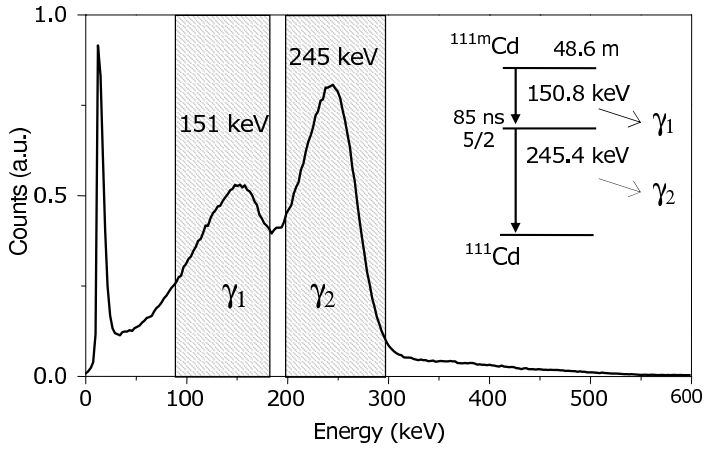

Figure 2.7: ^{111m}Cd energy γ spectrum from BaF_2 detectors. The shadowed areas show the SCA energy discrimination regions for γ_1 (start) and γ_2(stop).

$\gamma-\gamma$ Perturbed Angular Correlation set-up After the post annealing procedure samples are mounted in the perturbed angular correlation spectrometer. The $\gamma-\gamma$ PAC experiments reported here were performed with a highly efficient 6-detector PAC spectrometer (see figure 2.6) equipped with BaF_2-scintillators [114] which have 650 ps time resolution.

This setup produces 30 spectra from the detector paired combinations, 6 detectors at θ= 180° and 24 at θ= 90°. Summarily, a PAC spectrometer records the time-dependent histogram of events in which a photon γ_1 enters a detector and at a time t later a second photon γ_2 enters another detector. From each detector, the dynode (positive) signal is preamplified and sent to a linear amplifier (LA) unit. The LA unit integrates a fraction of the dynode signal to produce a proportional signal that is then analyzed by a single-channel analyzer (SCA) that is tuned to the energy of $\gamma_1(\gamma_2)$ (see figure 2.7). The SCA produce a digital positive gate signal each time a γ ray arrives with the selected energy (signal amplitude). In parallel the anode (negative) signal is reshaped in the constant-fraction (CF) units to provide optimum time markers for start/stop signals. A coincidence of the SCA signals, with energy information on γ_1 (start) or γ_2 (stop), is performed with the signal from the CF units, with information on the precise γ arrival-time. When these signals, with energy and time information overlap in coincidence, new start/stop signals are generated that contain now information of their provenance from γ_1 or γ_2. These signals are sent to actuate the time-amplitude converter (TAC), that produces an analogic signal with amplitude proportional to the time difference between the arrival of the start and stop signals. The TAC output signal is then digitized by an ADC and sent to a multichannel analyzer (MCA) to record the histogram of counts/versus time, of each detector pair. The signals from the SCA are also used to determine the combination of γ_1 and γ_2 detectors, *i.e.*, to determine

the spectrum number where the event should be stored in the MCA. The spectra recorded in the MCA are then transferred to a personal computer for data treatment and analysis.

For PAC measurements between 10 K up to room temperature, samples are mounted in a closed-cycle helium refrigerator equipped with resistive heater and PID temperature controller (stabilization $\sim$ 0.1 K). For temperatures above room temperature and up to 1100 °C, under O_2, N_2 or Ar atmospheres, a resistive furnace is used (stabilization $\sim$ 1 K). Both the furnace and the refrigerator are mounted in such way that the sample is at the center of the detector's assembly. Fast sample transfer systems exist, both for the refrigerator and furnace, that allow measurements with short lived isotopes by pre-setting the desired temperature.

Chapter 3

Nuclear methods

Hyperfine interactions, *i.e.*, the interactions between the nuclear moments and the extranuclear electromagnetic fields can be measured by several nuclear hyperfine techniques. The measurement of these interactions provides a very sensitive and accurate method to investigate condensed matter phenomena in a large variety of materials, providing direct information on the local charge distribution and magnetic hyperfine fields. Often, subtle differences in the microscopic aspects of materials originate very distinct macroscopic properties. Hence, nuclear hyperfine methods appear as important tools in solids state physics. Nuclear magnetic (quadrupolar) resonance, muon-spin rotation, nuclear orientation and perturbed angular correlation, are examples of such techniques. The information provided by these techniques is crucial in highly correlated systems such as the high-Tc superconductors and the manganites where intrinsic disorder, local distortions and local phase segregation are of key importance [21,22]. Phenomena like polaron formation, static and dynamic distortions in such complex systems requires real-lattice atomic scale studies with direct measurements on the local aspects.

In this section some aspects of hyperfine interactions,relevant for this work, will be presented focusing on those that are related to the perturbed angular correlation, technique. Detailed accounts can be found in [115–117].

3.1 Nuclear interactions

In this section we consider the subject of interactions between the nuclear quadrupolar and magnetic moments and the extranuclear electromagnetic fields (electric and magnetic fields). In a solid the nuclei are not isolated and interact with the local environment. If the nuclear moments are known the extranuclear electromagnetic fields can be determined via hyperfine measurements.

3.1.1 Electrical quadrupole interaction

The electrical quadrupole interaction energy, E_Q, can be introduced from the classical description of the interaction electrostatic energy of a nuclear charge density $\rho(\boldsymbol{r})$ with an external electrical potential $\Phi(\boldsymbol{r})$ [115, 116],

$$E = \int \rho(\boldsymbol{r})\, \Phi(\boldsymbol{r})\, d^3r \tag{3.1}$$

If the potential is slowly varying over the region where $\rho(\boldsymbol{r})$ is nonnegligible then it can be expanded in a Taylor series around the origin.

$$\Phi(\boldsymbol{r}) = \Phi(0) + \boldsymbol{r}.\nabla\Phi(0) + \frac{1}{2}\sum_{i,\,j} x_i\, x_j \left(\frac{\partial^2\Phi}{\partial x_i\, \partial x_j}\right)_0 + ... \tag{3.2}$$

Inserting this expression on the equation 3.1 and employing the definitions of total charge (q), electric dipole moment ($\boldsymbol{p}$), electric quadrupole moment tensor ($Q_{i\,j}$) and using, for simplicity, $\Phi_{ij} = (\frac{\partial^2\Phi}{\partial x_i\, \partial x_j})_0$ we find,

$$E = q\Phi(0) + \boldsymbol{p}.\nabla\Phi(0) + \frac{q}{6} < r^2 > \nabla^2\Phi(0) + \frac{e}{6}\sum_{i,\,j} \Phi_{i\,j} Q_{i\,j} \tag{3.3}$$

where e is the magnitude of the electron charge and the definitions of total charge, electric dipole moment and electric quadrupole moment tensor are the usual ones,

$$q = \int \rho(\boldsymbol{r}) d^3r \tag{3.4}$$

$$p_i = \int x_i \rho(\boldsymbol{r}) d^3r \tag{3.5}$$

$$Q_{i\,j} = \frac{1}{e}\int \rho(\boldsymbol{r})\, (3x_i\, x_j - r^2\delta_{i\,j})\, d^3r \tag{3.6}$$

and $< r^2 >$ is the mean square nuclear radius.

The first term in equation 3.3, the zero order term, is the electrostatic energy considering the nucleus as a point charge, thus, is a constant during electromagnetic nuclear internal transitions and do not contribute to energy splitting. The first order term represents the electric dipole interaction. Due to the well defined parity of the nuclear wave function, the electric dipole moment of the nuclear charge distribution is zero. From the second order term of the multipolar expansion two contributions arise (third and forth terms in equation 3.3). The first of these two is known as the monopole term and depends only on the mean square nuclear radius and on the electron charge density at the nucleus[1]. In this way this

[1]Note that the external electrostatic potential $\Phi(\boldsymbol{r})$ obeys the Poisson equation, $Tr(\Phi) = \sum_i \Phi_{ii} = \nabla^2\Phi(0) = \frac{e}{\varepsilon_0} \mid \psi(0) \mid^2$, where $-e \mid \psi(0) \mid^2$ is the electronic charge density at the nucleus, only nonnegligible for s electrons.

term only shifts the nuclear levels, not contributing to their splitting. The monopolar term is responsible for the so called isomer shift in mössbauer spectroscopy. In perturbed angular correlation, the observed frequencies depend only on the relative energy splitting of the measuring nuclear state, thus this term is not observed.

The last term in equation 3.3 is known as the electric quadrupole interaction energy. In nuclei with nonnegligible quadrupole moment this is the most relevant electric interaction being responsible for the nuclear level splitting. Since Q_{ij} is a traceless tensor one can introduce the electric field gradient tensor $V_{ij} = \Phi_{ij} - \frac{1}{3}Tr(\Phi)$ as the traceless part of the second partial derivatives tensor of the potential at the nucleus. The quadrupole energy defined above is invariant under the substitution of Φ_{ij} by V_{ij}. This emphasizes the fact that a hyperfine quadrupole interaction measurement can only access to the electric field gradient tensor, *i.e.*, such measurement is not sensitive to external charges present at the nucleus, as mentioned above. Accordingly the quadrupole energy is commonly written as,

$$E_Q = \frac{e}{6}\sum_{i,j} V_{ij}Q_{ij} \tag{3.7}$$

The electric field gradient is a symmetric tensor thus, it is possible to find an eigenvector basis where V_{ij} is diagonal. Since the EFG tensor is traceless it can be completely described by two of its components. It is common to chose the eigenvalue with largest magnitude and the asymmetry parameter η to describe it. By appropriate choice of the eigenvector basis the eigenvalues are arranged in such a way that $\mid V_{zz} \mid \geq \mid V_{yy} \mid \geq \mid V_{xx} \mid$. The asymmetry parameter $\eta = \frac{V_{yy}-V_{xx}}{V_{zz}}$, measures the deviation of the local charge distribution from axial symmetry (*e.g.*, tetragonal, rhombohedral or hexagonal).

The quadrupole energy can be written using explicitly the asymmetry parameter, η, and EFG principal component, V_{zz}, yielding,

$$E_Q = \frac{eV_{zz}}{12}[3Q_{zz} + \eta(Q_{xx} - Q_{yy})] \tag{3.8}$$

To calculate the effect of the quadrupole interaction in a nuclear level characterized by its angular momentum $\hbar\boldsymbol{I}$ the quantum formulation has to be used. The expression above remains valid for the interaction hamiltonian $\hat{H}_Q$ with the quadrupole tensor components, Q_{ii}, substituted by the correspondent quantum operators, $\hat{Q}_{ii}$. The Wigner-Eckart theorem [118] can be used to write $\hat{H}_Q$ in a more convenient form. Since the quadrupole operators are homogenous functions of the coordinates (x, y, z) their matrix elements in the $2I+1$ manyfold, $\langle I, m|\hat{Q}_{ii}|I, m'\rangle$, are proportional to those of an operator where each coordinate is substituted by the correspondent angular momentum operators ($\hat{I}_x$, $\hat{I}_y$, $\hat{I}_z$), *i.e.*, the Wigner-Eckart theorem allows us to write

$$\langle I, m|\hat{Q}_{ii}|I, m'\rangle = \alpha(I)\langle I, m|3\hat{I}_i^2 - I(I+1)|I, m'\rangle \tag{3.9}$$

The proportionality constant can be determined by the definition of the quadrupole moment Q, which is the expectation value of the quadrupole operator $\hat{Q}_{z\,z}$ in the nuclear state $|I, I\rangle$ [116], then

$$Q = \langle I,\, I|\hat{Q}_{z\,z}|I,\, I\rangle = I(2I-1)\alpha(I) \Rightarrow \alpha(I) = \frac{Q}{I(2I-1)} \tag{3.10}$$

Using equations 3.9 and 3.10 in 3.8 the quadrupole interaction hamiltonian can be written as,

$$\hat{H}_Q = \frac{eQV_{z\,z}}{4I(2I-1)}[3\hat{I}_z^2 - I(I+1) + \eta(\hat{I}_x^2 - \hat{I}_y^2)] \tag{3.11}$$

The pre-factor in equation 3.11 gives the energy scale for the nuclear quadrupole interaction from which one can define the quadrupole frequency,

$$\omega_Q = \frac{eQV_{zz}}{4I(2I-1)\hbar} \tag{3.12}$$

The quadrupole interaction hamiltonian cannot be diagonalized exactly for non-axial symmetric quadrupole interaction ($\eta \neq 0$) and numerical methods have to be employed.

For the particular case of an axial symmetric interaction the eigenvalues of the hamiltonian are given by

$$E_Q = \hbar\omega_Q \left[3m^2 - I\,(I+1)\right] \tag{3.13}$$

The transition energy between two sublevels m and m' is given by:

$$\Delta E_Q = 3\hbar\omega_Q \mid m^2 - m'^2 \mid \tag{3.14}$$

$\mid m^2 - m'^2 \mid$ is always integer so all transition frequencies are multiples of ω_Q and the fundamental observable frequency ω_0, the lowest transition frequency is:

$\omega_0 = 6\omega_Q$ - for I half-integer

$\omega_0 = 3\omega_Q$ - for I integer

Is also usual to define another quantity, the fundamental frequency:

$$\nu_Q = \frac{eQV_{zz}}{h} = \omega_0 \frac{4I(2I-1)}{2\pi\, k} \tag{3.15}$$

where k=3 (for I integer) or k=6 (I half-Integer).

3.1.2 Magnetic interaction

In a similar way as the electric quadrupole interaction energy, the magnetic dipolar energy E_m can be introduced from a classical description where a localized distribution of current

$\boldsymbol{J}(\boldsymbol{r})$ interacts with an external magnetic field $\boldsymbol{B}(\boldsymbol{r})$ that derives from a vector potential[2] $\boldsymbol{A}(\boldsymbol{r})$ [115, 117]

$$E_m = -\int \boldsymbol{J}(\boldsymbol{r}).\boldsymbol{A}(\boldsymbol{r})d^3r \tag{3.16}$$

Considering that the vector potential varies slowly over the region of current, the dominant terms in the energy can be find expanding the vector potential in a Taylor series around the origin. Due to the parity of the current function the even terms of the expansion vanish. The dominant term is thus the dipolar (first-order) term. To determine it it is not necessary to perform explicitly the Taylor expansion and it is sufficient to calculate the magnetic energy by equation 3.16 considering the vector potential of a uniform magnetic field

$$\boldsymbol{A}(\boldsymbol{r}) = \frac{1}{2}\boldsymbol{B}(\boldsymbol{r}) \times \boldsymbol{r} \tag{3.17}$$

Inserting equation 3.17 in equation 3.16 we find

$$E_m = -\frac{1}{2}\int (\boldsymbol{r} \times \boldsymbol{J}(\boldsymbol{r})).\boldsymbol{B}(\boldsymbol{r})d^3r \tag{3.18}$$

From the classical definition of the magnetic dipolar moment

$$\boldsymbol{\mu} = \frac{1}{2}\int \boldsymbol{r} \times \boldsymbol{J}(\boldsymbol{r})d^3r \tag{3.19}$$

We thus obtain the well known expression for the magnetic dipolar energy

$$E_m = -\boldsymbol{\mu}.\boldsymbol{B} \tag{3.20}$$

The dipole moment of a nuclear charge distribution is proportional to its angular momentum $\hbar\boldsymbol{I}$

$$\boldsymbol{\mu} = \gamma\hbar\boldsymbol{I} \tag{3.21}$$

where γ is the gyromagnetic ratio, which is often expressed by the nuclear magneton μ_n [3] and the dimensionless g-factor, *i.e.*, $\gamma = g\mu_n/\hbar$.

In quantum mechanics the expression for the magnetic dipolar energy has a similar form as the classical one substituting $\boldsymbol{\mu}$ by the correspondent quantum operator, $\hat{\boldsymbol{\mu}}$.

The hamiltonian of such a magnetic interaction is diagonal in the $|I, m\rangle$ basis, supposing the magnetic field applied parallel to the z axis. The corresponding eigenvalues are given by

$$E_m = -\gamma\hbar B_z m \tag{3.22}$$

This interaction lifts completely the degeneracy of the 2I+1 manyfold. Thus, the energy

[2] $\boldsymbol{B}(\boldsymbol{r}) = \nabla \times \boldsymbol{A}(\boldsymbol{r})$

[3] $\mu_n = \frac{e\hbar}{2m_p} = 5.05082(2)\times10^{-27}$ J·T^{-1}, where m_p is the proton mass [118].

splitting between any two adjacent, sublevels is

$$\Delta E_m = \gamma \hbar B_z = \hbar \omega_L \tag{3.23}$$

where $\omega_L = \gamma B_z$ is the Larmor frequency.

When both magnetic and electric interactions are present the hamiltonian for such combined static interactions, in the proper reference frame of the EFG tensor is given by [116]

$$\mathcal{H} = \hbar \omega_Q \left[3\, I_z^2 - I\,(I+1) + \frac{1}{2}\eta (I_+^2 + I_-^2) \right] + \boldsymbol{\mu} \cdot \boldsymbol{B} \tag{3.24}$$

where, for the quadrupole part, we have used the identity $I_x^2 - I_y^2 = \frac{1}{2}(I_+^2 + I_-^2)$. Whenever combined interactions are present the hamiltonian cannot be diagonalized analytically and its eigenvalues and eigenvectors must be calculated numerically.

3.2 Perturbed angular correlation technique

Perturbed angular correlations is a nuclear technique that makes use of radioactive isotope probes to extract both the Magnetic Hyperfine Field and the Electric Field Gradient, with great sensitivity and accuracy. PAC is particularly useful when: suitable nuclear states do no exist in stable isotopes to be used by NMR and NQR techniques; one aims to probe a small number of impurity atoms; large temperature ranges are to be studied. As a result, it has been used successfully for some decades not only in condensed matter physics but also in chemistry, biology and medicine [119].

Historically, the first application of radioactive isotopes in solid-state physics dates to 1920, when radioactive lead atoms were used to study self-diffusion in liquid and solid lead (for an account on this pioneer work see G. Havesy's noble lecture [120][4]). In 1940, D.R. Hamilton predicted the directional correlation of a $\gamma - \gamma$ cascade [123]. During several years the attempts to demonstrate this effect experimentally were inconclusive and only in 1947 Brady and Deutsch managed to measure such correlations [124]. An extension to Hamilton's calculations was made by G. Goertzel to take into account the perturbation of a magnetic field to the angular correlation [125]. Theoretical and experimental approaches were continuously improved and in 1953 a thorough treatment of PAC theory was published by A. Abragam and R.V. Pound [126]. The first report on a Perturbed Angular Correlation measurement was presented in 1955 by P. Lehmann and J. Miller [127]. In the early period, PAC experiments intended to systematically collect data on Electric Field Gradients in noncubic metals and on Magnetic Hyperfine Fields in ferromagnetic materials such as iron, nickel and other 3d ferromagnetic metals. Later, PAC studies of point lattice defects and radiation damage became the main topic of PAC research. From these early experiments till nowadays

[4] Original articles in German language [121, 122].

PAC has evolved into a method that is widely used in many research fields. In particular very interesting work has been done in high T_C superconductors [128–130], semiconductors [131–133] and intermetallic materials [134, 135]. Although PAC spectroscopy as been also extensively used to study perovskite compounds [136–140] in manganites systems only a few works have been published up to now. In fact, besides the work of our group only three reports in $LaMnO_3$ [112,141,142] and two publications in Hafnium doped $La_{0.67}Ca_{0.33}MnO_3$ and $La_{0.7}Sr_{0.3}MnO_3$ [143,144] are known in the literature. Thus a systematic study of hyperfine fields in manganites aiming to achieve atomic scale insight in these systems is missing.

In this section we will focus on the most relevant aspects of the perturbed angular technique. The general theory and mathematic formalism behind this technique is extensively reported in several thesis [52, 145–148], textbooks and review articles [116, 149–152].

3.2.1 Angular correlation

Perturbed angular correlation is based on the emission of two consecutive γ rays (or e-γ) from internal decay of a probe nucleus. Due to the conservation of the angular momentum, $\boldsymbol{I}$, there exists a correlation between the emission directions, $\boldsymbol{k_1}$ and $\boldsymbol{k_2}$, of these two γ. Normally, in a set of nucleus the spins are randomly oriented in space and the emitted radiation is isotropic.

To obtain an anisotropic γ angular distribution the $2I+1$ degenerate m sub-levels cannot be equally populated, *i.e.*, the state from which the radiation is emitted has to be polarized or aligned. The nuclei are considered to be "aligned" if the density of states $\rho(m)$ of the sub-levels depends only on its absolute value, *i.e.*, $\rho(m) = \rho(-m) \neq \rho(m')$. On the other hand, the set of nuclei is referred as "polarised" when the density of states $\rho(m)$ depends on m with $\rho(m) \neq \rho(-m)$ [150]. There are several methods to orient a set of nuclei, for example, an oriented state can be accomplished by applying low temperatures and a strong magnetic field giving rise to a dependence of the density of states $\rho(m)$ according to the Boltzman distribution. In the case of angular correlations the oriented set of nuclei is obtained by choosing only those nuclei whose spins happen to lie in a preferred direction. Considering a nuclei in a $|I_i, \pi_i, m_i\rangle$ initial state that decays through a cascade emitting two successive γ-rays (see figure 3.1) and assuming that the initial nuclear state is randomly oriented, *i.e.*, equal occupation of the different m_i states, the observation of γ_1 in a fixed direction $\boldsymbol{k_1}$ (that we can chose as the z axis) selects an ensemble of nuclei in the intermediate state whose m magnetic sub-levels are no longer equally populated. This is a consequence of the angular momentum conservation[5] and the angular distribution of the electromagnetic radiation with

[5] $\boldsymbol{I_i} = \boldsymbol{I} + \boldsymbol{L}$ where $\boldsymbol{I_i}$ and $\boldsymbol{I}$ are the angular momentum of the initial and intermediate nucleus state respectively and $\boldsymbol{L}$ is the photon angular momentum.

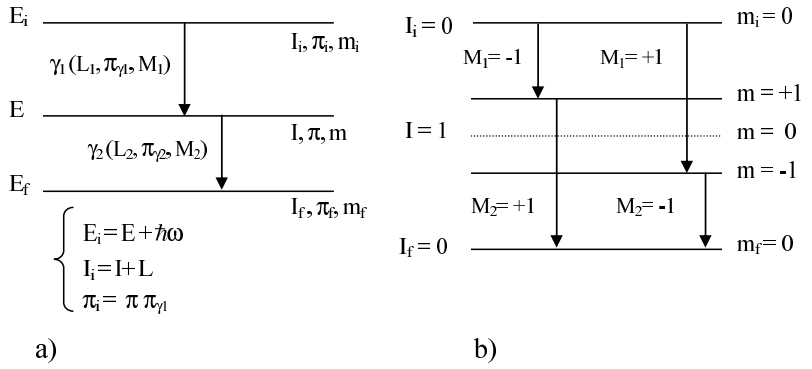

Figure 3.1: a) Scheme representing the emission of two γ particles from a radioactive decay through a cascade between the nuclear states $E_i \rightarrow E \rightarrow E_f$ (the index i and f refers to initial and final states respectively). The states are characterized by the angular moment, I, and parity, π. The conservation relations are shown in the same figure. b) On the right hand side is presented an example of the alignment of the intermediate state of the cascade $I_i = 0 \rightarrow I = 1 \rightarrow I_f = 0$, *i.e.*, the sublevel $m = 0$ is not populated.

respect to its angular momentum, $\boldsymbol{L}$[6]. The latter is responsible for the absence of radiation with $M \neq \pm 1$.

A schematic illustration of the intermediate state alignment can be observed in figure 3.1b. Due to the alignment of the intermediate state the emission pattern of γ_2 is anisotropic and shows a angular correlation with respect to the observation direction of γ_1 (see figure 3.2).

The probability $W(\theta)$ of finding γ_2 in a certain direction, $\boldsymbol{k_2}$, at an angle θ with respect to $\boldsymbol{k_1}$ and in coincidence with γ_1 can be expressed by [150][7]:

$$W(\boldsymbol{k_1}, \boldsymbol{k_2}) = W(\theta) = \sum_{k=0}^{k=k_{max}} A_k(\gamma_1) A_k(\gamma_2) P_k(\cos(\theta)) \tag{3.25}$$

where the sum runs over for even values of k as a result of parity conservation of the electromagnetic radiation. The upper limit, k_{max} is determined by the smallest of $2I$, $L_1 + L_1'$ and $L_2 + L_2'$ where $L_{1,2}$ and $L'_{1,2}$ are the multipolarities of the transitions. The cascade anisotropy terms, $A_k(\gamma_1)$ and $A_k(\gamma_2)$, describe the deviation of the coincidence probability from the isotropic case where $W(\theta) = 1$. In equation 3.25 the coefficient $A_k(\gamma_1)$ depends only

[6]The angular distribution, $F_{LM}(\theta)$, of an emitted γ-ray can be calculated from the solutions of the Maxwell equations, being $F_{LM}(\theta) = \frac{|\boldsymbol{L} Y_L^M|^2}{\sum_M |\boldsymbol{L} Y_L^M|^2}$. One should note that $F_{LM}(\theta = 0^\circ) = 0$ for $M \neq \pm 1$ [115, 116].

[7]The angular correlation function is derived using the density matrix formalism, $\hat{\rho}(\boldsymbol{k})$, within which W($\boldsymbol{k_1}$, $\boldsymbol{k_2}$) is simply given by W($\boldsymbol{k_1}$, $\boldsymbol{k_2}$)=Tr$\{\hat{\rho}(\boldsymbol{k_1})\hat{\rho}(\boldsymbol{k_2})\}$. Where the density matrixes in the intermediate and final states are respectively

$\langle m|\hat{\rho}(\boldsymbol{k_1})|m'\rangle = \sum_{m_i} \langle m|\hat{\mathcal{H}}_1|m_i\rangle\langle m'|\hat{\mathcal{H}}_1|m_i\rangle^*$,

$\langle m'|\hat{\rho}(\boldsymbol{k_2})|m\rangle = \sum_{m_f} \langle m_f|\hat{\mathcal{H}}_2|m\rangle\langle m_f|\hat{\mathcal{H}}_2|m'\rangle^*$.

$\hat{\mathcal{H}}_1$ and $\hat{\mathcal{H}}_2$ are the hamiltonians responsible for the radiation emission γ_1 and γ_2 respectively.

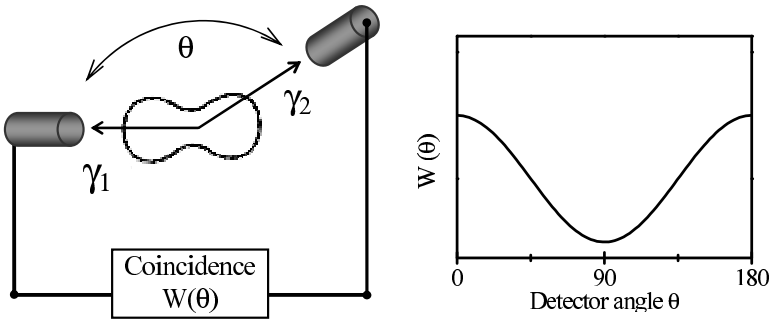

Figure 3.2: Experimental setup to measure the $\gamma-\gamma$ angular correlation, *i.e.*, the γ_2 intensity, $W(\theta)$, with respect to the emission direction of γ_1. On the right hand side is presented an illustrative representation of $W(\theta)$.

on the first transition and $A_k(\gamma_2)$ only on the second, more specifically they depend on the correspondent angular momentum of the involved levels and on the type and multipolarity of emitted radiation. Their values have been tabulated and can be found in [153, 154]. Finally, the Legendre polinomials P_k reflect the spatial angular distributions of the emitted particles. The emission pattern of the described situation can be obtained experimentally by placing two detectors in plane, one of them being fixed and the other movable (see figure 3.2). Note that although we have mentioned angular correlations between two emitted γ rays we find also angular correlations between other type of emitted particles[8].

3.2.2 Perturbed angular correlation

Equation 3.25 is valid for the free nuclei in the absence of extra-nuclear fields. In the presence of such fields an interaction between those fields and the nuclei moments (section 3.1) appear. In this case the angular correlation function will be perturbed becoming time dependent. The nuclear quadrupole moment coupling with an Electric Field Gradient and/or the nuclear magnetic moment coupling with a Magnetic Hyperfine Field is be responsible for the splitting on the nuclear magnetic sublevels. During the time t that a nucleus remains at the intermediate state (time elapsed between the emission of γ_1 and γ_2) the nucleus is subjected to a hyperfine interaction that promotes a change in the occupation of the different magnetic sublevels ($m - m'$ transitions) and consequently, the emission probability of γ_2, in a certain direction, becames time dependent.

In order to consider the perturbation into the angular correlation, the expression 3.25 has to be modified according the changes in the sublevel occupation during the elapsed time of the two γ-ray (re-population of the intermediate state). Within the density matrix

[8] Angular correlations between $\gamma - e_c^-$, $e_c^- - \gamma$ or $e_c^- - e_c^-$ are also possible (where e_c^- are conversion electrons from atomic orbitals). Note that the expression 3.25 is also valid for these correlations but with different anisotropy terms, $A_k(e_c^-) = b_k(e_c^-)A_k(\gamma)$ [150], where the parameter $b_k(e_c^-)$ takes into account the fact that the electron has finite mass. These b_k values can also be found in tables [153].

formalism, the density operator $\hat{\rho}(\boldsymbol{k_1})$, which describes the nuclear system immediately after the emission of the first radiation ($t = 0$), is no longer constant evolving according to the Liouville-von Neumann equation

$$\frac{d\hat{\rho}(\boldsymbol{k_1},\,\mathrm{t})}{dt} = -\frac{i}{\hbar}\,[\hat{\mathcal{H}},\hat{\rho}(\boldsymbol{k_1},\,\mathrm{t})] \tag{3.26}$$

Where the hamiltonian $\mathcal{H}$ accounts for the presence of the extranuclear fields. For a static hamiltonian the density operator $\hat{\rho}(\boldsymbol{k_1},\,\mathrm{t})$ is then given by:

$$\hat{\rho}(\boldsymbol{k_1},\,\mathrm{t}) = \hat{\Lambda}(t)\hat{\rho}(\boldsymbol{k_1})\hat{\Lambda}^{\dagger}(t) \tag{3.27}$$

The influence of the perturbation in the intermediate state is thus described by the unitary time-evolution operator $\hat{\Lambda}(t)$

$$\hat{\Lambda}(t) = e^{-\frac{i}{\hbar}\hat{\mathcal{H}}t} \tag{3.28}$$

The $W(\boldsymbol{k_1},\boldsymbol{k_2},t)$ angular correlation function is now given by

$$W(\boldsymbol{k_1},\boldsymbol{k_2},\,\mathrm{t}) = Tr\{\hat{\rho}(\boldsymbol{k_1},\mathrm{t})\hat{\rho}(\boldsymbol{k_2})\} = Tr\{\hat{\Lambda}(t)\hat{\rho}(\boldsymbol{k_1})\hat{\Lambda}^{\dagger}(t)\hat{\rho}(\boldsymbol{k_2})\} \tag{3.29}$$

The calculation of equation 3.29 requires the determination of the matrix elements of the emission hamiltonians which is mathematically elaborate and lengthy, being well described in [150]. Here we present only the final result.

$$W(\boldsymbol{k_1},\boldsymbol{k_2},\,\mathrm{t}) = \sum_{k_1,k_2,N_1,N_2} A_{k_1}(\gamma_1)A_{k_2}(\gamma_2)\frac{Y_{k_1}^{N_1}(\theta_1,\phi_1)Y_{k_2}^{N_2}(\theta_2,\phi_2)}{\sqrt{(2k_1+1)(2k_2+1)}}\;G_{k_1k_2}^{N_1N_2}, \tag{3.30}$$

where the A_k anisotropy terms were defined above and $Y_k^N(\theta,\phi)$ are the spherical harmonics with θ and ϕ being the usual angles of spherical coordinates for the emission directions $\boldsymbol{k}$. The last term in the equation 3.30 contains all the information about the hyperfine fields, depending only on the interaction of the intermediate nuclear state with its environment, but not on the nuclear transitions[9]. The perturbation function is given explicitly, in terms of 3j symbols and matrix elements of $\hat{\Lambda}$, by

$$G_{k_1k_2}^{N_1N_2}(t) = \sum_{m_a,m_b}(-)^{2I+m_a+m_b}\sqrt{(2k_1+1)(2k_2+1)}\begin{pmatrix} I & I & k_1 \\ m_a' & -m_a & N_1 \end{pmatrix} \begin{pmatrix} I & I & k_2 \\ m_b' & -m_b & N_2 \end{pmatrix}\langle m_b|\hat{\Lambda}|m_a\rangle\langle m_b'|\hat{\Lambda}|m_a'\rangle^* \tag{3.31}$$

[9]The part related with nuclear transitions, coming from the emission hamiltonians, is expressed by the anisotropy coefficients and by the spherical harmonics.

where $m_{a,b}$ are $m'_{a,b}$ are the m quantum numbers of the intermediate state, the summation runs over $|m_{a,b}| \leq I$ and $m'_{a,b} = m_{a,b} - N_{1,2}$. In the same way, indices $N_{1,2}$ are restricted to $|N_{1,2}| \leq k_{1,2}$.

The perturbed angular correlation function depends on the crystalline nature of the radioactive source being greatly simplified if the sample under study is polycrystalline. In this case the function is obtained by averaging the angular correlation over all possible orientations of the EFG/MHF fields and only the relative angle between the two emission directions becomes relevant. Moreover, if the interaction hamiltonian is static and diagonal (as in the case of magnetic interactions with the magnetic field along the quantization axis or axially symmetric quadrupole interactions) the matrix elements of the time evolution operator can be further specified since

$$\langle m_b|\hat{\Lambda}(t)|m_a\rangle = \langle m_b|e^{-\frac{i}{\hbar}\hat{\mathcal{H}}t}|m_a\rangle = e^{-\frac{i}{\hbar}E_m t}\delta_{m,m_a}\delta_{m,m_b} \tag{3.32}$$

In this special case the angular correlation function reduces to [149]:

$$W(\theta,t) = \sum_{k=0}^{k=k_{max}} A_k(\gamma_1)\, A_k(\gamma_2)\, G_{kk}(t)\, P_k(\cos(\theta)) \tag{3.33}$$

and using the relation 3.32 the perturbation function writes

$$G_{kk}(t) = \sum_{m,m'} \begin{pmatrix} I & I & k \\ m' & -m & m-m' \end{pmatrix}^2 e^{-\frac{i}{\hbar}(E_m - E_{m'})t}, \tag{3.34}$$

From $G_{kk}(t)$ one can obtain the energy splitting of the m sublevels of the intermediate state, and consequently the hyperfine fields can be measured through a Perturbed Angular Correlation experiment. The energy splitting $E_m - E_{m'}$ due to the magnetic dipolar and electric quadrupole interaction can be found in section 3.1, equations 3.23 and 3.14 respectively. The perturbation function $G_{kk}(t)$ for a static axial symmetric electric quadrupole interaction in a polycrystalline sample will be[10]

$$G_{kk}(t) = \sum_{n=0}^{n_{max}} s_{kn} cos(n\omega_0\, t), \tag{3.35}$$

where s_{kn}[11] are the frequency amplitudes, $n = |m^2 - m'^2|/2$ for I half integer and $n = |m^2 - m'^2|$ for for I integer. This simple case illustrates how the angular correlation is perturbed. The angular correlation 'precesses' with a superposition of several harmonics of a

[10] For a non-diagonal $\hat{\mathcal{H}}$ ($\eta \neq 0$) a diagonal matrix of eigenvalues can be obtained. In this case an equivalent expression to 3.35 can be derived but the new frequencies ω_n are functions of η and cannot be simply written as multiples of a fundamental frequency. Thus the cosine argument $n\omega_0$ writes ω_n [149].

[11] $s_{kn} = \sum_{m,m'} \begin{pmatrix} I & I & k \\ m' & -m & m-m' \end{pmatrix}^2$

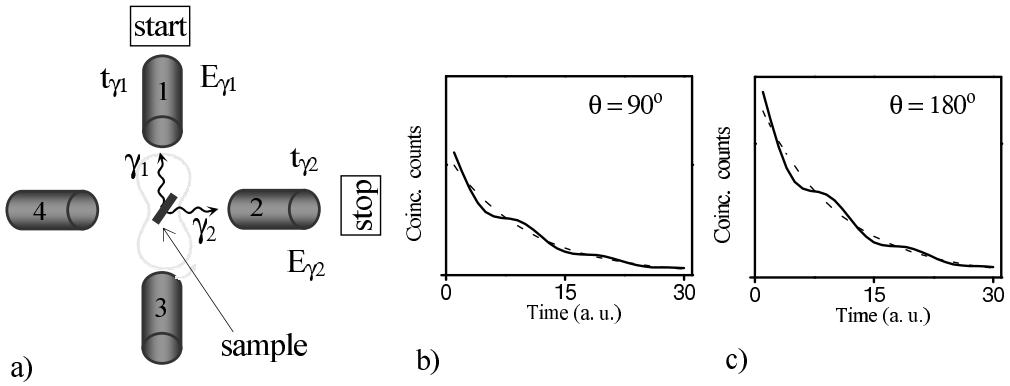

Figure 3.3: a) Scheme of a in-plane four detector $\gamma-\gamma$ PAC experimental setup. On the right hand side is presented an illustrative representation of the count rate at, b) 90° and c) 180° for "positive" anisotropy. The dashed line represents the count rate for a non perturbed system, *i.e.*, the pure exponential histogram associated to the radioactive decay of the intermediate nuclear level.

fundamental frequency ω_0. Examples of analytic expressions derived for other special cases and detailed information that is not presented here can be found in [116, 126, 149, 150, 155].

3.2.3 PAC experimental function and data analysis

To determine the perturbation factor $G_{kk}(t)$, which contains all information concerning the hyperfine fields, the coincidence count rates, N, as a function of time between the emission of the two gama-rays, γ_1 and γ_2, at a fixed detector angle, $N(\theta, t)$ should be measured.

As previously mentioned (section 2.4), a PAC experimental apparatus consist of a group of detectors geometrically arranged in such way that the angles between pairs of detectors is 90^o or 180^o. If a γ-ray is detected in detector, i, having the correct energy, E_{γ_1}, a clock is started. Then, after a certain time a second γ-ray will reach one of the other detectors, j. If this second γ-ray has the expected energy, E_{γ_2}, the clock will stop and this event will be stored in the coincidence counter of the i, j pair of detectors.

The experimental coincidence count rate between detectors i and j is given by:

$$N_{ij}(\theta, t) = N_0\, e^{-t/\tau}\, W(\theta, t) + B \tag{3.36}$$

where θ is the angle between the i and j detectors, $t = t_{\gamma_2} - t_{\gamma_1}$ is the time delay between detection of the two γ-rays. N_0 is proportional to the number of radioactive nuclei present in the sample and with the perturbed angular correlation, $W(\theta, t)$, already given in 3.33. Finally, B is proportional to the background random coincidence count-rate and here is assumed to be time independent for simplicity. Two examples of such count rate are presented in the right hand side of figure 3.3 for detectors with $\theta = 90°$ and $\theta = 180°$.

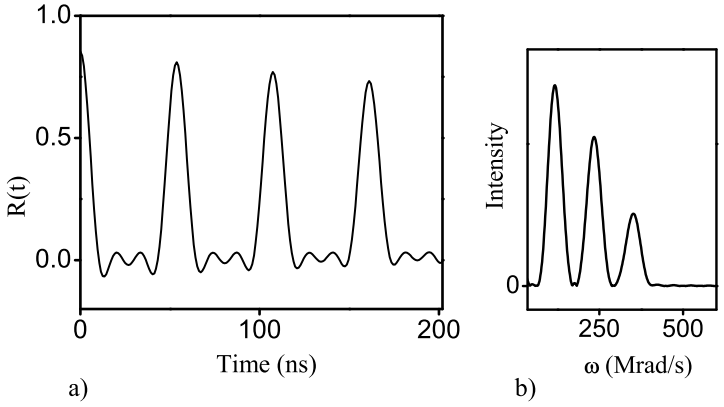

Figure 3.4: a) Example of the experimental $R(t)$ function. On the right hand side, b) the corresponding Fourier transform is presented. The three frequencies $(\omega_1, \omega_2, \omega_3)$ in the Fourier transform are characteristic from a spin 5/2 and fully characterize the EFG parameters, V_{zz} and η.

Once the coincidence count rate between detectors is measured the experimental perturbation function $R(t)$, quantity that provides all the relevant information, is constructed. Depending on the type of set-up, several spectra, usually taken for $\theta = 90°$ and $\theta = 180°$, are combined so that the exponential decay is removed to reveal the perturbation function. After background, B, subtraction, an appropriate average of all the coincidence count rate $N_{ij}(\theta, t)$, coming from detector pairs with the same angular separation is made: $N(\theta, t) = \sqrt[N_\theta]{\prod_{ij} N_{ij}(\theta, t)}$. Here N_θ is the total number of spectra at a certain angle. Then the $R(t)$ function is obtained from

$$R_{exp}(t) = 2\frac{N(180°, t) - N(90°, t)}{N(180°, t) + 2N(90°, t)} \tag{3.37}$$

Note that the geometric average of all spectra taken at the same detectors angle aims to correct for detector efficiency differences [156]. In figure 3.4 is shown an example of the $R(t)$ function (a) and correspondent Fourier transform (b). The measurable experimental quantity, $R_{exp}(t)$, can be related with $G_{kk}(t)$ that contains the information about the hyperfine fields.

Data analysis To extract quantitative information from a PAC measurement a theoretical fit of the experimental data is performed. The method relies on the construction of a theoretical function, $R_{fit}(t)$. In this way the perturbation function (equation 3.35) is calculated numerically by taking into account the full hamiltonian for the nuclear electric quadrupole and/or magnetic dipole hyperfine interactions. This is done using a computer software [145, 157] which calculates numerically the eigenvalues and eigenstates of the hamiltonian in equation 3.24. To take into account the finite time resolution of the PAC setup the $G_{kk}(t)$ is modified multiplying each term in the sum by $P(F^*_{whm}, \omega_n)$ (defined below). In

addition, possible EFG distributions are taken by into account multiplying the $G_{kk}(t)$ the distribution's fourier transform $D(F_{whm}, t)$ (see below).

$$G'_{kk}(t) = \sum_n s_{kn} \cos(\omega_n t) D(F_{whm}, t) P(F^*_{whm}, \omega_n) \tag{3.38}$$

The corresponding perturbed angular correlation functions $W'(\theta, t)$ are then calculated for $\theta = 90°$ and $\theta = 180°$. The function, whose parameters are changed to fit the $R_{exp}(t)$ function, is constructed as

$$R_{teor}(t) = 2\frac{W'(180°, t) - W'(90°, t)}{W'(180°, t) + 2W'(90°, t)} \tag{3.39}$$

We should stress that commonly distinct fractions of probes are subjected to distinct EFGs or MHFs and the effective fit function becomes in this case

$$\overline{W'(\theta, t)} = \sum_i f_i W'_i(\theta, t) \tag{3.40}$$

where f_i (with $\sum f_i = 1$) is the relative intensity of each $W'_i(\theta, t)$ angular correlation function characterizing the *ith* fraction of probe atoms interacting with a particular EFG/MHF.

Static attenuation Frequently, the hyperfine field responsible for the nuclear interaction is not exactly the same for all the probes and thus a distribution of frequencies around a central value is measured. Typical reasons for such slightly differences are the presence of lattice defects (*e.g.*, implantation defects) or chemical disorder in the probe's near vicinity. Such distributions of hyperfine fields induce an attenuation of the PAC time spectrum [158]. For low concentrations of defects these distributions can be represented by a gaussian or a lorentzian function in the frequency space. In the analysis program this is considered, as mentioned above, by multiplying the calculated perturbation function by the Fourier transform of the frequency distribution. In the case of a gaussian fields distribution, the attenuation function, in time space, can be written as:

$$D_{gauss}(F_{whm}, t) = e^{-\frac{F^2_{whm}}{16\,ln2}\,t^2} \tag{3.41}$$

where the standard deviation σ is defined as $\sigma = F_{whm}/\sqrt{8\,ln2}$ and F_{whm} stands for the distribution full width at half maximum. In the literature it is common to find the standard deviation instead of the F_{whm}. As output of the fit program the standard deviation is given as a fraction (δ) of the fundamental frequency $\delta = \sigma/\omega_0$.

In the case of a Lorentzian frequency distribution we have

$$D_{lorentz}(F_{whm}, t) = e^{-\frac{F_{whm}}{2}\,t} \tag{3.42}$$

Also here often we write $\sigma = \delta\omega_0$ where σ is now defined as $\sigma = F_{whm}/2$.

The amplitudes of the periodic components, s_{kn}, are attenuated by the finite time resolution of the spectrometer τ_{setup}. This attenuation becomes important when $\omega_n \tau_{setup} > 2\pi$ and a correction to the s_{k_n} coefficients is necessary. Such correction is taken into account by multiplying each coefficient by the term $P(F^*_{whm}, \omega_n)$ that is a function of the observed frequencies. The time resolution (prompt) function of the spectrometer, is also assumed to be gaussian-like and as the form:

$$P_(F^*_{whm}, w_n) = e^{-\frac{F^{*2}_{whm}}{16\,ln2}\,\omega_n^2} = e^{-\frac{1}{2}\,\tau^2_{setup}\,\omega_n^2} \tag{3.43}$$

3.3 Time dependent interactions

Dynamical processes in condensed matter such as ion or carrier hoping, defects or ion diffusion leads to hyperfine field fluctuations. Roughly, such EFG or MHF fluctuations of either magnitude, symmetry or orientation will contribute to attenuate the PAC signal if the fluctuation time-scale is comparable to the analysis range (lifetime) of the PAC probe state. Often a correspondence can be made between the attenuation strength and the frequency rate of the fluctuating fields. Thus, the analysis of these effects might give also information about dynamic effects in matter. This information is crucial to gain further insight on the microscopic nature of many systems, and might be particularly relevant in manganites where short-range charge diffusion coupled to lattice distortions (polarons) is the key of some unusual macroscopic physics phenomena.

While conceptually the distinction between a damped static interaction and an interaction with time-dependent effects is clear, experimentally the distinction of these two effects may be quite ambiguous. In the particular case of our compounds it is very likely that broadened lines will arise from randomly distributed dopant atoms and/or defects. Thus, the interpretation of the line-broadening as arising from a dynamic effect is not straightforward. Although in some particular cases, as we will see, the dynamic effect contribution to the $R(t)$ shows-up clearly, rarely few PAC spectra allows to infer about the presence of time time-dependent interactions. In these cases, only systematic temperature measurements, where a modification of the attenuation is produced, can reveal the underlying physical processes.

To describe the interaction between the nuclear moment and a fluctuating electromagnetic field, time-dependent hyperfine interactions theory must be considered. The perturbation of angular correlations by rapid isotropic fluctuations has been early described by Abragam and Pound using first-order time-dependent perturbation theory [126]. A generalization of this work was pursued by Blume [159] in the framework of stochastic processes. This solution assumes a Markovian modulation where the system hamiltonian is a random function of time with fluctuations between a finite number of states, N. The computation of the perturbation function in the exact Blume formalism requires the diagonalization of a matrix of rank

$(2I+1)^2N$. Thus, this process becomes rapidly impracticable due to the dimensions of the involved matrix and one as to resort to approximations. Using the Blume´s stochastic theory Winkler and Gerdau [160] developed an approach to calculate the PAC spectra and their formulation was applied to some simple cases. In literature several approaches have been reported depending on the specifications of the problem [161–164].

As mentioned in 3.2, the time-evolution operator $\Lambda(t)$, which describes the evolution of the intermediate state of the γ-γ PAC cascade is the central element in PAC theory. In the case of random time-dependent interactions the calculation of the perturbed angular correlation function can also be performed using the density matrix operators in a similar way as done for static interactions but the time evolution operator becomes a superoperator, $(\hat{\Omega})$ [155]. Thus, the time evolution of the density matrix of the intermediate state that for static interactions was given by equation 3.27 has to be modified to

$$\hat{\rho}(\boldsymbol{k_1},\,\mathrm{t}) = \hat{\Omega}(t)\,\hat{\rho}(\boldsymbol{k_1}) \tag{3.44}$$

Considering a time dependent hamiltonian $\hat{\mathcal{H}}(t)$ of a system which is subject to an interaction jumping at random between a finite number of states, N,

$$\hat{\mathcal{H}}(t) = \sum_{j=1}^{N} \hat{V}_j g_j(t) \tag{3.45}$$

where $\hat{V}_j$ is the static hamiltonian of the state j and the functions $g_j(t)$ are defined such that for any time, t, $g_{k\neq j}(t) = 0$ if $g_j(t) = 1$. If the fluctuation processes is Markovian, the time-evolution operator writes

$$\hat{\Omega}(t) = \exp[-\frac{i}{\hbar}\,(\hat{\mathcal{H}}^* + \hat{R})] \tag{3.46}$$

where $\hat{\mathcal{H}}^*$ is the super-hamiltonian constructed from the hamiltonians, $\hat{V}_j$, of the different, N, stochastic states and the transition matrix, $\hat{R}$, contains the transitions probabilities from $|a\rangle$ to $|b\rangle$ environment. The elements of this exponential argument matrix, the so-called Blume matrix, are given in [159]. The calculation of the perturbation function G_{kk} proceeds using the same formulae as those used for static interactions, *i.e.*, merging equation 3.46 for the time evolution operator into equation 3.31. The eigenvalues of this evolution operator matrix have in general both real and imaginary parts. The real parts are always negative and are responsible for the damping of the periodic components of the PAC spectra (damping factor, λ_n). Due to the complex prefactors the spectra now contain sine contributions or phase shifted cosines. From the eigenvectors and eigenvalues of the Blume matrix one can express the perturbation factor $G_{kk}(t)$ that for a polycrystal has the form

$$G_{kk}(t) \;=\; \sum_{n=1}^{(2I+1)^2 N} s_{kn}\, cos(\omega_n\, t + \phi_n)\, e^{-\lambda_n\, t} \tag{3.47}$$

The coefficients s_{kn}, ω_n , ϕ_n and λ_n are determined by the diagonalization of the Blume matrix. PAC analysis of the fluctuating fields, in particular the determination of the fluctuation frequencies, poses a considerable problem. To apply the exact Blume formalism is impracticable for most of the cases since the number of states is prohibitively large. Thus, either we work in systems with fluctuations between two or three states, within the same type of fluctuations (strength, symmetry or orientation), or one has to resort to approximations. Depending on the fluctuation rates, type of fluctuations and dynamics of the system, relaxation from a non-equilibrium state[12] or fluctuating hyperfine fields in thermal equilibrium[13], distinct features of dynamic spectra are observed. Here we will skip the details of the different regimes since a very good overview can be found in [155, 165]. Additionally, mathematical approximation formulae describing the relaxation processes and experimental examples are given in [155,163,166]. Thermal equilibrium EFG fluctuations are discussed by Evenson *et al.* [162], within the x,y,z model for the simple case of 3 different EFG orientations at constant strength. Strength EFG fluctuations at identical orientations are discussed by Achtziger and Witthuhn [166].

Whenever dynamic effects produce fluctuations of orientation, strength and symmetry of the hyperfine fields or the number of states is very large, a different approach is necessary. Baubry *et al.* [161] and Forker *et al.* [164] showed that the Winkler and Gerdau [160] approximation, where orientational EFG fluctuations[14] are described by a single exponential damping term, $e^{-\lambda_k\, t}$, multiplying the static perturbation factor of the time average interaction $\widetilde{G}_{kk}(t)$, is also valid for isotropic fluctuations in a large range of fluctuations rate w. Moreover, this approximation may satisfactorily describe stochastic processes whenever more than one type of fluctuations are present simultaneously. In this approximation the perturbation factor is written as:

$$G_{kk}(t) \;= \widetilde{G}_{kk}(t)\, e^{-\lambda_k\, t} \tag{3.48}$$

In the limit of very fast fluctuations rate, $w \to \infty$, the PAC probe experiences a time average interaction of the ensemble without damping due to the dynamic interactions. As w decreases and enters the PAC time window the dynamic effect becomes visible and as long as $w > 5\,\omega_Q$, where ω_Q is the average fluctuating frequency, the data can be fitted using

[12] In this case the system starts from a non equilibrium situation *e.g.*, after-effect in the decay of ^{111}In. The most simple example of relaxation is the one that the transitions occur from a initial non equilibrium state into a final state ($EFG_i \longrightarrow EFG_f$).

[13] This is the case of hoping or diffusion of ions and/or carriers where transitions between N different states and vice-versa occur at a certain rate ($EFG_a \longleftrightarrow EFG_b$).

[14] Fluctuations of the EFG orientation with no changes in the magnitude nor symmetry.

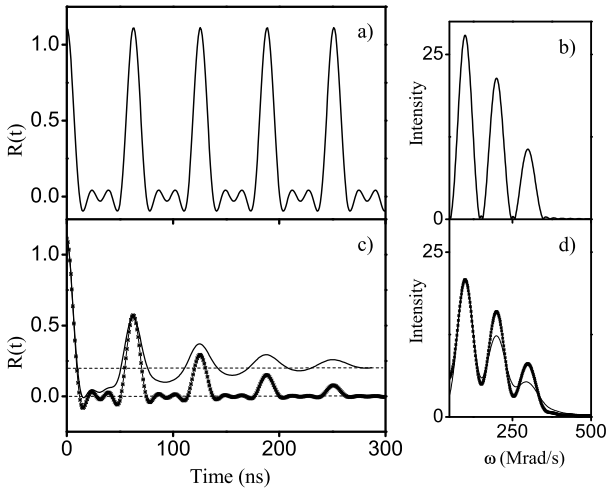

Figure 3.5: a) Schematic representation of the $R(t)$ function for a EFG with $\eta = 0$. No attenuation is present in this $R(t)$ function. On the right hand side, b) the correspondening Fourier transform is presented. c) Schematic representation of the $R(t)$ function for the same frequency as in (a) with static attenuation (line) and with dynamic attenuation (line plus symbol). The correspondent Fourier transforms are shown in the right hand side, d). In the frequency space the attenuation to ω_1, ω_2, ω_3 amplitudes diminish by the same factor in the case of damping due to dynamic interactions while for a static damping the attenuation is proportional to the frequency itself.

$$G_{kk}(t) = [s_{k0} + \sum_{n=1}^{3} s_{kn}\, cos(\omega_n\, t)\, e^{-\omega_n\, \delta\, t}]\, e^{-\lambda_k\, t} \tag{3.49}$$

here an EFG lorentzian distribution due to static disorder, lattice defects or chemical disorder, is accounted by the first exponential term. The second attenuation term accounts for the damping due to the dynamic effects.

The correspondence between the dynamic damping term λ_k, and the EFG fluctuation rate, w, is given by [160]

$$\lambda_k = \frac{3}{5}\frac{1}{Nw}(\omega_Q)^2 k(k+1)[4I(I+1) - k(k+1) - 1] \tag{3.50}$$

where N is the number of possible EFG states. For spin 5/2 we have that $\lambda_2 = 100.8(\omega_Q)^2/Nw$. The average residence time in each state, $\tau_r = 1/Nw$, can also be obtained.

For the slow fluctuations regime the dynamic damping term is written [167]

$$\lambda = (N-1)w \tag{3.51}$$

Examples of analysis of experimental data using this approach can be found in [168–170].

As mentioned, the experimentally distinction between a damped static interaction and

an interaction with time-dependent effects may be ambiguous. In a few particular cases, however, the dynamic effects contributions to the $R(t)$ attenuation show-up clearly, (e.g orientational EFG fluctuations). Here the so-called "hard core value", s_{k0}, asymptotic amplitude of a damped PAC spectrum at large times, is affected by the dynamical regime. In this case, when $t \to \infty$ $G_{kk} \to 0$ and not to s_{k0}, as happens in a spectrum attenuated by a static distribution of EFGs. This effect can be observed in figure 3.5 where a schematic representation of three distinct $R(t)$ functions and correspondent Fourier transforms for: $\delta = 0$ and $\lambda = 0$; $\delta \neq 0$ and $\lambda = 0$; $\delta = 0$ and $\lambda \neq 0$ are presented. A different situation occurs when EFG fluctuations preserve orientation and asymmetry. Here the "hard core value" is unaffected by the dynamical regime. In this case there is no obvious indication on what kind of interactions are present (dynamic or static). This also occurs when more than one local environment contributes to the $R(t)$. Generally, strong reversible temperature dependent changes of the $R(t)$ spectra attenuation is a good indication of the presence of time dependent interactions.

3.4 Electric field gradient

3.4.1 Electric field gradient calculations

The electric field gradient is non zero at a given point when an asymmetric charge distribution of electrons and ion cores occurs in the vicinity of that point. The contributions to the EFG are usually divided in those arising from the neighboring ionic cores (ionic lattice contribution, V_{zz}^{latt}), probe core electrons and conduction electrons. The contribution of the probe closed-shell core-electrons arises from a polarization effect and results in an amplification of the lattice EFG being accounted by the so-called Sternheimer antishielding coefficient, γ_∞, [$V_{zz}^{core} = -\gamma_\infty V_{zz}^{latt}$]. Usually γ_∞ ranges from -100 to -10 and its values can be found in tables [171–173]. Thus, the EFG can be parameterized as [116, 174, 175]

$$V_{zz} = V_{zz}^{latt} - \gamma_\infty V_{zz}^{latt} + V_{zz}^{el} \tag{3.52}$$

where the last term accounts for the electronic contribution usually attributed to conduction electrons or the effect of unfilled probe electron shells.

In the case of ionic insulators with non-overlapping ion-cores the EFG is approximately,

$$V_{zz} = (1 - \gamma_\infty) V_{zz}^{latt} \tag{3.53}$$

In the case of metals the computation of V_{zz}^{el} is particularly difficult, nevertheless, Raghavan *et al.* [176] showed experimentally the existence of an "universal correlation" between the electronic and the lattice contribution to the EFG in metals.

$$V_{zz}^{el} = -KV_{zz}^{latt}(1-\gamma_\infty) \qquad (with\ K=3) \tag{3.54}$$

This correlation was obtained by the systematic comparison of measured V_{zz} and EFG lattice contribution, the last one calculated with a simple point charge model. From equation 3.54 one can write that the measured V_{zz} is also proportional to the lattice EFG:

$$V_{zz} = V_{zz}^{latt}(1-\gamma_\infty)(1-K) \tag{3.55}$$

These simple models allow an estimation of the lattice EFG independently of the probing atom.

Electric field gradient point charge model calculations Owing to the difficulties for EFG accurate calculations, point charge model (PCM) estimations are widely used. This model assumes the ion cores as point charges, $Z_i\, e$, located at the ions lattice sites, *i.e.*, being an approximation for the lattice contribution to the EFG, V_{ij}^{latt}. The electric field gradient can thus be easily estimated. To do so, the second partial derivatives of the potential ϕ at the probe site created by the external charges $z_i\, e$ at the position r_i from the origin have to be calculated. The contributions of all lattice atoms, except from the probe itself, must be added, giving,

$$V_{ij}^{PCM} = \sum_i \frac{z_i e}{4\pi\epsilon_0 r_i^5} \begin{pmatrix} 3x_i^2 - r_i^2 & 3x_i y_i & 3x_i z_i \\ 3y_i x_i & 3y_i^2 - r_i^2 & 3y_i z_i \\ 3z_i x_i & 3z_i y_i & 3z_i^2 - r_i^2 \end{pmatrix} \tag{3.56}$$

After diagonalization the eigenvalues are chosen in such a way that $|V_{x\,x}| \leq |V_{y\,y}| \leq |V_{z\,z}|$ and the asymmetry parameter η can be obtained.

This method can provide a fair estimate of the EFGs in the case of ionic solids. On the other hand, only rough estimates and large deviations are reported for covalent solids. Nevertheless PCM has been extensively used, in particular to predict EFGs at the A site in perovskites oxides. In these materials, Wiarda [177] and [137] found empirically that when the probe-O bonds are larger than 2.1Å a fairly good agreement between experiment, PCM predictions and ab-initio calculations is found.

Electric field gradient first-principles calculations EFG calculations can be obtained using Ab-initio full potential linearized augmented plane wave (FLAPW) method developed by Blaha *et al.* [178] using the local spin density approximation (LSDA) [179] or the generalized gradient aproximation (GGA) [180]. This method has proven to be an accurate band structure calculation scheme allowing also the computation of the hyperfine fields in crystalline solids requiring only the lattice constants as input. Some applications of this method can be found in [137, 181]

3.4.2 Temperature dependence of EFG

The electrical field gradient temperature dependence has been extensively studied in solids and experimental data exist showing distinct trends, among these, however, the decrease of of $V_{z\,z}$ with increasing temperature is by far the most common. There are several contributions for the temperature dependence of $\mathrm{V}_{z\,z}$ and their relative magnitude depend strongly on the details of the studied system, thus no general description is available.

According to the initial theoretical descriptions, where the EFG is assumed to be proportional to the lattice contribution, (*e.g.*, H. Bayer [182] theory latter generalized by T. Kushida [183, 184] and T. Wang [185]) the changes in $V_{z\,z}$ with temperature result essentially from thermal expansion of the lattice parameters and thermal motion. Within these descriptions the temperature variation of $V_{z\,z}$ due to the (volume) thermal expansion, α, can be expressed, for a ionic crystal, as

$$\frac{1}{V_{z\,z}}\left(\frac{\partial V_{z\,z}}{\partial T}\right)_P = \frac{1}{V_{z\,z}}\left(\frac{\partial V_{z\,z}}{\partial V}\right)\left(\frac{\partial V}{\partial T}\right)_P = -\frac{1}{V}\left(\frac{\partial V}{\partial T}\right)_P \tag{3.57}$$

where it was considered that $V_{z\,z} \propto V^{-1}$ since $V_{z\,z}$ depends on the interatomic distances as $1/r^3$. A positive (volume) thermal expansion results, thus, in an increase of $V_{z\,z}$ with decreasing temperature. However, in solids, the thermal expansion is very small and rarely can account for the $V_{z\,z}$ temperature dependence (*e.g.*, in $LaMnO_3$ and $Pr_{1-x}Ca_xMnO_3$ manganites, for temperatures below 300 K, $\alpha \sim \frac{1}{V_0}\frac{\Delta V}{\Delta T} < 5 \times 10^{-5}$ [74, 78, 85, 186, 187]).

The other important contribution to the EFG temperature dependence arises from lattice vibrations that cause time-dependent EFG fluctuation, usually at frequencies ($\sim 10^{12} s^{-1}$) much higher than the quadrupole frequency ($\sim 10^{8} s^{-1}$), and thus a nuclear hyperfine measurement is only sensitive to the average EFG. If one considers harmonic vibrations around the atom's equilibrium positions one can find an expression for $\langle V_{z\,z}\rangle$. This was initially performed by H. Bayer [182], by expanding $\langle V_{z\,z}\rangle$ in terms of the normal modes, ξ, arriving, for the case of a rotation mode with inertia moment Θ, to the expression

$$\langle V_{z\,z}\rangle = V_{z\,z}^{eq}\left(1 - \frac{3}{2\Theta}\langle\xi^2\rangle\right) \tag{3.58}$$

where $V_{z\,z}^{eq}$ is the EFG principal component in the absence of fluctuation, *i.e.* $\xi = 0$. If the mean energy of the classical harmonic oscillator is equated with the mean energy of the corresponding Plank's oscillator and for the condition $\hbar\omega/k_BT \ll 1$ one can write

$$\langle V_{z\,z}\rangle = V_{z\,z}^{eq}\left(1 - \frac{3k_B}{2\Theta}\frac{T}{\omega^2}\right) \tag{3.59}$$

where ω is the angular frequency of the concerned normal mode.

In this particular case $\langle V_{z\,z}\rangle$ increases linearly with decreasing temperature (at sufficiently high temperatures $k_BT \gg \hbar\omega$).

A similar reasoning allows to determine the contribution of stretching modes to the EFG temperature dependence. According to T. Kushida [183, 184] one arrives to a similar expression as the H. Bayer equation (3.59), but with a positive sign. Accordingly one expects a decrease of the V_{zz} with decreasing temperature. Notice, however, that since the frequency of stretching modes is generally much higher than that of rotation modes the former can usually be neglected. A complete description of these issues can be found in references [183, 184].

The theory of Bayer and Kushida explains reasonably well the EFG temperature dependence in purely ionic lattices, failing in the case of metallic lattices. In simple terms this can be understood from the fact that above the electronic fluid was not included. In metals, the electronic contribution to the EFG temperature dependence is very important since electrons mediate the effect of lattice vibrations on the EFG. To evaluate this effect is rather complicate since it requires a knowledge of the conduction electron wave functions for all occupied states and their temperature dependence.

Experimentally, Christiansen *et al.* [188] found out that in most non-cubic metals the temperature dependence of the EFG follows the so called $T^{3/2}$-law:

$$V_{zz} = V_{zz}(0)(1 - bT^{3/2}) \tag{3.60}$$

Although several authors [174,189–191] tried to get some insight on this EFG trend, there is, up to now, no satisfactory theoretical explanation for the $T^{3/2}$-law and its general validity doesn't hold [192].

As a final remark, we stress that the EFG principal component decreases, in most cases, with increasing temperature in ABO_3 perovskite structures [138, 139, 193, 194].

Chapter 4

Lattice distortions and polaron clusters in $LaMnO_{3+\Delta}$ system

Motivation

The $LaMnO_{3+\Delta}$ system has been studied in the last years since it provides a prototypical system which presents the complex structural/magnetic phase diagram [83, 85, 195, 196] typical of manganite systems. The undoped compound ($\Delta = 0$) presents a cooperative JT distortion of the $Mn^{3+}O_6$ octahedra. The introduction of holes, Mn^{4+}, through cationic vacancies, reduces the static JT–distortion and favors the ferromagnetic interaction via dynamic electron transfer between Mn^{3+}/Mn^{4+} [4]. As the carrier density increases the ground state becomes fully ferromagnetic. Strikingly, the insulator nature of this system persists till very high hole density [85], even in the phase diagram region where the ferromagnetic state is well stabilized. The existence of a ferromagnetic insulator portion of the phase diagram is an ubiquitous property of the manganite system which cannot be understood within the simple double-exchange scenario. It was recently recognized that polaron formation must certainly play an important role in this respect [11, 13, 16, 17]. Polarons are formed due to the strong electron-lattice coupling that leads to charge localization via JT–distortions. The nature of such local distortions, their dynamics and correlations have been addressed by several authors [22, 59–61, 197] using a vast set of techniques including x-ray diffraction, EXAFS, Neutron PDF, Raman spectroscopy, NMR and NQR. In spite of such an effort, several issues as the detailed structure of polarons, the temperature evolution of polaron clusters or the effect of such evolution on the average macroscopic lattice structure still remain as open questions.

In this chapter the study of local distortions and their dynamics with the $\gamma-\gamma$ perturbed angular correlation spectroscopy in $LaMnO_{3+\Delta}$ is presented. Profiting from the fact that PAC efficiency is temperature independent, allowing to explore a wide range of temperatures, we study the microscopic nature of polaronic distortions, their spatial correlations and the

role of polarons in ferromagnetic insulator manganites. To do so we have undertaken a systematic study on the hyperfine fields of the $LaMnO_{3+\Delta}$ system and correlated them with the macroscopic characteristics of each sample. Particular attention is given to the compound $LaMnO_{3.12}$ since it is a prototypical FMI manganite that undergoes a rhombohedric (R)-orthorhombic (O) structural transition around room temperature, providing us with an ideal scenario to probe the evolution of local lattice distortions through different average lattice symmetries.

4.1 Sample characterization

4.1.1 Structural characterization

In the $LaMnO_{3+\Delta}$ system the hole concentration (x) is directly determined by the oxygen nonstoichiometry (x=2Δ), which can be easily changed through suitable annealing with controlled oxygen partial pressure. In this way a batch of samples with different Δ can be prepared from the same initial pellet and thus one expects good tuning of the hole concentration. Accordingly, all $LaMnO_{3+\Delta}$ ceramic polycrystalline samples used in this study were obtained from an initial pellet prepared by the standard solid-state reaction method [95]. Different oxidation nonstoichiometry (Δ) was attained through a subsequent heat treatment in an appropriate oxygen/nitrogen atmosphere with carefully controlled partial oxygen pressure, $P(O_2)$, followed by quenching to room temperature. To achieve this, an annealing system with controlled oxygen partial pressures and easy sample quench, was developed and mounted in a tubular furnace. Table 4.1 summarizes the thermal treatments, following the procedure described in [83,196], which allowed to accomplish a $0 \leq \Delta \leq 0.13$ range of oxygen content.

Table 4.1: $LaMnO_{3+\Delta}$ heat treatment conditions.

Sample	P(mbar)	Atmosph.	T(^{0}C)	t(h)
S1	0.02	O_2	1000	24
S2	0.1	O_2	1000	24
S3	0.4	O_2	1000	24
S4	10	O_2	1000	24
S5	25	O_2	1000	24
S6	1000	O_2+N_2	750	20
S7	1000	N_2	700	20
S8	200	O_2	1000	24
S9	1000	O_2	700	20
S10	original sample			
S11	1000	O_2	850	20

The correlation between the oxygen content in $LaMnO_{3+\Delta}$, temperature and oxygen partial pressure can be found in several former studies [83, 84, 196] and a compilation of the earlier experimental data is given by van Roosmalen and Cordfunke [198].

Analysis of the room temperature powder x-ray diffraction measurements show that the samples are chemically homogeneous. The crystallographic structures and correspondent lattice parameters were determined by refinement of X-ray diffraction patterns using the FULLPROF program [199]. The line shape of the diffraction peaks was generated by a pseudo-Voigt function. The XRD patterns of samples S1-S8 are characterized by a single-phase perovskite with orthorhombic symmetry whereas a coexistence between rhombohedral and orthorhombic symmetries characterizes the sample number S9. The original (S10) and S11 samples are characterized by a mono-phase perovskite structure with rhombohedric symmetry. In figure 4.1 some representative X-ray diffraction patterns (observed and calculated pattern and the reflections of the correspondent phases) are presented. These patterns were refined either in the $R\bar{3}C$ (Z=6) or Pbnm (Z=4) space groups. The good matching[1] of the fits is illustrated in figure 4.1 where no unidentified lines[2] nor additional splitting of the peaks are observed.

From the x-ray pattern matching we extracted the cell parameters for this set of samples. The oxygen content, Δ, was then determined comparing our structural data with those available in the literature for systems with controlled oxygen content. To do so we systematically collected the cell parameters obtained by several authors [83, 85, 195, 196, 200]. Figure 4.2 show a compilation of the unit volume cell as a function of Δ. As it can be seen there is a strong correlation between the unit cell volume and the oxygen content, which can be approximately modeled by a second-order polynomial fit. Dashed lines in figure 4.2 enclose the 95% confidence interval. The unit cell volumes obtained in our set of samples is represented in figure 4.2 by the horizontal lines. From the intersection of these lines with the trend fit to the literature data, we estimated the oxygen content for all samples. The obtained results are presented in table 4.2.

The different diffraction patterns observed in figure 4.1 correspond to three structural phases with different degree of distortions of the cubic perovskite structure that can be clearly identified as a function of the oxygen content. Table 4.3 summarizes the cell parameters and corresponding structural phases obtained for the $LaMn_{3+\Delta}$ system at room temperature.

Figure 4.3(a) shows the dependence of the lattice parameters on the oxygen content. In figure 4.3(b) the three different bond-lengths (m, s, l) between the manganese ion and the six

[1] Due to the small amount of powder, the quality of the XRD pattern of sample S8 is not optimal, even though, the refinement in the Pbnm space group is unquestionable. The discrepancy factors for samples where amount of powder was too small averages: $R_p \sim 19$, $R_{wp} \sim 26$, $\chi^2 \sim 0.8$. For the other samples those values averages: $R_p \sim 8$, $R_{wp} \sim 12$, $\chi^2 \sim 1.7$.

[2] In sample S9 extra peaks around 42.3-45.5 and 49.37-52.9 are present in the x-ray patterns. These extra lines belong to the reflections of the sample holder used for the measurement of this sample as a function of temperature.

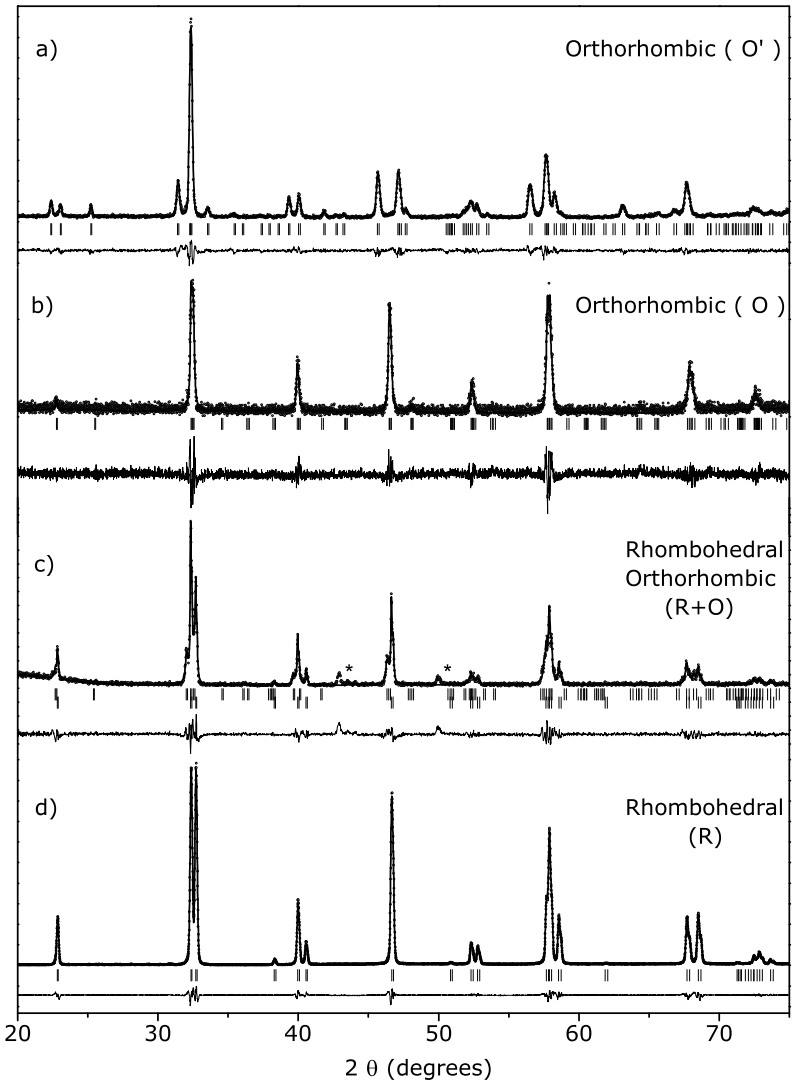

Figure 4.1: $LaMnO_{3+\Delta}$ room temperature representative X-ray diffraction patterns of a) sample S3, b) sample S8 c) sample S9 and d) original sample (S10). The observed pattern (dots), calculated (solid line), reflections of the correspondent phases (tick marks) and fit deviation (solid line in the bottom) are shown. For sample S9 (c) the first and second series of tick marks indicate the reflections of the orthorhombic and rhombohedral phases, respectively (the extra peaks signaled with $*$ belong to the reflections of the sample holder used for that measurement, see footnote 2).

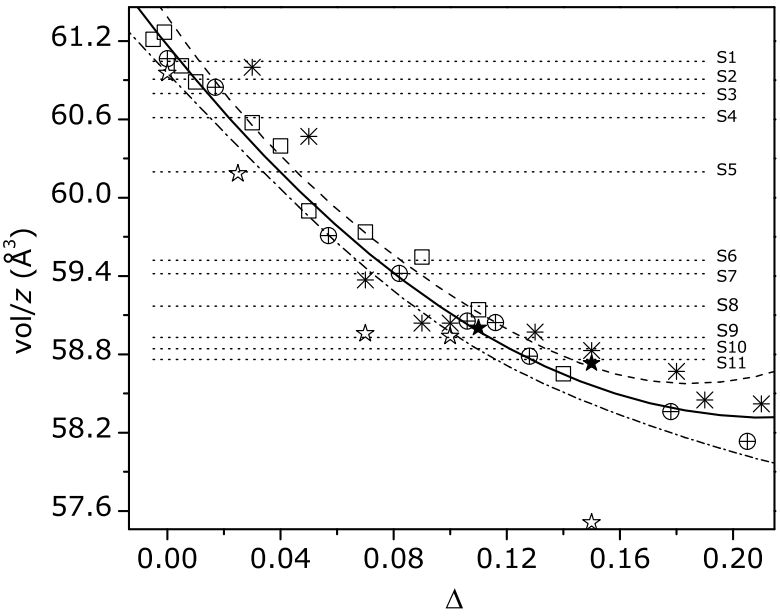

Figure 4.2: $LaMnO_{3+\Delta}$ unit cell volume obtained by F. Prado *et al.* [83] (□), C. Ritter *et al.* [85] (⊕), B. Dabrowvski *et al.* [196] (open ⋆), I. Maurin *et al.* [200] (⋆), J.A. Alonso *et al.* [195] (∗) and volume trend with correspondent confidence interval (95%) as a function of oxygen content. Horizontal lines represent the unit cell volumes obtained in our samples.

Table 4.2: Oxygen content for the $LaMnO_{3+\Delta}$ samples, estimated from figure 4.2.

Sample	S1	S2	S3	S4	S5	S6
Δ	0.004(8)	0.010(8)	0.014(7)	0.022(7)	0.040(6)	0.074(7)
notation ($\sim \Delta$)	0	0.01	0.01_b	0.02	0.04	0.07
Sample	S7	S8	S9	S10	S11	
Δ	0.080(8)	0.097(10)	0.115(11)	0.121(12)	0.128(12)	
notation ($\sim \Delta$)	0.08	0.10	0.12	0.12_b	0.13	

surrounding oxygens of the octahedra, obtained using expressions 1.4, 1.5 and 1.6 are shown. The different Mn-O bond length obtained through pair distribution function (PDF) analysis of neutron diffraction patterns by Th. Proffen *et al.* [201] and D. Louca *et al.* [202, 203][3] are also depicted in that figure (solid symbols). It can be seen how the deformation of the oxygen octahedra around Mn ions is reduced as the oxygen content increases. A good agrement between our data, calculated from the unit cell parameters, and the literature (using a local scale technique) is observed.

For the stoichiometric material and samples with $\Delta \leq 0.04$, where a large Jahn-Teller distortion (JTD) occurs, a relation $c/\sqrt{2} < a < b$ is observed in the orthorhombic Pbnm structure (O'). The orthorhombicity decreases with increasing Δ and the static JTD diminishes continuously as the oxygen content increases until approximately $\Delta \sim 0.05$, as indicated by a vertical line in figure 4.3(a). This value, which is used to define the transition from the O' phase to the O phase, is estimated by the cell parameters trend and the small discontinuity in the volume cell observed between $0.04 \leq \Delta \leq 0.07$[4]. The samples with oxygen content $0.04 < \Delta \leq 0.10$ are orthorhombic (O) with the same Pbnm structure, but characterized by a considerably smaller Jahn-Teller distortion and $c/\sqrt{2} \sim a \sim b$. As one can observe, the samples with the largest oxygen content $\Delta > 0.1$ have a rhombohedric symmetry and no coherent Jahn-Teller distortion is present in these compounds [83].

Between the orthorhombic and rhombohedral phase a coexistence region was observed; the sample with $\Delta = 0.12$ exhibits reflections of both O and R phases. In table 4.3 and figure 4.3(a) only the values corresponding to the more abundant phase at room temperature ($R\bar{3}c$) are shown. A similar phase coexistence was already observed in references [84,85,195,200] but

[3]In the work of D. Louca *et al.* the short and medium bonds are considered to be equal.

[4]Due to the lack of points between $0.04 < \Delta < 0.07$ our value is guided by the typical values found in the literature [83, 85, 196].

Table 4.3: $LaMnO_{3+\Delta}$ cell parameters in the Pbnm/$R\bar{3}c$ space group.

Sample	$\sim \Delta$	a(Å)	b(Å)	c(Å)	V(Å^3)	Structure
S1	0	5.5428	5.7210	7.7004	61.046	O'
S2	0.01	5.5423	5.6978	7.7151	60.908	O'
S3	0.01_b	5.5415	5.6920	7.7101	60.798	O'
S4	0.02	5.5332	5.6663	7.7330	60.613	O'
S5	0.04	5.5418	5.6058	7.7510	60.198	O
S6	0.07	5.5417	5.5029	7.8072	59.521	O
S7	0.08	5.5369	5.5028	7.8005	59.417	O
S8	0.10	5.5216	5.4976	7.7968	59.169	O
S9	0.12	5.5329	5.5329	13.3376	58.932	R+O
S10	0.12_b	5.5290	5.5290	13.3368	58.847	R
S11	0.13	5.5262	5.5262	13.3306	58.754	R

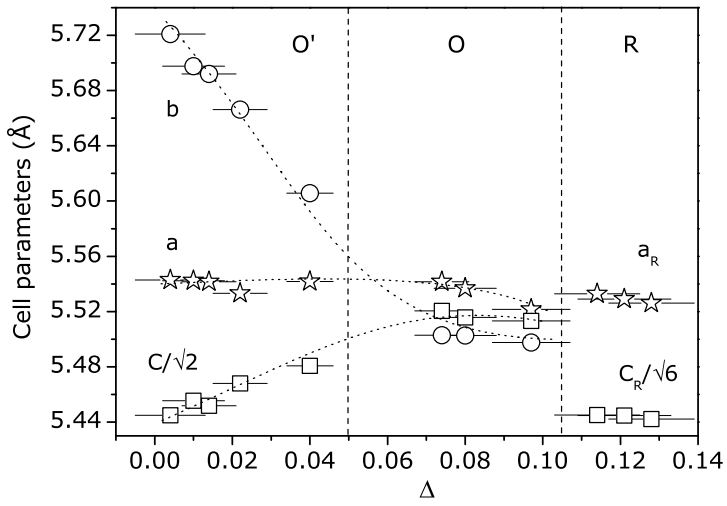

(a)

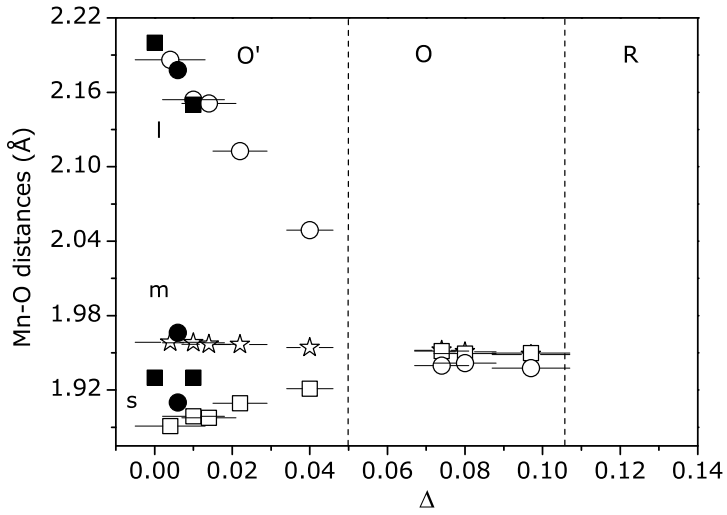

(b)

Figure 4.3: a) $LaMnO_{3+\Delta}$ unit cell parameters, b) (○), a) (open ⋆) and c) (□) as a function of oxygen content. Lines are guides for the eye. b) (open symbols) Mn-O bonds length, l (○), m (open ⋆) and s (□) calculated in this work, (solid symbols) Mn-O bond length obtained through PDF analysis by Th. Proffen *et al.* [201] (•) and D. Louca *et al.* [202, 203](■).

the value of oxygen content where the phase coexistence occurs is often shifted from reference to reference ($\Delta = 0.10$ [85], $\Delta = 0.11$ [195], $0.05 \leq \Delta \leq 0.07$ [200] and $\Delta = 0.07$ [84]). In the works of Prado *et al.* [83] and Dabrowvski *et al.* [196] this phase coexistence was not observed although the structural transition from O to R is within the range $0.09 < \Delta < 0.11$ in [83] and within the $0.11 < \Delta < 0.12$ in [196]. Due to the errors in the oxygen content determination the exact phase coexistence region and width is not precisely known. As expected structural results show that, in addition to the orthorhombic Pbnm O' and O structures, the rhombohedral $R\bar{3}C$ structure is stabilized at high oxygen contents ($\Delta \geq 0.12$). Furthermore the coexistence of both structural phases occurs for sample with $\Delta = 0.12$. In the next section magnetization data shows that although there is uncertainty about the absolute value of Δ, the hole concentration is reasonably controlled.

4.1.2 Magnetic and electric characterization

Magnetization studies were used to determine the Curie-Weiss, Néel and Curie temperatures (θ_P, T_N and T_C respectively) as well as the saturation magnetization, which are strongly dependent on doping (Mn^{3+}/Mn^{4+} contents). The zero-field cooling (ZFC) and field cooling (FC) curves were obtained using a 50 Oe applied magnetic field in a $10 < T < 340$ K temperature range. To evaluate the saturation magnetization the isothermal measurement at 5 K were obtained by sweeping the magnetic field up to 50 kOe. Figure 4.4 shows some representative susceptibility, χ (M/H), field cooling (and zero-field cooling, for $\Delta = 0.12$) curves as well as the inverse susceptibility curves.

For $\Delta > 0.04$ the low field FC curves exhibit typical features of a ferromagnet (see figure 4.4(c) and 4.4(d)), with a sharp rise in χ near T_C, which is defined as the temperature corresponding to the inflection point of the curve (minimum of the $d\chi/dT$ of the ZFC curves). The inverse susceptibility, $1/\chi$, versus T curves for $\Delta > 0.04$ also exhibit the typical behavior of ferromagnets, that is, the curves are roughly linear at high temperature and show a slight upward curvature near T_C. On the other hand, the curves for $\Delta \leq 0.04$, exhibit a sharper anomaly near T_C, *i.e.*, the curvature of the $1/\chi$ versus T curves changes from upward to downward as T_C is approached from above. This feature becomes more pronounced as Δ decreases, occurring in a temperature range close to T_N (see figure 4.4(a) and 4.4(b)). As usually performed, the Curie-Weiss temperature, θ_P, is defined as the temperature where the tangent of the $1/\chi$ versus T curve intersects the T-axis. In the paramagnetic phase, one expects that the magnetization obeys a Curie-Weiss law, *i.e.*, $M = CH/(T - \theta_P)$ where C the is Curie-Weiss constant. Figure 4.5(a) summarizes the dependence of the characteristic temperatures T_C/T_N and the paramagnetic Curie temperature θ_P on the oxygen content for samples measured in this work. Figure 4.5(b) summarizes the same dependence for the characteristic temperatures found in literature [83, 85, 200].

θ_P increases with Δ till $\Delta \leq 0.1$, showing that the overall strength of ferromagnetic

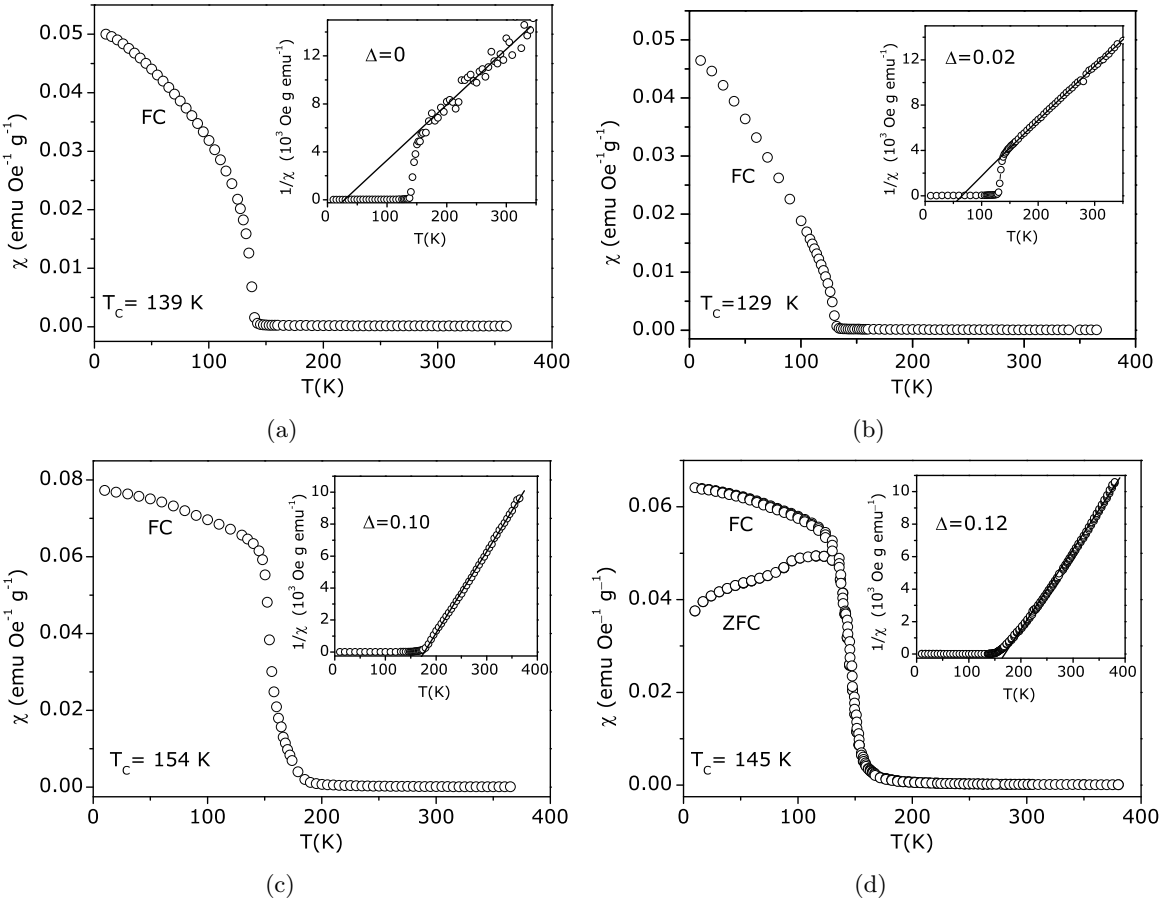

Figure 4.4: Zero field cooling and field cooling susceptibility versus temperature for: a) $LaMnO_3$; b) $LaMnO_{3.02}$; c) $LaMnO_{3.1}$; and d) $LaMnO_{3.12}$ samples. Insets: inverse susceptibility for the same samples.

interactions increases with Δ. Also it is found that in antiferromagnetic samples the critical temperature T_N decreases from 139 K, for the lower oxygen contents, to approximately 112 K for $\Delta = 0.04$ (see also table 4.4). The ferromagnetic samples, with $\Delta \geq 0.04$, have $T_C < \theta_P$, as expected for a ferromagnetic material, while for samples with $\Delta < 0.04$ $T_N > \theta_P$. T_C reaching a maximum for $\Delta \sim 0.1$. These results are in agrement with the ones found in literature [83, 85, 200], see figure 4.5(b).

Furthermore, for samples with $\Delta \geq 0.12$, deviations from the Curie-Weiss $1/\chi$ linear behavior were also found. Although the presence of stable magnetic clusters can justify the larger values of Curie-Weiss constant[5] that are commonly found in this system, specially for

[5]Larger than those expected for independent Mn^{3+}/Mn^{4+} spins where the Curie-Weiss constant should be simply the weighted sum [204]

$$\overline{C} = x\, C_S^{Mn^{4+}} + (1-x) C_S^{Mn^{3+}} \tag{4.1}$$

of Brillouin contributions

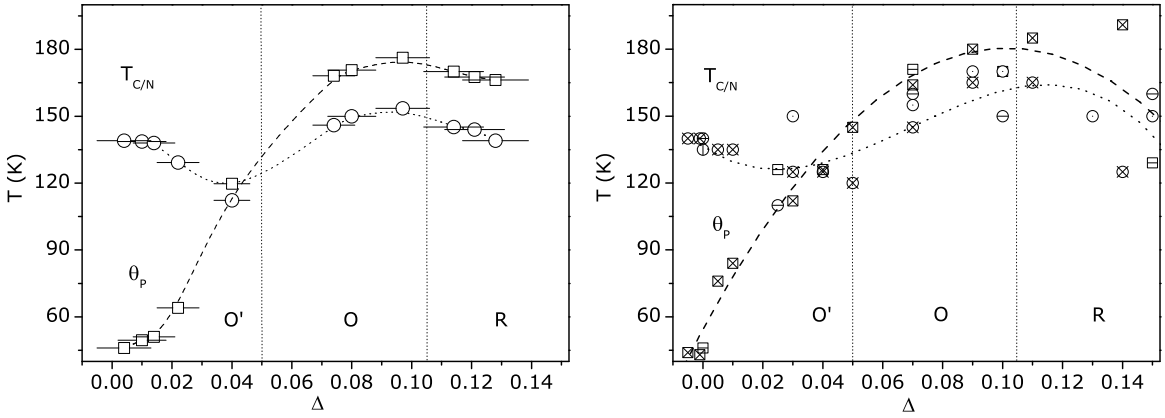

Figure 4.5: Characteristic temperatures T_C (∘) and θ_P (□) plotted as functions of oxygen content, Δ. a) measured in this work, b) obtained by F. Prado *et al.* [83] (⊕ and ⊞), C. Ritter *et al.* [85] (⊖ and ⊟) and I. Maurin *et al.* [200] (⊙ and ⊡). Lines are guides for the eye.

larger values of Δ, it cannot account for the non-linearity observed here and in literature [83]. This effect suggests a continuous growth of magnetic clusters with lowering temperature as found in other ferromagnetic manganites [19, 205, 206].

Table 4.4: Magnetic order transition temperatures (T_C and T_N), Curie-Weiss temperatures (θ_P) and saturation magnetic moment (μ) for $LaMnO_{3+\Delta}$ samples at T=5 K.

Sample	$T_{C/N}$(K)	θ_P(K)	$\mu(\mu_B)$
0	139	46	0.09
0.01	138	50	0.15
0.01_b	138	51	0.19
0.02	129	64	0.39
0.04	112	120	1.8
0.07	146	168	3.4
0.08	150	171	3.4
0.10	154	176	3.6
0.12	145	170	3.5
0.12_b	144	168	3.4
0.13	139	166	3.3

$$C_S = \frac{4}{3} S\,(S+1)\frac{\mu_B^2}{k_B} \tag{4.2}$$

where, $S^{Mn^{4+}} = 3/2$ and $S^{Mn^{3+}} = 2$.

If magnetic clusters are present in the system, spins cannot be any longer considered independent and an effective cluster spin has to be considered.

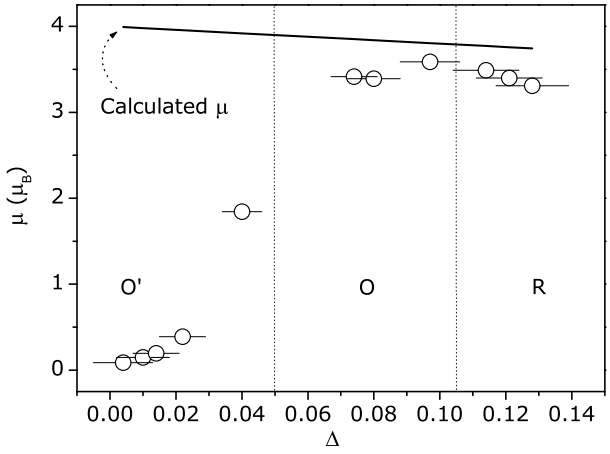

Figure 4.6: Saturation magnetic moment of the Mn ions as a function of the oxygen content. The spin-only calculated value, expected for full alignment of the Mn spins is depicted by the continuous line at the top of the figure.

To further characterize the magnetic behavior of the samples, isothermal magnetization measurement at 5 K were performed. Two methods to determine the saturation magnetic moment were used. For samples with no clear saturation (typically found in weak ferromagnetic and antiferromagnetic samples) the saturation magnetization was considered as the value of the linear high field extrapolation of the magnetization curve at H=0. For ferromagnetic samples that value was obtained by linear extrapolation of the M vs 1/H curve to $1/H \rightarrow 0$. Figure 4.6 depicts the evolution of saturation moment per formula unit with Δ. This data shows a very small ferromagnetic moment, of about 0.1 μ_B, for the stoichiometric sample (see figure table 4.4). A similar value was observed in a neutron diffraction study [85]. This can be an indication of the existence of a canted antiferromagnetic structure as discussed in literature [85, 207–209]. The other samples with $\Delta \leq 0.02$ also present a small saturation magnetic moments that can be attributed either to the existence of a magnetic canted structure or to the coexistence of ferro and antiferromagnetic regions. In the Ritter *et al.* neutron diffraction study [85] this effect is ascribed to the existence of a canted antiferromagnetic structure since AFM and FM contribution appear at same temperature. For $\Delta > 0.02$ the saturation magnetization strongly increases approaching the theoretical value expected for full alignment of the spins (straight line at the top of the figure 4.6) around $\Delta = 0.1$. A slight decrease is then observed for compositions with high oxygen content. This effect has been explained in literature [83–85] as being due to the larger amount of cationic vacancies present in these systems which break long-range ferromagnetic order.

Finally we report the resistivity measurements that were performed in a 100 K$\leq$ T $\leq$ 350 K temperature range. All samples show a characteristic insulator behavior with resistivity

decreasing as the temperature increases. Figure 4.7 depicts the measurement as a function of temperature for samples with $\Delta = 0.04$ and $\Delta = 0.12$.

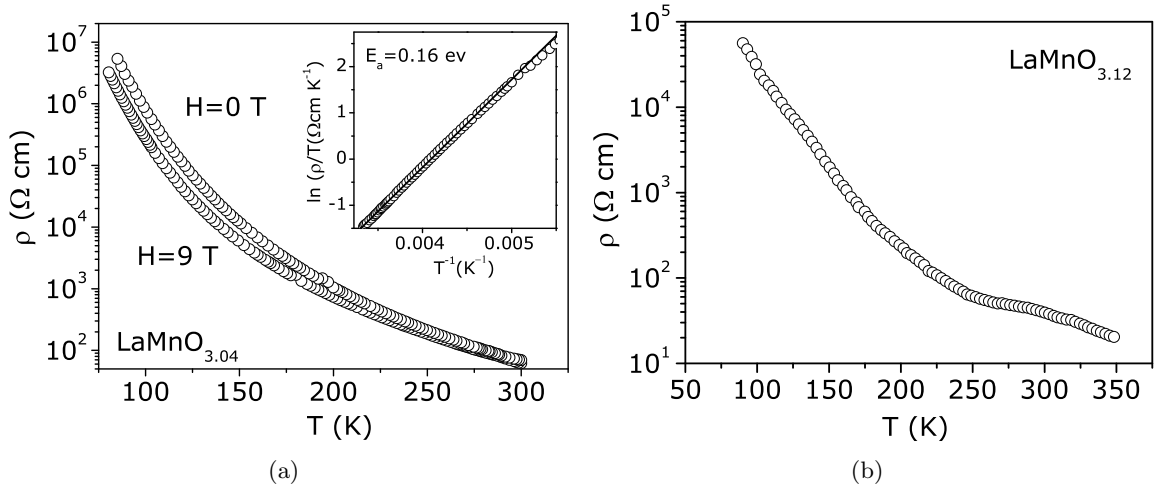

(a) (b)

Figure 4.7: Electrical resistivity as a function of temperature for: a) $LaMnO_{3.04}$; b) $LaMnO_{3.12}$. Inset: plot to determine the activation energy, E_a, according to the polaron hopping model (equation 4.3).

The resistivity measurement as a function of temperature displays always a insulator behavior both above and below the magnetic transition *i.e.* lowering the temperature no insulator to metal transition is observed even for the sample with $\Delta = 0.12$ where the amount of Mn^{4+} is already appreciable (24%). Although ferromagnetism and metallicity appear almost simultaneously in the $La_{1-x}Ca_xMnO_3$ system for x> 0.18, the persistence of a low-temperature ferromagnetic-insulating (FMI) regime for an extended range of compositions in the $LaMnO_{3+\Delta}$ was thoroughly reported in the literature [84, 85, 200, 210, 211]. Metallic behavior only appears at high hole contents, $\Delta = 0.14$ [84], $\Delta = 0.15$ [211], $\Delta > 0.15$ [85,210], $\Delta = 0.19$ [200], beyond the studied range.

Usually in these compounds the resistivity regime at high temperatures can be described by the adiabatic polaron hopping mechanism (PH). The activation energy E_a can be extracted from resistivity measurements in the paramagnetic regime by modeling the data with the equation

$$\rho(T) \propto T\, e^{E_a/k_B T} \tag{4.3}$$

where $E_a = E_b/2$, being E_b the polaron binding energy [212].

The value found for the $LaMnO_{3.04}$ compound was E_a ~0.16 eV in agrement with the literature [200, 210]. For the $LaMnO_{3.12}$ sample, the observed changes on the curvature didn't allow a precise determination of the activation energy and one would need resistivity measurements at much higher temperatures. In contrast with the Ca-doped system, where E_a

gradually decreases upon doping, correlated with the decrease in the Mn-O bond length [200], in the self-doped samples the activation energy barely changes upon doping and remains above a value of ~ 0.170 eV [200, 210].

4.2 EFG dependence on the average lattice symmetry

In this section we present a systematic study of the EFG behavior in the $LaMnO_{3+\Delta}$ system for several values of Δ and correlate these data with the corresponding crystallographic structures.

To perform PAC measurements, samples were implanted following the standard procedure described in chapter 2. To remove implantation damage, an annealing was performed for 20 minutes at temperatures and atmosphere according to the table 4.1. This annealing procedure allowed to preserve the oxygen content of the samples. After the annealing, the experimental

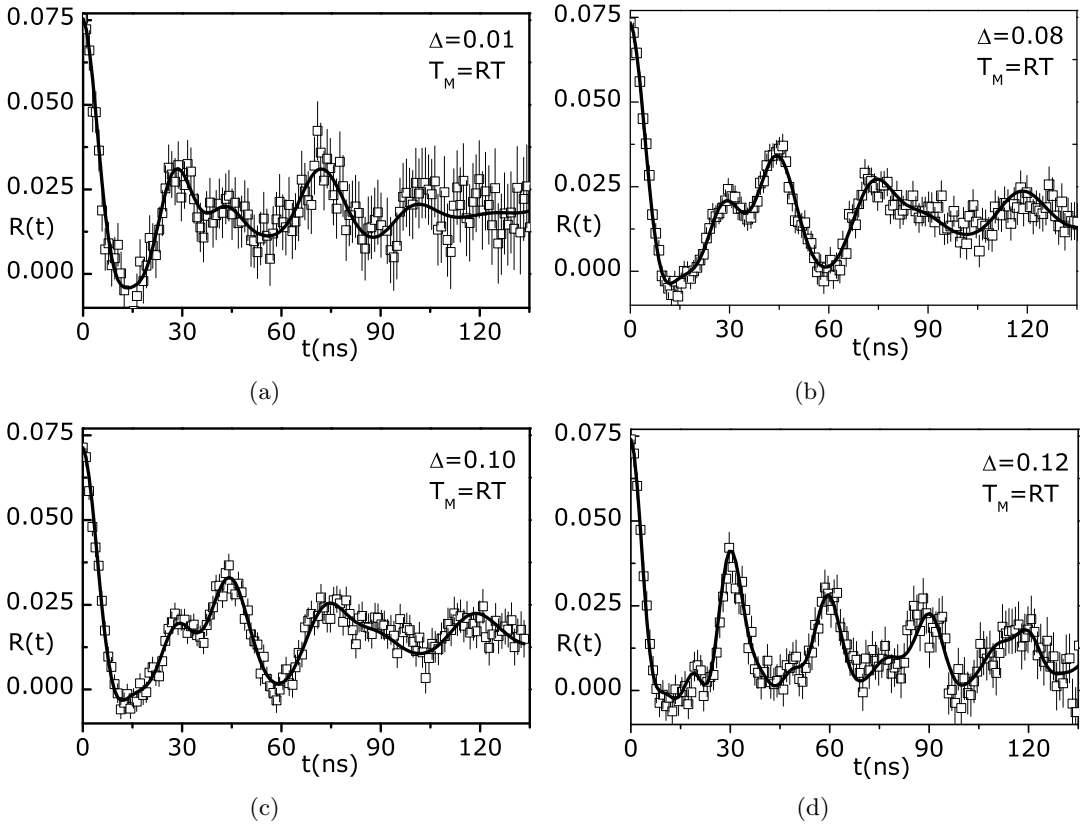

Figure 4.8: Representative R(t) experimental functions and correspondent fits for $LaMnO_{3+\Delta}$ samples with Δ=0.01, 0.08, 0.10 and 0.12, taken at room temperature.

R(t) spectra were measured. Figure 4.8 shows representative R(t) data measured at room temperature for samples with $\Delta \sim 0.01$ a), $\Delta \sim 0.08$ b), $\Delta \sim 0.10$ c), $\Delta \sim 0.12$ d). The fit to each experimental PAC spectrum, continuous lines over the R(t), were calculated numerically

by taking into account the hamiltonian for the nuclear quadrupole interaction [157]. This same procedure was applied to all other samples with different oxygen content. The fit to each spectrum shows that the Cd probes interact with one main EFG distribution, which was assumed to be Lorentzian-like. In some samples a contribution from a second EFG distribution, also assumed to be Lorentzian-like, had to be taken into account to make a proper fit, showing that distinct local environments coexist in some of these compounds. In this section we will focus firstly on the EFG parameters of the main local environment and after we will analyze in detail the contribution of the minor EFGs (named EFG_B for $\Delta \leq 0.02$ and EFG_d for $\Delta \geq 0.12$).

As one can observe in figure 4.8 the R(t) functions, corresponding to samples with different crystallographic phases (O', O and R), are quite distinct. While for samples with oxygen content Δ=0.01, 0.08 and 0.01 (orthorhombic phase) the observable frequencies, ω_0, are very similar, for the compound with $\Delta = 0.12$ a very distinct frequency appears. Is is also possible to see in the same figure that the asymmetry parameter η decreases from $\eta > 0.5$ for $\Delta = 0.01$ to $\eta < 0.5$ for Δ=0.08 and 0.10 (this is evident from the relations between the intensity of the oscillations at ∼29 ns and ∼44 ns in the R(t) function). Moreover, as one can observe, for $\Delta = 0.12$ the η parameter almost vanishes.

Table 4.5: Electrical field gradient parameters the for $LaMnO_{3+\Delta}$ samples at room temperature (the index B/d refers to the minor EFG, *i.e.*, EFG_B for $\Delta \leq 0.02$ and EFG_d for $\Delta \geq 0.12$)

Sample	$V_{zz}(V/Å^2)$	η	δ (%)	f (%)	$V_{zz}^{B/d}(V/Å^2)$	$\eta^{B/d}$	$\delta^{B/d}$ (%)	$f^{B/d}$(%)
0^a	63.7(11)	0.85(3)	5	75	43.5(13)	0.64(4)	19	25
0.01	70.8(11)	0.60(3)	6	87	43.9(13)	0.48(4)	13	13
0.01_b	70.9(11)	0.55(3)	5	88	40.2(13)	0.42(4)	10	12
0.02	70.7(10)	0.53(2)	6	96	42.9(15)	0.43(5)	9	4
0.07	71.3(9)	0.42(2)	10	100				
0.08	71.3(8)	0.43(2)	9	100				
0.1	71.9(9)	0.40(2)	10	100				
0.12	111(1)	0.15(3)	4	58	61.3(25)	0.80(4)	2^b	37
0.13	110(1)	0.13(3)	6	86	63.0(25)	0.82(3)	2^b	14

[a] This sample was measured using ^{111}In isotope (see section 4.3).

[b] The relative width, δ, was fixed to that values. Note that these fits were performed using time dependent interactions and in addition to that attenuation a dynamic damping term was used (see section 4.5).

Table 4.5 presents the parameters used to perform the fits to the R(t) function, EFG principal component, V_{zz}[6], asymmetry parameter, η, and the attenuation parameter, δ.

[6]The parameter used in the fit programme is the observable frequency ω_0 instead of V_{zz}. The two quantities are related by: $\omega_0 = 3eQV_{zz}/(20\hbar)$ for I=5/2 (see chapter 3).

We stress that when presenting the fit results to the experimental data, we made the option of quoting the principal component of the EFG, V_{zz}, instead of the fundamental quadrupole frequencies ν_Q (or ω_0). Our

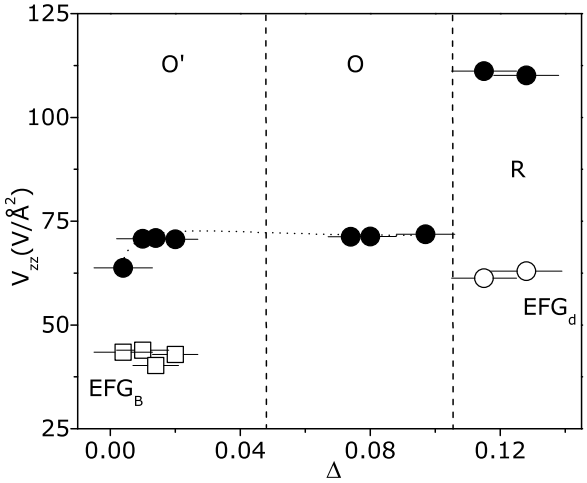

(a)

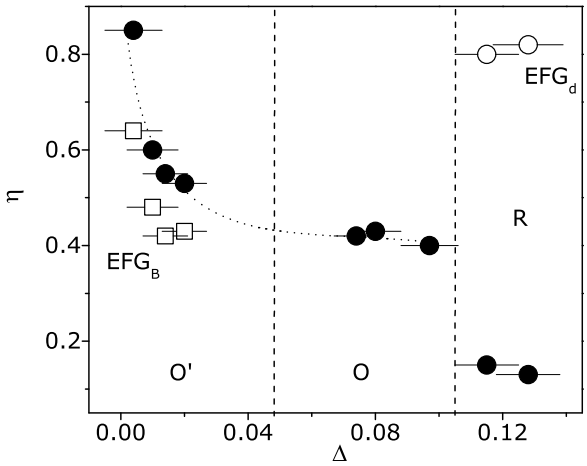

(b)

Figure 4.9: EFG principal component V_{zz}, a) and asymmetry parameter η, b) for the major (•) and minor (□ and ○) local environments as functions of oxygen content for the $LaMnO_{3+\Delta}$ system. Lines are guides for the eye.

Figure 4.9 shown the EFG parameters, V_{zz} and η, obtained for the main EFG at room temperature (blacks circles). The same figure also presents the parameters of the minoritary $EFG_{B/d}$ (EFG_B for $\Delta \leq 0.02$ and EFG_d for $\Delta \geq 0.12$). As one can observe, the stoichiometric $LaMnO_3$ sample is characterized by a highly asymmetric main EFG, η= 0.85 and V_{zz}= 63.7 V/Å^2. Increasing the oxygen content the asymmetry parameter of the main EFG decreases rapidly from its maximum value reaching, within the O crystallographic phase, the value $\eta \sim 0.4$ for the $\Delta = 0.10$ sample. The trend of this asymmetry parameter shows that the

aim is to simplify the plots and discussion, regarding the evolution of V_{zz} . We further point that the relative fit uncertainties of V_{zz} is usually below 3 %, while the absolute value of V_{zz} has $\sim$ 16% uncertainty, due to the associate quadrupole error, in this work Q=0.83(0.13) b.

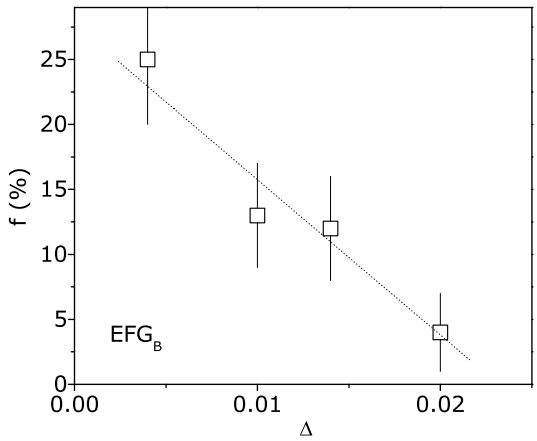

Figure 4.10: Fraction of probes interacting with EFG_B as a function of the oxygen content (at room temperature). The line is a guide for the eye.

transition from $\eta > 0.5$ to $\eta < 0.5$ occurs approximately for $\Delta = 0.05$, *i.e.*, at the O' to O transition (see figure 4.3(a)). Apart from its slight increase for the non stoichiometric samples, V_{zz} shows no significant changes in all range of compositions till $\Delta \leq 0.10$. In contrast for $\Delta > 0.10$, in a small Δ window, the parameters of the main EFG change drastically to a much higher value of V_{zz} and a lower η. For $LaMnO_{3.12}$ sample this almost axial symmetric EFG is characterized by $\eta = 0.15$ and $V_{zz} = 111$ V/Å^2.

As mentioned in the beginning of this section, in some cases a second EFG had to be considered to perform a proper fit. The local environment coexistence was observed in the two limits of the phase diagram, *i.e.*, for $\Delta \leq 0.02$ and $\Delta \geq 0.12$ (squares and open circles in figure 4.9 respectively). For $\Delta = 0.12$ and $\Delta = 0.13$ samples the second EFG_d is characterized by $\eta_d = 0.80$, $V_{zz}^d = 61.3$ V/Å^2 and $\eta_d = 0.82$, $V_{zz}^d = 63.0$ V/Å^2 respectively. One can easily note that the parameter values of this second EFG_d are nearly the ones measured for the main EFG in the low doped orthorhombic O' samples. One should note that although a macroscopic orthorrombic/romboedral phase coexistence was observed for the $\Delta = 0.12$, the sample with $\Delta = 0.13$ presents a single rhombohedric average lattice symmetry. In the low doped phase diagram, $\Delta \leq 0.02$ where the samples present a single orthorhombic O' structure, the principal component of the minoritary EFG_B averages $V_{zz}^B \sim 42$ V/Å^2 and the η_d parameter decreases from $\eta_d \sim 0.64$ for the stoichiometric sample to $\eta_d \sim 0.43$ for the sample with $\Delta = 0.02$. One should refer that the EFG_B parameters determination was not very accurate due to the large width of the EFG_B distributions or/and due to the small percentage of probes interacting with this EFG_B. Figure 4.10 presents the volume fraction of probes interacting with the second EFG_B as a function of Δ. One can observe that that fraction rapidly decreases with delta increasing being almost negligible for $\Delta = 0.02$.

As already mentioned, the oxygen excess in the $LaMnO_{3+\Delta}$ system cannot be accommo-

dated interstitially in the lattice but results in the creation of equivalent amounts (υ) of La and Mn vacancies [$\upsilon = \frac{\Delta}{3+\Delta}$] [81]. Vacancies can affect the EFG so it is important to address immediately this issue. Although the amount of vacancies in our systems is not higher than $\upsilon \sim 4\%$, one should note that with a few percent vacancies one has a probability of the order of a few ten percent to find a vacancy around a generic La site. For $\sim 4\%$ chance of a Mn (or La) vacancy, one should expect a probability $1 - 0.96^8 \sim 27\%$ of finding at least one vacancy in the surrounding Mn of a generic La site. This probability is even higher if the possibility of having a La vacancy in the next shell is taken into account, $1 - 0.96^{14} \sim 44\%$ ($14 = 8Mn + 6La$). In the range $0.04 \leq \Delta \leq 0.1$ (orthorhombic samples), the amount of vacancies is already appreciable ($\upsilon = 1.3\%$ for $\Delta = 0.04$, $\upsilon = 2.6\%$ for $\Delta = 0.08$ and $\upsilon = 3.2\%$ for $\Delta = 0.10$), which implies that the fraction of generic La sites with at least one vacancy in its immediate Mn neighborhood should be 10%, 19% and 23%, respectively (same calculation as above). A local environment with such amounts however is not observed in our results; we didn't detect (within detection limits) an EFG distribution that could be associated with such a large and increasing amount of vacancies. Facing these results, we had to admit that the vacancies should be further away than the Mn (or next La shell) immediate probe neighborhood. This can be understood admitting that preferentially Cd probes are naturally incorporated in existent La vacancies. The probability that a La vacancy is surrounded by one or more Mn/La vacancies is much lower: $0.04 * 0.44 \sim 2\%$ for the sample with $\Delta = 0.13$ (supposing that the presence of La and Mn vacancies in the same cell is not correlated). In this way, the majority of Cd probes (98%) are shielded by at least two oxygen atomic shells, which means that vacancies should only affect the relative width (δ) of the main EFG distributions. Generally, randomly distributed vacancies and/or other defects contribute to attenuate the PAC signal, *i.e.*, increasing the width of the EFG distributions. Thus our data suggest that, apart from a possible increase of the δ with increase of the oxygen content, vacancies do note play an important role in the observed EFG parameters.

Having ruled out the hypothesis of a direct influence of vacancies in the measured EFGs, one can state that the compounds with orthorhombic and rhombohedral crystallographic structure clearly present distinct main EFGs. Interestingly, evidences for local phase coexistence in the two limits of the phase diagram were observed. On the other hand, in the orthorhombic O region no evidence for such a phase segregated state was found (but higher δ). To better understand the nature and stability of the local phase coexistence a study of the thermal dependence of the EFG and MHF in representative samples of each section of the phase diagram will be presented in the next sections.

4.3 Hyperfine fields in the stoichiometric end-member ($\Delta = 0$)

To study in detail the electrical field gradient and magnetic hyperfine field in the $LaMnO_3$ compound we used the ^{111}In probe. Due to its half-life, 2.8 day, this probe allows to measure several temperatures with a single implantation (or diffusion). Two series of experiments were performed. In one, the ^{111}In probe was incorporated into the sample via ion implantation whereas in the other the isotope was diffused into the compound by wetting the sample with a $^{111}InCl_3$. To eliminate implantation damage or to promote the In diffusion, a subsequent annealing during 5 hours in the same pressure and temperature conditions as the ones presented in table 4.1 was performed. After this annealing, the experimental R(t) spectra were measured from 11 up to 320 K temperature range.

Figure 4.11 shows representative R(t) spectra measured at different temperatures.

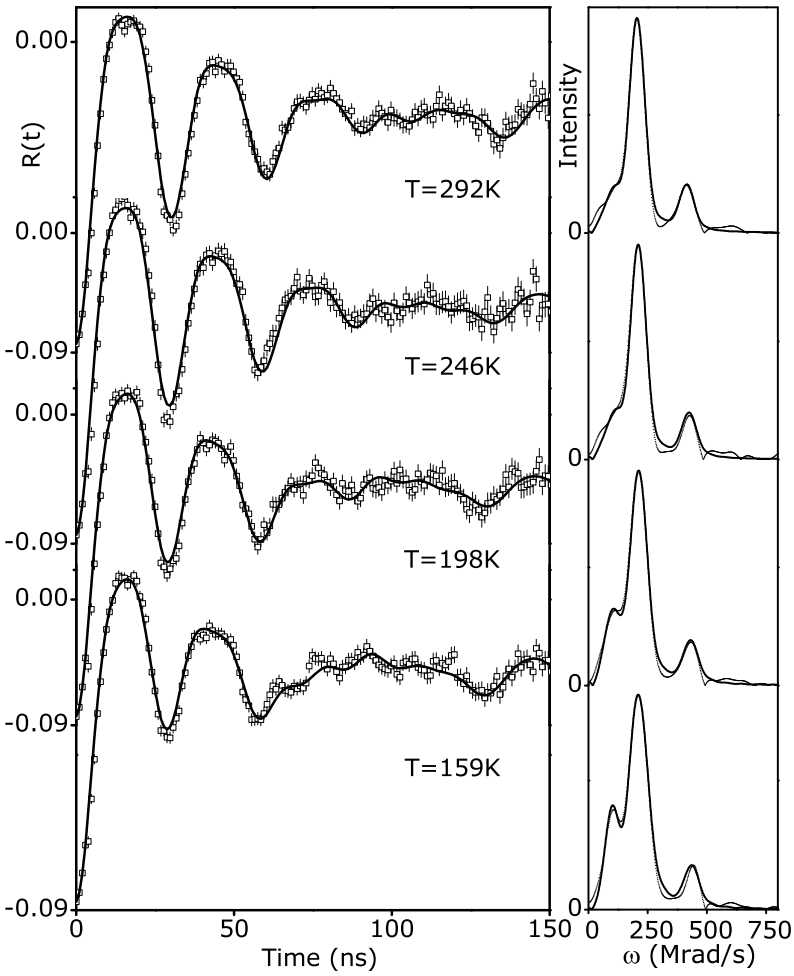

Figure 4.11: Representative R(t) experimental functions and the correspondent fits for $LaMnO_3$ at temperatures above T_N (diffused ^{111}In). Corresponding Fourier transforms are displayed on the right side.

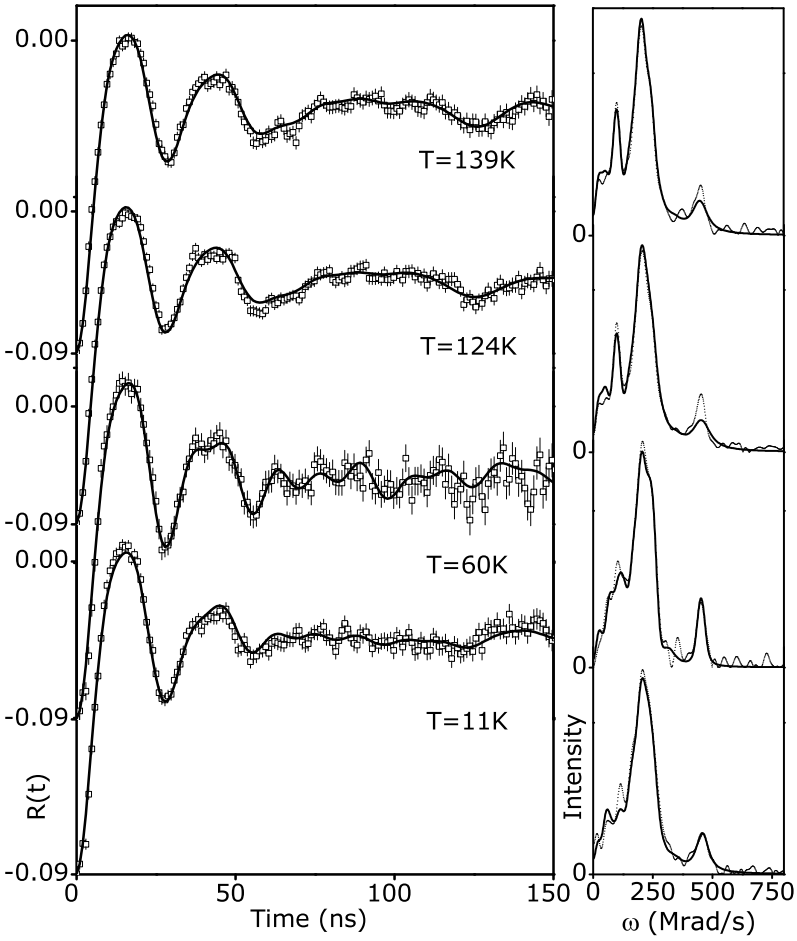

Figure 4.12: Representative R(t) experimental functions and the correspondent fits for $LaMnO_3$ at temperatures below T_N. Corresponding Fourier transforms are displayed on the right side.

The fit to each experimental PAC spectrum (continuous lines over the R(t)) was obtained considering two static EFG distribution, *i.e.*, a main EFG_A and minoritary EFG_B, which were assumed to be Lorentzian-like. As one can observe from the Fourier transforms of the R(t) functions (figure 4.11) the intensity of the FT first peak, corresponding to the lower frequency, ω_B^1, of the EFG_B triplet[7], increases with decreasing temperature. Hence the number of probes interacting with each local environment is temperature dependent. Accordingly, to perform a proper fit, the percentage of probes interacting with each local environment (A and B) were allowed to vary with temperature. As referred above, the spectrum obtained at room temperature was fitted admitting two frequency triplets revealing

[7]In the Fourier transforms of figure 4.11 the two triplets ω_A^i and ω_B^i (i=1, 2 ,3) corresponding to the EFG_A and EFG_B are not visible due to the overlap of the frequencies. When two (or more) local environments are present, it may happen that distinct EFGs give rise to frequency triplets for which some harmonics overlap in the frequency spectrum. Furthermore, since $\eta_A \sim 0.84$ one has $\omega_A^1 \sim \omega_A^2$.

that 75% of the probes interact with a strongly non-axially symmetric EFG_A, characterized by V_{zz}^A ~63.7 V/Å^2 and $\eta_A \sim 0.85$. The remaining 25% of the probes interact with a slightly weaker EFG_B, V_{zz}^B ~43.5 V/Å^2, also non-axially symmetric, $\eta_A \sim 0.64$. In figure 4.12 some representative R(t) spectra measured at temperatures below T_N=139 K are presented. As one can observe the R(t) spectra is strongly damped in the 50 to 100 ns range. As the temperature is decreased the damping of the R(t) spectra, in that range, increases and for temperatures as low as 60 K and 10 K only small wiggles are observed. Table 4.6 summarizes the EFG parameters obtained by fitting the spectra in the temperature range studied.

Table 4.6: Electrical Field Gradient parameters for the stoichiometric $LaMnO_3$ sample.

T(K)	$V_{zz}^A(V/Å^2)$	η^A	δ^A (%)	f^A (%)	$V_{zz}^B(V/Å^2)$	η^B	δ^B (%)	f^B (%)
320.0	62.1(11)	0.85(3)	5.5	78	45.7(14)	0.70(4)	21	22
305.0	63.0(11)	0.85(3)	5.3	77	44.5(13)	0.69(4)	20	23
297.0	64.1(10)	0.84(3)	4.8	76	42.0(11)	0.64(4)	21	24
292.0	63.7(11)	0.85(3)	5.1	75	43.5(13)	0.64(4)	19	25
291.0	64.5(10)	0.83(3)	6.0	77	42.9(12)	0.59(5)	19	23
274.0	65.5(10)	0.83(3)	5.9	76	42.4(13)	0.60(7)	19	24
245.5	65.8(10)	0.84(3)	5.5	75	42.2(11)	0.54(4)	19	25
218.0	65.6(10)	0.83(3)	5.9	76	42.5(13)	0.52(6)	17	24
197.6	67.2(10)	0.83(3)	4.9	67	43.1(11)	0.48(6)	17	33
176.0	66.7(10)	0.83(3)	6.0	69	43.6(12)	0.43(5)	15	31
158.6	68.3(10)	0.82(3)	5.7	60	43.7(11)	0.40(6)	14	40
149.0	68.3(12)	0.82(3)	6.7	66	42.7(12)	0.44(5)	12	34
139.0	68.0(12)	0.83(3)	5.6	57	41.9(14)	0.47(5)	9	43
138.7	69.1(12)	0.84(3)	6.8	52	41.8(14)	0.43(7)	10	48
124.0	68.5(12)	0.86(3)	7.0	52	42.2(14)	0.40(6)	9	48
123.0	68.5(13)	0.85(3)	6.7	56	42.4(15)	0.47(6)	8	44
109.0	67.7(13)	0.86(3)	5.6	55	43.4(15)	0.39(7)	9	45
89.6	68.0(13)	0.86(3)	5.8	55	43.1(14)	0.46(7)	10	45
70.0	69.6(13)	0.85(3)	5.8	53	44.5(14)	0.43(7)	9	47
60.0	69.4(13)	0.87(3)	4.5	51	42.4(15)	0.49(8)	8	49
35.0	70.3(15)	0.83(4)	6.0	52	43.9(14)	0.45(7)	9	48
20.0	69.6(13)	0.86(3)	6.0	54	45.5(14)	0.39(8)	9	46
10.9	71.7(13)	0.82(3)	5.6	52	43.9(14)	0.44(8)	9	48

Figure 4.13 displays the thermal dependence of the EFG parameters, principal component, V_{zz}, and asymmetry parameter, η, a) and b), respectively. The magnitude of the EFG principal components, V_{zz}^A and V_{zz}^B, are quite distinct. The magnitudes of both EFG principal components decrease with the increase of temperature. This trend is common for perovskite structures and is frequently associated with the increase of the atomic vibrations and (volume) thermal expansion, α, when increasing temperature. However the thermal ex-

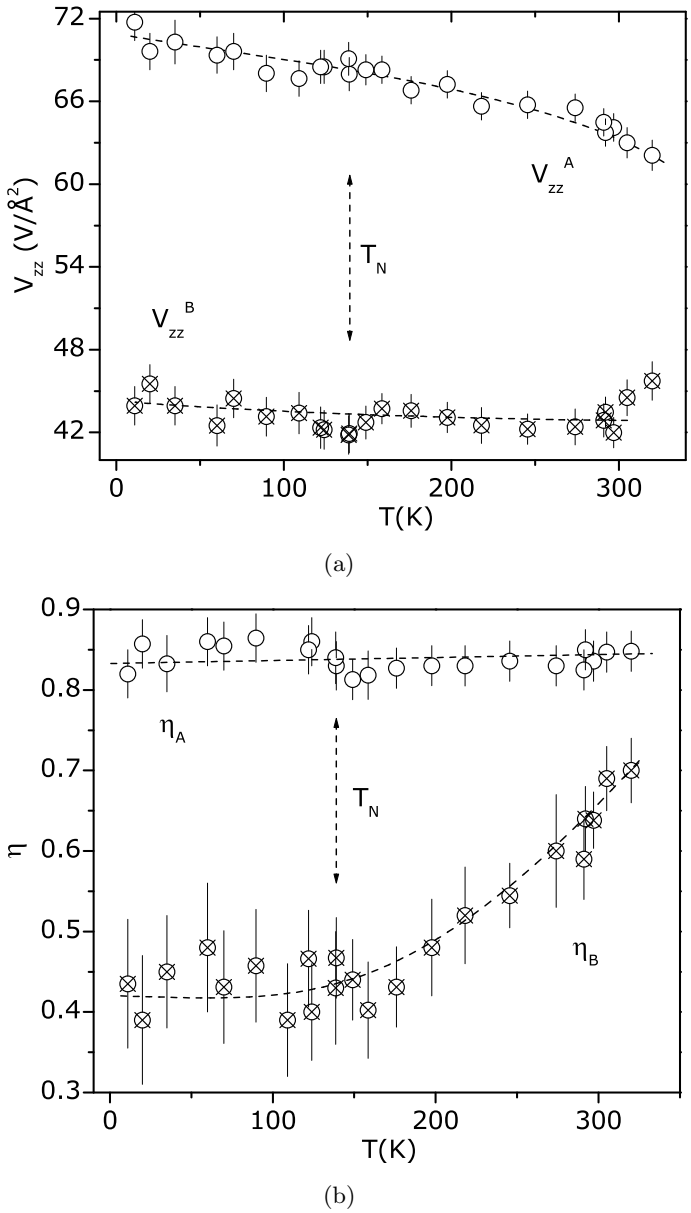

Figure 4.13: $LaMnO_3$ EFG principal component V_{zz}, a) and asymmetry parameter η, b) for the A ($\circ$) and B ($\otimes$) local environments as a function of the temperature. Lines are guides for the eye.

pansion is very small and alone cannot account for the $V_{z\,z}$ temperature dependence. For the stoichiometric $LaMnO_3$ compound $\alpha \sim 1.2 \times 10^{-5}$ K^{-1} (unit cell volume parameters taken from [85]) while $\frac{1}{V_{zz}^{0A}}\frac{\Delta V_{zz}^{A}}{\Delta T} \sim$ -4.3×10^{-4} K^{-1} and $\frac{1}{V_{zz}^{0B}}\frac{\Delta V_{zz}^{B}}{\Delta T} \sim$ -1.1×10^{-4} K^{-1} (for $T>T_N$), *i.e.*, correct sign[8] but $\frac{1}{V_{zz}^{0}}\frac{\Delta V_{zz}}{\Delta T}$ is one order of magnitude higher. In the same figure one can observe that the A local environment is characterized by a highly asymmetric EFG which is

[8] V_{zz} is expected to decrease with cell volume increase, see equation 3.57.

almost temperature independent averaging $\eta_A \sim 0.85$. The B local environment is characterized by a η parameter essentially constant which averages $\eta_B \sim 0.45$ in the range of 10 K to 150 K ($\sim T_N$), substantially increasing for temperatures above 150 K.

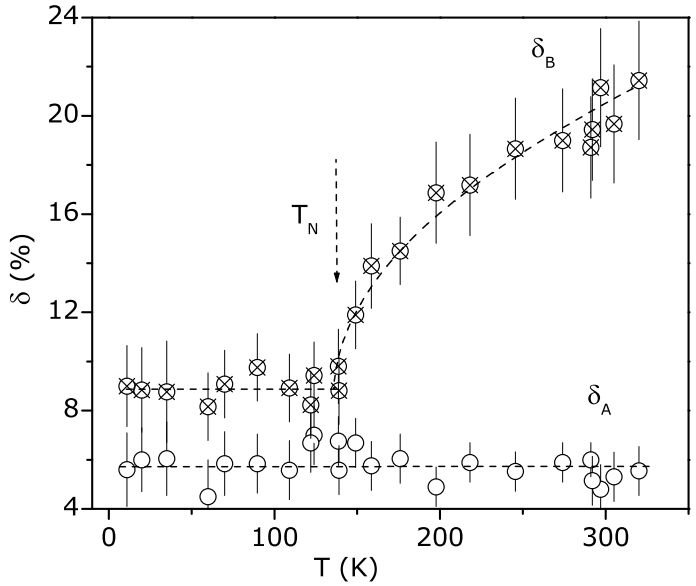

(a)

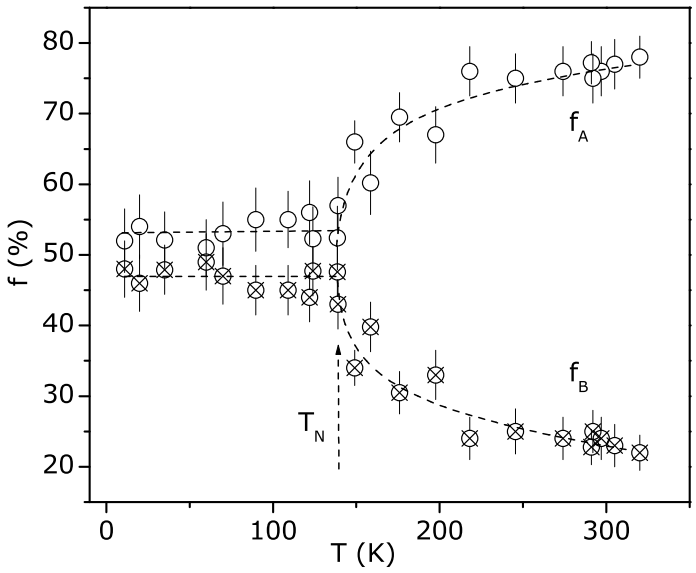

(b)

Figure 4.14: Temperature dependence of the EFG static attenuation parameter, δ, a) and probe volume fractions, f_A and f_B, b) corresponding to the A ($\circ$) and B ($\otimes$) local environments for the $LaMnO_3$ sample. Lines are guides for the eye.

In figure 4.14 the temperature dependence of the relative width of the EFG distributions, δ, and the fraction of probes interacting with the different local environments, f, are

presented (top and bottom respectively). One can see that the relative width of the EFG_A distribution is relatively narrow ($\delta_A \sim 5\%$) and temperature independent. On the other hand, for EFG_B, a broader distribution was found. Decreasing temperature δ_B decreases stabilizing around $\delta_B \sim 9\%$ for $T<T_N$. One can also see that the number of probes interacting with each local environment change continuously (figure 4.14(b)). At high temperatures the most of probes interact with the A environment. On decreasing temperature the fraction of probes experiencing the EFG_B continuously increases in detriment of the fraction of probes experiencing EFG_A. These changes halt when the fraction of both local environments reaches approximately equal amounts. This occurs very close to the Néel temperature T_N. One further observes from figure 4.14(a) that the trend of the relative width of the EFG_B distribution, δ_B, seems to be correlated with the number of probes interacting with B local environment. This correlation is shown in figure 4.15(a) where δ_B versus f_B is presented. It is apparent the decrease of the relative width of the EFG_B distribution with the increase of the B local environment fraction. This suggests that, at high temperatures, the B local environment should be dispersed in the A matrix and without long range correlation. As the temperature decreases the regions with the B local environment smoothly increase and a much well defined EFG_B sets in.

The variation of δ_B (or equivalently f_B, since they are linearly correlated) when the temperature changes, down to a temperature where it stabilizes, hints for a continuous phase transition possibly from an incoherent random distributed to a coherent local environment. To further investigate this assumption we assumed $\delta_B - \delta_B^0$ (equivalently f_B-f_B^0) as the phase transition order parameter that must follow a power law behavior when the critical temperature T_s is approached, *i.e.*, $\delta_B - \delta_B^0 \sim (T - T_s)^\beta$. In the figure 4.15(b) $\delta_B - \delta_B^0$ is displayed against the reduced temperature $t = (T - T_s)/T_s$ in a log-log plot. As one can observe, the data follow a critical behavior from which we estimate a critical temperature $T_s \sim 145 \pm 5$ K and a critical exponent $\beta = 0.35 \pm 0.05$. The value estimated for the critical temperature T_s is the Néel temperature T_N within error bars.

From a close inspection of the spectra and their FT transforms it is apparent the splitting of the frequency triplets for temperatures $T \leq 140$ K. This immediately suggests the presence of a magnetic hyperfine field below T_N, although accounting for the fully A-type antiferromagnetic alignment of spins one would expect no magnetic hyperfine field at the La-site. One remarks that several fitting approaches were tried and the features in the R(t) spectra and corresponding FT could only be modeled considering the presence of a magnetic hyperfine field. However, two different models satisfactory fit the data. The first presupposes that only the probes in the B local environment experience a MHF, whether in the second both local environments have non-vanishing MHFs. The fits presented above were performed assuming the latter model, since the chi-squared values are slightly lower and the overall systematic trend of the EFG/MHF are more consistent. One should however remark that the presence of combined interactions adds additional attenuation of the R(t) spectra, considerably limiting

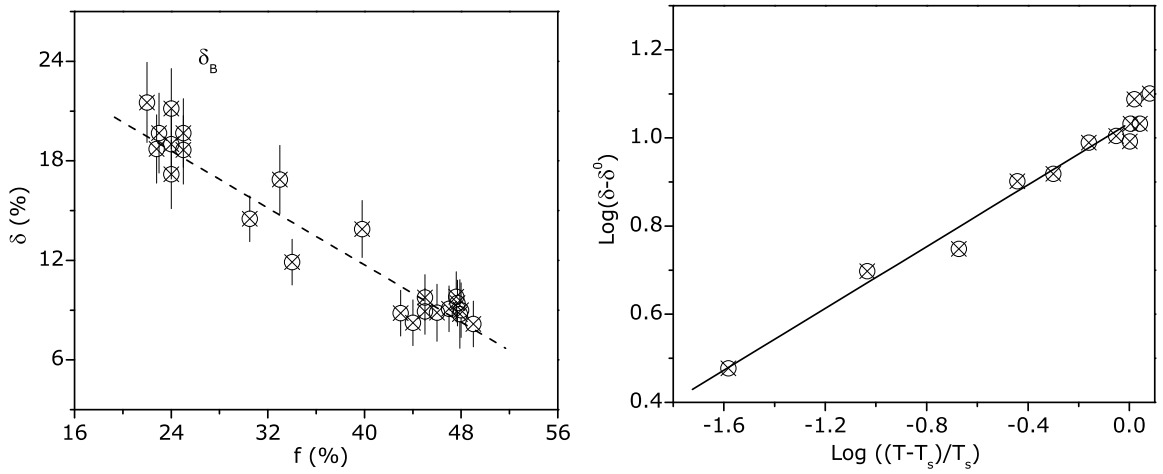

(a) (b)

Figure 4.15: EFG static attenuation parameter, δ_B, as a function of the probe volume fractions, f_B, for the B local environments (right). Log-log plot of $\delta_B - \delta_B^0$ against the reduced temperature $t = (T - T_s)/T_s$ (left). Lines are guides for the eyes.

the accuracy of the EFG/MHF parameters determination. This is responsible for the higher dispersion of the EFG parameters below T_N=139 K.

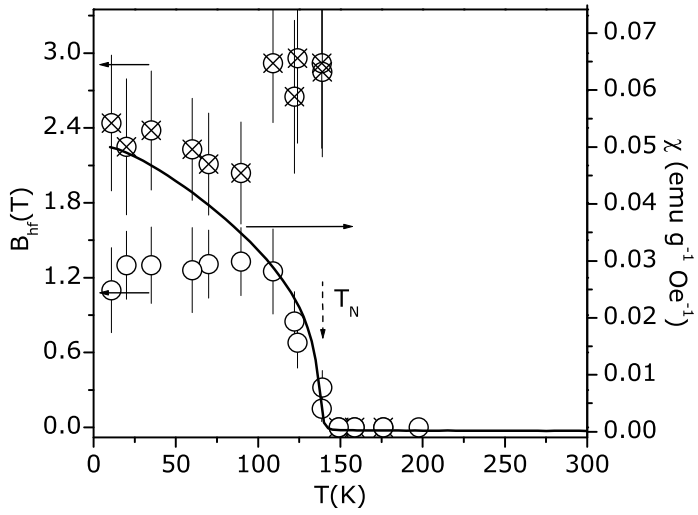

Figure 4.16: Temperature dependence of the magnetic hyperfine field corresponding to the A (○) and B (⊗) local environments and macroscopic susceptibility (line) for the $LaMnO_3$ sample.

In figure 4.16 is plotted the obtained MHF as a function of temperature. In the same figure and for comparison the macroscopic susceptibility curve is also shown. It is apparent that the hyperfine field only appears below the magnetic transition. The magnetic hyperfine

field of the B local environment, MHF_B, appears almost discontinuously and with a small downturn near T≈ 110 K, after which MHF_B increases with decreasing temperature. MHF_A, on the other hand has, near T_N, a similar temperature dependence as the susceptibility. The low temperature values, T=11 K, for the MHF of environments A and B are B^A_{hf} ∼1.1(3) T and B^B_{hf} ∼ 2.4(5) T, respectively. The angle between the MHF and V_{ZZ} averages $\beta^A \sim 24°$ and $\beta^B \sim 90°$.

4.4 Hyperfine fields in the weakly Jahn-Teller distorted $LaMnO_{3.08}$

The weakly Jahn-Teller distorted ferromagnetic insulator $LaMnO_{3.08}$ sample was implanted with ^{111}Cd following the standard procedure (see in chapter 2) to perform the PAC measurements as a function of temperature. To remove implantation damage a 20 minutes annealing in controlled atmosphere (see table 4.1) was performed. The experimental R(t) spectra were measured in the 10 to 292K temperature range, as shown in figure 4.17.

The fit to each experimental PAC spectrum (continuous lines over the R(t)) was obtained considering only one static EFG distribution which was assumed to be Lorentzian-like. The frequency triplet correspondent to the measured EFG can be viewed in the Fourier transforms of the R(t) functions. As presented in section 4.2 of this chapter, the spectrum obtained at room temperature revealed that all the ^{111}Cd nuclei interact with a non-axially symmetric EFG, characterized by V^A_{zz} =71.3 V/Å^2 and $\eta_A \sim 0.43$. Table 4.7 summarizes the EFG parameters and the MHF obtained in the studied temperature range.

Table 4.7: Electrical field gradient parameters and magnetic hyperfine field for the $LaMnO_{3.08}$ sample.

T(K)	V^A_{zz}(VÅ^2)	η^A	δ^A (%)	B_{hf} (T)
292	71.3(8)	0.43(2)	9.0	-
266	72.0(8)	0.43(2)	9.5	-
197	73.6(8)	0.41(2)	9.5	-
100	75.7(15)	0.41(3)	10	4.4(4)
10	78.4(15)	0.43(3)	10	4.3(4)

The thermal dependence of the EFG parameter principal component, V_{zz}, is shown in figure 4.18. The inset displays the asymmetry parameter, η, as a function of temperature. As shown, the magnitude of the EFG principal component increases with temperature decrease. Again, this is the common trend for perovskite systems and also here the (volume) thermal

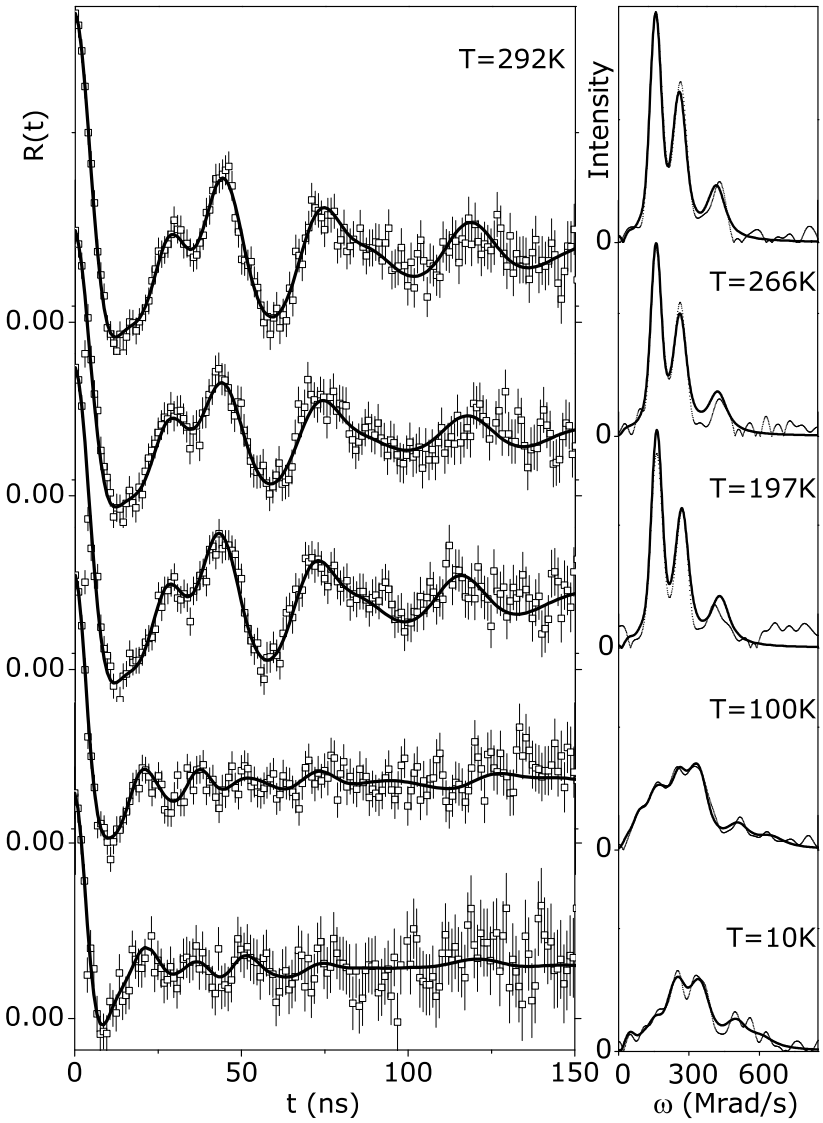

Figure 4.17: R(t) experimental functions and the correspondent fits for $LaMnO_{3.08}$ at different temperatures. Corresponding Fourier transforms are displayed on the right side.

expansion, α, cannot account for the V_{zz} temperature dependence[9]. One the other hand, η is almost constant in this temperature range, averaging $\eta \sim 0.42$. The relative width of the EFG distribution, $\delta \sim 9.5\%$, was found to be temperature independent[10]. As already referred this broadening of the distribution should be connected to the presence of vacancies in the system.

As one can observe in figure 4.17 the R(t) spectra is strongly damped below T_C ($\sim$ 150

[9] $\alpha \sim 1.3 \times 10^{-5}$ K^{-1} (unit cell volume parameters taken from [85]) and $\frac{1}{V_{zz}^0}\frac{\Delta V_{zz}}{\Delta T} \sim$ -2.9×10^{-4} K^{-1} (for $T>T_C$), $\frac{1}{V_{zz}^0}\frac{\Delta V_{zz}}{\Delta T}$ has the correct sign but is one order of magnitude higher.

[10] The relative width of the EFG distribution below T_C had to be fixed ($\delta = 10\%$) to perform a proper fit

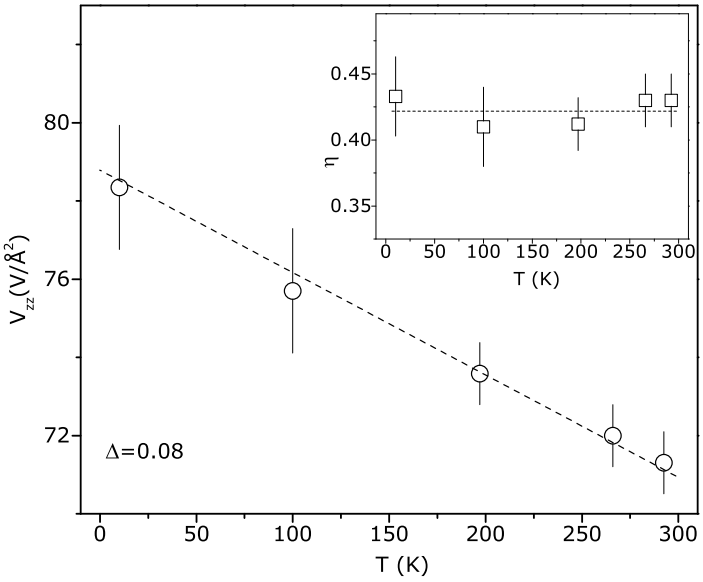

Figure 4.18: $LaMnO_{3.08}$ EFG principal component V_{zz} and asymmetry parameter η (inset) as a function of the temperature.

K). This feature in the R(t) spectra and the new frequencies in the FT transforms shows that the probes interact with a magnetic hyperfine field, additionally to the EFG. Accordingly, the fits were performed considering a magnetic hyperfine field below T_C. The obtained MHF was B_{hf}=4.4(4) T and B_{hf}=4.3(4) T for 100 and 10 K, respectively. The angle between the MHF and the principal component of the EFG was found to be $\beta \sim 22°$. The obtained values for the magnetic hyperfine fields are consistent with a full ferromagnetic environment of the surrounding Mn ions below T_C [20, 213].

4.5 Local distortions and polaron clusters in $LaMnO_{3.12}$

To gain further insight on the microscopic nature of polaronic distortions, their spatial correlations and the role of these local distortions in ferromagnetic insulator manganites (FMI), we have studied in detail the sample $LaMnO_{3.12}$. This is a prototypical ferromagnetic insulator manganite that undergoes a rhombohedral (R)-orthorhombic (O) structural transition around room temperature, providing us with an ideal scenario to probe the evolution of local lattice distortions through different average lattice symmetries. In this way one can correlate the study of the macroscopic R/O phase transition as function of temperature with the EFG temperature dependence through the different average lattice symmetries.

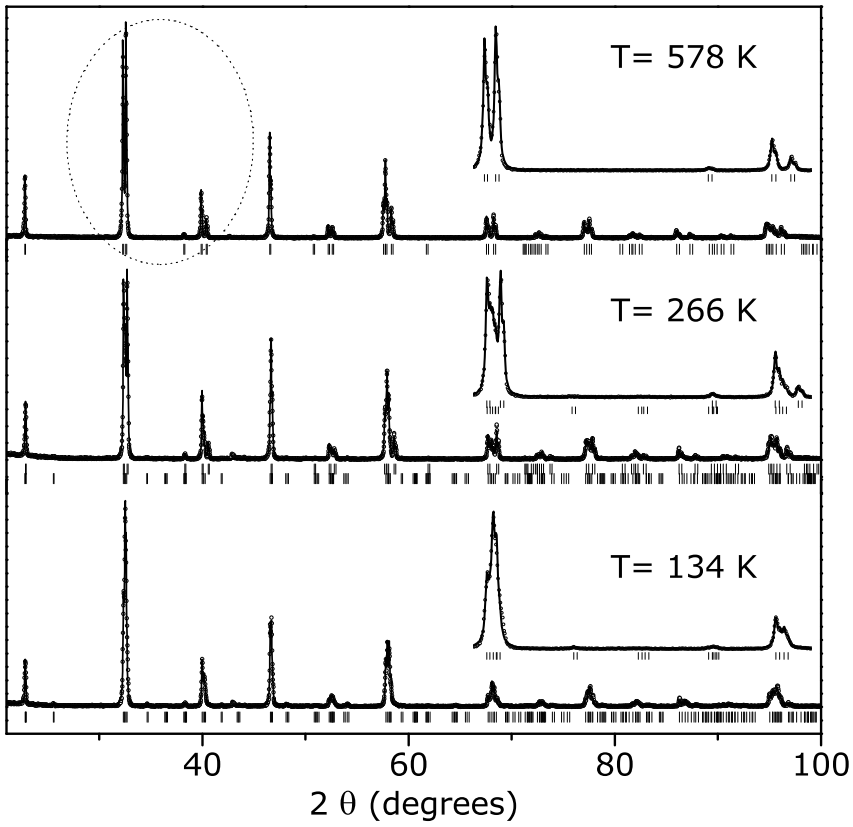

Figure 4.19: $LaMnO_{3.12}$ representative X-ray diffraction patterns at different temperatures. The observed pattern (dots), calculated (solid line) and reflections of the correspondent phases (tick marks) are shown. For T=266 K the first series of tick marks indicates the reflections of the rhombohedral symmetry and the second the orthorhombic reflections. Inset: detail on the 32.0° to 40.9° 2θ range.

4.5.1 Rhombohedric to orthorhombic structural phase transition

The characteristic macroscopic properties of the polycrystalline $LaMnO_{3.12}$ system were presented in the beginning of this chapter. We find for this sample a ferromagnetic insulator state, $T_C \approx 145$ K and $\theta_P \sim 170\,K$ (see figure 4.4(d) and 4.7(b)).

To characterize the average lattice structure of the $LaMnO_{3.12}$ sample as a function of temperature (100 K$\leq$T$\leq$578 K), powder x-ray diffraction measurements in a 15° to 110° 2θ range were performed. The analysis of the powder x-ray diffraction measurements allowed to determined the crystallographic structures and correspondent lattice parameters for different temperatures. The refinement of X-ray diffraction patterns was performed using the FULLPROF program [199]. The line shape of the diffraction peaks was generated by a pseudo-Voigt function.

In figure 4.19 some representative X-ray diffraction patterns for a 21° to 100° 2θ range at T=578 K, T=266 K and T=134 K are presented. In the inset, a detail on the 32.0°

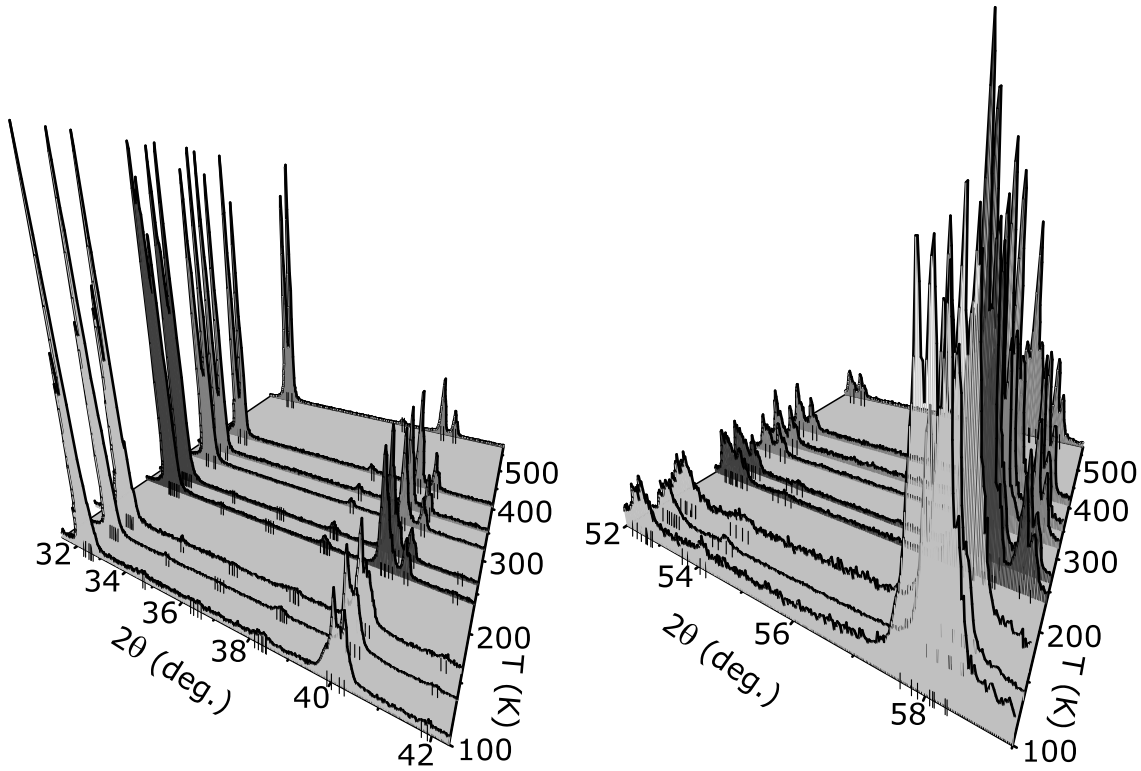

(a) (b)

Figure 4.20: Detail on the $LaMnO_{3.12}$ X-ray diffraction patterns at different temperature a) 31.3 to 42.3 2θ, b) 52.0 to 59.0 2θ. Tick marks indicate the reflections of the rhombohedral and /or orthorhombic symmetry.

to 40.9° 2θ range is depicted. The diffraction patterns at different temperature, observed in figure 4.19, can be clearly identified with the rhombohedral and/or orthorhombic structural phases accordingly, the patterns were refined ether in the $R\bar{3}c$ or/and Pbnm space groups. A good matching of the fits were obtained and no unidentified lines[11] nor additional splitting of the peaks were observed. In figure 4.20 a detail on the XRD pattern, a) 31.3° to 42.3° and b) 52.0° to 59.0° 2θ range, as a function of the temperature is shown. The temperature evolution of the O/R crystallographic phases is evident through those graphics. XRD patterns for temperatures higher than T≥318 K are characterized by a single-phase perovskite with rhombohedral symmetry whereas a coexistence between rhombohedral and orthorhombic symmetries occurs for temperatures between 197 K<T< 318 K. The presence of the rhombohedral crystallographic phase, in that range of temperatures, is obvious not only through the more intense peaks at at $2\theta \sim 32.3°$ and $2\theta \sim 32.7°$ but also through the

[11]The discrepancy factors averages: $R_p \sim 13$, $R_{wp} \sim 18$, $\chi^2 \sim 0.6$. At some temperatures extra peaks around 42.3°-45.5° and 49.37°-52.9° are present in the x-ray patterns. These extra lines belong to the reflections of the sample holder used for the measurement of this sample as a function of temperature.

well defined though less intense reflections around $2\theta \sim 40.4°$ and $2\theta \sim 58.5°$ (see figure 4.20 a) and b)). These reflections clearly vanish for temperature above 197 K where the orthorhombic single-phase sets in.

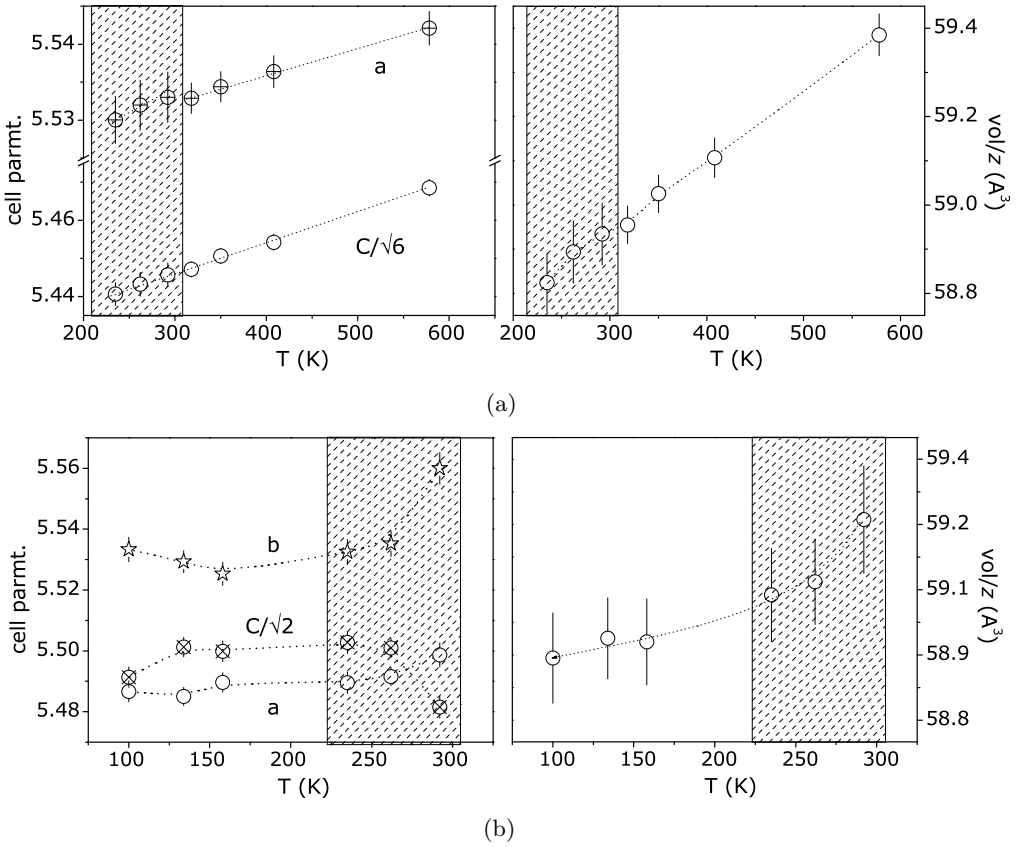

Figure 4.21: $LaMnO_{3.12}$ unit cell parameters as a function of temperature for the rhombohedric, a) and orthorhombic, b) phases. Lines are guides for the eye and the shadowed zones delimit the phase coexistence as measured by x-ray.

In figure 4.21 the evolution of the lattice parameters with temperature obtained for the two crystallographic phases is depicted. As one can observe, the cell parameters of the rhombohedric phase decreases almost linearly with temperature decreasing presenting a small "discontinuity" at the temperature where the phase coexistence starts. This discontinuity is noticeable in the unit cell volume and in the a parameter (see figure 4.21(a)). The unit cell volume of the orthorhombic phase also decreases with decreasing of temperature however, it does not present the same linear behavior as found in the rhombohedral phase. Figure 4.21(b), where the cell parameters of the orthorhombic phase are presented, shows, around room temperature, a change in the cell parameter from $c/\sqrt{2} < a < b$ to a $c/\sqrt{2} \sim a < b$. Although the number of points in that region is insufficient and significant errors are present in the determination of the cell parameters, this data suggests a decreasing in the orthorhom-

bicity above room temperature. For temperatures below RT the cell parameters trend is almost constant. Table 4.8 presents the unit cell volume of the R and O crystallographic phases found in the $LaMn_{3.12}$ sample at different temperatures.

As already observed in literature [84, 85, 195, 200] a rhombohedral/orthorhombic structural phase coexistence occurs around room temperature for the $\Delta = 3.12$ compound. The rhombohedral $R\bar{3}c$ single phase is stabilized at high temperatures (T≥318 k) whereas the single phase orthorhombic perovskite structure sets below room temperature. The variation of the cell parameters with temperature is less than 1% in both phases. Similar results were obtained by C. Ritter *et al.* [85] in a neutron refraction study.

4.5.2 PAC Experimental results

To carry out the $\gamma - \gamma$ PAC measurements in the $LaMnO_{3.12}$ system, samples arising from the same initial pellet with $\Delta = 0.12$ were implanted at room temperature with ^{111m}Cd following the standard procedure described in chapter 2. In this particular case the annealing performed to eliminate point defects created during implantation was carried out at $700\,^{\circ}C$ during 20 minutes in flowing O_2. The PAC measurements were performed in a temperature range of 12 K≤ T≤ 776 K. According to the work of Dabrowski *et al.* no changes in the oxygen concentration, Δ, occur below 700 °C (973 K), independently of the value of Δ. This allowed us to perform the PAC measurement in a very wide range of temperature without risking oxygen out-diffusion. Although the oxygen concentration should remain constant for $T_{measure} \leq 776$ K), our high temperature measurements were performed in a furnace with an oxygen controlled atmosphere. More importantly, the sample measured at the highest temperature was characterized (x-ray, magnetization) after PAC measurements to confirm that the sample was unchanged by the thermal cycling.

In figure 4.22, we present some representative R(t) experimental curves, obtained for

Table 4.8: $LaMnO_{3+\Delta}$ cell parameters in the Pbnm/$R\bar{3}c$ space group.

Temperature	$V_R(Å^3)$	$V_O(Å^3)$
578	59.39	-
408	59.11	-
350	59.03	-
318	58.96	-
292	58.93	59.26
262	58.89	59.11
235	58.82	59.09
158	-	58.98
134	-	58.99
100	-	58.94

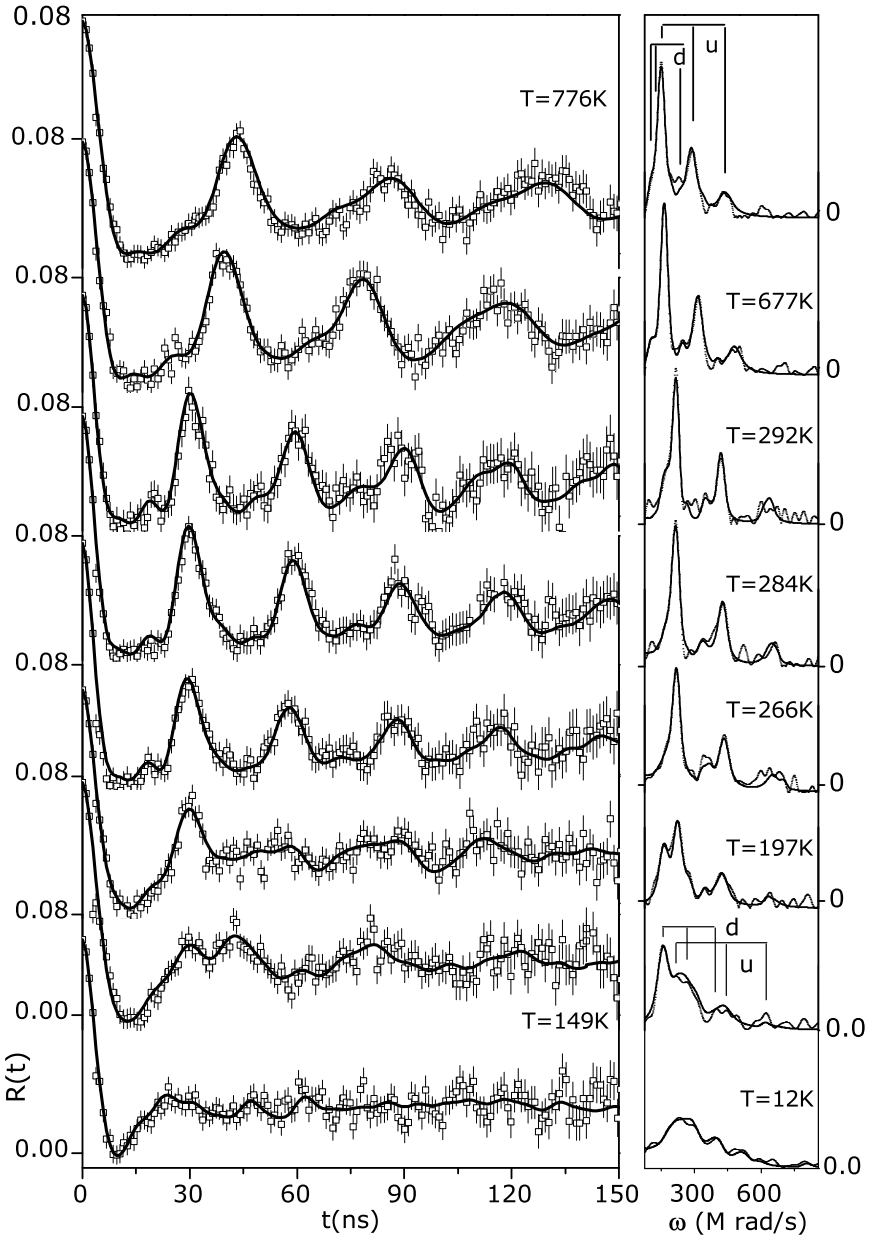

Figure 4.22: Representative R(t) experimental functions and the correspondent fits for $LaMnO_{3.12}$ at different temperatures. Corresponding Fourier transforms are displayed on the right side.

$LaMnO_{3.12}$ at different temperatures. The Fourier transforms of the R(t) function are displayed on the right side of the figure.

Several systematic fitting approaches were tried before arriving at the final result shown in figure 4.22. An evident feature of these spectra is that the main frequency triplet present at high temperature is quite distinct from the low temperature one. Thus, a first approach considered a single fraction fit in the limiting temperatures plus a two fraction fit in the temperature range where the two macroscopically crystallographic phases, R/O, coexist. This was clearly not enough. The best fits, considering static attenuation parameters, were obtained admitting for all temperature range the coexistence of two main local environments, named f_u and f_d[12], and a temperature independent residual fraction, named f_r. Still, the static attenuation parameter corresponding to the d environment (δ_d) shows a strong temperature dependence, with a sharp peak, in the range 266 K <T< 350 K (see figure 4.23(a)). The parameters characterizing the other local environments (u and r), on the contrary, did not show any anomalous behavior in temperature.

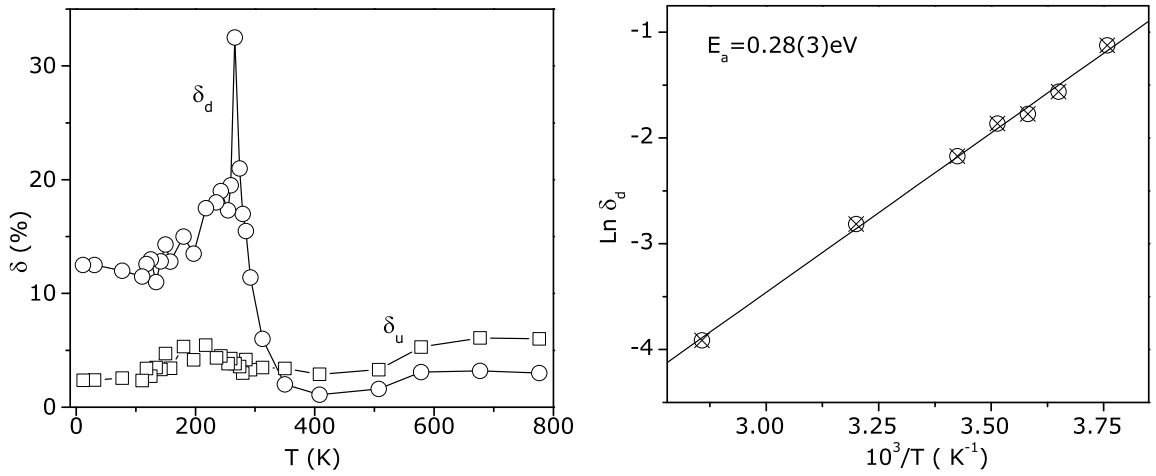

(a) (b)

Figure 4.23: a) Temperature dependence of static attenuation parameter, δ, corresponding to u (□) and d (○) environments for sample $LaMnO_{3.12}$. b) Arrhenius plot of δ_d to estimate the activation energy.

Since we are not aware of any static process in manganites that could justify the presence of such strong peak in one component and at the same time its absence in the other we attributed the temperature variation of $\delta_d(T)$ in the range 266 K < T< 350 K to EFG fluctuations. Following this idea we performed the fits shown in figure 4.22 using the dynamic attenuation parameter λ_d as described in chapter 3.

[12]The reasons for the adopted nomenclature will become clearer later.

Table 4.9: Electrical Field Gradient parameters for $LaMnO_{3.12}$ sample.

T(K)	$V^u_{zz}(V\text{Å}^2)$	η^u	$\delta^u(\%)$	$f^u(\%)$	$V^d_{zz}(V\text{Å}^2)$	η^d	$\delta^d(\%)$	λ^d(MHz)	$f^d(\%)$
776	75.8(11)	0.19(3)	6.0	86	38.1(23)	0.80(7)	3	–	10
677	83.4(11)	0.18(3)	6.1	84	41.2(20)	0.77(8)	3	–	11
578	90.8(11)	0.16(3)	5.3	82	47.9(19)	0.82(7)	3	–	13
507	96.9(10)	0.12(2)	3.3	78	52.6(19)	0.85(4)	2	–	17
408	104.3(9)	0.15(2)	2.8	72	58.2(17)	0.87(4)	1	–	23
350	107.6(8)	0.17(2)	3.4	67	60.0(19)	0.87(4)	2	4(1)	28
313	109.6(9)	0.16(2)	3.5	63	60.8(24)	0.82(4)	2	12(2)	32
292	111.2(12)	0.15(3)	3.5	58	61.2(25)	0.80(4)	2	23(4)	37
284	112.0(13)	0.11(3)	4.0	54	61.0(28)	0.83(7)	2	32(4)	41
279	113.6(13)	0.15(3)	3.0	55	61.2(31)	0.77(6)	2	34(5)	41
274	111.2(16)	0.16(3)	3.9	52	59.6(33)	0.72(6)	2	40(6)	43
266	113.3(13)	0.11(3)	4.6	52	61.0(33)	0.79(7)	2	58(8)	43
259	112.5(13)	0.15(3)	4.7	48	61.0(28)	0.69(6)	19	–	47
255	114.3(11)	0.17(3)	4.1	46	60.6(30)	0.70(5)	18	–	49
243	113.3(16)	0.15(4)	4.5	49	60.3(30)	0.66(5)	19	–	47
235	113.6(11)	0.18(3)	4.6	46	60.6(25)	0.59(5)	18	–	50
217	114.3(11)	0.13(4)	6.0	42	65.3(25)	0.49(4)	18	–	54
197	112.8(19)	0.16(4)	5.0	33	66.7(24)	0.52(4)	14	–	62
180	116.5(21)	0.17(4)	5.6	21	67.4(20)	0.48(4)	15	–	74
158	117.5(23)	0.12(5)	3.7	13	67.1(14)	0.46(4)	13	–	83
149	113.3(24)	0.08(5)	5.0	12	69.0(14)	0.43(5)	14	–	85
142	117.0(30)	0.14(4)	3.6	10	69.5(30)	0.49(6)	13	–	86
134	117.0(30)	0.09(5)	3.5	10	68.0(34)	0.44(6)	11	–	87
125	116.5(30)	0.12(5)	3.0	11	66.9(37)	0.49(6)	13	–	85
118	119.6(34)	0.11(5)	3.4	10	69.6(37)	0.47(7)	13	–	85
111	119.1(34)	0.12(5)	1.8	12	70.2(37)	0.49(7)	12	–	84
77	120.7(40)	0.10(5)	2.0	11	73.2(37)	0.48(7)	12	–	85
31	123.9(40)	0.09(5)	1.7	11	73.2(37)	0.47(8)	13	–	85
12	121.8(40)	0.12(4)	2.1	12	76.8(36)	0.51(8)	13	–	84

Note that in this temperature range, we fixed the static attenuation parameter δ_d to the average value found in the range of 350 K$\leq$ T$\leq$ 600 K (assuming that such value represents well the static attenuation of f_d). In a later section we will discuss the observed EFG fluctuations of the d local environment in terms of slow dynamics of lattice distortions. The results obtained from the fits are summarized in table 4.9.

Local environment characterization From the fit results presented here we observed in all temperature range above T_C, from 149 K to 776 K, the coexistence of three main local environments (u, d, r), *i.e.*, three fractions of probes (f_u, f_d, f_r) interacting with different local EFG distributions. This is clearly seen in the Fourier transforms of the figure 4.22 where the EFG_u and EFG_d triplets are displayed, ω_u^i and ω_d^i (i=1, 2 ,3) respectively. Remark that in the high temperature Fourier transforms the middle frequency of the environment d (ω_d^2) is missing from FT plots. This is due to it's overlap with the first frequency of the u triplet (ω_u^1). This occurs not only for the referred example but also for other harmonics at other temperatures. In the FT plots of figure 4.22 the frequencies corresponding to the third fraction f_r are not assigned since it would result in a confusing picture. This EFG_r with its low and essentially temperature independent fraction (5%) is at the limit of our characterization precision. The EFG parameter, $\eta_r \sim 0.9$, is almost constant for all temperature range and, $V_{zz}^r \approx 102$ V/Å^2 at room temperature. This local environment might have its origin into probes located in lattice zones with local defects, which are intrinsic to the material or not recovered by the annealing process. Some examples are local cation vacancies (probes in the vicinity of Mn/La vacancies[13]), extended defects and grain boundaries.

In figures 4.24(a) and 4.24(b), the temperature dependence of the EFG principal component V_{zz}, a) and asymmetry parameter η, b) for the u (dominant environment at high temperatures) and d (dominant environment at low temperatures) environments is displayed. For comparison, the EFG parameters obtained for other samples with different oxygen content namely $LaMnO_3$ and $LaMnO_{3.08}$, are also displayed in the same figure.

We observed that both V_{zz}^d and V_{zz}^u present an increase with decreasing temperature, $\frac{1}{V_{zz}^{0d}}\frac{\Delta V_{zz}^{d}}{\Delta T} \sim$ -6.2×10^{-4} K^{-1} and $\frac{1}{V_{zz}^{0u}}\frac{\Delta V_{zz}^{u}}{\Delta T} \sim$ -5.2×10^{-4} K^{-1}, and that the magnitude of V_{zz}^u is always higher than the one observed for the d local environment. The increase of the EFG principal component on cooling, common in perovskite structures, cannot be accounted by the (volume) thermal expansion, $\alpha_u \sim 2.8 \times 10^{-5}$ K^{-1} $> \alpha_d$. However, using the H. Bayer and T. Kushida expression for rotation modes [182–184], $V_{zz}=V_{zz}^{eq}(1+bT)$ with $b=-3x_0^2/4R^2T$ where x_0^2 is the vibrational amplitude and R the La-O distances[14], we obtain to b=4×10^{-4} K^{-1} for the u environment ($\eta \sim 0$). This suggests that these lattice vibrations might explain

[13] As explained in the beginning of this chapter, if one assumes that the positions of the vacancies are not correlated, the probability that a Cd siting in a La vacancy has in its surrounding a Mn or next shell La vacancies is roughly 2%.

[14] R was taken as the average La-O distance and x_0 the oxygen vibrational amplitude, data from [195].

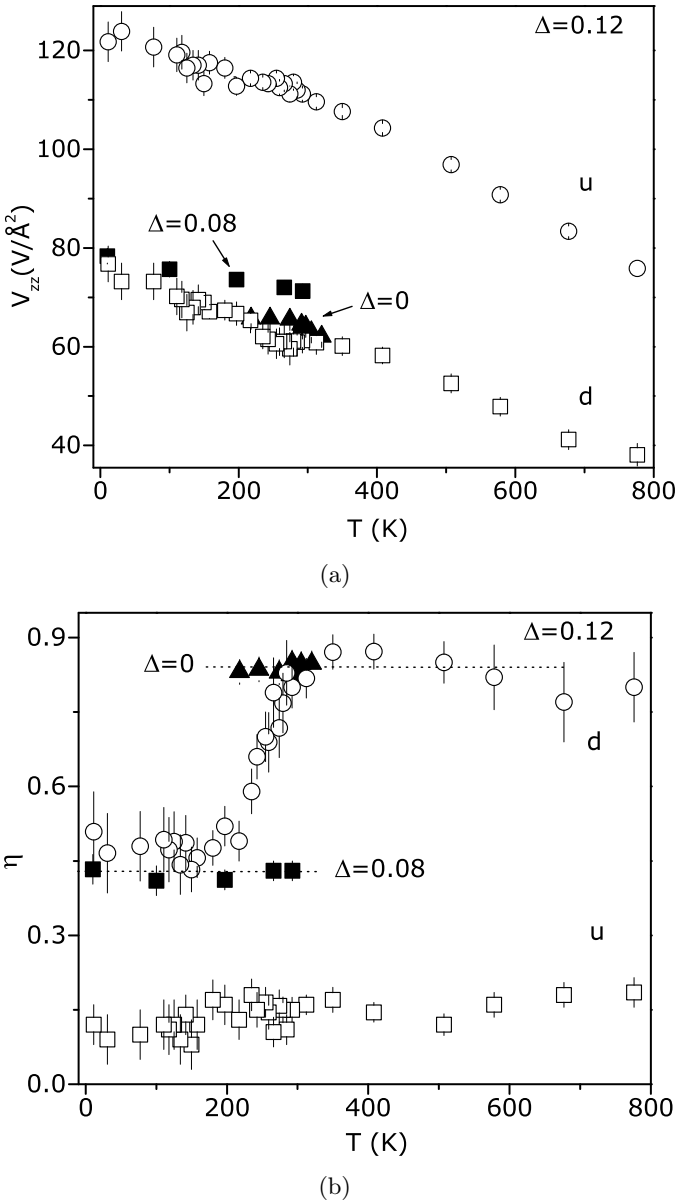

Figure 4.24: EFG principal component V_{zz}, a) and asymmetry parameter η, b) for $LaMnO_{3.12}$ as a function of temperature. EFG parameters for $\Delta = 0.08$ and $\Delta = 0$ are also showed.

the V_{zz}^{u} trend. As shown in figure 4.24(b) the η parameters for both environments are substantially different, both in magnitude and temperature dependence. Whereas η value for the u environment, dominant at high T, shows an almost axially symmetric EFG ($\eta_u \sim 0$) which is nearly temperature independent, η_d is characteristic of axially asymmetric environment ($\eta_d > 0.45$) and diminishes strongly between 300 and 200 K.

From the results obtained in the previous sections one can infer a relation between the average lattice structure and the observed values of V_{zz} and η. At very high temperatures,

the dominant microscopic environment is u and the average lattice structure is rhombohedric. Hence, the observed values of η_u and V_{zz}^u at those temperatures are associated with the rhombohedric lattice structure. In a rhombohedric structure the MnO_6 octahedra are constrained by symmetry to be JT–undistorted (equal Mn-O bond lengths) thus we name this local environment *undistorted*. At very low temperatures, on the other hand, the dominant local environment is d (*distorted*). This environment is characterized by a weaker and highly asymmetric EFG as mentioned above. The η_d and V_{zz}^d values for this environment are associated with a lower symmetry as happens in the orthorhombic average lattice structure present at low temperatures in this compound. The degree of distortion of the d environment is also evident from the comparison of the EFG parameters obtained for the $LaMnO_{3.12}$ sample with those measured for samples with different oxygen content. As we can see in figure 4.24(a) and 4.24(b) where the EFG parameters found in $\Delta = 0.08$ and $\Delta = 0$ samples are included, the EFG parameters for the d environment compare well, at low temperatures, with the ones found in the sample with $\Delta = 0.08$ (and also samples with $0.04 \leq \Delta \leq 0.1$ shown in figure 4.9(a) and 4.9(b)), *i.e.*, they compare extremely well with the EFG parameters found for samples with a orthorhombic O crystallographic structure. The EFG parameters, η_d and V_{zz}^d, obtained for the d local environment above room temperature coincide with the ones observed for the stoichiometric $LaMnO_3$ (full triangles in figure 4.24(a) and 4.24(b)). Note that the stoichiometric system, $\Delta = 0$, has a fully JT–distorted and orbital ordered arrangement of the manganese ions. Consequently, at high temperatures the d local environment must be characterized by a distortion involving several (minimum eight) $Mn^{3+}O_6$ octahedra, similar to the collective JT-distorted lattice.

Local scale continuous transition Further insight in the behavior of d, u and r environments may be achieved by studying the temperature dependence of the volume fractions f_u, f_d, f_r, *i.e.*, the fraction of probes interacting with the different EFG distributions. As may be seen in figure 4.25(a), the u environment is dominant at very high temperatures ($f_u \sim 86\%$ at T=776 K), though d regions survive up to that temperature ($f_d \sim 9\%$). The fraction of probes interacting with EFG_r remains constant through all temperature with $f_r \approx 5\%$. For temperatures above and below the temperature interval of the macroscopic R/O coexistence, *i.e.*, when a single rhombohedric or orthorhombic crystallographic structure is observed by x-ray, the minoritary local environments have to be random (or dynamically) distributed within the macroscopic matrix, in such way that they are observed by PAC and not by x-ray diffraction as this technique requires long range structural correlations. As can be seen in figure 4.25(a) the fraction of probes interacting with EFG_d (EFG_u) smoothly increases (decreases) on lowering temperature reaching a stable value only below 170 K. In figure 4.25(a) we compare the volume fraction of the observed EFGs, f_u, f_d, f_r as function of temperature with the temperature dependence of the volume of the orthorhombic crystallographic phase measured by x-ray diffraction. It is obvious from this picture that local phase coexistence

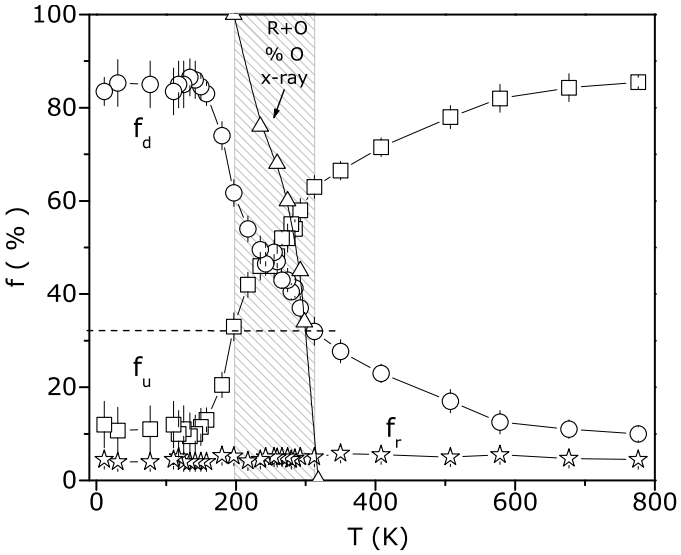

(a)

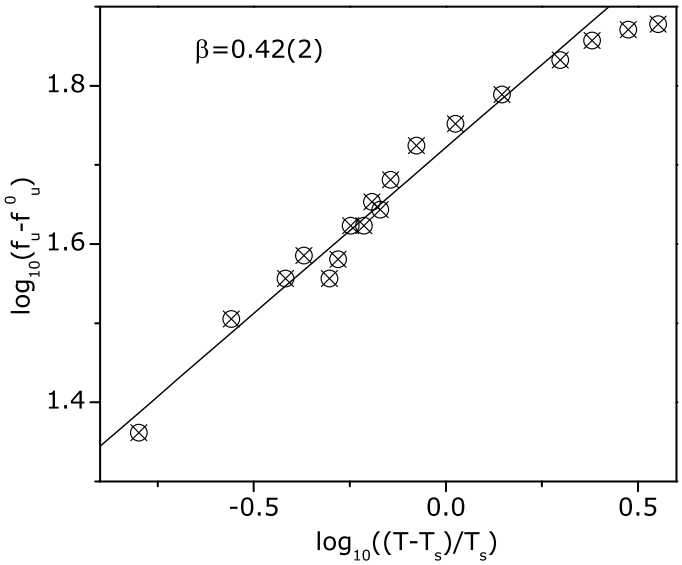

(b)

Figure 4.25: a) Temperature dependence of the probe volume fractions f_u, f_d and f_r. Triangles: orthorhombic phase percentage from x-ray diffraction. The shadowed region is limited by the temperatures where the percolation thresholds occur. b) Log-log plot of $(f_u - f_u^0)$ vs the reduced temperature $t = (T - T_s)/T_s$.

extends over a much broader temperature range than the rhombohedric/orthorhombic crystallographic (macroscopic) phase coexistence that only exists in the temperature range 197 <T< 318 K.

The smooth variation of f_u (and symmetrically f_d) when the temperature changes, patent in figure 4.25(a), down to a temperature where it stabilizes, hints for a continuous phase tran-

sition from the undistorted to the JT–distorted dominant environment. To investigate further this scenario we assumed that the variation of f_u is due to a continuous phase transition. If this is the case the order parameter, $f_u - f_u^o$, follows a power law behavior $f_u - f_u^o \sim (T - T_s)^\beta$ when the critical temperature T_s is approached from above. In the figure 4.25(b), f_u vs T is displayed in a log-log plot. To extract correctly a critical exponent one should have enough data points very close to T_C (small reduced temperature $t = (T - T_s)/T_s \ll 1$). As one can observe the points for $t \lesssim 1$ fit a straight line, so we conclude that the data essentially follow a critical behavior from which we estimate a value for $T_s \sim 170 \pm 10$ K (relatively close to T_C) and a $\beta = 0.42 \pm 0.02$. The value of this critical exponent is close to the one corresponding for free percolation on a $3D$ cubic lattice ($\beta_p = 0.41\ldots$ [214]). From this result we see that if the data are treated in the same way as in any continuous (second or higher order) phase transition, it adjusts pretty well to a scaling behavior close to T_s.

The percolative nature of the structural transition is supported by the x-rays measurements. In fact, the random distributed clusters of the d environment (symmetrically for u) should not be detected by x-rays diffraction methods unless their average size is big enough. The x -rays diffraction measurements detect a structural transition (R–O) that lies exactly between the temperatures corresponding to the percolation thresholds of the nanoscopic components, *i.e.*, when the fraction of the invading components approach the percolation threshold, $f \sim 31\%$ [214]. At these temperatures the minority cluster suffers a sudden size divergence becoming macroscopically observable. This is precisely the effect that can be observed in figure 4.25(a), x-rays only detect a mixture of phases in the shaded area of the figure that spans between the percolation thresholds of the u and d environments (horizontal dashed line). Associated to the transition there must also exist a correlation length, *i.e.*, correlation between d clusters, that should diverge at T_s. As may be seen in figure 4.24(b), for temperature below ~ 320 K η_d starts to fall, on decreasing temperature as the d component percolates and only stabilizes below T$\sim T_s$.

EFG fluctuations and Polaron dynamics The temperature dependence of the attenuation of the R(t) function provides information about the dynamics of the u and d environments. ^{111}Cd PAC spectroscopy can probe dynamics that occurs in a time range between ns and μs. Figure 4.26(a) depicts a complete sketch of dynamic and static attenuation to the R(t) function in both environments. The best fit to the R(t) spectra discards the presence of time dependent interactions for the u environment ($\delta_u \sim 4\%$ independently of T and $\lambda_u = 0$), *i.e.*, no dynamics that falls into the above mentioned time scales was observed in the u environment. Thus, either the dynamic is too fast to be detected or there is no dynamics associated with this local environment. However, since holes (24%) are present in this sample there must be a fast hopping between Mn^{3+} and Mn^{4+} ions in this undistorted environment u, in agreement with the literature [65, 215, 216]. Thus, for the undistorted environment, in the whole temperature range, the charge transfer between Mn^{3+} and Mn^{4+}

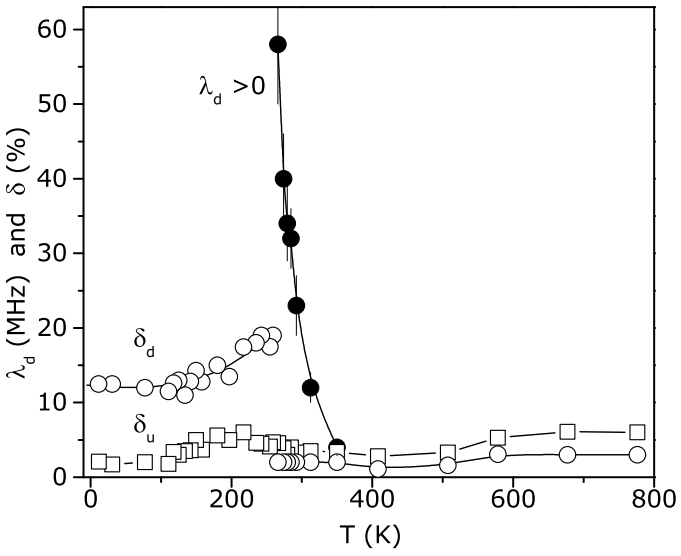

(a)

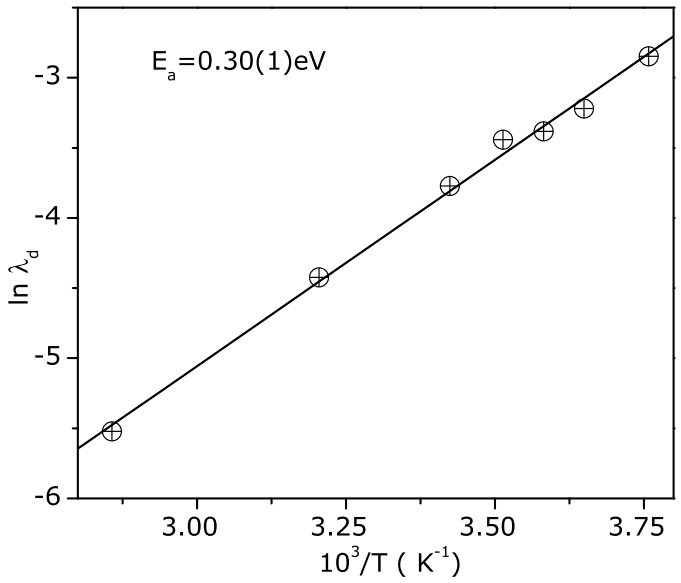

(b)

Figure 4.26: a) Temperature dependence of static δ_d ($\circ$) and dynamic λ_d ($\oplus$) attenuation parameters to the R(t) function for d environment. Static attenuation δ_u ($\square$) for u environment. b) Arrhenius plot of λ_d to estimate the activation energy.

(hopping) should occur with a hopping frequency higher than we can probe. On the other hand, as mentioned before, for the d environment the best fits were obtained admitting a fluctuating EFG ($\lambda_d \neq 0$ and $\delta_d = 2\%$) in the temperature region spanning from T=266 K to T=350 K. Notice that this time dependent effects cannot be attributed to Cd/O and/or defects diffusion since it would be detected in both fractions. The temperature dependence of

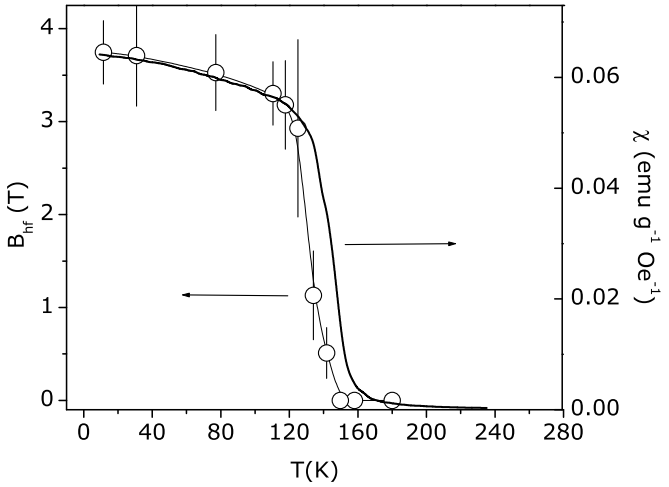

Figure 4.27: Temperature dependence of the magnetic hyperfine field, B_{hf} corresponding to the d local environment ($\circ$) and macroscopic susceptibility (line) for the $LaMnO_{3.12}$ sample.

the dynamic attenuation parameter, λ_d, allows us to estimate an activation energy E_a. This energy is obtained from $\lambda_d = \lambda_\infty \, e^{E_a/kT}$. In figure 4.26(b) $ln\lambda_d$ is presented as a function of the reciprocal temperature. From the slope of the curve an activation energy $E_a = 0.31\, eV$ was obtained, close to the polaron binding energy reported in the literature for low doped manganites [217, 218].

Magnetic hyperfine fields The study of the temperature dependence of the hyperfine fields for both environments u and d below the paramagnetic ferromagnetic phase transition ($T<T_C$) was also performed. As one can observe in figure 4.22 the spectrum at 12 K ($T \ll T_C$) is extremely attenuated, this is simply due to the presence of the combined interaction which considerably broadens the hyperfine lines.

Below T_C both d and u local environments experience increasing magnetic hyperfine fields upon decreasing temperature, presenting at 12 K similar values of $B^d_{hf} = 3.8(3)$ T and $B^u_{hf} = 4.6(7)$ T. The angle between the MHF and V_{zz} averages $\beta^d \sim 50°$ and $\beta^u \sim 40°$.

The obtained values for the magnetic hyperfine fields are consistent with a full ferromagnetic environment of the surrounding Mn ions [20, 213]. In figure 4.27 the magnetic hyperfine field at the d environment is plotted as a function of temperature and compared to the macroscopic susceptibility. As we can see there is a a difference between the critical temperature measured macroscopically and the one measured locally. We have to remark that the magnetic hyperfine field is measured with large error bars. Moreover, only a small number of data points were measured in this region. In this way, the assignment of T_C from the magnetic hyperfine field is difficult. The temperature dependence of the magnetic hyper-

fine field measured at the u local environment is not shown since due to the small fraction of probes below 150 K one can only provide a crude estimation of its values.

4.6 Discussion and Conclusion

In the previous sections of this chapter the experimental study of the hyperfine fields in a series of members of the $LaMnO_{3+\Delta}$ family was presented. In order to have a good controllability of the studied system, especially the control of the oxygen non-stoichiometry Δ, we have systematically performed the macroscopic characterization of all samples in study, and correlated our results with the ones available in the literature.

Macroscopic structural data revealed that the stoichiometric material and samples with $\Delta \leq 0.04$ are characterized by a large Jahn-Teller distortion, with $c/\sqrt{2} < a < b$ within the orthorhombic Pbnm structure (O'). Accordingly, the Mn-O bond lengths, deduced from the measured lattice parameters in our set of samples, showed three distinct bond-lengths, in agreement with microscopic results obtained with neutron PDF by [201–203]. For this set of samples, increasing Δ, the orthorhombicity decreases with a corresponding decrease of the cooperative JTD. The samples with oxygen content $0.04 < \Delta \leq 0.10$ are orthorhombic (O) with the same Pbnm structure but characterized by a considerably smaller Jahn-Teller distortion with only slight differences in the Mn-O bond lengths. A rhombohedric symmetry and no collective Jahn-Teller distortion was found in samples with the oxygen content $\Delta > 0.1$. The sample with $\Delta = 0.12$ exhibits x-ray diffraction peaks of both O and R phases in the temperature range of 235 K to 292 K due to an O/R structural phase transition that was found to occur near room temperature in this compound. All structural data was found to be in agreement with the literature [83–85, 195, 196, 200].

The study of the magnetic properties showed that samples within the O' average lattice symmetry have strong antiferromagnetic correlations and very low saturation moment. Increasing Δ, the ferromagnetic correlations increase reaching a maximum for $\Delta \approx 0.1$, in agreement with [83, 85, 200]. It was also found that the system is insulator for all Δ, and no spontaneous or field induced metal-insulator transition was found in accordance with the literature where metallic behavior is only reported for samples with $\Delta \geq 0.14$ [84,85,200,210,211].

This macroscopic characterization allowed to determine the structural, electric and magnetic properties of this system, thus enabling us to fully correlate them with the microscopic ones. In particular we studied the dependence of the electric field gradient in different average lattice symmetries (ALS).

The stoichiometric $LaMnO_3$ (with O' ALS) compound presents a majority highly axial asymmetric EFG compatible with a cooperative Jahn-Teller distorted orbital ordered $Mn^{3+}O_6$ octahedra. Our values for this EFG parameters are in fair agreement with the results reported in the literature on the same undoped compound using NMR [20, 219] and from ab-initio FLAPW theoretical calculations [220] (see table 4.10). Moreover, all EFG

values found for samples with $\Delta \leq 0.10$, in particular the η values are compatible with the orthorhombic lattice structure where only an axis of twofold rotational symmetry exists. In the orthorhombic O' crystallographic phase, away from the stoichiometric compound, the pronounced and continuous decrease of η parameter (η decreases from $\eta \approx 0.85$ for the stoichiometric sample to $\eta \approx 0.5$ for the $LaMnO_{3.05}$) can be associated with the relaxation of the distortions in the $Mn^{3+}O_6$ octahedra. The EFG principal component V_{zz}, apart from an initial increase close to the stoichiometric compound, was found to be independent of Δ, within the orthorhombic structures. In contrast, large changes were observed in main EFG parameters for samples with $\Delta > 0.10$ which are correlated with the change in the average lattice symmetry (O ALS for $\Delta \leq 0.10$ and R ALS for $\Delta > 0.10$). When the dominant crystallographic structure is rhombohedric the main local environment shows an almost axially symmetric EFG ($\eta_u \sim 0.15$). This value characterizes an EFG with an axis of threefold or higher rotational symmetry, which is compatible with the rhombohedral lattice structure. Note that in this R phase the MnO_6 octahedra are constrained by symmetry to be undistorted, *i.e.*, equal Mn-O bond lengths in the MnO_6 octahedra. Theoretically η should vanish in such axial symmetric lattice, however, when a distribution of frequencies occurs that represents the average axial symmetry, a small but non-vanishing asymmetry parameter is observed experimentally, as discussed by Catchen *et al.* [194]. A curious point is that the higher EFG principal component was observed in the more symmetric R phase ($V_{zz}^{O} < V_{zz}^{R}$), a similar result was reported by Dogra *et al.* [138] in stoichiometric perovskites (see table 4.10).

Table 4.10: EFG parameters in lanthanum site for different average lattice symmetries.

Method	Sample	ALS	$V_{zz}^{latt.}(V/Å^2)^a$	η	ref
^{111}Cd PAC	$LaMnO_3$	O'	1.9(4)	0.85	This work
^{111}Cd PAC	$LaMnO_{3.10}$	O	2.1(5)	0.40	This work
^{111}Cd PAC	$LaMnO_{3.12}$	R	3.3(8)	0.15	This work
^{111}Cd PAC	$LaCrO_3$	O	1.9(4)	0.45	[138]
^{111}Cd PAC	$LaCrO_3$	R	2.7(7)	∼0	[138]
^{139}La NQR	$LaMnO_3$	O'	1.4(3)	0.92	[20]
^{139}La NQR	$LaMnO_3$	O'	1.4(3)	0.90	[219]
FLAPW	$LaMnO_3$	O'	1.5	0.80	[220]

[a] $V_{zz}^{latt.}=V_{zz}^{exp.}/(1-\gamma_\infty)$ with the Sternheimer antishielding factor, γ_∞, from [172, 173].

In fact, the ratios V_{zz}^{R}/V_{zz}^{O} of our study and that from Dogra *et al.* are approximately the same ($V_{zz}^{R}/V_{zz}^{O} \sim 1.5$). In perovskite related structures the difference between the EFG parameters in the O and R phases must be connected with the fact that EFG principle axis is not along the same direction in both phases. By symmetry considerations, the EFG principal axis, in the $R\bar{3}C$ R structure, must be pointing along the rhombohedral axis while

in the Pbnm space group, due to the existence of a mirror plane symmetry element, one of the eigenvectors of EFG tensor must be along the c direction which implies that the others must be within the b, a plane. In this way, if a small change in atomic positions occur in such way that the symmetry of the lattice changes from R to O this can be accompanied by a strong change of η and V_{zz} due to the change of the principal axis direction. There is thus a good correlation between the average lattice symmetry and the main EFG parameters. Interestingly, evidences for local phase coexistence in the two limits of the phase diagram, *i.e.*, for $\Delta \leq 0.02$ and $\Delta \geq 0.12$ were observed independently of the sample's average lattice structure. In orthorhombic O the region, on the other hand, no evidence of any phase segregated state was observed.

At the present knowledge, inhomogeneous intrinsic phases are present in many manganites systems, thus it is realistic to think that the minor local environments corresponds to local distortions within a macroscopic matrix. To better understand this inhomogeneous phase-segregated states, its nature and stability it is necessary to correlate the results obtained, through thermal dependence of the EFG and MHF, in representative samples of each section of the phase diagram, namely the JT–distorted stoichiometric compound, the weakly distorted, O, $\Delta = 0.08$ and the rhombohedric $\Delta = 0.12$ samples.

For the $LaMnO_3$ end-member, our macroscopic measurements showed that this compound presents an antiferromagnetic insulator behavior with a JT–distorted MnO_6 octahedra within a single orthorhombic O' structure. Our $^{111}In- >^{111}Cd$ PAC measurements, on the other hand, showed that two distinct local environments, with asymmetry parameters compatible with the ALS, coexist in all range of temperatures. Whereas the main local environment, as referred above, is characterized by EFG parameters compatible with those reported in the literature, the origin of the second EFG_B is still not clear, and its observation is not directly reconcilable with the available literature. One can speculate about the possibility of defects formed around the In/Cd probe. Its seems however, improbable, that defects like vacancies would increase on lowering temperature. Such large and increasing fraction up to 50% cannot be attributed to such static disorder. Another aspect is that this fraction (at room temperature) is rapidly decreasing upon increasing oxygen content Δ and for Δ=0.02 is almost negligible whereas the amount of vacancies is higher. The fact that similar EFG parameters are measured by the ^{111m}Cd and ^{111}In probes adds additional arguments for discarding trapping of defects by the In probe, an effect that is known to occur in semiconductors [163]. Similar arguments help to discard the presence of after-effects related with the $^{111}In- >^{111}Cd$ electron-capture decay [163]. Another hypothesis would be related with local doping due to the substitution of trivalent In by a divalent Cd atom due to the nuclear transmutation. In fact for each $^{111}In^{3+}- >Cd^{2+}$ charge equilibrium implies that a Mn^{4+} is formed. The Cd excited nuclear state populated by this decay has 0.9 ns half-life. Since in such insulator materials holes are known to diffuse very slowly ($t < ns$ [20]) one could attribute the second EFG to hole trapping *i.e.* a hole would be in the neighbourhood of

the probe untill the PAC measuring is finished (5 × 85 ns). The fact the second EFG was also found for ^{111m}Cd measurements, for which the PAC intermediate state is fed by a much longer lived ($T_{1/2}$=48.6 minutes) nuclear state, eliminates this possibility. Other local probe techniques like neutron PDF, NMR, NQR or EXAFS didn't find evidence for coexistence of different local environments in the undoped compound. Most studies using diffraction techniques agree for a single phase orthorhombic (O') structure. However report exist which argue for a monoclinic $P2_1/c$ [17,221]. The latter scenario could explain the existence of two La/Cd lattice sites but fails to explain their temperature dependent occupancies. The fact that two local environments coexist, stabilizing critically near 50% below the magnetic transition, can only be attributed to some new local phenomena not yet detected by other techniques. Although recently several reports exist regarding the nature of magnetic ground-state [207–209] and the dominant interactions responsible for stabilization of orbital-ordering, which can be coulombic [222, 223] or phonon mediated [224–226], none of these studies gave hints for the interpretation of our results in $LaMnO_3$. We speculate on the existence of local perturbation of the orbital and/or fully Jahn-Teller distortion order leading to a phase segregated state with subtle differences only detected by their different EFGs. We substantiate this speculation on the fact that this second fraction rapidly disappears (at room temperature) with increasing Δ, in a similar way as the reduction of Jahn-Teller distortions and strength of orbital ordered states with doping. Our data suggest that the onset of magnetic order makes equally likely these two local environments. The fact that the attenuation parameter of the EFG_B and the amount of probes (f_B) sensing this electrical field gradient show criticality (critical exponent β=0.35) with a characteristic temperature very close to T_N hints for a microscopic phase transition driven by magnetic fluctuations. The magnitude and temperature dependence of the magnetic hyperfine fields shows undoubtedly that canting of the A-type antiferromagnetic structure occurs [207–209] and contributes significantly to the magnetic hyperfine fields at the La site. Further studies should be performed to clarify this issue, but we remark that the coexistence of two local environments characterized by different magnetic hyperfine fields was also observed by ^{140}La→^{140}Ce PAC studies in $LaMnO_3$ [112].

Contrarily to the low doped compounds ($\Delta \leq 0.02$) the ferromagnetic insulator $LaMnO_{3.08}$ O orthorhombic sample showed no local phase coexistence in the studied temperature range (from RT down to 10 K). The temperature dependence of the EFG principal component shows the normal increase with decreasing temperature and no anomaly was observed in the EFG parameters. These EFG parameters are characteristic of a weakly distorted Jahn-Teller local environment. The measured magnetic hyperfine field is compatible with the fully ferromagnetic environment as measured by ^{139}La NMR.

The nature of such ferromagnetic insulator state is far from being understood and the phase separation scenario with polaronic distortion has been pointed as the most relevant feature for this behavior [22]. Insight on this nanoscopic phase coexistence and polaronic distortions in manganites has been provided with help of a vast set of techniques, trying

to find a global picture and answers to the remaining open questions as the nature of such distortions, their evolution and relevance for Colossal Magnetoresistance.

The study of the hyperfine fields and their temperature dependence in the ferromagnetic insulator $LaMnO_{3.12}$ compound, which at room temperature exhibits macroscopic coexistence of the orthorhombic and rhombohedric crystallographic structures provided an insightful view of the nanoscopic phase segregation. Independently of the average lattice symmetry (ALS) two local environments were observed to coexist in the 12 K$\leq$ T$\leq$ 776 K range. Nevertheless, in the high temperature limit the almost axial symmetric main EFG_u is compatible with the x-ray measurement where a single rhombohedric phase was observed. On the other, at low temperatures a single orthorhombic structure was measured and the asymmetric main EFG_d has the same EFG parameters as the ones measured in weakly distorted orthorhombic O samples as the $\Delta = 0.08$ sample. Since in these limits our x-ray data did not detect any other crystallographic phase than the mentioned ones, the minority local environments at each temperature limit have to be dispersed in the matrix associated with the average lattice symmetry. At high temperatures, in the rhombohedric phase, random distributed nanoclusters, characterized by EFG_d, survive till temperatures as high as 776 K. Remarkably, this EFG is the same as the one measured in the stoichiometric compound where the collective JT–distortion spreads through the whole crystal. Thus the high temperature distortions observed in $LaMnO_{3.12}$ compound must be as strong as in the undoped orbital-ordered compound and characterized by a similar local collective distortion of several (minimum 8) $Mn^{3+}O_6$ octahedra. Remark that such distortions occur in the rhombohedric macroscopic crystallographic phase and these symmetry constrains the MnO_6 octahedra to be undistorted. This confirms the high stability of the inhomogeneous phase-segregated states, compatible with a scenario where random distributed JT–distorted nanoclusters are embedded in a undistorted matrix as predicted by [45]. The indication for the presence of polaronic distortions in doped manganites, initially predicted by Millis *et al.* [11], has been found by means of a number of experimental probes with a range of temporal and spatial resolutions [13,16,18,19] *e.g.*, PDF analysis of neutron diffraction patterns [13] and by oxygen isotopic effects [16]. In addition to single polarons, observed both in the orthorhombic and rhombohedric paramagnetic phases, correlated regions where recently observed by neutron and x-ray scattering in the orthorhombic lattices [59,60]. As mentioned by Dagoto [45] these correlated regions can be seen as polaron clusters. Their importance was recently pointed out [45, 227] since it was recognized that small individual polarons may not be sufficient to explain CMR manganites. Our results add to previous knowledge, evidence that even in the rhombohedric structure the distortions cannot be viewed as single polarons but random distributed polaron clusters. This result is complementary to the recent work of Kiruyikin *et al.* [59,60] since, as they mention, their techniques are unable to characterize uncorrelated distortions thus not able to distinguish between the single/small-cluster polaron picture.

According to some authors there should be a temperature scale below which polaron clus-

tering starts ($T_{clust.}$) [45]. Above this temperature a gas of individual polaronic distortions exists, and only in a much higher temperature scale, $T_{pol.}$, such distortions would completely disappear. Since we have evidence for polaron clusters at temperatures as high as 776 K one can set a lower bound for this temperature scale ($T_{clust.} > 776$ K). Similar findings were very recently reported by X. Qui *et al.* [228] in the stoichiometric compound above the O/R transition ($T_{O/R}$=1010 K). These authors also claim that the Jahn-Teller splitting persists in the R crystallographic phase and is very robust remaining till the highest studied temperatures (T=1150 K). Moreover they claim that the observed distortions are not single polaron but clusters with minimum diameter of 16 Å growing in size upon cooling.

Through the study of the volume fraction of probes sensing the distorted local environment one also followed the growth of these distorted regions in the $LaMnO_{3.12}$ compound.

The smooth increase of the distorted regions with lowering temperature lies undetected macroscopically up to this local fraction reaches about 32%, above which one detects macroscopic phase coexistence of orthorhombic and rhombohedric phase. This macroscopic phase coexistence was found to exist only between the percolation thresholds of the microscopic environments. The study of the asymmetry parameter of the distorted region through this percolative transition shows interesting features connected with the nature of spatial correlations. At high temperatures (above $312\,K$) severe Jahn-Teller distorted clusters are randomly distributed (*i.e.* uncorrelated). Below the percolation the asymmetry parameter of the distorted environment decreases, hinting an increasing correlation between clusters. Interestingly, the η parameter stabilizes for temperatures below T$\sim$170 K at a value close to that observed for the weakly distorted sample. This behavior suggests that the increase of spatial correlations has to be balanced by a weakening of the JT–distortions.

The connection between such lattice distortion and the electric transport was possible through the study of the EFG fluctuations. Our results suggest a fast hopping between Mn^{3+} and Mn^{4+} ions in the undistorted environment. For the undistorted environment, on the other hand, the temperature dependence of the dynamic attenuation parameter followed an activation law with a activation energy close to the polaron binding energy reported by several authors [217, 218]. We can further estimate the EFG fluctuation time (τ) from the maximum of $\lambda_d(T)$ [160]. Considering that a carrier (hole) can hop to any of the 8 octahedra around a La site (8 possible EFG states) we find $\tau = 0.5\,\mu s$ at T=266 K, corresponding to a ultra–slow polaron diffusion. Similar polaron residence times have been reported, in related samples, by Allodi *et al.* in a NMR study [20]. However the activation energy, E_a, measured in that study was smaller compared to ours due to the intense magnetic field (7 T) needed to perform NMR measurements. The distinct dynamics of the undistorted (fast hopping) and distorted (polaronic conduction) environments is responsible for the macroscopic ferromagnetic insulator behavior observed in these systems [215, 216]. Below T_C both local environments experience increasing magnetic hyperfine fields compatible with fully ferromagnetic environments [20, 213] and a phase coexistence between metallic/undistorted and

insulator/distorted regions exists. However, the majority phase, distorted, is characterized by ultra–slow diffusion of charge carriers imposing an insulator behavior.

Finally we refer to the microscopic phase transition observed at T_s where the both the volume fraction of the coexistent local environments and the η value of the distorted environment stabilizes. We have seen that there is criticality in the approach to this temperature, signalizing a microscopical phase transition occurring at T_s. This temperature is rather close to T_C and whether they are the same is still an open issue. Interestingly, a similar critical behavior was also found in the stoichiometric compound. In this one the difference between the values found for T_s and T_N is negligible. The same stabilization for the η value and volume fractions was observed. Although the origin of this effect is not yet clear we speculate that the presence of an internal magnetic field below the magnetic transition halt the changes in the competing phases. Only above T_C/T_N when the macroscopic magnetization vanishes the different local environments are able to evolve. The observed criticality (above T_s) can be related with the decrease of the magnetic correlation length that diverges at T_C.

Chapter 5

Coexistence of electric and magnetic order in $Pr_{1-x}Ca_xMnO_3$ system

Motivation

The $Pr_{1-x}Ca_xMnO_3$ system has received considerable attention due to the richness of its phase diagrams and their concomitant complexity. In particular, much attention has been devoted to the charge and orbital ordered (CO, OO) phases. The charge-order picture with a real-space ordering of Mn^{3+} and Mn^{4+} charge carriers, proposed by Wollan and Koeller [23] and Radaelli *et al.* [229], was recently proved to be oversimplified [34–40, 230]. In a x-ray absorption near edge structure spectroscopy study, Garcia and co-workers argues that the electronic state of Mn atoms in CO compounds cannot be considered as a mixture of Mn^{3+} and Mn^{4+} pure states [34]. They suggest two inequivalent Mn sites with valence $3.5 + \delta$ ($\delta \ll 0.5$). Neutron diffraction data in $Pr_{0.6}Ca_{0.4}MnO_3$ reveals that all Mn ions in the crystal are virtually identical and the authors propose an electronic ground state where one e_g electron is shared by two Mn ions, the so-called Zener polaron [35, 36]. However this is not confirmed in $Pr_{0.5}Ca_{0.5}MnO_3$ studied by highly resolved powder x-ray and neutron diffraction [231]. Another alternate picture is that of a bond-charge-density wave, with no charge contrast of the Mn ions [232, 233]. Using the crystal structure proposed by Radaelli *et al.* [26], Zheng and Patterson [230] performed periodic Hartree-Fock (UHF) calculations and found an electronic ground state formed by ferromagnetically coupled Mn^{3+}- O^{-}- Mn^{3+} units that indicate important charge transfer effects. The importance of charge transfer effects was also indicated by Ferrari and co-workers, in similar periodic UHF calculations [37]. However, in the solution found by these authors a zig-zag ordering of Mn^{3+}- O^{-}- Mn^{3+}- O^{-}- Mn^{3+} trimers appears. In a theoretical study Efremov *et al.* proposed, in addition to the Zener

polaron phase and the the classical charge ordering description, a third state described as a superposition of these two, [234, 235].

An atomic-scale view of this phenomena, at the A (Pr,Ca) perovskite sites, can contribute to a better understanding of the complexity of this system. In this work we present the first PAC spectroscopy study of the $Pr_{1-x}Ca_xMnO_3$ determining the EFG parameters as a function of Ca concentration and as a function of temperature via the ^{111m}Cd-^{111}Cd decay.

5.1 Sample characterization

5.1.1 Structural characterization

Polycrystalline samples of $Pr_{1-x}Ca_xMnO_3$ used in this work were prepared as described in chapter two. Scanning electron microscopy showed that nominal concentration is in a good agreement with the measured one (see table 1 chapter 2). Some representative scanning electron microscope (SEM) photographs performed at room temperature for x=0.05 and 0.14 samples are shown in figure 5.1. The high homogeneity of the samples is clearly visible through the narrow grain size distribution (typical size $\sim 3\mu$m). The other samples with different Ca concentrations have a similar microstructure.

The sample chemical homogeneity was checked by room temperature powder x-ray diffraction measurements. The crystallographic structures and correspondent lattice parameters were determined by refinement of x-ray diffraction patterns using the Rietica or FULLPROF programs. The line shape of the diffraction peaks was generated by a pseudo-Voigt function. In figure 5.2 some representative x-ray diffraction pattern obtained at room temperature are presented. The fits to the XRD patterns showed that all the samples are characterized by a single-phase perovskite-related structure with orthorhombic symmetry. The patterns were refined within the Pbnm (Z=4) space group. A good matching of the fits was always obtained and no unidentified lines nor additional splitting of the peaks was observed[1]. From x-ray pattern matching we extracted the cell parameters for the $Pr_{1-x}Ca_xMnO_3$ system. Table 5.1 summarizes the obtained results.

Figure 5.3 depicts the orthorhombic cell parameters for the $Pr_{1-x}Ca_xMnO_3$ system as a function of Ca content (x). As one can observe, compounds with high Pr^{3+} (Mn^{3+}) content, (*i.e.* for $0 \leq x \leq 0.3$), stabilize in a orthorhombic O'-type structure, $c/\sqrt{2} \leq a \leq b$. Increasing the Ca (Mn^{4+}) content the O'-type structure becomes unstable and for $0.3 \leq x \leq 0.9$ the system crystallographic structure stabilizes in a pseudo-tetragonal phase for which $c/\sqrt{2} \simeq a \leq b$. In the range of $0.9 \leq x \leq 1$ a pseudo-cubic structure, $c/\sqrt{2} \simeq a \simeq b$, sets in[2]. The dependence of the cell parameters on Ca content is in good agrement with the results found in literature for this system [24, 236, 237]. Figure 5.4(a), where the unit cell

[1]The discrepancy factors averages: $R_p \sim 11$, $R_{wp} \sim 17$, $\chi^2 \sim 1.3$.

[2]The delimitations of the different orthorhombic phases (O', T and O) are assumed to be the same as in Jirak *et al.* work [24].

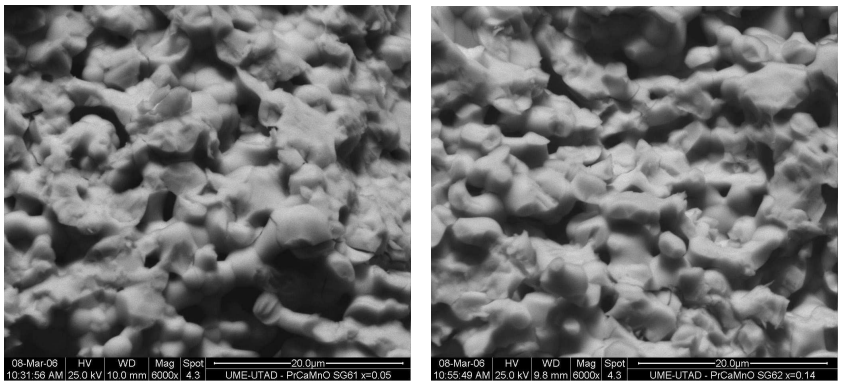

(a) (b)

Figure 5.1: $Pr_{1-x}Ca_xMnO_3$ representative scanning electron microscope photograph performed at room temperature for x=0.05, a) and 0.14, b) samples.

Table 5.1: $Pr_{1-x}Ca_xMnO_3$ cell parameters in the Pbnm space group.

x	a(Å)	b(Å)	$c/\sqrt{2}$(Å)	V/z(Å^3)
0	5.4458	5.7500	5.3741	59.496
0.05	5.4508	5.6984	5.3876	59.165
0.14	5.4410	5.6020	5.3910	58.096
0.25	5.4479	5.4846	5.4339	57.404
0.32	5.4379	5.4607	5.4399	57.112
0.35	5.4401	5.4792	5.4357	57.284
0.40	5.4025	5.4415	5.4429	56.572
0.45	5.4196	5.4172	5.4012	56.064
0.50	5.3943	5.4163	5.3861	55.638
0.60	5.3804	5.3863	5.3607	54.927
0.65	5.3627	5.3670	5.3574	54.516
0.75	5.3245	5.3282	5.3297	53.459
0.85	5.3040	5.3320	5.3198	53.191
0.95	5.2849	5.2932	5.3084	52.502
1	5.2703	5.2753	5.2793	51.893

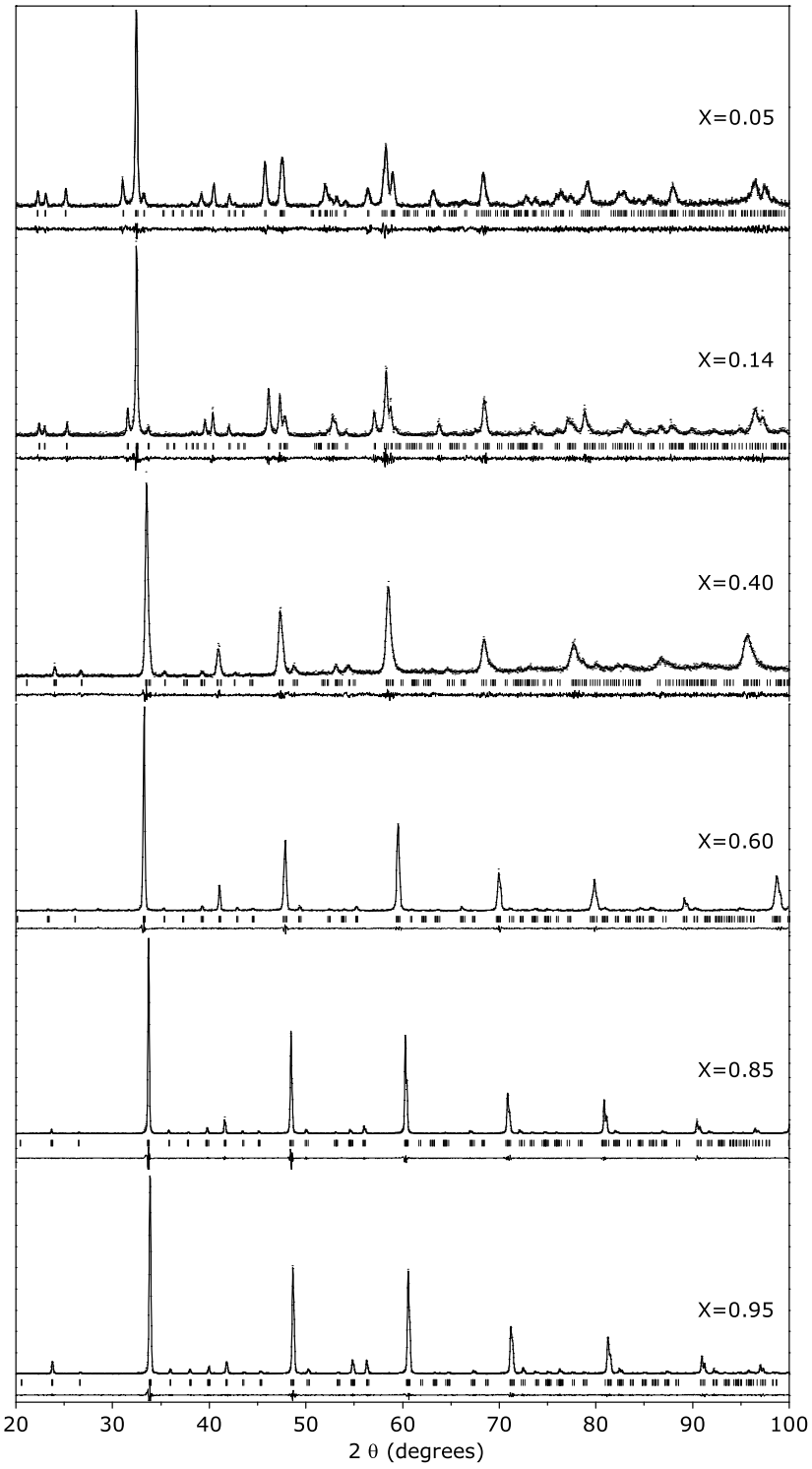

Figure 5.2: $Pr_{1-x}Ca_xMnO_3$ representative x-ray diffraction pattern at room temperature for x=0.05, 0.14, 0.40, 0.60, 0.85 and x=0.95 samples. The observed pattern (dots), calculated (solid line), fit deviation (solid line in the bottom) and reflections of the Pbnm phase (tick marks) are shown.

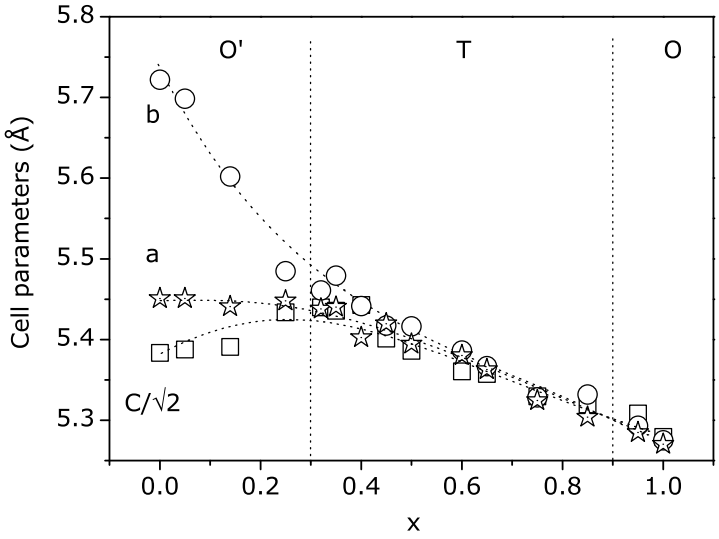

Figure 5.3: Calcium content dependence of the lattice parameters for the $Pr_{1-x}Ca_xMnO_3$ system. The vertical lines depicted in the graphic, separate the different orthorhombic phases(O', pseudo tetragonal (T) and O) as defined in the reference [24]. Lines are guides for the eye.

volume obtained in this work and the results from reference [24,236] are depicted, shows this agreement. The unit cell volume shows a linear trend on Ca content. From the obtained lattice parameters and in a similar way as performed in previous chapter one can calculate the long (l), short (s) and medium (m) Mn-O bond-lengths (see equations 1.4, 1.5 and 1.6). In figure 5.4(b) the dependence of l, m and s bonds on Ca content is depicted. The Mn-O bond lengths obtained through Neutron diffraction measurements by different authors [36, 74, 78] for the $Pr_{1-x}Ca_xMnO_3$ system and the results of PDF analysis of neutron diffraction patterns by D. Louca *et al.* [202] in $Pr_{0.7}Ca_{0.3}MnO_3$[3] are depicted in the same figure[4].

The Mn-O bond lengths calculated from the unit cell parameters show that the deformation of the oxygen octahedra around Mn ions is reduced as the Ca content increases. For $x > 0.3$ only a small (and decreasing) difference between the three distances are observed. Although our results agree with the measured by neutron diffraction [36, 74, 78], they differ from the ones obtained through PDF analysis in related systems. Indeed, it is well known that local distortions are present in manganites, not only for small concentrations of dopant element but also in metallic phases (*e.g.*, $La_{1-x}Ca_xMnO_3$) [13, 17, 238]. The Mn-O bond length calculated from the unit cell parameters give us just an average value of the MnO_6 octahedra deformation. Thus is expected that the mean value of the deformation decreases

[3] In this reference the short and medium bonds are consider to be equal.

[4] The result obtained for the $Pr_{0.7}Ca_{0.3}MnO_3$ compound by [202] can be extended for other compositions since PDF results, in similar systems, showed only a small dependence of the distortion strength upon doping [13, 17].

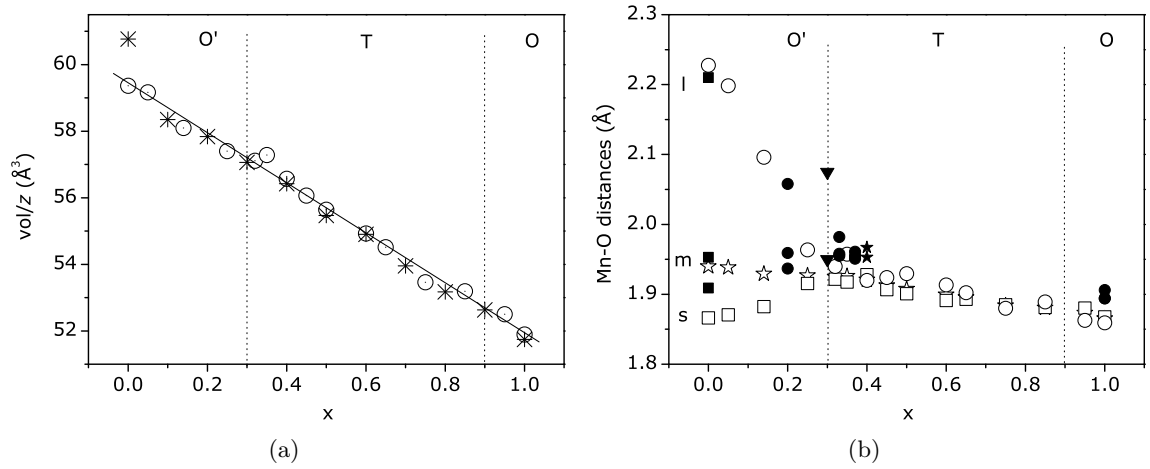

Figure 5.4: a) $Pr_{1-x}Ca_xMnO_3$ unit cell volume as a function of Ca content (⊙ obtained in this work, ∗ from [24,236]. b) Mn-O bonds length, l (○), m (open ⋆) and s (□) calculated in this work. Mn-O bond length obtained through neutron diffraction measurements (■) [78], (•) [74] and ★ [36] and PDF analysis of neutron diffraction patterns (▼) [202]. Lines are guides for the eye.

with the incorporation of Ca, *i.e.*, the creation of regular Mn^{4+}-O_6 octahedra. In any case, this study reveals that the dependence of average octahedra deformation on Ca content is the expected one, demonstrating that the sample composition is well controlled and enabling the use of these set of sample for hyperfine measurements.

5.1.2 Magnetic characterization

To determine the Curie-Weiss, Néel/Curie and charge-order temperatures (θ_P, T_N/T_C and T_{CO} respectively) magnetization data was obtained using a commercial SQUID as described in chapter 2. The thermal dependence of the magnetization curves (or susceptibility χ) was measured after cooling the sample under a small magnetic field (field cooling; H∼ 50 Oe) and sweeping the temperature in a range of 10 K up to 300 K. In some cases the magnetization was also measured after cooling the sample at zero magnetic field (zero field cooling; ZFC). The FC and/or ZFC susceptibilities, χ, were measured for all samples used in this work and some representative curves are presented in figure 5.5. In the same figure the $1/\chi$ curves are also depicted as function of temperature (right side scale). As usually, the Curie-Weiss temperature, θ_P, is determined through the intersect with the T-axis of the high temperature linear dependence of the reciprocal susceptibility which in some cases is hard to find in the temperature range studied.

Table 5.2 summarizes the quantities obtained from the analysis of the susceptibility measurements.

Figure 5.5(a) and 5.5(b) presents the susceptibility behavior representative for low Ca

doped x$\leq$ 0.14 samples for which a antiferromagnetic or spin-canted magnetic structure[5] sets in below ∼110 K [24, 28, 240, 241].

Table 5.2: Charge-ordering temperature, T_{CO}; critical temperature, T_{crit}, and paramagnetic Curie temperature, θ_p obtained for the $Pr_{1-x}Ca_xMnO_3$ system.

x	T_{CO} (K)	T_{crit} (K)[a]	θ_p (K)
0	-	89	50
0.05	-	92	75
0.14	-	108	127
0.25	-	118	143
0.32	210	113	180[b]
			88[c]
0.35	235	140	200[b]
			70[c]
0.40	240	159	198[b]
			34[c]
0.45	245	158	226*
0.50	250	142	210*
0.60	275	145	208*
0.65	274	160	238*
0.75	205	168	144*
0.85	151	108	117*
0.95	-	108	-52
1	-	121	-500

[a] T_C for x= 0.25 and T_N for x$\neq$ 0.25.
[b] θ_P for $T>T_{CO}$
[c] θ_P for $T_N < T< T_{CO}$
* not possible to determine θ_P for $T_N < T< T_{CO}$

The linear behavior of $1/\chi$ versus temperature at high temperature with a downward curvature near the critical temperature can be visualized in the right side scale of the figure 5.5(a). For the x=0.14 sample a upward curvature near the critical temperature, T_N=108 K < θ_P=127 K, is observed. Moreover, a second transition around T=52 K is apparent (see figure 5.5(b)). The characteristic Néel temperatures, T_N=89 K for x=0 and T_N=92 K for x=0.05, obtained for these samples were found to be higher than the Curie-Weiss ones, θ_P=50 K and θ_P=75 K respectively. Commonly, these three samples show a low susceptibility at 10 K. Contrarily, a much higher susceptibility and a well defined transition from the paramagnetic to the ferromagnetic phase was observed for the x=0.25 compound. The inverse susceptibility versus temperature exhibit a upward curvature near T_C with a Curie-Weiss temperature higher than the critical temperature. This behavior is apparent in

[5] Pure PrMnO3 has an A-type antiferromagnetic arrangement, changing discontinuously to a spin-canted-insulator (SCI) structure with small amounts of Mn^{4+} dopant [239]

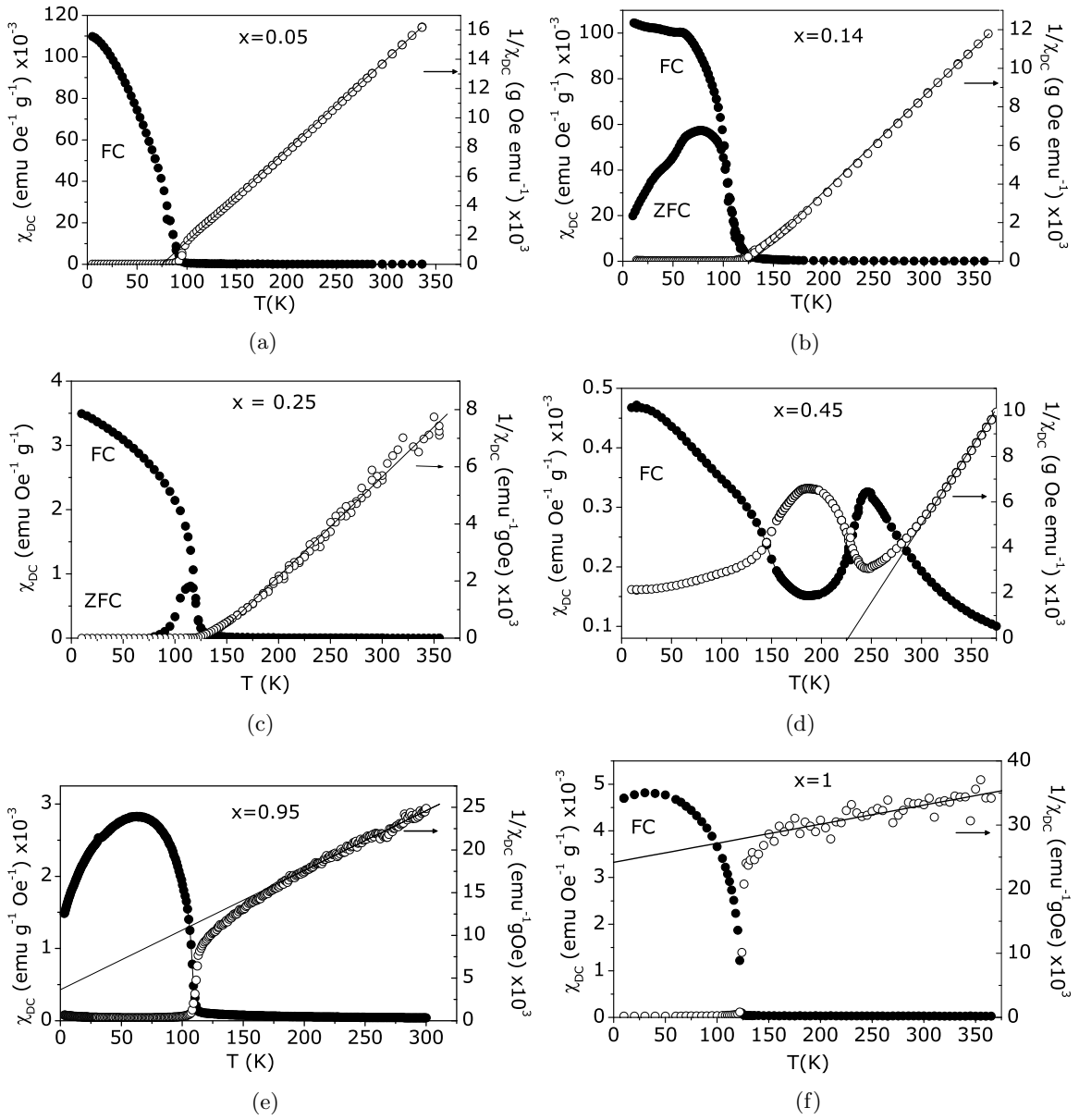

Figure 5.5: Representative susceptibility curves as a function of temperature. Left axis: zero-field-cooled (ZFC) and field-cooled (FC) susceptibility, χ, for different Ca content, a) x=0.05, b) x=0.14, c) x=0.25, d) x=0.45, e) x=0.95 and f) x=1 (•). Right axis: temperature dependence of the inverse of the susceptibility (○).

figure 5.5(c) where a representative magnetization curve for samples with composition below the onset concentration for charge-ordering (x$\leq$ 32%) is depicted. The susceptibility, after field cooling and after zero-field-cooling cycle shows strong irreversibility effects. For this sample the ferromagnetic order establishes for temperatures below the Curie temperature around 118 K, in accordance with the literature [9, 28, 240, 241].

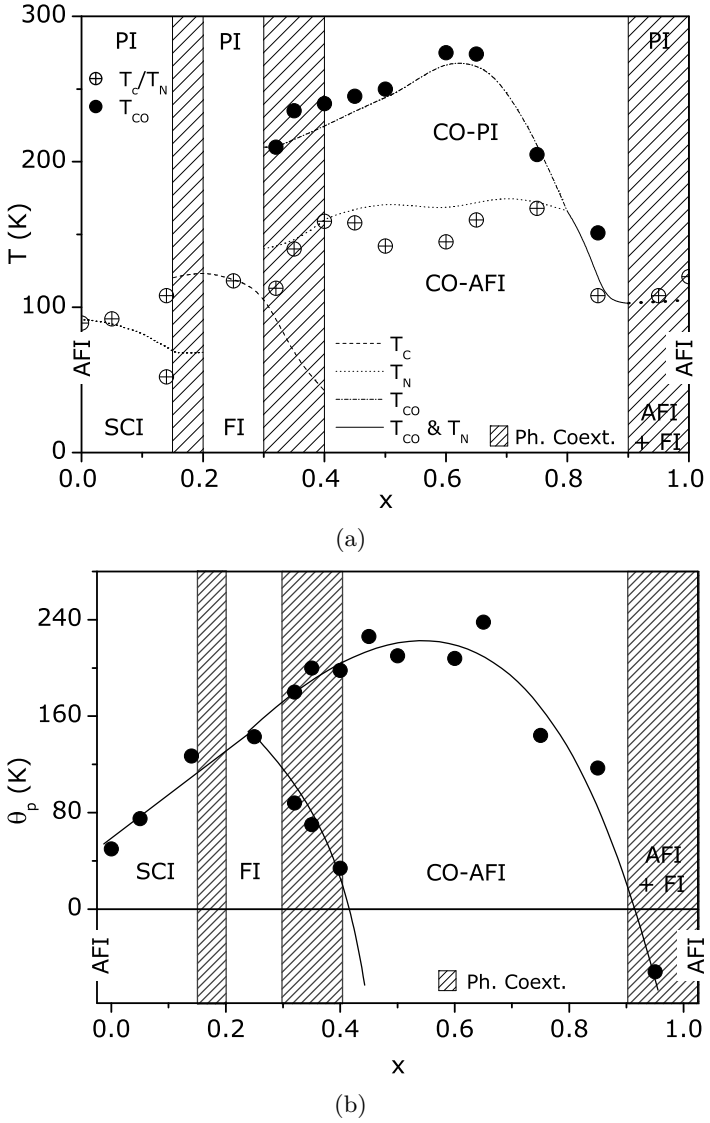

Figure 5.6: Characteristic temperatures for $Pr_{1-x}Ca_xMnO_3$ system as a function of Ca content. a) Néel/Curie (⊗) and charge-order (•) temperatures. These temperatures are compared with the phase diagram from the literature (lines and shadow region), b) Curie-Weiss temperatures (shadow region as defined in a)).

Although for x=0.25 an usual ferromagnetic behavior is found, for higher Ca concentrations within the $0.32 \leq x < 0.95$, different features emerge. The susceptibility presents a maximum at temperatures above the transition from the paramagnetic to the antiferromagnetic phase. For x=0.45, for instance, one can observe a hump, around 226 K (see figure 5.5(d)), corresponding to the establishment of the charge-ordering in accordance with several works [24,28,240,242]. Thus, for these compositions, an antiferromagnetic-insulator AFI phase establishes for temperatures typically below 170 K coexisting with a charge-ordered

CO state with onset temperature T_{CO} ranging from T_{CO}=275 K, for x=0.60, and T_{CO}=151 K, for x =0.85. Additionally, for these compositions, the reciprocal susceptibility versus temperature shows a significative change in its slope around the charge-order temperature, T_{CO}, and a second Curie-Weiss regime can be observed, with a much lower θ_p (see also figures 5.22(a) and 5.22(b)). For $T>T_{CO}$ ferromagnetic correlations are evident in the paramagnetic phase of the CO-AFI samples (positive paramagnetic Curie temperatures with $\theta_p > T_N$). For $T_N < T < T_{CO}$ the second second Curie-Weiss regime presents a $\theta_p \ll T_N$. The paramagnetic Curie temperature for $T_N < T < T_{CO}$ is hard to find and for x>40 one can only say that this value is negative. For x=0.95 and x=1 (figure 5.5(e) and 5.5(f)), a simple curve arises with a defined transition from the paramagnetic to the non-charge-ordered antiferromagnetic AFI phase. As one can observe in figures 5.5(e) and 5.5(f) the charge-ordering feature completely disappears. In literature this is quoted as occurring for x>0.90 (see phase diagram in figure 1.14(b)). The positive Curie temperature, observed in the paramagnetic phase of the CO-AFI samples, shifts gradually towards negative temperatures, reaching θ_P=-52 K for x=0.95 and θ_P=-500 K for x=1. These quantities can be visualized in figure 5.6 where the Néel/Curie, charge-order (a) and Curie-Weiss (b) temperatures are presented. In figure 5.6(a) the characteristic temperatures T_N/T_C and T_{CO} (symbols) are compared with the phase diagram known from the literature (lines). The good agrement between our results and the ones obtained in the literature is evident, thought a deviation in the critical temperature T_N is observed in Ca concentration region with charge-ordering. Figure 5.6(b) shows the dependence of the Curie-Weiss temperature on Ca concentration. For the lowest x, within the CO region, the two Curie-Weiss temperatures, corresponding to the $T> T_{CO}$ and $T_N < T < T_{CO}$ regimes, are presented. For higher Ca concentration, within the CO region, the Curie-Weiss temperature corresponding to the antiferromagnetic correlations are not presented.

5.2 $Pr_{1-x}Ca_xMnO_3$ EFG phase diagram

In this section the room temperature electrical field gradient measurements in the $Pr_{1-x}Ca_xMnO_3$ system as a function of calcium content are presented.

To perform PAC measurements, samples were implanted at room temperature with ^{111m}Cd following the standard procedure described in chapter 2. After the annealing treatment, the room temperature experimental R(t) spectra were obtained.

Figure 5.7 shows representative R(t) spectra (left) and corresponding Fourier transforms (right) measured at room temperature for samples with x=0, 0.25, 0.50 and x=1. The fit to each experimental PAC spectrum (continuous lines over the R(t)) was obtained as described in chapter 3. This same procedure was applied to all samples with different calcium content. For all compositions the fit to each spectrum shows that the Cd probes interact with one main EFG distribution, which was assumed to be Lorentzian-like. In some cases a small contribution from a second EFG distribution had to be taken into account. The number of

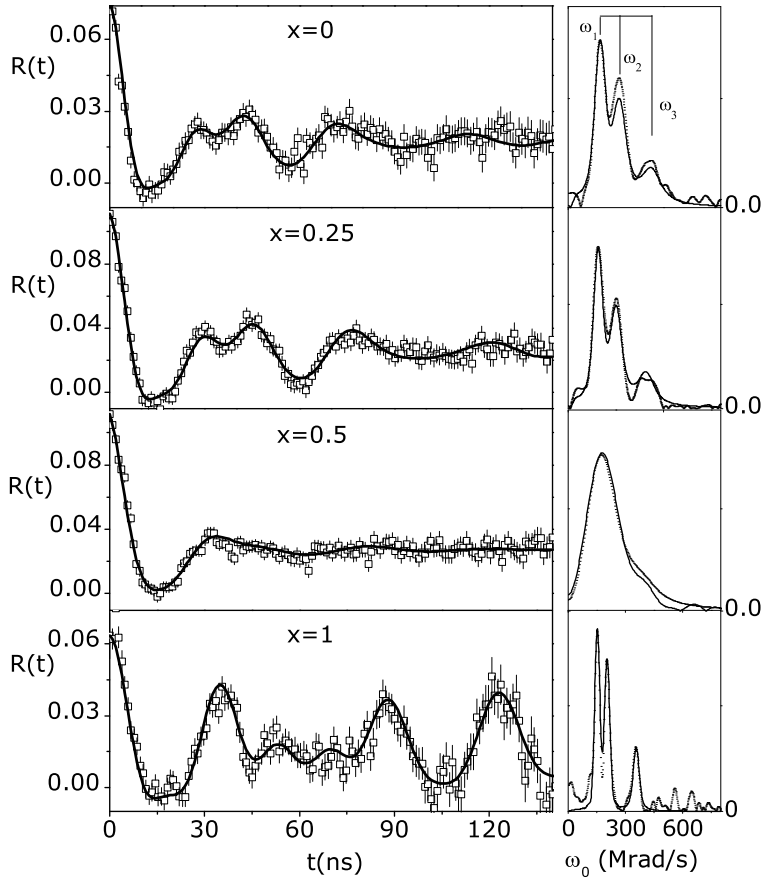

Figure 5.7: Room temperature $Pr_{1-x}Ca_xMnO_3$ (x=0, 0.25, 0.5 and 1)representative R(t) experimental functions and fits to the experimental PAC spectrum (continuous lines over the R(t))(left). Corresponding Fourier transforms (right).

probes interacting with such second EFG was distribution was always less than 5%. This minor local environment, at the limit of our characterization precision, might have its origin into probes located in lattice zones with local defects as grain boundaries and point defects. Table 5.3 presents the EFG parameters measured at room temperature for this set of samples.

As one can observe in figure 5.7 the R(t) functions and Fourier spectra, corresponding to samples with different calcium content, present distinct features. Although drastic changes with doping are not evident, the increase of the η value[6] with increasing doping and the growth of the attenuation to the R(t) spectra in samples with compositions around x=0.5 is apparent. The existence of a wide distribution of local environments and dynamic effects within the PAC time window are usually responsible for the broadening of the measured frequency line-shapes. This broadening was found to be maximum close to x=0.50, suggesting that the chemical disorder due to random cation (Pr/Ca) distribution, should be the main

[6]This increase can be noticed through the decrease of the $w_2 - w_1$ difference.

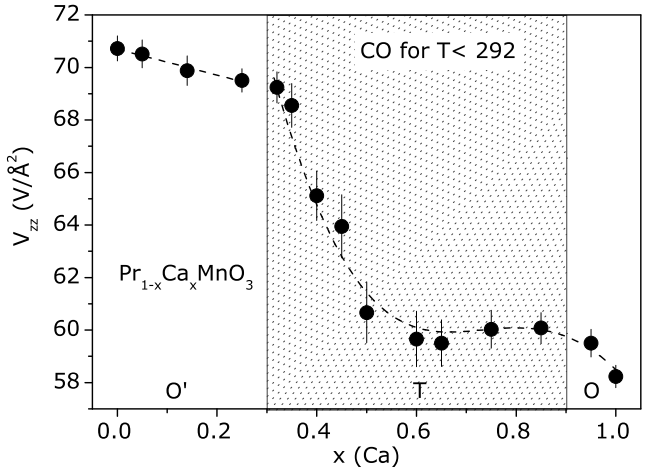

(a)

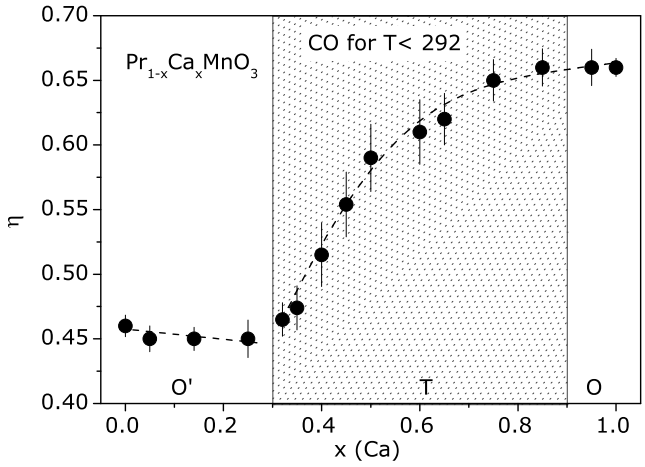

(b)

Figure 5.8: EFG parameters, V_{zz}, a) and η, b), as a functions of calcium content, x, for the $Pr_{1-x}Ca_xMnO_3$ system. Lines are guides for the eye. The shadowed area represents the phase diagram region where charge ordering occurs at lower temperatures.

reason for the observed attenuation. Changes in the observable frequency ω_0, are not noticed by the simple inspection of the R(t) and corresponding Fourier spectra presented in figure 5.7. Nevertheless ω_0 does not remain constant with Ca doping. Figure 5.8 presents the variation of the principal component of the EFG tensor, V_{zz}, a) and the asymmetry parameter η, b) with Ca content. The region of compositions with charge ordering features (below room temperature) is marked by the shadowed area. As one can observe the principal component of the EFG decreases from V_{zz} ~70.7 V/Å^2 for $PrMnO_3$ to V_{zz} ~58.1 V/Å^2 for $CaMnO_3$. For compositions x≤0.3, V_{zz} decreases linearly with the increasing of Ca content, for values higher than x~0.3 (samples within the CO region) a sharp decrease is observed. The asymmetry parameter, η, is almost constant with the increasing of Ca content for x<0.3. This trend

changes for x≥0.3 where the asymmetry parameter experience a substantial increase upon increasing Ca doping, stabilizing then for calcium concentrations x≥0.85.

5.2.1 Low temperature measurement in the end-members and low doped compounds

The $PrMnO_3$ and $CaMnO_3$ end-members were also measured at T∼77K and T=10 K. The compositions with x=0.05, 0.14 and 0.95 were measured at T=77K. Figures 5.9 and 5.10 shows the R(t) experimental functions and corresponding FT at the measured temperatures for $CaMnO_3$ and $PrMnO_3$ respectively.

Table 5.3: EFG parameters measured at room temperature for the $Pr_{1-x}Ca_xMnO_3$ system.

x	V_{zz}(V/Å^2)	η	δ (%)
0	70.7(5)	0.46(1)	7
0.05	70.5(5)	0.45(1)	8
0.14	69.9(6)	0.45(1)	10
0.25	69.5(4)	0.45(2)	11
0.32	69.3(6)	0.47(1)	11
0.35	68.6(8)	0.47(2)	18
0.4	65.1(9)	0.52(3)	17
0.45	64.1(10)	0.55(3)	20
0.5	60.7(12)	0.59(3)	23
0.6	59.7(11)	0.61(3)	21
0.65	59.5(9)	0.62(2)	19
0.75	60.1(7)	0.65(2)	16
0.85	60.1(6)	0.66(2)	16
0.95	59.5(5)	0.66(1)	13
1	58.2(4)	0.66(1)	5

Table 5.4: Low temperature EFG parameters for the end-members $PrMnO_3$ and $CaMnO_3$ and for the compositions x=0.05, 0.14 and 0.95.

x	T(K)	V_{zz}(V/Å^2)	η	δ (%)	B_{hf} (T)
0	77	74.6(11)	0.44(2)	7	-
0	10	74.8(15)	0.41(2)	7	1.2(3)
0.05	77	74.4(12)	0.46(3)	7	0.48(14)
0.14	77	73.6(12)	0.46(3)	9	0.68(15)
0.95	77	60.3(12)	0.64(3)	12	-
1	80	59.3(6)	0.64(2)	4	-
1	10	59.7(5)	0.60(2)	5	-

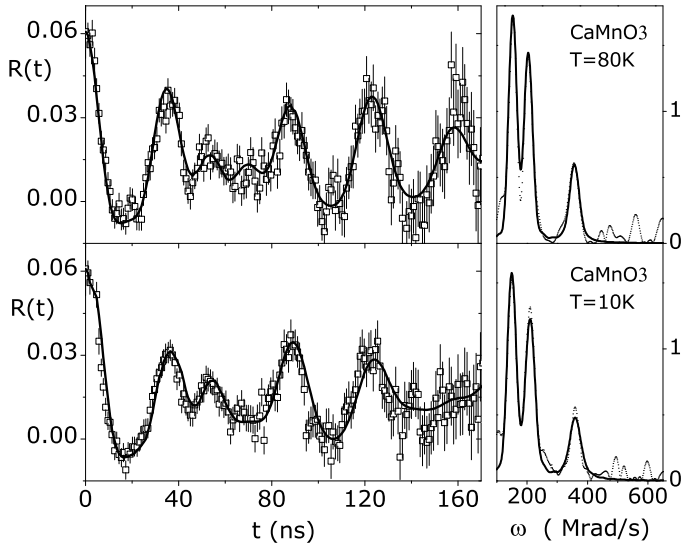

Figure 5.9: R(t) experimental functions (left) and corresponding Fourier spectra (right), at 80K (top) and 10K (bottom) for the $CaMnO_3$. The continuous lines over the R(t) and Fourier transform correspond to the fits to the experimental PAC spectra.

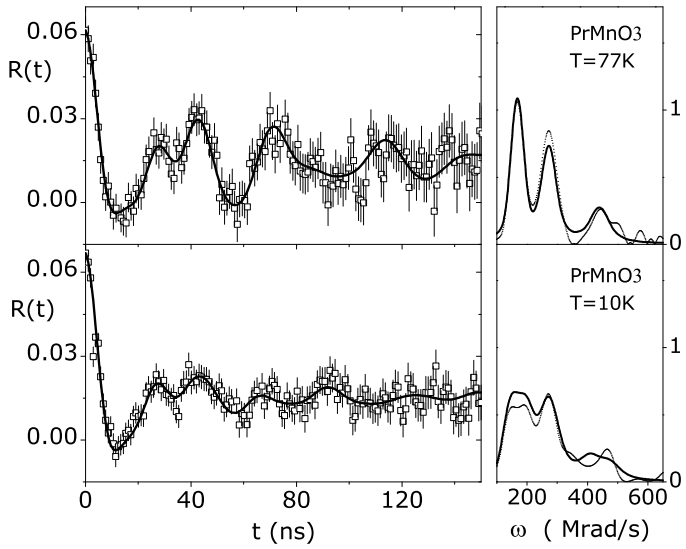

Figure 5.10: R(t) experimental functions (left) and corresponding Fourier spectra (right), at 77K (top) and 10K (bottom) for $PrMnO_3$ compound. The continuous lines over the R(t) and Fourier transform correspond to the fits to the experimental PAC spectra.

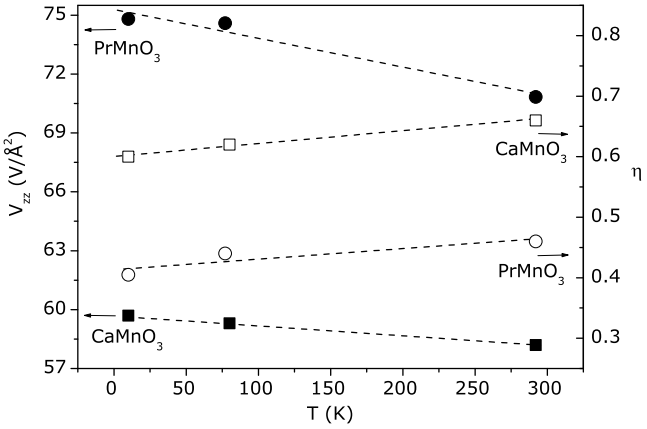

Figure 5.11: EFG parameters, V_{zz} (left scale, black symbols) and η (right scale, open symbols), as a functions of temperature, for the $PrMnO_3$ (• and ∘) and $CaMnO_3$ (■ and □) samples. Lines are guides for the eye.

Table 5.4 presents the obtained EFG and MHF parameters. Figure 5.11 shows the principal component of the EFG tensor, V_{zz}, and asymmetry parameter η temperature evolution for $PrMnO_3$ and $CaMnO_3$ compounds. An increase of V_{zz} with decreasing temperature, as usually occurs in perovskite systems, is observed in end-members and low doped compositions. All these compounds show similar dependences with temperature, *i.e.*, $\frac{1}{V_{zz}^0}\frac{\Delta V_{zz}}{\Delta T} \sim$ -2.0×10^{-4}, -2.4×10^{-4}, -2.3×10^{-4}, -6.5×10^{-5} and , -8.9×10^{-5} K^{-1} for x=0, 0.05, 0.14, 0.95 and 1 respectively. For this system the volume thermal expansion is small, $\alpha \sim 2 \times 10^{-5}$ K^{-1} [74, 78, 186, 187], and is not enough to account for the V_{zz} temperature dependence. Small changes in the asymmetry parameter η were observed and contrarily to V_{zz}, the asymmetry parameter was found to decrease with decreasing temperature. Furthermore, for the $CaMnO_3$ compound no detectable MHF at the probe site was found. In fact, by observation of figure 5.7 (bottom) and figure 5.9, where the R(t) experimental functions are depicted, one cannot see any significant differences, as would occur if a magnetic field would be present. Notice that $CaMnO_3$ is a G type antiferromagnetic system [23] thus the MHF must vanish at the A perovskite site where the probe sits. In $PrMnO_3$ the Mn spins have an A type antiferromagnetic arrangement [23], and for the same reasons the MHF must vanish at the probe site. Although no MHF was detected at 77 K for this sample, at 10 K a magnetic hyperfine field B_{hf}=1.2(3) T ($\beta \sim 43°$) was measured (see figure 5.10). This effect may be related to the arrangement of the Pr magnetic moments that occurs below 70 K [74]. This ordering is referred in literature [74] as being responsible for a small canting of both the Pr and Mn magnetic sub-lattices yielding a non vanishing magnetic field at the probe site. For the x=0.05 and x=0.14 a B_{hf}=0.48(14) and B_{hf}=0.68(15) T MHF, with $\beta \sim 52°$, was measured at 77K. For these compositions the magnetic hyperfine field can also be associated with the spin canting magnetic phase reported.

5.3 Ferromagnetic Insulator $Pr_{0.75}Ca_{0.25}MnO_3$ compound

The ferromagnetic insulator $Pr_{0.75}Ca_{0.25}MnO_3$ compound was measured in the $11 \leq T \leq 500K$ temperature range.

Figure 5.12 shows representative R(t) spectra (left) and corresponding Fourier spectra (right) measured at several temperatures. The fit to each experimental PAC spectrum (continuous lines over the R(t)) shows that the Cd probes interact with one main EFG distribution, which was assumed to be Lorentzian-like. A small contribution, always less than 8%, from a second EFG was taken into account to improve the fits. The parameters of this second EFG were found to be similar to the ones obtained for main EFG.

As one can observe in figure 5.12 no drastic changes in the R(t) and corresponding Fourier spectra are observed. Possible modifications in the observable frequency ω_0, and η parameter are not noticed by the simple inspection of these plots. The results of the fits to these spectra, EFG and MHF parameters, are summarized in table 5.5.

Table 5.5: EFG parameters and MHF for the $Pr_{0.75}Ca_{0.25}MnO_3$ compound at different temperatures.

x	$V_{zz}(V/Å^2)$	η	δ (%)	B_{hf} (T)
500	67.8(3)	0.46(2)	15	–
403	68.5(3)	0.45(2)	10	–
292	69.5(4)	0.45(2)	11	–
250	69.8(3)	0.44(2)	11	–
230	70.1(3)	0.45(2)	11	–
200	70.3(3)	0.46(2)	10	–
169	70.5(3)	0.44(2)	11	–
132	70.8(3)	0.44(2)	11	–
77	71.1(5)	0.49(4)	11	4.4(4)
11	71.2(5)	0.47(4)	11	4.4(4)

The measured principal component of the EFG tensor, V_{zz}, is plotted as a function of temperature in figure 5.13. The asymmetry parameter, η, is depicted in the inset of that figure. Figure 5.13 shows that V_{zz} increases with decreasing temperature following the common trend observed in perovskite structures. The relative thermal dependence of V_{zz}, above T_C, $\frac{1}{V_{zz}^0}\frac{\Delta V_{zz}}{\Delta T} \sim$ -1.2×10^{-4} K^{-1}, is similar to the ones found for the end-members. The relative width of the EFG distribution, $\delta \sim 11\%$, was found to be temperature independent[7]. In the inset of the same figure one can observe that the asymmetry parameter is essentially temperature independent, averaging $\eta \sim 0.45$. Thought for temperatures below T_C the measured η values were higher than the ones measured for temperatures above, one should

[7]The width of the EFG distribution below T_C was fixed ($\delta = 11\%$)

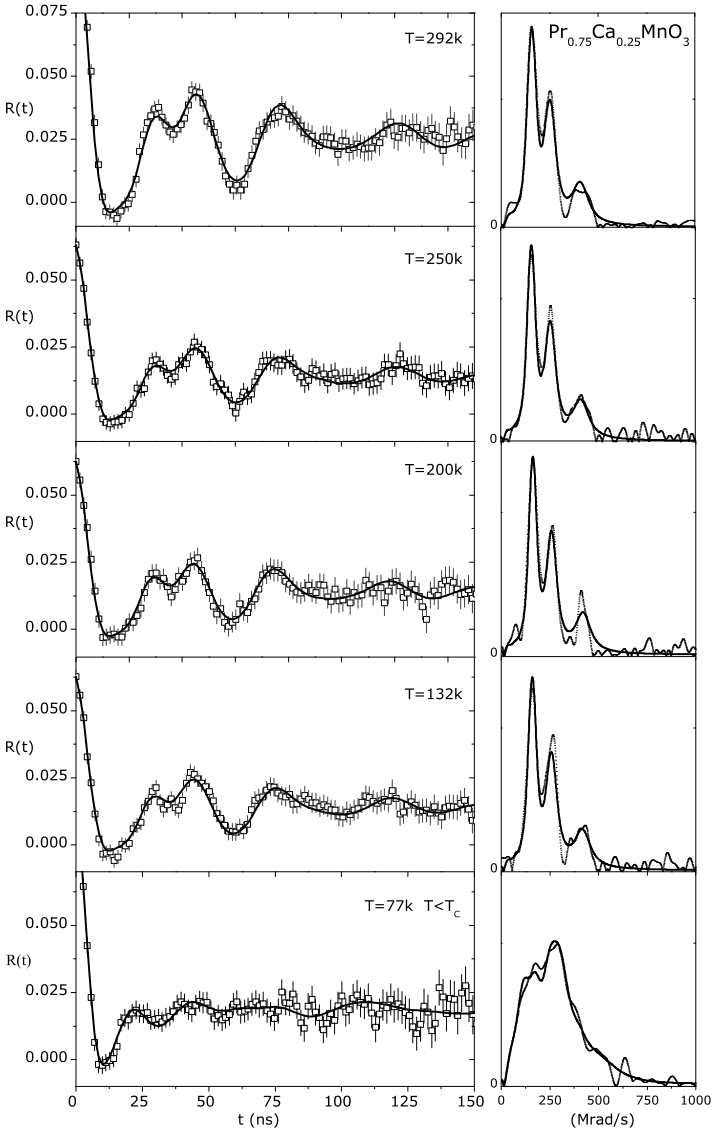

Figure 5.12: Representative R(t) experimental functions (left) and corresponding Fourier spectra (right), for several temperatures for the $Pr_{0.75}Ca_{0.25}MnO_3$ compound. The continuous lines over the R(t) and Fourier transform are the fits to the experimental PAC spectra.

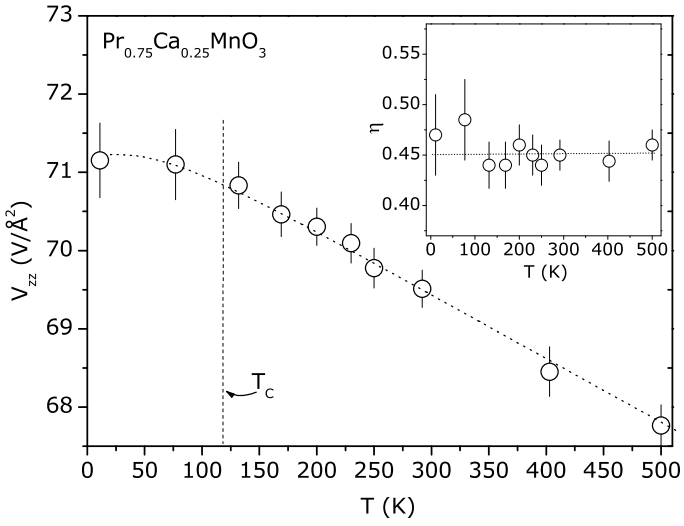

Figure 5.13: EFG parameters, V_{zz} and η, as a functions of temperature for the $Pr_{0.75}Ca_{0.25}MnO_3$ compound. Lines are guides for the eye.

remark that the broadening of the spectra, connected to the presence of a MHF, makes difficult the accurate determination of the EFG parameters.

As one can observe in the bottom of figure 5.12 the R(t) spectra is strongly damped below T_C. This feature in the R(t) spectra and the new frequencies in the FT transforms show that the probes experience a magnetic hyperfine field below T_C (118 K). Accordingly, the fits were performed considering a magnetic hyperfine field below that temperature. The obtained MHF was B_{hf}=4.4(4) T and B_{hf}=4.4(4) T for 77 and 11 K, respectively. The angle between the MHF and the principal component of the EFG was found to be approximately $\beta \sim 85°$. As shown in the beginning of this chapter at low temperatures this sample is ferromagnetic, thus the presence of a MHF would be expected.

5.4 Local probing of charge-order transition

5.4.1 $Pr_{0.65}Ca_{0.35}MnO_3$ compound

The $Pr_{0.65}Ca_{0.35}MnO_3$ antiferromagnetic insulator compound was measured in a $11 \leq T \leq 506K$ range of temperatures.

Figure 5.14 shows representative R(t) spectra (left) and corresponding Fourier spectra (right) measured for several temperatures. The fit to each experimental PAC spectrum (continuous lines over the R(t)) shows that the Cd probes interact with one main EFG distribution, which was assumed to be Lorentzian-like. As before, a small contribution from a second EFG was taken into account to improve the fit. The number of probes interacting

with this minor EFG averages 4%. At the limit of our characterization precision this EFG may be related to probes at zones with local defects as grain boundaries.

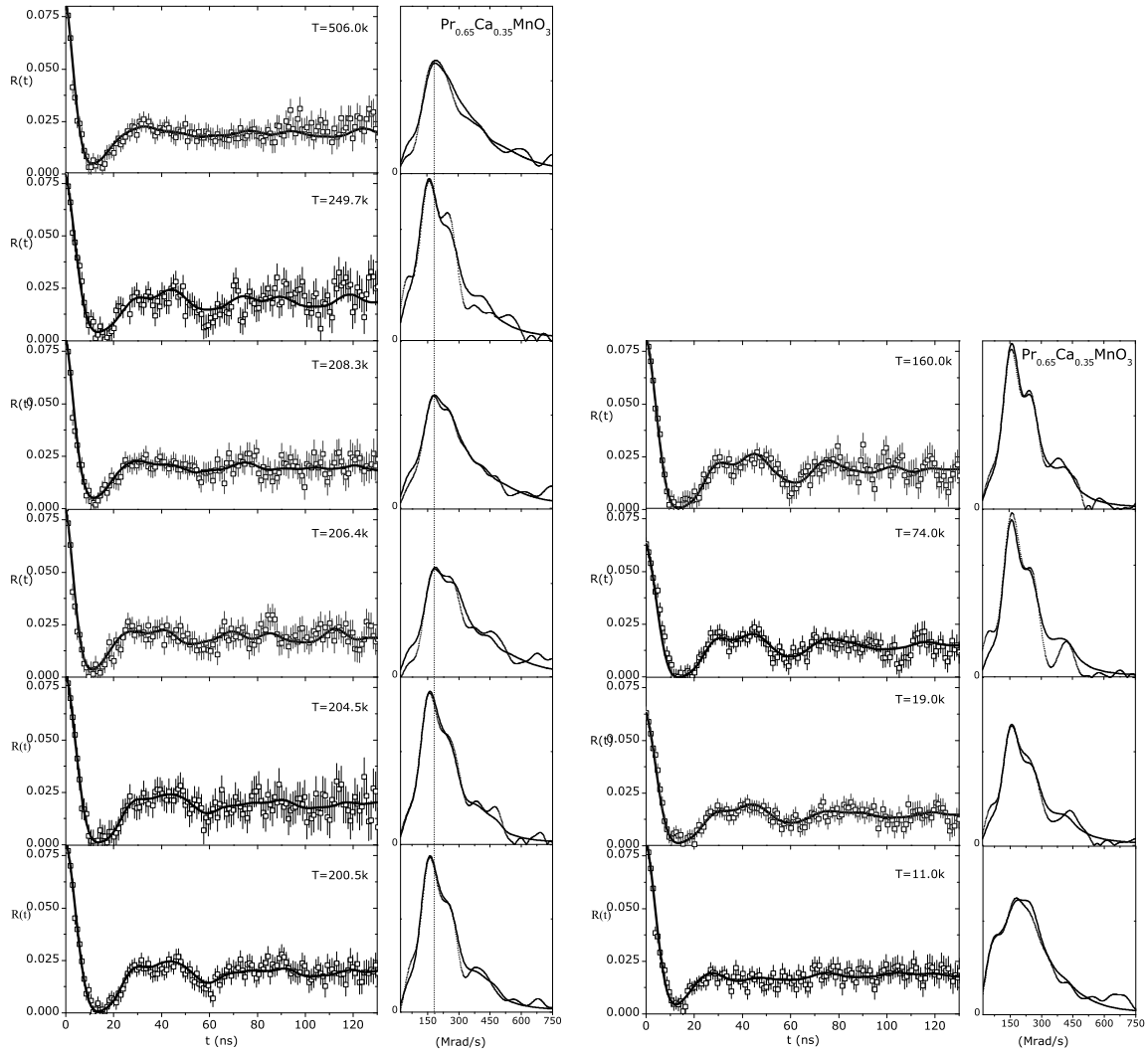

(a) (b)

Figure 5.14: Representative R(t) experimental functions (left) and corresponding Fourier spectra (right), at several temperatures for the $Pr_{0.65}Ca_{0.35}MnO_3$ compound. The continuous lines over the R(t) and Fourier transform are the fits to the experimental PAC spectra.

As presented in figure 5.14 the R(t) functions and Fourier spectra present distinct features when the temperature is lowered. The changes in the characteristic frequencies, are apparent in the Fourier spectra. Also, the changes in the attenuation to the R(t) spectra are evident in that figure. Table 5.6 presents the EFG parameters measured at the different temperatures for this system.

Figure 5.15 showns the EFG parameters, V_{zz}, a) and η, b) measured for this compound.

The asymmetry parameter is almost constant averaging 0.46 for the measured temperatures. On the contrary, the V_{zz} shows very anomalous features as a function of temperature. For high temperatures, T$\geq$ 250K ($\sim T_{CO}$), the EFG principal component, V_{zz}, decreases lowering temperature. This behavior is contrary to the one observed in all other studied compounds (*e.g.*, see figure 5.13). Further lowering temperature a sharp increase followed by a discontinuity is observed. The occurrence of this discontinuity is limited by a narrow temperature window, 204.5$\leq$ T $\leq$ 206.4K, where V_{zz} drops from 85.0 V/Å^2 to 67.0 (V/Å^2). For temperatures below 204.5 K the V_{zz} usual trend for perovskite systems is observed, *i.e.*, V_{zz} increases with decreasing temperature. Moreover, a large V_{zz} relative width (δ) is apparent in all spectra having its maximum in the range of temperatures where the V_{zz} rises sharply (see table 5.6).

Between 19 and 11 K the spectra change significatively, and the fit to the 11 K spectrum had to be performed considering both the presence of a magnetic hyperfine field and an EFG distribution. Since in literature either a canted AF-CE-type magnetic structure [28, 74, 243, 244] or a AF-CE[8]/ FM phase coexistence [67, 245, 246] has been reported for compositions 0.3$\leq$ x $\leq$0.4 we performed two distinct fits for this spectrum. One was performed considering that all the probes experience the presence of a MHF. The results of this fit yielded a magnetic

[8]This Mn spin antiferromagnetic arrangement yields a vanishing MHF at the probe site.

Table 5.6: $Pr_{0.65}Ca_{0.35}MnO_3$ EFG parameters measured at different temperatures.

T (K)	V_{zz}(V/Å^2)	η	δ (%)	B_{hf}(T)
506.0	84.7(13)	0.47(4)	29	–
400.0	79.4(11)	0.50(3)	31	–
292.0	68.6(8)	0.47(2)	18	–
249.7	67.0(8)	0.48(3)	26	–
230.0	68.4(7)	0.47(2)	24	–
219.7	68.7(8)	0.46(2)	24	–
215.0	70.9(11)	0.49(2)	17	–
211.0	71.1(12)	0.43(4)	35	–
210.1	72.8(11)	0.44(3)	34	–
208.3	78.9(11)	0.49(2)	32	–
206.4	85.0(11)	0.48(2)	31	–
204.5	67.0(8)	0.48(2)	18	–
200.5	67.2(8)	0.48(2)	19	–
160.5	67.5(8)	0.46(2)	18	–
129.8	67.8(11)	0.45(2)	20	–
74.0	68.0(9)	0.47(3)	18	–
19.0	68.3(12)	0.46(2)	22	–
11.0	68.5(16)	0.46(3)	19	2.8(3)

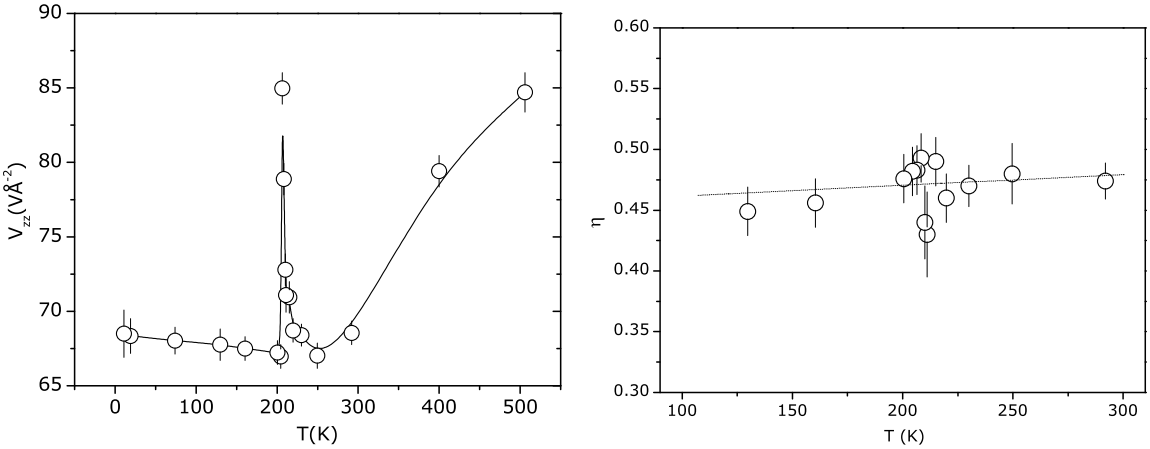

(a) (b)

Figure 5.15: EFG parameters, V_{zz} and η, as a function of temperature for the $Pr_{0.65}Ca_{0.35}MnO_3$ compound. Lines are guides for the eye.

hyperfine filed $B_{hf} \sim 2.8(3)$ T ($\beta \sim 55°$). The obtained EFG parameters are presented in table 5.6 and the fit is presented in figure 5.14. The second approach was performed considering that only part of the probes interact with a MHF (probes within FM regions). This last fit gave a magnetic hyperfine filed $B_{hf} \sim 4.1$ T (similar to the value found for the ferromagnetic x=0.25 compound, $B_{hf} \sim 4.4$ T). The EFG parameters of both fractions where, within the error bars, the same as the ones found in the first case. The percentage of probes corresponding to the AF environment(*i.e.*, without MHF) was found to be around 32%. Both approaches gave similar quality of the fits, and although the first one yields a slightly smaller χ^2 it is difficult to base the preference for one of the approaches based only on this criterium. In this region of the phase diagram, phase coexistence can only be admitted as small volume fraction of ferromagnetic regions within a antiferromagnetic matrix and this is not compatible with 68% of the probes experiencing a MHF. Thus our results suggest that the magnetic configuration of the Mn ions should be a canted AF-CE-type. According to Tokura *et al.* work [28] the AF to canted AF magnetic transition should occur around 60 K for x=0.35 and 42 K for x=0.40. Although one cannot exclude the presence of a tiny MHF for T=19 K (B_{hf} <0.8 T) the fits presented in figure 5.14 do not include such MHF. Recent neutron diffraction results for the x=0.37 showed however a transition from a AF-CE to a canted AF-CE magnetic configuration for temperatures below 30 K stabilizing at 10 K with an ∼18° canting angle [74]. Similar results were reported before by Lees and co-authors for the x=0.4 compound at temperatures below 25 K and attributed to a reorientation of the Mn ions (out of a-b plane due to the coupling to the Praseodymium ions) [244].

5.4.2 $Pr_{0.60}Ca_{0.40}MnO_3$ compound

The $Pr_{0.60}Ca_{0.40}MnO_3$ antiferromagnetic insulator system was measured in a $9 \leq T \leq 500K$ temperature range.

Figure 5.16 shows representative R(t) spectra (left) and corresponding Fourier spectra (right) measured for several temperatures. The continuous lines over the R(t) function represents the fit to each experimental PAC spectrum calculated assuming static nuclear quadrupole interactions. The fit to each spectrum shows that the Cd probes interact with one main EFG distribution, which was assumed to be Lorentzian-like. A small contribution, always less than 3%, from a second EFG was taken into account to improve the fit.

In contrast to the R(t) functions of the $Pr_{0.65}Ca_{0.35}MnO_3$ compound (see figure 5.14) in these spectra changes are more difficult to detect and a simple inspection of this figure does not allow to resolve possible changes in the observable frequency ω_0 (see figure 5.16). Figure 5.17 presents the variation of the principal component of the EFG tensor, V_{zz}. Table 5.7 presents the EFG parameters extracted from the fits at the different temperature.

Table 5.7: $Pr_{0.60}Ca_{0.40}MnO_3$ EFG parameters measured at different temperatures.

T (K)	$V_{zz}(V/Å^2)$	η	δ (%)
500.0	62.5(11)	0.55(2)	20
381.0	64.2(11)	0.54(3)	16
292.0	65.1(9)	0.52(3)	17
260.0	63.9(8)	0.50(3)	17
242.5	63.0(5)	0.50(2)	16
234.3	63.5(5)	0.50(2)	23
229.6	64.6(8)	0.52(3)	23
224.3	65.6(7)	0.50(2)	23
220.0	67.6(7)	0.50(2)	23
214.6	64.6(6)	0.52(2)	18
210.0	64.8(5)	0.51(3)	18
203.3	65.0(6)	0.50(3)	18
100.2	66.9(5)	0.47(2)	18
9.0	68.2(6)	0.47(3)	19

The EFG parameters presented in figure 5.17 show that η decreases very slightly with decreasing temperature averaging $\eta \sim 0.5$ in the $260 \leq T \leq 200$ K temperature range while, V_{zz} shows anomalous features when decreasing temperature. At high temperatures, between $292 \leq T \leq 500$ K, V_{zz} increases with decreasing temperature following the common trend observed in perovskite structures. The V_{zz} relative thermal dependence, $\frac{1}{V_{zz}^0}\frac{\Delta V_{zz}}{\Delta T} \sim -2.0\times10^{-4}$ K^{-1}, is similar to the ones found for compositions without charge-order features. For temperatures below room temperature and in similar way as occurs in the x=0.35 compound,

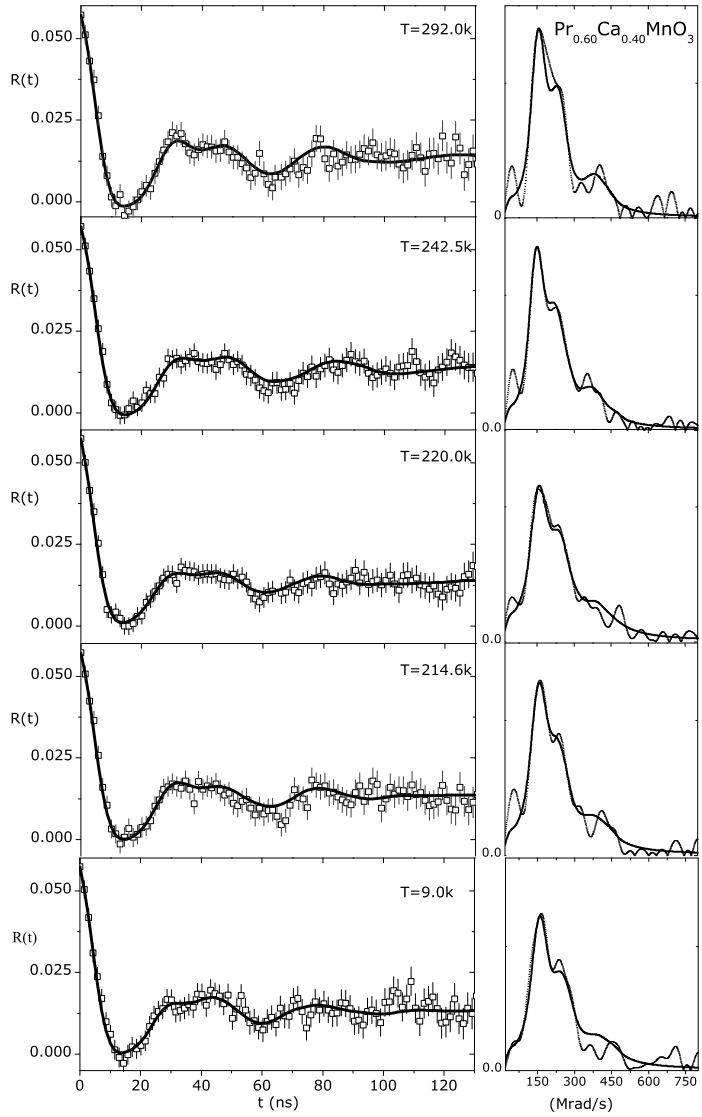

Figure 5.16: Representative R(t) experimental functions (left) and corresponding Fourier spectra (right), for several temperatures for the $Pr_{0.60}Ca_{0.40}MnO_3$ compound. The continuous lines over the R(t) and Fourier transform are the fits to the experimental PAC spectrum.

V_{zz} decreases with lowering temperature till T$\sim$ 243 K. Further lowering the temperature, this tendency is reversed and also where a sharp V_{zz} increase, followed by a discontinuity is observed. Similarly as in the compound with x=0.35, the anomalies observed in V_{zz} occur, around the charge ordering temperature (T_{CO} $\sim$ 240 K). The discontinuity, in this compound, occurs within the narrow 220.0$\leq$ T $\leq$214.6 K temperature window. In this temperature range V_{zz} drops from 67.6 to 64.6 V/Å^2. As one can observe, in the 214$\leq$ T $\leq$ 243 K temperature window, the V_{zz} variation does not exceed 7%. The large EFG distribution relative width (δ), observed in all spectra, has its maximum in the range of temperatures where V_{zz} rises sharply (see table 5.7).

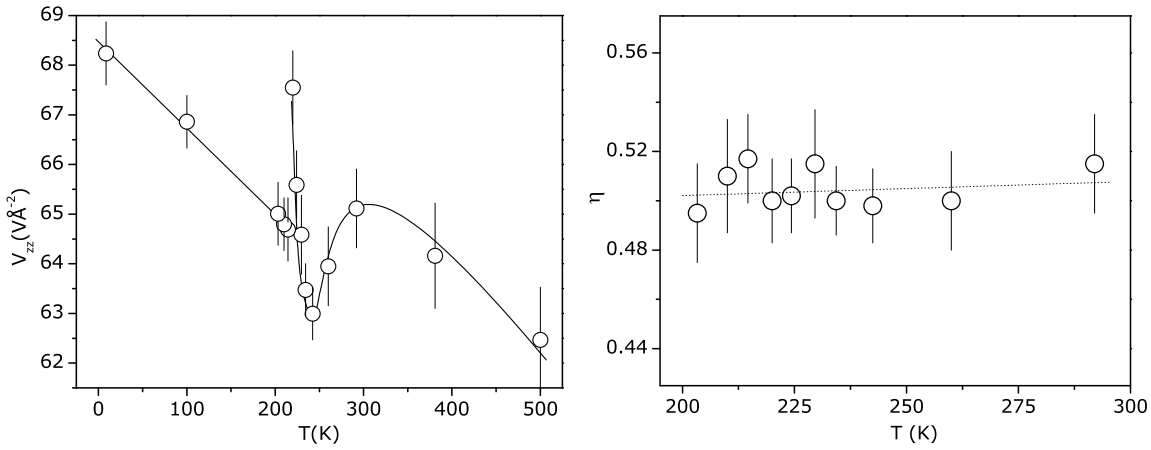

(a) (b)

Figure 5.17: EFG parameters, V_{zz} and η, as a functions of temperature for the $Pr_{0.60}Ca_{0.40}MnO_3$ compound. Lines are guides for the eye

The common trend of V_{zz} is recovered for temperatures below T $\leq$214.6 K. For these temperatures V_{zz} increases with decreasing temperature reaching V_{zz} =68.2 V/Å^2 at T=9 K. At this temperature according to the literature a canted AF-CE-type magnetic structure [28, 243, 244] should be present. To ascertain to the presence of a MHF due to the AF-CE-type magnetic structure two types of fits were done: one by considering that all the probes experience both an EFG and a MHF; the other considering a pure EFG interaction. Both approaches give similar quality of the fits, consequently one cannot resolve this question and the presence of a small MHF (B_{hf} <0.8 T) cannot be excluded.

5.4.3 $Pr_{0.15}Ca_{0.85}MnO_3$ compound

The high Ca doped $Pr_{0.15}Ca_{0.85}MnO_3$ antiferromagnetic insulator system also presents a CO transition around T_{CO} $\sim$ 151 K. In order to achieve some insight in the nanoscopic features of the CO state in the high Ca doped phase diagram region a similar study as the one performed in the x=0.35 and x=0.40 systems was carried out. With this purpose, a

PAC study of the $Pr_{0.15}Ca_{0.85}MnO_3$ compound was carried out in the 18.7≤ T ≤ 902.0K temperature range.

Figure 5.18 shows illustrative R(t) spectra (left) and corresponding Fourier transforms (right). Continuous lines over the R(t) and Fourier experimental function represent the fits to those PAC spectra. For all temperatures the fits were performed considering that the Cd probes interact with one main EFG distribution, which was assumed to be Lorentzian-like. A small contribution from a second EFG, always less than 3 %, was taken into account to improve the fit. Table 5.8 summarizes the parameters of the main EFG distribution measured at different temperatures.

Table 5.8: $Pr_{0.15}Ca_{0.85}MnO_3$ EFG parameters measured at different temperatures.

T (K)	$V_{zz}(V/Å^2)$	η	δ (%)
902.0	55.9(3)	0.68(1)	9
773.0	58.3(7)	0.71(2)	13
500.0	60.7(6)	0.70(2)	11
292.0	60.1(6)	0.66(2)	16
197.0	58.9(5)	0.65(1)	15
174.4	57.7(4)	0.64(1)	14
148.0	58.4(4)	0.61(1)	13
134.0	59.0(4)	0.61(1)	17
125.0	59.6(4)	0.61(1)	13
120.0	59.8(4)	0.61(1)	14
115.0	60.3(4)	0.61(1)	15
113.6	60.9(4)	0.60(1)	15
110.5	57.6(4)	0.61(1)	14
105.6	57.8(3)	0.60(1)	13
100.0	57.7(3)	0.60(1)	13
78.0	58.2(3)	0.63(2)	13
18.7	59.0(4)	0.62(1)	12

Alike in the $Pr_{0.60}Ca_{0.40}MnO_3$ compound (see figure 5.16) a simple inspection of the R(t) and corresponding Fourier spectra presented in figure 5.18 does not allow to resolve potential changes in the observable frequency. Those changes can be visualized however through the temperature dependence of the principal component of the EFG tensor, V_{zz}, presented in figure 5.19(a). In the same figure the asymmetry parameter η is depicted in the right side (figure 5.19(b)). Through this figure is possible to observe a slight decrease of the asymmetry parameter when the temperature is lowered, in the 100≤ T ≤ 175 K temperature range the asymmetry parameter averages $\eta \sim 0.61$.

When decreasing temperature the same features as observed in the EFG principal component of the x=0.40 compounds are apparent in figure 5.19(a). As before, for temperatures

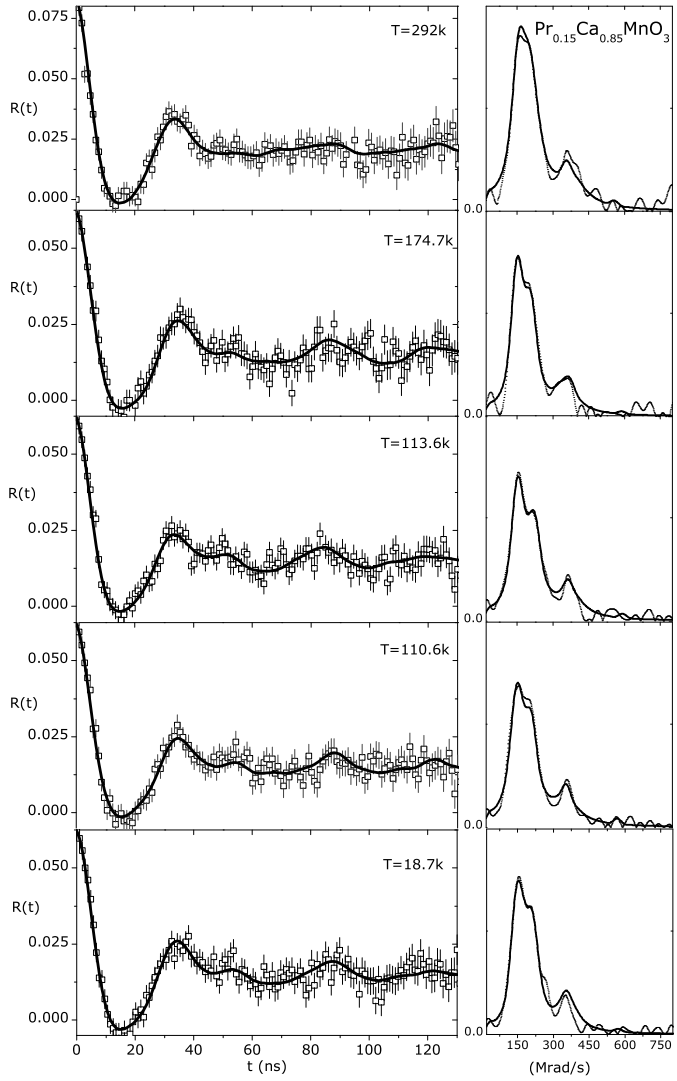

Figure 5.18: Representative R(t) experimental functions (left) and corresponding Fourier spectra (right), at different temperatures for the $Pr_{0.15}Ca_{0.85}MnO_3$ compound. The continuous lines over the R(t) and Fourier transform are the fits to the experimental PAC spectra.

between between $400 \lesssim T \leq 902$ K V_{zz} increases with decreasing temperature following the common trend observed in perovskite systems. The V_{zz} relative thermal dependence , $\frac{1}{V_{zz}^0}\frac{\Delta V_{zz}}{\Delta T} \sim$ -1.8×10^{-4} K^{-1}, is very similar to the one obtained for x=0.40 and to the ones found for compositions without charge-order features. In the $148 < T \lesssim 400$ K temperature range the EFG principal component decreases with lowering T, as occurs in x=0.35 and x=0.40 compounds. Around the charge ordering temperature, $T_{CO} \sim 151$, K V_{zz} starts to sharply increase with decreasing temperature, displaying a discontinuous decrease at a lower temperature. The discontinuity is limited by $110.5 \leq T \leq 113.6$ K temperature window and the V_{zz} drops from 60.9 V/Å^2 to 57.6 (V/Å^2). Alike the x=0.35 compound, V_{zz} drops to a similar value as the one measured around the charge-order temperature, however, the variation in the V_{zz} does not exceed 7% as in the x=0.40 system. The EFG relative width, δ, of these spectra is visibly lower than in the former compounds, probably due to the lower chemical disorder. The increase of δ below the CO transition and its decrease below the discontinuity, although occurring, is not so evident in these data (see table 5.7).

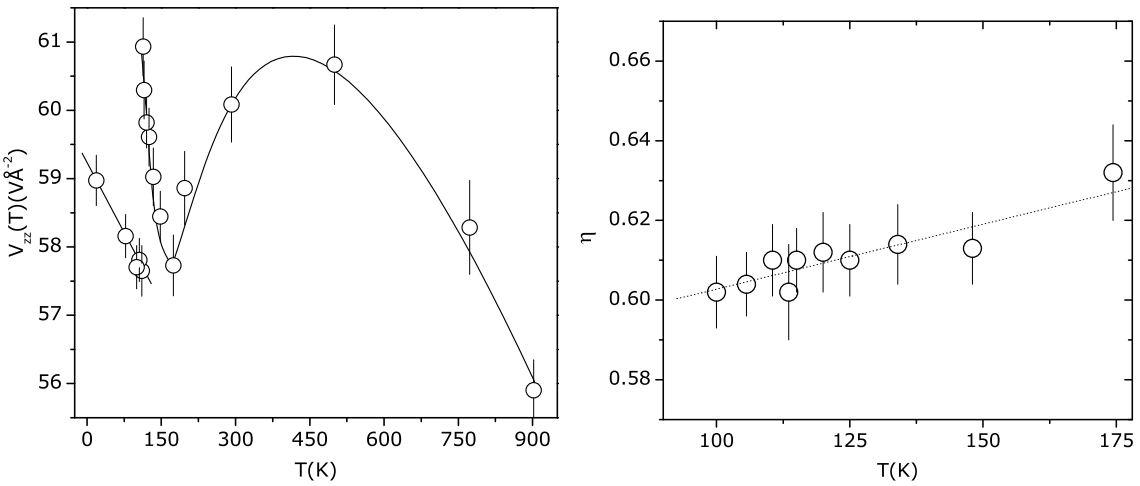

(a) (b)

Figure 5.19: EFG parameters, V_{zz} and η, as a function of temperature for the $Pr_{0.85}Ca_{0.15}MnO_3$ compound. Lines are guides for the eye.

For temperatures below the discontinuity, $T \leq 110.5$ K, V_{zz} again increases with the decreasing temperature reaching V_{zz} =59 V/Å^2 at T∼18.7 K. At these temperatures according to the literature the system presents a AF-CE-type magnetic structure [28, 243, 244]. Hence the low temperature fits were performed considering only a pure EFG interaction.

5.5 Discussion and conclusions

PAC spectroscopy via the ^{11m}Cd probe was used to characterize the $Pr_{1-x}Ca_xMnO_3$ local environment at the Pr/Ca site. To obtain local scale information on the different magnetic and electronic states along the $Pr_{1-x}Ca_xMnO_3$ phase diagram, in particular the nature of the charge ordered state, a hyperfine field systematic study was performed.

In the first section of this chapter we presented a macroscopic characterization of all samples under study and correlated our results with the ones available in the literature.

Our structural analysis revealed that compounds with composition within $0 \leq x \leq 0.3$, *i.e.*, large Pr^{3+} (Mn^{3+}) concentration, stabilize in a orthorhombic O'-type structure. With the increase of Ca (Mn^{4+}) concentration the O'-type structure becomes unstable and for $0.3 \leq x \leq 0.9$ the system stabilizes in a pseudo-tetragonal crystallographic structure. Further increasing Ca content a pseudo-cubic structure sets in for $0.9 \leq x \leq 1$. A linear decrease of the unit-cell volume with increasing Ca content is observed. These results were found to be in a good agreement with the ones available in literature for this system [24,236,237]. The different bond-length between the manganese ion and the six surrounding oxygens octahedra deduced from the measured lattice parameters indicate a reduction of the JT-distortion as the Ca concentration is increased. For x> 0.30 only tiny differences between those distances are observed. The Mn-O bond length calculated from our lattice parameters are also in good agrement with the ones obtained through neutron diffraction measurements [36,74,78]. Nevertheless a discrepancy is observed when these results are compared with the ones obtained by PDF analysis of neutron diffraction patterns by D. Louca *et al.* [202]. In the $Pr_{0.7}Ca_{0.3}MnO_3$ compound these authors obtained for the short and medium Mn-O bond lengths s=m$\sim$1.95Å and l$\sim$2.08Å for the large Mn-O bonds. In contrast our results show that these distances are nearly the same. Furthermore, accordingly to these same authors upon increasing/decreasing doping only a small dependence of the distortion strength should be observed. Indeed, it is well known that local distortions are present in manganites, not only for small concentrations of dopant element but also in metallic phases (*e.g.*, $La_{1-x}Ca_xMnO_3$) [13,17,238]. This result shows that the Mn-O bond length calculated from the unit cell parameters give us just an average value of the MnO_6 octahedra deformation. Consequentially is expected that the mean value of the deformation decreases with the incorporation of Ca, *i.e.*, creation of regular Mn^{4+}- O_6 octahedra. Nevertheless, this study reveals that the dependence of average octahedra deformation on Ca content is the expected one.

The study of the magnetic properties showed that samples with low Ca doping x$\leq$ 0.14 present an antiferromagnetic or spin-canted magnetic structure that sets in below 108 K in accordance with literature [24,28,240,241]. A second transition around T=52 K is observed for x=0.14 sample. This may be connected with a Mn spin reorientation due to onset of the magnetic order of the praseodymium ions. Neutron powder diffraction and bulk magnetization measurements as a function of temperature in single crystal of $Pr_{0.80}Ca_{0.20}MnO_3$ had

shown two ferromagnetic transitions near 140 and 70 K, which were ascribed to the ordering of Mn and Pr spins, respectively [247]. Moreover, other authors have shown that the magnetic order of the praseodymium ions can in fact induce a Mn spin reorientation. [74, 244] For the compositions x=0.25 a well defined transition from the paramagnetic to the ferromagnetic phase is present. The ferromagnetic order establishes for temperatures below $T_C \leq 118$ K, in conformity with the literature ($T_C \sim 120$ K) [9, 28, 240, 241]

Increasing the Ca concentration, for $0.32 \leq x < 0.95$, an antiferromagnetic-insulator phase establishes for temperatures typically below 170 K. Furthermore, in accordance with several works [24, 28, 240, 242], this phase coexists with a charge-ordered CO state with onset temperature T_{CO} ranging from T_{CO}=275 K, for x=0.60, and T_{CO}=151 K, for x =0.85. Additionally, in these compositions, ferromagnetic correlations are apparent for $T > T_{CO}$ whereas for $T < T_{CO}$ antiferromagnetic correlation are observed. In literature, samples within $0.30 < x \leq 0.40$ are referred, by some authors [67, 245], as presenting AFI/FMI phase coexistence. Other authors, however, did not found any evidence for such phase coexistence and discuss their results in terms of spin canting [28, 74]. In the samples studied in this work no obvious features of such AFI/FMI phase coexistence was observed. Further increasing the Ca concentration the charge-ordering feature disappears and well defined paramagnetic-antiferromagnetic transitions are observed in samples with x=0.95 and x=1. In literature this is quoted as occurring for x>0.90 and some authors reported the existence of a small amount of ferromagnetic phase in this phase diagram region [239]. These magnetization results are in good agreement with several works reported in the literature [28, 240], including those using neutron diffraction [24, 74, 237, 242, 243, 248].

This macroscopic characterization allowed to access to the structural and magnetic properties of this system, allowing the correlation of such macroscopic information with the local probe results obtained in the same samples.

We performed an electrical field gradient characterization in all the available ceramic samples of this system at room temperature. The principal component of the EFG, V_{zz}, decreases with increasing Ca content, *i.e.*, with the decrease of the orthorhombic distortion. Moreover we found that the CO region of the phase diagram delimits distinct regimes for the dependance of EFG parameters on Ca content. In particular, for samples without CO features V_{zz} and η decrease with the increase of Ca content (*i.e.*, with the decrease of orthorhombicity). For samples that belong to the region of the phase diagram where CO effects occur, at lower temperatures, we found that the EFG parameters depend strongly on Ca content. Although a decrease of V_{zz} with Ca content could be expected in terms of the trend of the lattice parameters the sharp decrease around x=0.32 is rather surprising. This shows that at the Cd probe atom, contributions to V_{zz} other than the lattice contribution become important. This is connected with the anomalous behavior of the V_{zz} parameters near the CO transition and will be further addressed later in this discussion.

In contrast to the V_{zz} trend , the EFG asymmetry parameter, η, was found to increase

with the Ca content. This behavior is the opposite to the expected one taking into account the dependence of lattice parameters on Ca content. Nevertheless a similar EFG asymmetry trend (also V_{zz}) was reported by Catchen *el al* [139] in the orthoferrite system ($AFeO_3$, A=La, Pr, Ho, Lu), *i.e.*, the more symmetric crystals showed a more asymmetric EFG. In fact, the near tetragonal compounds $LaFeO_3$ and $PrFeO_3$ have a much higher η than the highly orthorhombic distorted $LuFeO_3$ system. Following their argument, this hints that the EFG principal axes are not aligned with the crystallographic ones. In fact, point charge model calculations at the Ca site for $CaMnO_3$ confirm that only one of the principal directions is along one crystallographic axis (the c axis)[9]. The EFG distribution relative width relates primarily with cation chemical disorder peaking around x=0.50.

Low temperature measurements on the $Pr_{1-x}Ca_xMnO_3$ system end-members revealed the presence of a 1.2(3) T hyperfine magnetic field at 10 K in $PrMnO_3$ compound while no visible MHF is present in the $CaMnO_3$. Both systems are quoted in literature as having a pure antiferromagnetic arrangement of the Mn ions (A type for $PrMnO_3$ and G type for $CaMnO_3$) [23, 239], thus the MHF should vanish at the probe site. The MHF measured below 77 K (T_N=89 K) for $PrMnO_3$ may be associated to the onset of magnetic order of Pr moments. This ordering is refereed in literature [74] as being responsible for a small canting of both the Pr and Mn magnetic sub-lattices yielding a non vanishing magnetic field at the probe site. For samples with low Ca concentrations (x=0.05 and x=0.14) a small MHF (< 0.7 T) was detected at 77 K in accordance with the spin canted magnetic state [239] whereas for sample with x=0.95 no MHF was found although some reports claim the existence of a small percentage of ferromagnetic domains embedded in an antiferromagnetic matrix [69, 250]. Moreover, the available data for these compounds shows a small thermal dependence of the EFG principal component (increase with decreasing temperature). For these samples the V_{zz} vs T normalized slopes are all of the same order of magnitude averaging $\sim$-1.6$\times 10^{-4}$ K^{-1}. The volume thermal expansion in this system is one order of magnitude lower and cannot account for the V_{zz} temperature dependence (see figure 5.20(a)).

The thermal dependence of the EFG parameters in the ferromagnetic insulator $Pr_{0.75}Ca_{0.25}MnO_3$ shows also the expected behavior for perovskites systems, *i.e.*, an increase of V_{zz} with decreasing temperature $\left(\frac{1}{V_{zz}^0}\frac{\Delta V_{zz}}{\Delta T} \sim -1.2\times 10^{-4}\,K^{-1}\right)$ and an almost constant asymmetric $\eta \sim 0.45$. Furthermore, the relative width of the EFG distribution was found to be temperature independent. Below T_C the R(t) spectra clearly show the present of a magnetic hyperfine field. The obtained MHF (B_{hf}=4.4 T and B_{hf}=4.4 T for 77 and 11 K, respectively) is compatible with a fully ferromagnetic environment expected from the ferromagnetic spin arrangement.

[9] Using the lattice parameters and atomic positions from ref. [249] we found $\eta \sim$0.9 with principal directions [0, 0, 1],[0.78, 0.63, 0] and [0.63, -0.78, 0] for V_{xx}, V_{yy} and V_{zz}, respectively

Evidences for electric and magnetic order coexistence The so-called stripe and checkerboard phases have been identified in manganites [23, 25, 72, 251, 252] as well as other system (cuprates [253], cobaltites [254] , and ferrites [255]). These phases are characterized by long-range charge modulations which are believed to result from a strong electron-lattice coupling that localizes Mn valence charges in certain planes. These modulations have been described in terms of the idealized cations Mn^{3+} and Mn^{4+} despite the high Coulomb cost of complete charge disproportionation. However, several authors have previously cast doubt upon this interpretation and, as previously mentioned, considerable controversy remains on the nature of the charge ordered states in manganites. [35, 36, 232, 234, 235].

Our PAC study in $Pr_{1-x}Ca_xMnO_3$ for compositions within the CO phase diagram region, shows that only one major local environment is found above and below the CO temperature. Our results are difficult to reconcile with models where Mn^{3+}/Mn^{4+} charge disproportionation occurs for other ratios then the 1:1. Although models with 1:1 Mn^{3+}/Mn^{4+} CO states with charge stacking faults cannot be discarded directly from our results, recent TEM studies [232] brought evidence that charge disproportionation models should be re-interpreted in terms of a charge superlattice with uniform periodicity.

The study of the thermal dependence of the principal component of the EFG revealed a rich variety of behaviors. Samples outside the CO region of the $Pr_{1-x}Ca_xMnO_3$ phase diagram showed the expected increase of V_{zz} with decreasing temperature without any noticeable anomaly. In contrast, samples within the CO region (x=0.35, 0.40 and 0.85) present very unusual EFG principal component thermal dependence. The common increase of V_{zz} with decreasing temperature is only observed for T>T' (T'$\sim$300 K for x=0.40 and T'$\sim$400 K for x=0.85), a scale of temperatures much above the CO transition. Within this temperature range the V_{zz} vs T normalized slopes average $\sim$-1.8$\times10^{-4}$ K^{-1}, *i.e.*, same order of magnitude as samples outside the CO region (see figure 5.20(a)). Below that temperature and above T_{CO} a clear anomalous decrease of V_{zz} is found when decreasing temperature. This feature remains till the charge-order temperature is reached. Further decreasing temperature a sharp rise of V_{zz} occurs followed by a discontinuity at a temperature T^*. A subsequent increase of V_{zz} with decreasing temperature is observed for T<T^*. Moreover, contrarily to what is observed in the $Pr_{0.75}Ca_{0.25}MnO_3$ system the relative width of the EFG distributions in these compounds does not remain constant and a visible increase of δ below T_{CO} and subsequent decrease for temperatures lower than T^* is apparent. The asymmetry parameter remains practically constant in this temperature range. The lattice parameters thermal dependence [74, 243, 248, 256] cannot directly account for any of these anomalous dependencies.

We point out that, at room temperature, not only the value of V_{zz} depends on Ca content, as discussed above, but also its temperature derivative. Figure 5.20(b) show $\frac{1}{V_{zz}^0}\frac{\Delta V_{zz}}{\Delta T}$ at room temperature as a function of Ca content. We see that near x=0.32 the V_{zz} thermal slope

changes from a small negative value to a large positive one suggesting strong changes in the local properties of this system near this composition.

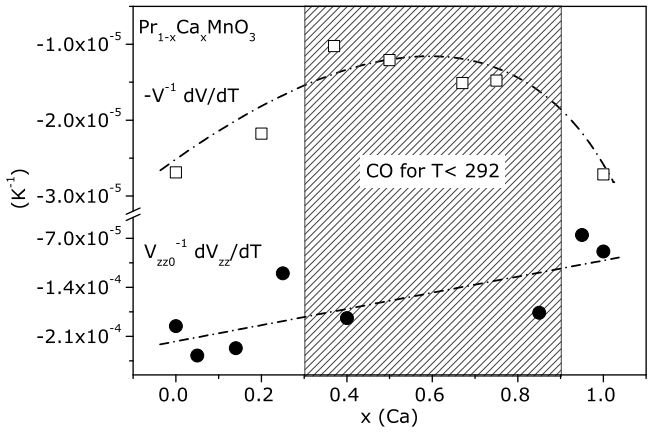

(a)

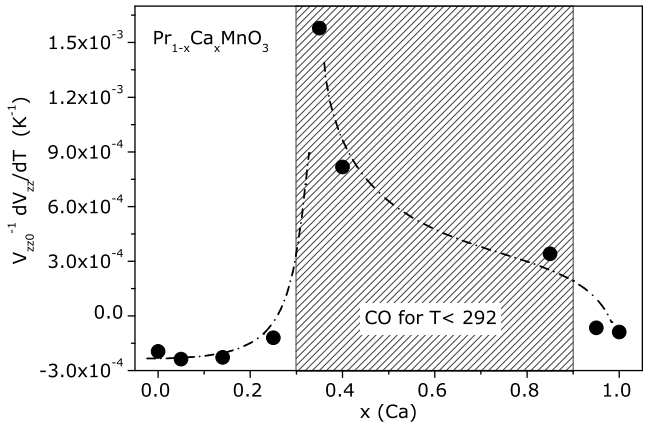

(b)

Figure 5.20: a) (•) $\frac{1}{V_{zz}^0}\frac{\Delta V_{zz}}{\Delta T}$ as a function of Ca content for the $Pr_{1-x}Ca_xMnO_3$ system: at T>T' for x=0.40 and x=0.85 and at room temperature for the other samples. (□) volume thermal expansion as a function of Ca content (data from [74, 78, 186, 187]). b) $\frac{1}{V_{zz}^0}\frac{\Delta V_{zz}}{\Delta T}$ at room temperature as a function of Ca content. Lines are guides for the eye.

Such positive dV_{zz}/dT are very unusual in perovskite systems. However, Catchen *et al.* [128] found a similar trend in YBCO high-T_c superconductors and attributed the rise of the magnitude of the EFG principal component with increasing temperature to anisotropic oxygen vibrational mode(s). The sensitivity of these mode(s) to temperature was claimed to indicate a softening of the O vibrations. In fact in a recent ultrasonic study of $Pr_{1-x}Ca_xMnO_3$ single crystal Hazama *et al.* [257] found evidence for several types of elastic softening above the CO phase transition, in the x=0.35, 0.40 and 0.50 compounds. In spite of this we are not aware of neutron diffraction refinements taking into account possible anisotropic lattice vibrations of oxygens and/or Mn ions which, according to our data should be a precursor

effect of the charge ordering phase transitions. Inelastic neutron scattering, Raman and Far-Infrared (FTIR) spectroscopies studies should also reveal signatures of phonon softening and the importance of lattice dynamics in the CO transition. In fact the softening and line broadening of some phonons modes, measured by those techniques, is discussed as a possible signature of charge-order stripes in High-Tc superconductors [258–260]. Nevertheless, we did not find any reference addressing directly this subject in long-range CO manganites.

Related with this issue one can speculate that in $Pr_{1-x}Ca_xMnO_3$ the possible softening of a mode mode towards the CO transition could result in a vibration instability near T_{CO}. If the charge ordering phase transition can be seen as a kind of soft-mode transition as usually encountered in perovskite ferroelectric compounds remains as an open question. However, the study of H. Hazama *et al.* [257] shows that the instability of certain charge fluctuations (Mn^{3+}:Mn^{4+} 1:1) gives rises to elastic softening already giving some firm steps in this direction. The elastic softening has been suggested to originate from the coupling of the orbital quadrupolar moment of the e_g orbital of Mn^{3+} ion to the elastic strain. In the same line of reasoning W. J. Lu *et al.* [261] and C. X. Chen *et al.* [262] reported a "remarkable softening of elastic modulus in the vicinity of T_{CO}" in manganite systems. Moreover, they argue "that the elastic softening is the soft mode and reflects the instability of the lattice to a strain of a given symmetry". The comparison of the EFG principal component with magnetization data obtained in the same samples allowed to correlate the CO temperature, T_{CO}, with the minimum observed in $V_{zz}(T)$ (see figures 5.5 and 5.23(b)).

Lowering temperature below T_{CO} a sharp rise of $V_{zz}(T)$ followed by a discontinuity is observed. An increase of V_{zz} with decreasing temperature is sometimes attributed to vibrational anharmonicity [128, 190, 263] which causes changes in lattice parameters with temperature. In fact the lattice parameters below charge ordering change significantly [74, 248,256] and a structural phase transition is mentioned by some authors, although the nature of the low symmetry phase is still a matter of debate, [36,231,256]. The sharp rise of $V_{zz}(T)$ near charge ordering, followed by a discontinuity has features proper of a phase transition. However, the referred structural changes alone cannot account for such rise in $V_{zz}(T)$ near and below T_{CO}, as these structural changes (*e.g.*, lattice parameter variation) occur in a much broader temperature range (100 K). Very few studies in $Pr_{1-x}Ca_xMnO_3$ show features near T_{CO} as sharp as those observed in the EFG principal component. In fact, discontinuities near, or at, the charge ordering transition were only observed in the elastic properties accessed by ultrasound measurements [257] and in the specific heat measurement [264]. Such prominent EFG features are only found in paraelectric to (anti)ferroelectric phase transitions. In fact, very similar thermal dependence of V_{zz} was observed in the paraelectric to anti-ferroelectric transition by Yeshuru *et al.* in $PbHfO_3$ [265]. This rises the question whether or not we are in the presence of a paraelectric-(anti)ferroelectric phase transition closely related with the charge ordering. In fact, the classical picture of charge-ordering, the so-called site centered model, with Mn^{3+} and Mn^{4+} chequer-board arrangements below T_{CO}, has been recently

questioned, since other types of structures were found to be more consistent with experimental neutron and x-ray diffraction data [36]. One of such alternative models is the so-called Zener polarons [36] (bond centered model), in which pairs of Mn^{3+} cations share a hole on a bridging O^- ion. These oxygen holes may form a soft charge-density wave [37, 40, 230, 232, 266].

In line with other experimental [34, 36, 232, 267] and computational [37, 230] work, Herrero-Martin *et al.* [268] have probed the local structure around the manganese ions in $Nd_{0.5}Sr_{0.5}MnO_3$ by using x-ray resonant scattering. They found two manganese sites, one of them is distorted as expected. However, intermediate-valence states according to a fractional charge segregation $Mn^{+3.42}$-$Mn^{+3.58}$ were deduced, evidencing that there is little charge and magnetic moment contrast in manganese ions on different sites.

More recently, Efremov *et al.* [234, 235] suggested that the Zenner polaron state may be favored in a certain part of the phase diagram of $Pr_{1-x}Ca_xMnO_3$. Moreover, they suggest that a net polarization would appear favoring a ferroelectric phase, closely connected with the magnetic order. Within such a scenario an anomaly on the dielectric constant at the charge-ordering state would be expected. Although initial reports of giant dielectric response near CO in $Pr_{1-x}Ca_xMnO_3$ system appeared in the year 1999 [269, 270] and the most recent one in 2004 [271], they cannot infer from these measurements the existence of electric dipoles and (anti)ferroelectricity, since other phenomena like the existence of charge density waves (CDW) or the presence of large interfaces due to phase segregation may bias the results [271]. Additionally, it was recently showed by N. Biskup [272] that extrinsic phenomena like electrode/sample interface can also give rise to similar anomalies in the dielectric constant shadowing the existence of the colossal dielectric constant materials.

Guided by the possible existence of electric dipoles and (anti)ferroelectricity in $Pr_{1-x}Ca_xMnO_3$ as claimed by Efremov *et al.* [234, 235] and by the similarity of our data with the results of the anti-ferroelectric transition in $PbHfO_3$ [265] we used the theoretical model developed by [273] to analyze our data.

Following closely the work of Yeshuru *et al.* [273] there exists a relationship between the dynamic properties of the lattice and the EFG fluctuation. If the ions shifts in such a way that the center of positive charges does not coincide with the center of negative charge an electric dipole develops in the unit cell. Being ζ the separation between the negative and positive charge centers, the size of the dipole, ζ, is proportional to the ionic charge displacements. Accordingly, the time dependance of ζ is expressed as

$$\zeta(t) = z_0 + \Delta z(t) \tag{5.1}$$

where z_0 is the average charge separation and $\Delta z(t)$ represents the time dependent fluctuations around z_0.

V_{zz} at the instant t can be expanded in powers of ζ:

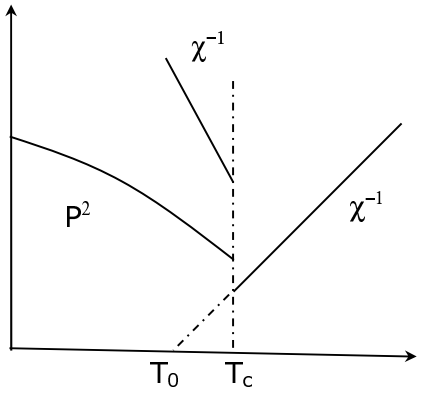

Figure 5.21: Thermal dependence scheme of the the quadratic polarization, P^2, and reciprocal susceptibility, χ^{-1}.

$$V_{zz} = V_{zz}^{eq} + \left(\frac{dV_{zz}}{d\zeta}\right)_0 \zeta + \left(\frac{d^2V_{zz}}{d\zeta^2}\right)_0 \zeta^2 + ... \tag{5.2}$$

Performing the time average, one finds that in the paraelectric phase, z_0=0,

$$\langle V_{zz}\rangle_t \approx V_{zz}^{eq} + const.\langle \Delta z^2\rangle_t \tag{5.3}$$

as the time average of $\Delta z(t)$ vanishes. Using the fluctuation-dissipation theorem [274], $\langle \Delta z^2\rangle_t \propto \chi\ T$, one can write

$$\langle V_{zz}\rangle_t \approx V_{zz}^{eq} + const.\chi\ T \tag{5.4}$$

where χ is the electric susceptibility.

Below T_C, on the other hand, $z_0 \neq 0$. Since z_0 is related with the dipole moment of the lattice (sublattice) and thus proportional to the local spontaneous polarization, one arises to

$$\langle V_{zz}\rangle \approx V_{zz}^{eq} + \alpha P^2 + \beta\chi\ T \tag{5.5}$$

where the average is performed both locally in time as well over the number of sites.

One sees in equation 5.5 that V_{zz} has a contribution from the static polar displacements of the ions being connected with a local polarization and a contribution from the fluctuations of the ions about their equilibrium positions, being connected with the local susceptibility. Interestingly, one sees that the electric susceptibility contributes to the electric field gradient which means that even in crystals with cubic symmetry a non vanishing EFG can be observed. Accordingly, we can attribute the sharp rise of the principal EFG component to such lattice fluctuations that contribute to the electric susceptibility.

In order to simply model and apply equation 5.5 to our data one can use the Landau

theory of phase transitions. Since our data suggests that a discontinuous phase transitions occurs one has to use a free energy power expansion up to sixth order.

$$F(T,P) = \frac{a}{2}(T-T_0)P^2 - \frac{b}{4}P^4 + \frac{c}{6}P^6 - PE \tag{5.6}$$

where P, the polarization, is order parameter and E the electric field. The numbers a, b and c have to be positive in order that a discontinuous phase transition occurs. T_0 is the temperature where the susceptibility would diverge. Minimizing the free energy with respect to the order parameter P one finds the state equation

$$a(T-T_0)P - bP^3 + cP^5 = E \tag{5.7}$$

The critical temperature where the order parameter changes discontinuously from P=0 to a finite value occurs at a temperature T_c given by

$$T_c = T_0 + \frac{3b}{16ac}^2 \tag{5.8}$$

To fit our V_{zz}(T) data one needs the expressions for the zero field susceptibility (E=0) and polarization above and below T_C. For the disordered phase, T>T_C, the polarization and susceptibility are given by

$$\begin{aligned} P^2 &= 0 \\ \chi^{-1}(T) &= a(T-T_c) + \tfrac{3b^2}{16c} \end{aligned} \tag{5.9}$$

whereas in the ordered phase, T<T_C, the polarization and susceptibility writes

$$\begin{aligned} P^2 &= \tfrac{b}{4c}\left[2 + \sqrt{1 + \tfrac{16ac}{b^2}(T_c - T)}\right] \\ \chi^{-1}(T) &= \tfrac{b^2}{4c}\left[\left(\sqrt{1 + \tfrac{16ac}{b^2}(T_c - T)} + 1\right)^2 - 1\right] \end{aligned} \tag{5.10}$$

A schematic representation of the thermal dependence of the polarization P and χ^{-1} is depicted in figure 5.21. One sees, lowering temperature, the decrease of the reciprocal susceptibility in the disordered phase (abrupt increase in the susceptibility approaching T_C from above) and a characteristic increase of slope below T_C, as well as the discontinuous appearance of a Polarization in the ordered phase. Moreover, one remarks that in such discontinuous phase transition the susceptibility does not diverge (the reciprocal susceptibility is always finite, $\chi^{-1}(T_C^+)=3b^2/16c$ and $\chi^{-1}(T_C^-)=3b^2/4c$).

Using the Yeshuru model and the Landau theory of discontinuous phase transitions one

can fit the principal component thermal dependence close and below T_{CO} for samples with x=0.35, 045 and 0.85. The simplified expressions used to fit the data were:

for the disordered phase, T>T_C

$$V_{zz}(T) = \beta \frac{T}{(T-T_C)+1/2m} + V_{zz}^{eq} \tag{5.11}$$

in the ordered phase, T<T_C

$$V_{zz}(T) = \frac{2}{3}\frac{(\Delta V_{zz}+\alpha)}{mT_C}\frac{T}{8(T_C-T)+2/m} + \alpha[1+m(T_C-T)] + V_{zz}^{eq} \tag{5.12}$$

where $m = 8ac/3b^2$, $\Delta V_{zz} = -\alpha + 4ac\beta T_C/b^2$ (discontinuity, ΔV_{zz}=$V_{zz}(T_C^+)$-$V_{zz}(T_C^-)$) and V_{zz}^{eq}[10] as defined in 5.2. Note that the proportionality constants between the EFG and the polarization/susceptibility, β and α, were redefined to have the same dimensions as V_{zz}.

Table 5.9 summarizes the fit results. The same table presents also the T_0 (temperature where the susceptibility would diverge) and $\alpha \times m$ (initial slope below T_C) values.

Table 5.9: V_{zz}(T) fit parameters for the compositions x=0.35, 0.40 and 0.85. The values of T_0 and $\alpha \times m$ are also presented.

sample	0.35	0.40	0.85
T_C(K)	206.3(2)	218.4(14)	111.7(15)
ΔV_{zz} ($V Å^{-2}$)	17(2)	4(3)	4(1)
β($V Å^{-2}$)	0.18(2)	0.20(6)	0.44 (11)
α($V Å^{-2}$)	0.036(8)	0.22(11)	0.43 (10)
m (K^{-1})	0.31(4)	0.09(2)	0.05(1)
V_{zz}^{eq}($V Å^{-2}$)	66.4(2)	62.7(3)	56.8(2)
$\alpha \times m$ ($V Å^{-2} K^{-1}$)	0.011(4)	0.020(14)	0.021(9)
T_0(K)	204.6(2)	213(2)	101(4)

The results of such fits are shown in figures 5.22(c), 5.22(d) and 5.23(b) together with the reciprocal magnetic susceptibility data for the same samples. As one can observe in those figures this simple model adjusts quite well to our data. There is also a close agrement between the features observed in magnetization and the EFG principal component, *i.e.*, one see that the minimum in the reciprocal magnetic susceptibility, usually used to identify the charge ordering transition, corresponds to a minimum in V_{zz}(T) and the discontinuity

[10] For the x=0.45 compound two slightly different V_{zz}^{eq}, at T_C^+ and T_C^-, had to be considered to perform a proper fit ($\Delta V_{zz}^{eq} \sim 1(V/Å^2)$). The value presented in table 5.9 is the average of those two values. Although this could justify, partially, the high uncertainty in the determination of the ΔV_{zz} value, accordingly to the β value (close to the one obtained for x=0.35) a very sharp increase of V_{zz}(T) occurs. This suggests that for this sample the discontinuity at T_C may be much higher than the one that we obtain with the available data.

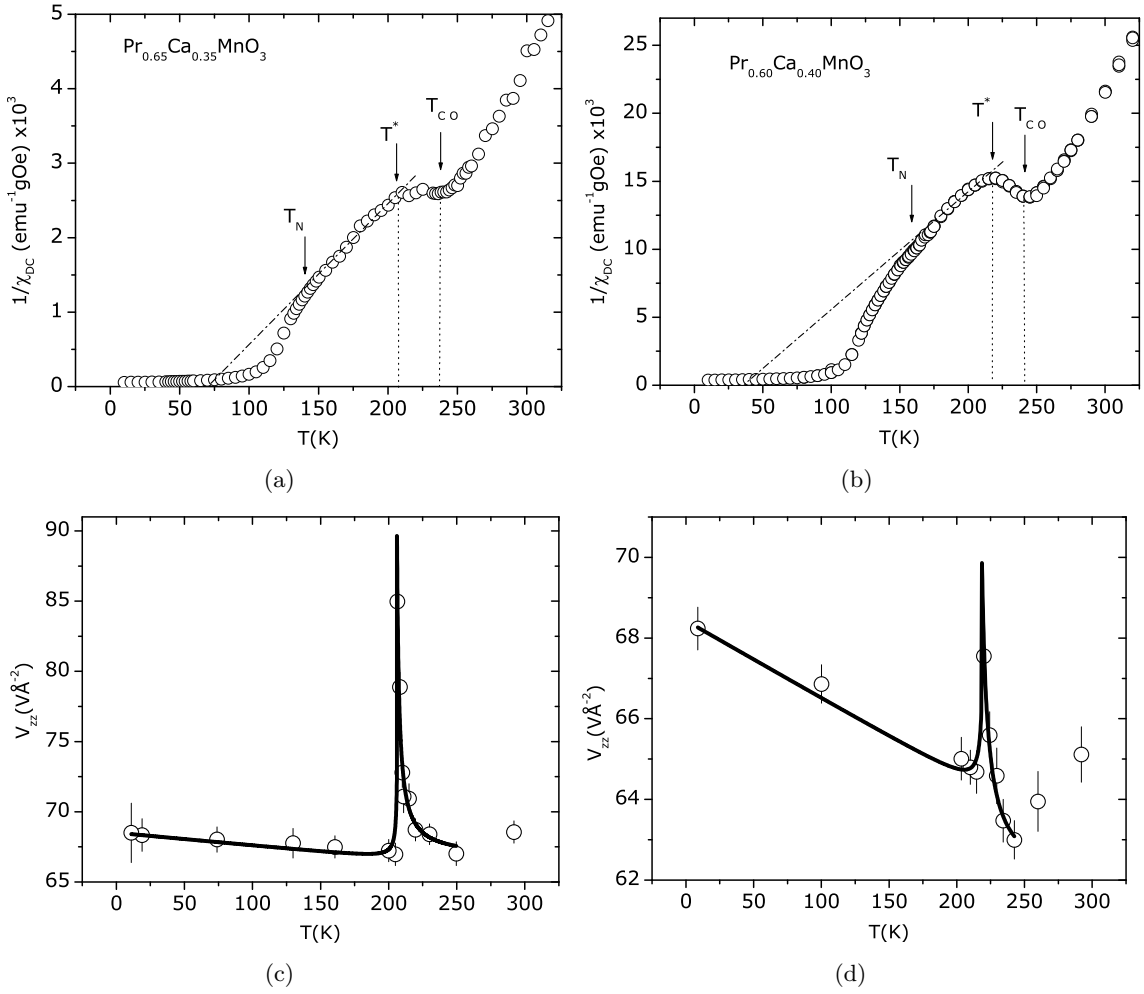

Figure 5.22: Bottom) V_{zz} vs temperature for the $Pr_{0.65}Ca_{0.35}MnO_3$ (c) and $Pr_{0.40}Ca_{0.60}MnO_3$ (d) compounds and correspondent fits using the model expressed by equations 5.11 and 5.12. a) and b) magnetic susceptibility for the same samples.

found at T_c is very close to the features in the magnetic $\chi^{-1}(T)$ where antiferromagnetic fluctuations appear (in the magnetic $\chi^{-1}(T)$ graphics the discontinuity in $V_{zz}(T)$ is signed by T^*).

This analysis shows that our results are compatible with a scenario where electric dipoles appear below T_{CO}. Diffraction results show, as referred above, that a change of the crystal symmetry occurs at T_{CO} [36,74,231,248] although there is not a general agreement in what is the low temperature structure. According to literature this lower symmetry phase can favor the appearance of a ferroelectric state [234, 235] and S. Mercone *et al.* [271] point out the possibility of an paraelectric antiferroelectric transition[11]. In fact, below T_{CO} we witness the

[11] According to S. Mercone *et al.* [271] an antiferroelectric phase can be obtained with two (or more) compensated dipoles in each unit cell providing no net polarization in the ordered phase.

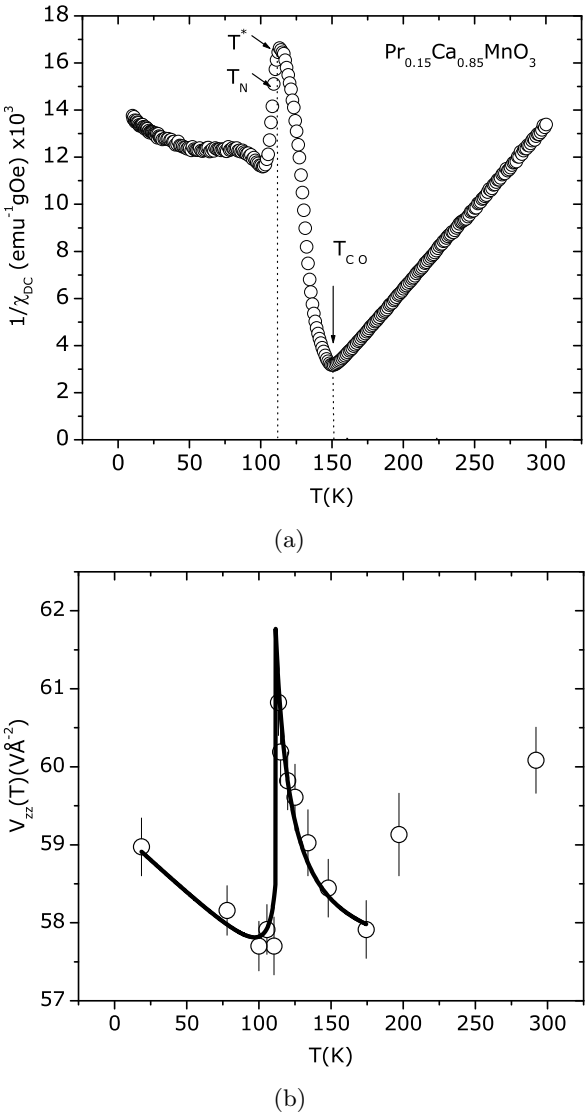

Figure 5.23: a) Magnetic susceptibility for the $Pr_{0.15}Ca_{0.85}MnO_3$ compound. b) V_{zz} vs temperature for the same sample and correspondent fit using the model expressed by equation 5.11 and 5.12.

sharp rise of V_{zz} which we attribute mainly to critical fluctuations that contribute greatly to the local electric susceptibility. At T^* we find a discontinuity that one can assign to a paraelectric/(anti)ferroelectric transition. Also, as referred above, close to T^* the antiferromagnetic fluctuations start, thus a close connection should exist between (anti)ferroelectricity and magnetism in these compounds as predicted in the theoretical work of [234, 235]. Below T^* the data is also fairly fitted by this simple model with an increase of V_{zz} connected with the increase of the local electric polarization.

Our results thus provide strong evidence for dielectric phase transitions occurring in

the in CO region of the $Pr_{1-x}Ca_xMnO_3$ phase diagram. In literature of ferroelectrics two major types of (anti)ferroelectric phase transitions are described: the displacive type (or soft mode) and the order disorder type. Also, these two types of transitions can occur simultaneously as discussed recently by B. Zalar *et al.* [275, 276] in the $BaTiO_3$ and $SrTiO_3$ perovskite compounds. Usually, the effects of a displacive phase transition is associated with static EFG whereas the order disorder phenomena with time dependent interactions [194]. Since time dependent interactions can contribute to strongly attenuate the PAC spectra (and indeed we observed a increase of the attenuation parameter below T_{CO} with a considerable decrease below T^*) one can speculate that the phase transition occurring at T^*, can be of the order-disorder type. In fact B. Zalar *et al.* and G. L. Catchen *et al.* [194, 275, 276] associate the characteristic line-width broadening close the dielectric phase transitions in perovskite systems to the order-disorder phenomena.

In summary, PAC spectroscopy via the ^{111m}Cd probe was used to study the $Pr_{1-x}Ca_xMnO_3$ near the charge/orbital order transition. Strong anomalies of EFG close to the CO/OO transition allowed to distinguish from the Wigner crystal site centered CO, Zener polaron bond centered CO and incipient (anti)ferroelelectric scenarios. Our results hint for (anti)ferroelectric behavior as suggested by D. Efremov *et al.* [235] occurring at a temperature T^* slightly below T_{CO}. Additionally our analysis suggest that the charge-ordering transition is driven by lattice softening. The new state below T_{CO} seems to favor the existence of dipole electric moments. Our data does not allow to conclude about the ferroelectric or antiferroelectric nature of the observed dielectric phase transition though one can conclude for its first-order nature with order-disorder signatures.

Conclusions and perspectives

To give a broader view of the main achievements of this work we briefly review the conclusions, which were already punctually presented in the two last chapters, in a more general perspective. We finalize with some suggestions for further research.

This thesis combines different techniques and methods to achieve new insight on the local distortions and electronic correlations in CMR Manganites. In this way, this work includes synthesis and structural, magnetic and electric characterization in order obtain detailed knowledge on the macroscopic properties of the studied CMR systems. This information stands as a starting point to engage on a local scale study of several manganites compounds ranging from the low doped large bandwidth $LaMnO_{3+\Delta}$ to the small bandwidth $Pr_{1-x}Ca_xMnO_3$.

To obtain such local scale information we have used the perturbed angular correlation spectroscopy via the ^{111}Cd probe state to measure the electrical field gradient and magnetic hyperfine field at the perovskite A(La/Pr/Ca) site.

The room temperature PAC study of $LaMnO_{3+\Delta}$ system reveled very distinct EFG parameters in the orthorhombic and rhombohedric samples thus providing clear signatures of the different local probe environments associated to the different degree of octahedra distortions present in each type of samples.

The PAC study of the stoichiometric $LaMnO_3$ as a function of temperature in the 11-320 K temperature range, revealed, unexpectedly, the presence of two local environments which the relative amount vary significantly with temperature, stabilizing critically around 50%-50% for temperatures below the magnetic transition. These data suggest the existence of new local phenomena probably related with a perturbation of the orbital order leading to a phase separated state with very subtle differences only noticeable by their different EFGs. Very recent theoretical studies by W. G. Yin *et al.* [277] point to the competition of electron-electron and electron-lattice interactions in the $LaMnO_3$ as giving origin to orbital mixing. We speculate that our data in $LaMnO_3$ could be a quantification of such orbital mixing. Further studies are definitely necessary in order to clarify this assumption, in particular EFG calculations within this model.

A important issue studied in this work is the microscopic nature of polaronic distortions, their temperature evolution and the role of polarons in ferromagnetic insulator manganites

(FMI). Having this in mind we have studied in detail the $LaMnO_{3.12}$ compound since it is a prototypical FMI manganite that undergoes a rhombohedral (R) / orthorhombic (O) structural transition around room temperature, which provides us with an ideal scenario to probe the evolution of local lattice distortions through different average lattice symmetries. PAC measurements clearly revealed a continuous transition between two different local atomic environments (one JT–distorted (d) and another undistorted (u)). The macroscopic R/O structural transition, studied by x-ray powder diffraction, arises as a consequence of these microscopic changes, since it occurs between the percolation thresholds of the two local components. Remarkably, within the rhombohedral crystallographic phase, where the octahedra are constrained to be undistorted, uncorrelated polarons clusters with a fully distorted $Mn^{3+}O_6$ octahedra survive up to 776 K. These distortions are as strong as in the orbital ordered end-member $LaMnO_3$ compound. Our results show that the temperature scale (T*), suggested by E. Dagotto [22], below which single polarons start to cluster is higher than 776 K, a surprisingly high temperature. The correlation of these clusters, formed above T*, increases for temperatures below the distorted phase percolation threshold diverging at critical temperature close to ferromagnetic transition. At this temperature distortions relax and are accommodated in a weak JT–distorted phase. Furthermore we found evidence for an ultra-slow charge dynamics responsible for the overall insulator behavior in this system, which, below the magnetic phase transition can viewed as composed by a ferromagnetic metallic minority phase within a ferromagnetic insulator matrix. Some of these conclusions are in the same line of thinking to those recently presented by X. Qui *et al.* [228] in the study by pair distribution function (PDF) analysis of neutron diffraction patterns of stoichiometric $LaMnO_3$ through its R/O structural transition.

The nature of local distortions in the small bandwidth $Pr_{1-x}Ca_xMnO_3$ compounds were also accessed by means of PAC spectroscopy, with special emphasis within the region of the phase diagram where the charge/orbital ordered state occurs. In this small bandwidth system no evidence for phase separation was found and, in all samples, a unique local environment was always observed.

The evolution of the EFG principal component at room temperature revealed a strong decrease with increasing Ca content within the CO region of the phase diagram. This anomalous behavior is further evidenced by the EFG temperature slope above room temperature. Whereas samples outside the CO region exhibit the normal negative slope the others show deviant positive ones. These positive slopes are attributed to anomalous lattice dynamics effects and related with phonon softening. From our results the charge ordering can be viewed as soft mode transition resulting from strong electron-lattice interaction.

Indeed our study of several samples exhibiting charge ordering showed that in all samples this decrease of V_{zz} with decreasing temperature halts precisely at T_{CO}. Below this temperature charge localization seems to favor the appearance of electric dipoles. Our results indeed show a sharp increase of the EFG principle component below T_{CO}, compatible with

existence of an electric susceptibility, followed by a discontinuous decrease associated with the onset of (anti)ferroelectric order. These effects were absent in all studied compounds where CO does not occur. This phase transition is satisfactory modeled by Landau theory of discontinuous phase transitions.

Such strong anomalies of the EFG principal component allowed to contribute to a recent debate around the nature of the CO state. According to literature three scenarios are in conflict, the Wigner crystal site centered CO, the Zener polaron bond centered CO and the recently theoretically predicted intermediate scenario [235], which combines the first two, and shows a type of charge ordering that breaks inversion symmetry and is therefore predicted to be ferroelectric. Our results stand as one of the first experimental data strongly supporting this latter scenario.

The fact that other macroscopic and microscopic techniques failed to see this effect can be related to the nanoscopic nature of such (anti)ferroelectric regions and the high amount of charge carriers. In such nanoscopic regions the applicability of the Landau theory of phase transitions, which relies in a thermodynamic approach, can be justified by the recent results of Scott *et al.* [278] who showed that for ferroelectric structures with typical sizes above 2.4 nm display essentially bulk ferroelectric properties.

The question then arises on how the electric and magnetic degrees of freedom correlate. From our results it is also clear that the temperature where the paraelectric /ferroelectric transition occurs is nearly the same as the temperature where the antiferromagnetic correlations starts. This hints for the close connection between the magnetic (antiferromagnetism) and electric (ferroelectric) order, as predicted by D. Efremov *et al.* [235]

As a final remark one can return to the work of E. Dagotto [22] that lists the important challenges and open questions concerning manganite systems, which we reproduced in the introduction of this thesis. We believe that this work contributed to give additional insight on the raised issues, attesting also the ability of Perturbed Angular Correlation Technique to access on very subtle local scale phenomena that play a crucial roles in the physics of manganites.

perspectives This thesis also provides a basis for future work which we shortly put on perspective in the following:

It would be interesting to extend our study in ferromagnetic insulator samples to other large and intermediate bandwidth series like $La_{1-x}Sr_xMnO_3$ and $La_{1-x}Ca_xMnO_3$ systems including the ferromagnetic metallic compositions, aiming specifically to further characterize polaron clusters, associated phase coexistence and cluster stability at very high temperatures. Moreover the range of temperatures close to the microscopic phase transition observed in the $LaMnO_{3+\Delta}$ should be further investigated as well as the relation of this transition with the

magnetic one. The confirmation that this microscopic phase transition has a general nature in the manganites should be established.

It is of great importance to continue the study in the charge/orbital order states and broaden this work to other small and intermediate bandwidth manganite systems. Furthermore high temperature measurements on the transition from the normal to the deviant lattice dynamics and the influence of doping in the para/(anti)ferroelectric phase transition are extremely necessary to provide an overall picture of this phenomena.

Besides those studies, one can foreseen new promising research topics that includes:

Static and/or dynamic mechanisms associated with the large $^{18}O/^{16}O$ isotopic effect including different magnetic and electric behaviors and metal-insulator transition in manganites system and also the $^{18}O/^{16}$ O isotopic effect that converts the quantum paraelectric $SrTiO_3$ into a ferroelectric system.

Perovskite A-site order/disorder as a new mechanism for CMR effects. EFG PAC parameters are expected to reveal the static and/or dynamic aspects associated with metal or insulator behavior according to the degree of disorder, as in the $Nd_{0.5}Ba_{0.5}MnO_3$ system.

Ferroelectro-magnets displaying simultaneous electric and magnetic order (*e.g.*, $YMnO_3$ and $BiMnO_3$). PAC studies should provide new insight in the static and/or dynamic aspects associated with the magnetoelectric coupling. Preliminary PAC studies were already performed in these materials with very promising results.

Bibliography

[1] G. H. Jonker and J. H. van Santen, "Ferromagnetic compounds of manganese with perovskite structure", *Physica*, vol. 16, pp. 337–349, March 1950.

[2] J. H. van Santen and G. H. Jonker, "Electrical conductivity of ferromagnetic compounds of manganese with perovskite structure", *Physica*, vol. 16, pp. 599–600, July 1950.

[3] G. H. Jonker and J. H. van Santen, "Magnetic compounds with perovskite structure: Ferromagnetic compounds of cobalt", *Physica*, vol. 19, pp. 120–130, January 1953.

[4] C. Zener, "Interaction between the d-Shells in the Transition Metals. II. Ferromagnetic Compounds of Manganese with Perovskite Structure", *Physical Review*, vol. 82, no. 3, pp. 403–405, May 1951.

[5] P. W. Anderson and H. Hasegawa, "Considerations on Double Exchange", *Physical Review*, vol. 100, no. 2, pp. 675–681, October 1955.

[6] J. B. Goodenough, "Theory of the Role of Covalence in the Perovskite-Type Manganites [La, M(II)]MnO_3", *Physical Review*, vol. 100, no. 2, pp. 564–573, October 1955.

[7] K.-I. Chahara, T. Ohno, M. Kasai, and Y. Kozono, "Magnetoresistance in magnetic manganese oxide with intrinsic antiferromagnetic spin structure", *Applied Physics Letters*, vol. 63, pp. 1990–1992, October 1993.

[8] R. von Helmolt, J. Wecker, B. Holzapfel, L. Schultz, and K. Samwer, "Giant negative magnetoresistance in perovskite like $La_{2/3}Ba_{1/3}MnO_x$ ferromagnetic films", *Physical Review Letters*, vol. 71, no. 14, pp. 2331–2333, October 1993.

[9] C. Martin, A. Maignan, M. Hervieu, and B. Raveau, "Magnetic phase diagrams of $L_{1-x}A_xMnO_3$ manganites ($L = Pr, Sm; A = Ca, Sr$)", *Physical Review B*, vol. 60, no. 17, pp. 12191–12199, November 1999.

[10] J. C. Loudon, N. D. Mathur, and P. A. Midgley, "Charge-ordered ferromagnetic phase in $La_{0.5}Ca_{0.5}MnO_3$", *Nature*, vol. 420, pp. 797–800, December 2002.

[11] A. J. Millis, P. B. Littlewood, and B. I. Shraiman, "Double Exchange Alone Does Not Explain the Resistivity of $La_{1-x}Sr_xMnO_3$", *Physical Review Letters*, vol. 74, no. 25, pp. 5144–5147, June 1995.

[12] A. J. Millis, "Cooperative Jahn-Teller effect and electron-phonon coupling in $La_{1-x}A_xMnO_3$", *Physical Review B*, vol. 53, no. 13, pp. 8434–8441, April 1996.

[13] S. J. L. Billinge, R. G. DiFrancesco, G. H. Kwei, J. J. Neumeier, and J. D. Thompson, "Direct Observation of Lattice Polaron Formation in the Local Structure of $La_{1-x}Ca_xMnO_3$", *Physical Review Letters*, vol. 77, no. 4, pp. 715–718, July 1996.

[14] C. H. Booth, F. Bridges, G. H. Kwei, J. M. Lawrence, A. L. Cornelius, and J. J. Neumeier, "Direct Relationship between Magnetism and MnO_6 Distortions in $La_{1-x}Ca_xMnO_3$", *Physical Review Letters*, vol. 80, no. 4, pp. 853–856, January 1998.

[15] C. H. Booth, F. Bridges, G. H. Kwei, J. M. Lawrence, A. L. Cornelius, and J. J. Neumeier, "Lattice effects in $La_{1-x}Ca_xMnO_3\,(x = 0 \rightarrow 1)$: Relationships between distortions, charge distribution, and magnetism", *Physical Review B*, vol. 57, no. 17, pp. 10440–10454, May 1998.

[16] G.-M. Zhao, K. Conder, H. Keller, and K. A. Müller, "Giant oxygen isotope shift in the magnetoresistive perovskite $La_{1-x}Ca_xMnO_{3+y}$", *Nature*, vol. 381, pp. 676–678, June 1996.

[17] D. Louca, T. Egami, E. L. Brosha, H. Röder, and A. R. Bishop, "Local Jahn-Teller distortion in $La_{1-x}Sr_xMnO_3$ observed by pulsed neutron diffraction", *Physical Review B*, vol. 56, no. 14, pp. R8475–R8478, October 1997.

[18] P. Dai, J. Zhang, H. A. Mook, S. H. Liou, P. A. Dowben, and E. W. Plummer, "Experimental evidence for the dynamic Jahn-Teller effect in $La_{0.65}Ca_{0.35}MnO_3$", *Physical Review B*, vol. 54, no. 6, pp. R3694–R3697, August 1996.

[19] J. M. de Teresa, M. R. Ibarra, P. A Algarabel, C. Ritter, C. J. Marquina, J. Blasco, J. García, A. del Moral, and Z. Arnold, "Evidence for magnetic polarons in the magnetoresistive perovskites", *Nature*, vol. 386, pp. 256–259, 1997.

[20] G. Allodi, M. Cestelli Guidi, R. De Renzi, A. Caneiro, and L. Pinsard, "Ultraslow Polaron Dynamics in Low-Doped Manganites from ^{139}La NMR-NQR and Muon Spin Rotation", *Physical Review Letters*, vol. 87, no. 12, pp. 127206, August 2001.

[21] E. Dagotto, S. L. Cooper, G. Alvarez, and A. L. Cornelius, *Nanoscale phase separation and colossal magnetoresistance*, Springer-Verlag, Amesterdam, 2003.

[22] E. Dagotto, "Open questions in CMR manganites, relevance of clustered states and analogies with other compounds including the cuprates", *New Journal of Physics*, vol. 7, pp. 67, February 2005.

[23] E. O. Wollan and W. C. Koehler, "Neutron Diffraction Study of the Magnetic Properties of the Series of Perovskite-Type Compounds $[(1-x)La, xCa]MnO_3$", *Physical Review*, vol. 100, no. 2, pp. 545–563, October 1955.

[24] Z. Jirák, S. Krupička, Z. Šimša, M. Dlouhá, and S. Vratislav, "Neutron diffraction study of $Pr_{1-x}Ca_xMnO_3$ perovskites", *Journal of Magnetism and Magnetic Materials*, vol. 53, pp. 153–166, November 1985.

[25] C. H. Chen and S.-W. Cheong, "Commensurate to Incommensurate Charge Ordering and Its Real-Space Images in $La_{0.5}Ca_{0.5}MnO_3$", *Physical Review Letters*, vol. 76, no. 21, pp. 4042–4045, May 1996.

[26] P. G. Radaelli, D. E. Cox, M. Marezio, and S.-W. Cheong, "Charge, orbital, and magnetic ordering in $La_{0.5}Ca_{0.5}MnO_3$", *Physical Review B*, vol. 55, no. 5, pp. 3015–3023, February 1997.

[27] Y. Tomioka, A. Asamitsu, Y. Moritomo, H. Kuwahara, and Y. Tokura, "Collapse of a Charge-Ordered State under a Magnetic Field in $Pr_{1/2}Sr_{1/2}MnO_3$", *Physical Review Letters*, vol. 74, no. 25, pp. 5108–5111, June 1995.

[28] Y. Tomioka, A. Asamitsu, H. Kuwahara, Y. Moritomo, and Y. Tokura, "Magnetic-field-induced metal-insulator phenomena in $Pr_{1-x}Ca_xMnO_3$ with controlled charge-ordering instability", *Physical Review B*, vol. 53, no. 4, pp. R1689–R1692, January 1996.

[29] Y. Moritomo, H. Kuwahara, Y. Tomioka, and Y. Tokura, "Pressure effects on charge-ordering transitions in Perovskite manganites ", *Physical Review B*, vol. 55, no. 12, pp. 7549–7556, March 1997.

[30] I. Isaac and J. P. Franck, "Oxygen-isotope effect on the charge-ordering transition of $La_{1-x}Ca_xMnO_3$ ", *Physical Review B*, vol. 57, no. 10, pp. R5602–R5605, March 1998.

[31] G.-M. Zhao, K. Ghosh, H. Keller, and R. L. Greene, "Very strong magnetic-field dependence of the oxygen isotope shift of the charge-ordering transition in $La_{0.5}Ca_{0.5}MnO_3$", *Physical Review B*, vol. 59, no. 1, pp. 81–84, January 1999.

[32] K. Miyano, T. Tanaka, Y. Tomioka, and Y. Tokura, "Photoinduced Insulator-to-Metal Transition in a Perovskite Manganite", *Physical Review Letters*, vol. 78, no. 22, pp. 4257–4260, June 1997.

[33] V. Kiryukhin, D. Casa, J. P. Hill, A. Keimer, A. Vigliante, Y. Tomioka, and Y. Tokura, "An X-ray-induced insulator-metal transition in a magnetoresistive manganite", *Nature*, vol. 386, pp. 813–815, April 1997.

[34] J. García, M. Concepción Sánchez, J. Blasco, G. Subías, and M. Grazia Proietti, "Analysis of the x-ray resonant scattering at the Mn K edge in half-doped mixed valence manganites", *Journal of Physics Condensed Matter*, vol. 13, pp. 3243–3256, April 2001.

[35] J. Rodríguez-Carvajal, A. Daoud-Aladine, L. Pinsard-Gaudart, M. T. Fernández-Díaz, and A. Revcolevschi, "A new interpretation of the CO state in half-doped manganites: new results from neutron diffraction and synchrotron radiation experiments", *Physica B: Condensed Matter*, vol. 320, pp. 1–6, July 2002.

[36] A. Daoud-Aladine, J. Rodríguez-Carvajal, L. Pinsard-Gaudart, M. T. Fernández-Díaz, and A. Revcolevschi, "Zener Polaron Ordering in Half-Doped Manganites", *Physical Review Letters*, vol. 89, no. 9, pp. 097205, August 2002.

[37] V. Ferrari, M. Towler, and P. B. Littlewood, "Oxygen Stripes in $La_{0.5}Ca_{0.5}MnO_3$ from Ab Initio Calculations", *Physical Review Letters*, vol. 91, no. 22, pp. 227202, November 2003.

[38] K. J. Thomas, J. P. Hill, S. Grenier, Y.-J. Kim, P. Abbamonte, L. Venema, A. Rusydi, Y. Tomioka, Y. Tokura, D. F. McMorrow, G. Sawatzky, and M. van Veenendaal, "Soft X-Ray Resonant Diffraction Study of Magnetic and Orbital Correlations in a Manganite Near Half Doping", *Physical Review Letters*, vol. 92, no. 23, pp. 237204, June 2004.

[39] C. de Graaf, C. Sousa, and R. Broer, "Ab initio study of the charge order and Zener polaron formation in half-doped manganites", *Physical Review B*, vol. 70, no. 23, pp. 235104, December 2004.

[40] M. Coey, "Charge-ordering in oxides", *Nature*, vol. 430, pp. 155–157, July 2004.

[41] V. M. Goldshmitt, *Geochemistry*, Oxford university Press, Oxford, 1958.

[42] J. A. M. van Roosmalen, P. van Vlaaderen, E. H. P. Cordfunke, W. L. Ijdo, and D. J. W Ijdo, "Phases in the perovskite-type $LaMnO_{3+\delta}$ solid solution and the La_2O_3-Mn_2O_3 phase-diagram", *Journal of Solid State Chemistry*, vol. 114, pp. 516–523, February 1995.

[43] M. S. Reis, *Não-Extensividade Magnética em Manganitas*, PhD thesis, Centro Brasileiro de Pesquisas Físicas, Rio de Janeiro, Brasil, September 2003.

[44] Y. Tokura, *Colossal magnetoresistance oxides*, Gordon and Breach Science Publishers, London, 2000.

[45] E. Dagotto, T. Hotta, and A. Moreo, "Colossal magnetoresistant materials: the key role of phase separation", *Physics Reports*, vol. 344, pp. 1–3, April 2001.

[46] S. Satpathy, Z. S. Popović, and F. R. Vukajlović, "Electronic Structure of the Perovskite Oxides: $La_{1-x}Ca_xMnO_3$", *Physical Review Letters*, vol. 76, no. 6, pp. 960–963, February 1996.

[47] A. K. Bogush, V. I. Pavlov , and L. V. Balyko, "Structural phase-transitions in the $LaMnO_{3+\lambda}$ system", *Crystal Research and Technology*, vol. 18, pp. 589–598, May 1983.

[48] T. Holstein, "Studies of polaron motion : Part II. The "small" polaron", *Annals of Physics*, vol. 8, pp. 343–389, November 1959.

[49] H. Y. Hwang, S.-W. Cheong, P. G. Radaelli, M. Marezio, and B. Batlogg, "Lattice effects on the magnetoresistance in doped LaMnO_3", *Physical Review Letters*, vol. 75, no. 5, pp. 914–917, July 1995.

[50] J. Volger, "Further experimental investigations on some ferromagnetic oxidic compounds of manganese with perovskite structure", *Physica*, vol. 20, pp. 49–66, January 1954.

[51] K. Kubo, "Quantum-theory of double exchange", *Journal of the Physical Society of Japan*, vol. 33, pp. 21–32, January 1972.

[52] J. P. Araújo, *Local probe and bulk property studies on highly correlated electron systems: high-T_c Superconductors an CMR magnetic oxides*, PhD thesis, Universidade do Porto, Portugal, January 2002.

[53] M. Fath, S. Freisem, A. A. Menovsky, Y. Tomioka, J. Aarts, and J. A. Mydosh, "Spatially inhomogeneous metal-insulator transition in doped manganites", *Science*, vol. 285, pp. 1540–1542, September 1999.

[54] J. Tao and J. M. Zuo, "Nanoscale phase competition during charge ordering in intrinsically strained $La_{0.33}Ca_{0.67}MnO_3$", *Physical Review B*, vol. 69, no. 18, pp. 180404, May 2004.

[55] D. D. Sarma, D. Topwal, U. Manju, S. R. Krishnakumar, M. Bertolo, S. La Rosa, G. Cautero, T. Y. Koo, P. A. Sharma, S.-W. Cheong, and A. Fujimori, "Direct Observation of Large Electronic Domains with Memory Effect in Doped Manganites", *Physical Review Letters*, vol. 93, no. 9, pp. 097202, August 2004.

[56] M. Uehara, S. Mori, C. H. Chen, and S.-W. Cheong, "Percolative phase separation underlies colossal magnetoresistance in mixed-valent manganites", *Nature*, vol. 399, pp. 560, June 1999.

[57] J. X. Ma, D. T. Gillaspie, E. W. Plummer, and J. Shen, "Visualization of Localized Holes in Manganite Thin Films with Atomic Resolution", *Physical Review Letters*, vol. 95, no. 23, pp. 237210, December 2005.

[58] P. Dai, J. A. Fernandez-Baca, N. Wakabayashi, E. W. Plummer, Y. Tomioka, and Y. Tokura, "Short-Range Polaron Correlations in the Ferromagnetic $La_{1-x}Ca_xMnO_3$", *Physical Review Letters*, vol. 85, no. 12, pp. 2553–2556, September 2000.

[59] V. Kiryukhin, T. Y. Koo, H. Ishibashi, J. P. Hill, and S.-W. Cheong, "Average lattice symmetry and nanoscale structural correlations in magnetoresistive manganites", *Physical Review B*, vol. 67, no. 6, pp. 064421, February 2003.

[60] V. Kiryukhin, A. Borissov, J. S. Ahn, Q. Huang, J. W. Lynn, and S.-W. Cheong, "Uncorrelated and correlated nanoscale lattice distortions in the paramagnetic phase of magnetoresistive manganites", *Physical Review B*, vol. 70, no. 21, pp. 214424, December 2004.

[61] N. Mannella, A. Rosenhahn, C. H. Booth, S. Marchesini, B. S. Mun, S.-H. Yang, K. Ibrahim, Y. Tomioka, and C. S. Fadley, "Direct Observation of High-Temperature Polaronic Behavior in Colossal Magnetoresistive Manganites", *Physical Review Letters*, vol. 92, no. 16, pp. 166401, April 2004.

[62] J. Deisenhofer, D. Braak, H.-A. Krug von Nidda, J. Hemberger, R. M. Eremina, V. A. Ivanshin, A. M. Balbashov, G. Jug, A. Loidl, T. Kimura, and Y. Tokura, "Observation of a Griffiths Phase in Paramagnetic $La_{1-x}Sr_xMnO_3$", *Physical Review Letters*, vol. 95, no. 25, pp. 257202, December 2005.

[63] G. Allodi, R. De Renzi, and G. Guidi, "^{139}La NMR in lanthanum manganites: Indication of the presence of magnetic polarons from spectra and nuclear relaxations", *Physical Review B*, vol. 57, no. 2, pp. 1024–1034, January 1998.

[64] G. Allodi, R. De Renzi, F. Licci, and M. W. Pieper, "First Order Nucleation of Charge Ordered Domains in $La_{0.5}Ca_{0.5}MnO_3$ Detected by ^{139}La and ^{55}Mn NMR", *Physical Review Letters*, vol. 81, no. 21, pp. 4736–4739, November 1998.

[65] M. M. Savosta, V. I. Kamenev, V. A. Borodin, P. Novák, M. Maryško, J. Hejtmanek, K. Dorr, and M. Sahana, "Ferromagnetic insulating state in manganites: ^{55}Mn Mn NMR study", *Physical Review B*, vol. 67, no. 9, pp. 094403, 2003.

[66] J. M. De Teresa, M. R. Ibarra, J. Blasco, J. García, C. Marquina, P. A. Algarabel, Z. Arnold, K. Kamenev, C. Ritter, and R. von Helmolt, "Spontaneous behavior and magnetic field and pressure effects on $La_{2/3}Ca_{1/3}MnO_3$ perovskite", *Physical Review B*, vol. 54, no. 2, pp. 1187–1193, July 1996.

[67] V. Hardy, A. Wahl, C. Martin, and Ch. Simon, "Low-temperature specific heat in $Pr_{0.63}Ca_{0.37}MnO_3$: Phase separation and metamagnetic transition", *Physical Review B*, vol. 63, no. 22, pp. 224403, May 2001.

[68] C. Frontera, J. L. García-Muñoz, A. Llobet, M. Respaud, J. M. Broto, J. S. Lord, and A. Planes, "Phase coexistence, magnetic inhomogeneity, and disorder in the charge-ordered state of $Pr_{2/3}Ca_{1/3}MnO_3$ ", *Physical Review B*, vol. 62, no. 5, pp. 3381–3388, August 2000.

[69] M. S. Reis, V. S. Amaral, J. P. Araújo, P. B. Tavares, A. M. Gomes, and I. S. Oliveira, "Magnetic entropy change of $Pr_{1-x}Ca_xMnO_3$ manganites ($0.2 \leq x \leq 0.95$)", *Physical Review B*, vol. 71, no. 14, pp. 144413, April 2005.

[70] Ch. Simon, S. Mercone, N. Guiblin, C. Martin, A. Brûlet, and G. André, "Microphase Separation in $Pr_{0.67}Ca_{0.33}MnO_3$ by Small-Angle Neutron Scattering", *Physical Review Letters*, vol. 89, no. 20, pp. 207202, October 2002.

[71] M. Viret, F. Ott, J. P. Renard, H. Glattli, L. Pinsard-Gaudart, and A. Revcolevschi, "Magnetic Filaments in Resistive Manganites", *Physical Review Letters*, vol. 93, no. 21, pp. 217402, 2004.

[72] S. Mori, C. H. Chen, and S.-W. Cheong, "Pairing of charge-ordered stripes in $(La, Ca)MnO_3$", *Nature*, vol. 392, pp. 473–476, April 1998.

[73] Y. Yamada, O. Hino, S. Nohdo, R. Kanao, T. Inami, and S. Katano, "Polaron Ordering in Low-Doping $La_{1-x}Sr_xMnO_3$", *Physical Review Letters*, vol. 77, no. 5, pp. 904–907, July 1996.

[74] N. Guiblin, *Synthese, structures et mises e ordre electroniques d'oxydes a valence mixte dans le systeme Pr-Ca-Mn-O*, PhD thesis, Universite de Caen, Basse-Normandie, France, January 2004.

[75] S. W. Cheong and H. Y. Huang, "Ferromagnetism vs. charge/orbital ordering in mixed-valent manganites", *In Colossal magnetoresistance oxides, Y. Tokura, Gordon and Breach Science Publishers, London*, pp. 237–280, 2000.

[76] J. Rodríguez-Carvajal, M. Hennion, F. Moussa, A. H. Moudden, L. Pinsard, and A. Revcolevschi, "Neutron-diffraction study of the Jahn-Teller transition in stoichiometric $LaMnO_3$", *Physical Review B*, vol. 57, no. 6, pp. R3189–R3192, February 1998.

[77] Y. Murakami, J. P. Hill, D. Gibbs, M. Blume, I. Koyama, M. Tanaka, H. Kawata, T. Arima, Y. Tokura, K. Hirota, and Y. Endoh, "Resonant X-Ray Scattering from Orbital Ordering in $LaMnO_3$", *Physical Review Letters*, vol. 81, no. 3, pp. 582–585, July 1998.

[78] D. Sánchez, J. A. Alonso, and M. J. Martínez-Lope, "Neutron-diffraction study of the Jahn-Teller transition in $PrMnO_3$", *Journal of the Chemical Society-Dalton Transactions*, vol. 23, pp. 4422–4425, November 2002.

[79] L. M. Rodríguez-Martínez and J. P. Attfield, "Cation disorder and size effects in magnetoresistive manganese oxide perovskites", *Physical Review B*, vol. 54, no. 22, pp. R15622–R15625, December 1996.

[80] L. M. Rodríguez-Martínez and J. P. Attfield, "Cation disorder and the metal-insulator transition temperature in manganese oxide perovskites", *Physical Review B*, vol. 58, no. 5, pp. 2426–2429, August 1998.

[81] J. A. M. van Roosmalen, E. H. P. Cordfunke, R. B. Helmholdt, and H. W. Zandbergen, "The Defect Chemistry of $LaMnO_{3\pm\delta}$. 2. Structural Aspects of $LaMnO_{3+\delta}$", *Journal of Solid State Chemistry*, vol. 110, pp. 100–105, May 1994.

[82] M. Tovar, G. Alejandro, A. Butera, A. Caneiro, M. T. Causa, F. Prado, and R. D. Sánchez, "ESR and magnetization in Jahn-Teller-distorted $LaMnO_{3+\delta}$: Correlation with crystal structure", *Physical Review B*, vol. 60, no. 14, pp. 10199–10205, October 1999.

[83] F. Prado, R. D. Sánchez, A. Caneiro, M. T. Causa, and M. Tovar, "Discontinuous Evolution of the Highly Distorted Orthorhombic Structure and the Magnetic Order in $LaMnO_{3+\delta}$ Perovskite", *Journal of Solid State Chemistry*, vol. 146, pp. 418–427, September 1999.

[84] J. Topfer and J. B. Goodenough, "$LaMnO_{3+\delta}$ revisited", *Journal of Solid State Chemistry*, vol. 130, pp. 117–128, April 1997.

[85] C. Ritter, M. R. Ibarra, J. M. de Teresa, P. A. Algarabel, C. Marquina, J. Blasco, J. García, S. Oseroff, and S.-W. Cheong, "Influence of oxygen content on the structural, magnetotransport, and magnetic properties of $LaMnO_{3+\delta}$", *Physical Review B*, vol. 56, pp. 8902–8911, October 1997.

[86] A. P. Ramirez, "Colossal magnetoresistance", *Journal of Physics Condensed Matter*, vol. 9, pp. 8171–8199, September 1997.

[87] Y. Tokura and Y. Tomioka, "Colossal magnetoresistive manganites", *Journal of Magnetism and Magnetic Materials*, vol. 200, pp. 1–3, October 1999.

[88] J. Goodenough, "Colossal magnetoresistance in $Ln_{1-x}A_xMnO_3$ perovskites", *Australian Journal of Physics*, vol. 52, pp. 155–186, January 1999.

[89] C. N. R. Rao, A. Arulraj, A. K. Cheetham, and B. Raveau, "Charge ordering in the rare earth manganates: the experimental situation", *Journal of Physics Condensed Matter*, vol. 12, pp. 83, February 2000.

[90] J. M. D. Coey, M. Viret, and S. von Molnár, "Mixed-valence manganites", *Advances in Physics*, vol. 48, pp. 167–293, March 1999.

[91] M. B. Salamon and M. Jaime, "The physics of manganites: Structure and transport", *Reviews Moderdn Physics*, vol. 73, no. 3, pp. 583–628, August 2001.

[92] Y. Tokura, "Critical features of colossal magnetoresistive manganites", *Reports on Progress in Physics*, vol. 69, pp. 797–851, March 2006.

[93] Y. Tokura and Y. Tomioka, "Samples prepared by solid state reaction at Joint Research Center for Atom Technology, Tsukuba, and Departement of Applied Physics, University of Tokio, Japan".

[94] P. B. Tavares and M. S. Reis, "Samples prepared by solid state reaction at Universidade de Trás-os-montes e Alto-Douro (UTAD), Vila Real, Portugal".

[95] R. Suryanarayanan, "Samples prepared by solid state reaction at Laboratoire de Physico-Chemie et de l'etat solide, Universite Paris-Sud, Orsay France".

[96] C. Vázquez-Vázquez, M. C. Blanco, M. López-Quintela, R. D. Sánchez, J. Rivas, and S. B. Oseroff, "Characterization of $La_{0.67}Ca_{0.33}MnO_{3\pm\delta}$ particles prepared by the sol-gel route", *Journal of Materials Chemistry*, vol. 8, pp. 991–1000, April 1998.

[97] L. E. Hueso, J. Rivas, F. Rivadulla, and M. A. López-Quintela, "Tuning of colossal magnetoresistance via grain size change in $La_{0.67}Ca_{0.33}MnO_3$", *Journal of Applied Physics*, vol. 86, pp. 3881–3884, October 1999.

[98] A. M. L. Lopes, J. P. Araújo, A. M. Gomes, T. M. Mendonça, P. B. Tavares, J. G. Correia, and V. S. Amaral, "Cd-doped $LaMnO_3$ manganites prepared by the sol-gel technique", *Materials Science Forum*, pp. 289–293, February 2006.

[99] J. P. Araújo, A. M. L. Lopes, T. M. Mendonça, E. Rita, J. G. Correia, and V. S. Amaral, "Electrical Field Gradient Studies on $La_{1-x}Cd_xMnO_{3+\delta}$", *Hyperfine Interactions*, vol. 158, pp. 347–351, September 2004.

[100] A. M. L. Lopes, J. P. Araújo, A. M. Gomes, M. S. Reis, V. S. Amaral, and P. B. Tavares, "Cadmium doping at Mn site in $Pr_{0.5}Ca_{0.5}MnO_3$", *Journal of Magnetism and Magnetic Materials*, vol. 272, pp. 1767–1768, May 2004.

[101] M. T. Weller, *Inorganic Materials chemistry*, Oxford Uiversity Press, Oxford, 1994.

[102] M. R. T. Soares, *A Transição Morfotrópica dos Cerâmicos PZT*, PhD thesis, Universidade de Aveiro, Portugal, February 2001.

[103] B. G Almeida, *Filmes finos e multicamadas metálicas magnéticas*, PhD thesis, Universidade do Porto, Portugal, December 1997.

[104] "Detailed information concerning the experimental setup is available online in http://www.fei.com".

[105] J. A. M. Santos, *Magnetismo e fenómenos de transporte com comportamento não-convencional*, PhD thesis, Universidade do Porto, Portugal, January 2006.

[106] "Detailed information concerning the experimental setup is available online in http://www.qdusa.com".

[107] J. A. S. Mendes, *Materiais amorfos, nanocristalinos e filmes de grão orientado-Técnicas de preparação, caracterização e estudo de propriedades físicas*, PhD thesis, Universidade do Porto, Portugal, November 2000.

[108] M. M. P. Azevedo, *Propriedades Magnéticas e de Transporte de Filmes Granulares e Multicamadas*, PhD thesis, Universidade do Porto, Portugal, November 1998.

[109] E. Kugler, D. Fiander, B. Johnson, H. Haas, A. Przewloka, H. L. Ravn, D. J. Simon, and K. Zimmer, "The new CERN-ISOLDE on-line mass-separator facility at the PS-Booster", *Nuclear Instruments and Methods in Physics Research B*, vol. 70, pp. 41–49, August 1992.

[110] J. F. Ziegler, J. P. Biersack, and U. Littmark, *The stopping and range of ions in solids*, Pregamon, New-York, 1985.

[111] P. Raghavan, "", *Atomic Data and Nuclear Data Tables*, vol. 42, pp. 189, 1989.

[112] A. C. Junqueira, A. W. Carbonari, R. N. Saxena, and J. Mestnik-Filho, "Study of the local magnetic environment in $LaMnO_3$ perovskite by measuring hyperfine interactions", *Journal of Magnetism and Magnetic Materials*, vol. 272, pp. E1639–E1641, May 2004.

[113] A. M. L. Lopes, J. P. Araújo, E. Rita, J. G. Correia, V. S. Amaral, Y. Tomioka, Y. Tokura, and R. Suryanarayanan, "Perturbed angular correlation study of $Pr_{1-x}Ca_xMnO_3$", *Journal of Magnetism and Magnetic Materials*, vol. 272, pp. E1667–E1668, May 2004.

[114] T. Butz, S. Saibene, T. Fraenzke, and M. Weber, "A TDPAC-camera", *Nuclear Instruments and Methods in Physics Research A*, vol. 284, pp. 417–421, December 1989.

[115] D. J. Jackson, *Classic Electrodynamics*, John Wiley and Sons, New-York, 1975.

[116] G. Schatz and A. Weidinger, *Nuclear Condensed Matter Physics*, John Wiley and Sons, England, 1996.

[117] R. P. Feynman, R. B. Leighton, and M. Sands, *The Feynman Lectures on Physics, Vol. II*, Addison-Wesley Publishing Company, Massachusets, 1964.

[118] C. Cohen-Tannoudji, B. Diu, and F. LaLoë, *Quantum Mechanics*, John Wiley and Sons, New-York, 1977.

[119] L. Hemmingsen, K.Ñ. Sas, and E. Danielsen, "Biological applications of perturbed angular correlations of gamma-ray spectroscopy", *Chemical reviews*, vol. 104, pp. 4027–4061, September 2004.

[120] G. V. Hevesy, "Some applications of isotopic indicators", *Nobel Lecture Available at* $http://nobelprize.org/nobel\_prizes/chemistry/laureates/1943/hevesy-lecture.pdf$.

[121] J. Gróh and G. V. Hevesy, "Die Selbstdiffusionsgeschwindigkeit des geschmolzenen Bleis", *Annalen der Physik*, vol. 368, no. 17, pp. 85–92, 1920.

[122] J. Gróh and G. V. Hevesy, "Die Selbstdiffusion in festem Blei", *Annalen der Physik*, vol. 370, no. 11, pp. 216–222, 1921.

[123] D. R. Hamilton, "On Directional Correlation of Successive Quanta", *Physical Review*, vol. 58, no. 2, pp. 122–131, July 1940.

[124] E. L. Brady and M. Deutsch, "Angular Correlation of Successive Gamma-Ray Quanta", *Physical Review*, vol. 72, no. 9, pp. 870–871, November 1947.

[125] G. Goertzel, "Angular Correlation of Gamma-Rays", *Physical Review*, vol. 70, no. 11-12, pp. 897–909, December 1946.

[126] A. Abragam and R. V. Pound, "Influence of Electric and Magnetic Fields on Angular Correlations", *Physical Review*, vol. 92, no. 4, pp. 943–962, November 1953.

[127] P. Lehmann and J. Miller, "Interaction quadrupolaire dans Cd-111", *Comptes Rendus Hebdomadaires des Seances de L' Academie des Sciences*, vol. 240, no. 3, pp. 298–299, 1955.

[128] G. L. Catchen, M. Blaszkiewicz, A. J. Baratta, and W. Huebner, "Anomalous temperature dependence of the electric field gradient at the Y site in $In_{0.1}Y_{0.9}Ba_2Cu_3O_{9-\delta}$: Evidence for soft vibrational modes", *Physical Review B*, vol. 38, no. 4, pp. 2824–2827, August 1988.

[129] J. G. Correia, J. P. Araújo, S. M. Loureiro, P. Toulemonde, S. Le Floch, P. Bordet, J. J. Capponi, R. Gatt, W. Tröger, B. Ctortecka, T. Butz, H. Haas, J. G. Marques, and J. C. Soares, "Local O_δ probing in the high-T_c superconductor $HgBa_2CuO_{4+\delta}$ ", *Physical Review B*, vol. 61, no. 17, pp. 11769–11775, May 2000.

[130] A. V. Tsvyashchenko, L. N. Fomicheva, A. A. Sorokin, G. K. Ryasny, B. A. Komissarova, L. G. Shpinkova, K. V. Klementiev, A. V. Kuznetsov, A. P. Menushenkov, V. N. Trofimov, A. E. Primenko, and R. Cortes, "High-pressure phase of $CeRu_2$: A magnetic superconductor with two charge states of Ru ions", *Physical Review B*, vol. 65, no. 17, pp. 174513, April 2002.

[131] K. Lorenz and R. Vianden, "Anomalous Temperature Dependence of the EFG in AlN Measured with the PAC-Probes ^{181}Hf and ^{111}In", *Hyperfine Interactions*, vol. 158, pp. 273–279, September 2004.

[132] V. Ostheimer, S. Lany, J. Hamann, H. Wolf, Th. Wichert, and ISOLDE Collaboration, "Defect interactions of group-I elements in cubic II-VI compounds", *Physical Review B*, vol. 68, no. 23, pp. 235206, December 2003.

[133] H. Hohler, N. Atodiresei, K. Schroeder, R. Zeller, and P. H. Dederichs, "Cd-vacancy and Cd-interstitial complexes in Si and Ge", *Physical Review B*, vol. 70, no. 15, pp. 155313, October 2004.

[134] M. O. Zacate and G. S. Collins, "Temperature- and composition-driven changes in site occupation of indium solutes in $Gd_{1+3x}Al_{2-3x}$", *Physical Review B*, vol. 69, no. 17, pp. 174202, May 2004.

[135] A. W. Carbonari, J. Mestnik-Filho, R. N. Saxena, and M. V. Lalic, "Magnetic hyperfine interaction in $CeMn_2Ge_2$ and $CeMn_2Si_2$ measured by perturbed angular correlation spectroscopy", *Physical Review B*, vol. 69, no. 14, pp. 144425, April 2004.

[136] M. Dietrich, C. Buchal, J. G. Correia, M. Deicher, M. Schmid, M. Uhrmacher, U. Vetter, and U. Wahl, "Annealing of $BaTiO_3$ thin films after heavy ion implantation", *Nuclear Instruments and Methods in Physics Research B*, vol. 216, pp. 110–115, February 2004.

[137] G. Fabricius and A. López García, "First-principles study of the orthorhombic $CdTiO_3$ perovskite", *Physical Review B*, vol. 66, no. 23, pp. 233106, December 2002.

[138] R. Dogra, A. C. Junqueira, R. N. Saxena, A. W. Carbonari, J. Mestnik-Filho, and M. Moralles, "Hyperfine interaction measurements in $LaCrO_3$ and $LaFeO_3$ perovskites using perturbed angular correlation spectroscopy", *Physical Review B*, vol. 63, no. 22, pp. 224104, May 2001.

[139] T. M. Rearick, G. L. Catchen, and J. M. Adams, "Combined magnetic-dipole and electric-quadrupole hyperfine interactions in rare-earth orthoferrite ceramics", *Physical Review B*, vol. 48, no. 1, pp. 224–238, July 1993.

[140] G. L. Catchen, J. M. Adams, and T. M. Rearick, "High-temperature partitioning of ^{181}probe impurities between Li and group-V sites in $LiNbO_3$ and $LiTaO_3$", *Physical Review B*, vol. 46, no. 5, pp. 2743–2749, August 1992.

[141] Robert L. Rasera and G. L. Catchen, "Mn-site hyperfine fields in $LaMnO_3$ and $NdMnO_3$ measured using perturbed-angular-correlation spectroscopy", *Physical Review B*, vol. 58, no. 6, pp. 3218–3222, August 1998.

[142] G. L. Catchen, W. E. Evenson, and D. Allred, "Structural phase transition and T_c distribution in Hf-doped $LaMnO_3$ investigated using perturbed-angular-correlation spectroscopy", *Physical Review B*, vol. 54, no. 6, pp. R3679–R3682, August 1996.

[143] R. Govindaraj, C. S. Sundar, L. S. Lakshmi, V. Sridharan, M. Premila, and D. V. Natarajan, "Perturbed-angular-correlation studies in hafnium doped $La_{0.67}Ca_{0.33}MnO_3$", *Chemical Physics*, vol. 302, pp. 185–192, July 2004.

[144] R. Govindaraj and C. S. Sundar, "Linear relationship between magnetic hyperfine field and electric-field gradient at Mn sites in lanthanum strontium manganite", *Physical Review B*, vol. 70, no. 22, pp. 220405, December 2004.

[145] N. Barradas, *Sistemas Magnéticos Baseado em Cobalto*, PhD thesis, Universidade de Lisboa, Portugal, 1994.

[146] J. G. Correia, "Estudo da dependência do gradiente de campo eléctrico com a temperatura no sistema ^{181}TaBe", Master's thesis, February 1990.

[147] J. G. Correia, *Aplicações da técnica de correlações angulares perturbadas e−γ no isolde-CERN*, PhD thesis, Universidade de Lisboa, Portugal, February 1993.

[148] J. G. Marques, *Interacções Hiperfinas em monocristais de cobalto e niobato de litio usando ^{111}Cd, ^{181}Ta, ^{197}Hg e ^{199}Hg. Desenvolvimento experimental e determinação precisa de constantes de interacção*, PhD thesis, Universidade de Lisboa, Portugal, 1996.

[149] T. Butz, "Analytic perturbation functions for static interactions in perturbed angular-correlations of gamma-rays", *Hyperfine Interactions*, vol. 52, pp. 189–228, 1989.

[150] H. Frauenfelder and R. M. Stefen, *Alpha-beta- and Gamma-ray spectroscopy, Chapter XIX* , Eds. K. Siegbahn, 1965.

[151] E. Matthias E. Karlsson and K. Siegbahn, Eds., *Perturbed Angular Correlations*, North Holland-Publishing Company, Amesterdam, 1964.

[152] Th. Wichert and E. Recknagel, "Microscopic methods in metals", *Topics in Current Physics*, vol. 40, pp. 1, 1986.

[153] R. S. Hager and E. C. Seltzer, "Internal Conversion Tables: -Part II- Directional and Polarization. Particle Parameters for Z=30 to Z=103", *Nuclear Data Tables*, vol. 4, pp. 397–641, 1968.

[154] A. J. Ferguson, *Angular Correlation Methods in Gamma-Ray Spectroscopy*, North-Holland Publishing Co. and Amsterdam, 1965.

[155] D. Lupascu, M. Neubauer, S. Habenicht, T. Wenzel, M. Uhrmacher, and K. P. Lieb, "PAC-Studies of dynamic hyperfine interactions in oxides", in *Condensated Matter Studies by Nuclear Methods, Proceedings of the XXX Zakopane School of Physics*, Krzysztof Tomala and E. A. Görlich, Eds., Poland, 1995, pp. 196–213.

[156] A. R. Arends, C. Hohenemser, F. Pleiter, H. de Waard, L. Chow, and R. M. Suter, "Data reduction methodology for perturbed angular correlation experiments", *Hyperfine Interactions*, vol. 8, pp. 191–213, 1980.

[157] N. P. Barradas, M. Rots, A. A. Melo, and J. C. Soares, "Magnetic anisotropy and temperature dependence of the hyperfine fields of ^{111}Cd in single-crystalline cobalt", *Physical Review B*, vol. 47, no. 14, pp. 8763–8768, April 1993.

[158] M. Forker, "The problematic of the derivation of the electric field gradient asymmetry parameter from TDPAC measurements or Mössbauer spectroscopy in imperfect crystal lattices", *Nuclear Instruments and Methods*, vol. 106, pp. 121–126, 1973.

[159] M. Blume, "Stochastic Theory of Line Shape: Generalization of the Kubo-Anderson Model", *Physical Review*, vol. 174, no. 2, pp. 351–358, October 1968.

[160] H. Winkler and E. Gerdau, "Gamma-gamma-angular correlations perturbed by stochastic fluctuating fields", *Zeitschrift fur Physik*, vol. 262, pp. 363–376, 1973.

[161] A. Baudry and P. Boyer, "Approximation of the blume stochastic-model by asymptotic models for pac relaxation analysis ", *Hyperfine Interactions*, vol. 35, pp. 803–806, 1987.

[162] W. E. Evenson, A. G. Mckale, H. T. Su, and J. A. Gardner, "PAC perturbation factor for spin 5/2 nuclei subject to a rapidly fluctuating EFG", *Hyperfine Interactions*, vol. 61, pp. 1379–1382, August 1990.

[163] Doru Lupascu, Sonke Habenicht, Klaus-Peter Lieb, Matthias Neubauer, M. Uhrmacher, and Thorsten Wenzel, "Relaxation of electronic defects in pure and doped La_2O_3 observed by perturbed angular correlations", *Physical Review B*, vol. 54, no. 2, pp. 871–883, July 1996.

[164] M. Forker, W. Herz, and D. Simon, "Approximation of the theory of stochastic perturbations of angular correlations for fluctuating distributions of electric quadrupole interactions", *Nuclear Instruments and Methods in Physics Research A*, vol. 337, pp. 534–543, January 1994.

[165] M. Deicher, "Dynamics of defects in semiconductors", *Hyperfine Interactions*, vol. 79, pp. 681–700, 1993.

[166] Norbert Achtziger and Wolfgang Witthuhn, "Perturbed-angular-correlation spectroscopy of the fluctuating hyperfine interaction at Cd-donor pairs in silicon: An approach to electronic transitions at impurities in semiconductors", *Physical Review B*, vol. 47, no. 12, pp. 6990–7004, March 1993.

[167] A. G. Marshall and C. F. Meares, "Effect of slow rotational diffusion on angular correlations ", *Journal of Chemical Physics*, vol. 56, pp. 1226–1229, February 1972.

[168] S. M. Van Eek and M. Forker, "Perturbed angular correlation study of static and dynamic hyperfine interactions at ^{181}Ta in the Laves-phase hydrides $ErFe_2H_x$ ", *Physical Review B*, vol. 65, no. 17, pp. 174307, May 2002.

[169] M. Gebhard, B. Vogt, and W. Witthuhn, "Direct evidence for localized motion of hydrogen in Cd-H complexes in silicon", *Physical Review Letters*, vol. 67, no. 7, pp. 847–850, August 1991.

[170] R. Vianden and U. Feuser, "Dynamics of an Indium Impurity in the Relaxed Divacancy in Iridium", *Physical Review Letters*, vol. 61, no. 17, pp. 1981–1984, October 1988.

[171] R. P. Gupta and S. K. Sen, "Sternheimer Shielding-Antishielding. II", *Physical Review A*, vol. 8, no. 3, pp. 1169–1172, September 1973.

[172] P. C. Schmidt, K. D. Sen, T. P. Das, and Alarich Weiss, "Effect of self-consistency and crystalline potential in the solid state on nuclear quadrupole Sternheimer antishielding factors in closed-shell ions", *Physical Review B*, vol. 22, no. 9, pp. 4167–4179, November 1980.

[173] F. D. Feiock and W. R. Johnson, "Atomic Susceptibilities and Shielding Factors", *Physical Review*, vol. 187, no. 1, pp. 39–50, November 1969.

[174] Elton N. Kaufmann and Reiner J. Vianden, "The electric field gradient in noncubic metals", *Review Modern Physics*, vol. 51, no. 1, pp. 161–214, January 1979.

[175] A. C. Beri, T. Lee, T. P Das, and R. M Sternheimer, "Theory of nuclear-quadrupole interactions in ionic iron-group compounds - role of antishielding effects", *Hyperfine Interactions*, vol. 4, no. 1-2, pp. 509–514, January 1978.

[176] P. Raghavan, E. N. Kaufmann, R. S. Raghavan, E. J. Ansaldo, and R. A. Naumann, "Sign and magnitude of the quadrupole interaction of ^{111}Cd in noncubic metals: Universal correlation of ionic and electronic field gradients", *Physical Review B*, vol. 13, no. 7, pp. 2835–2847, April 1976.

[177] D. Wiarda, M. Uhrmacher, A. Bartos, and K. P. Lieb, "Electric field gradients at ^{111}Cd in binary oxides ", *Journal of Physics Condensed Matter*, vol. 5, pp. 4111–4124, June 1993.

[178] P. Blaha, K. Schwarz, P. Sorantin, and S. B. Trickey, "Full-potential, linearized augmented plane wave programs for crystalline systems", *Computer Physics Communications*, vol. 59, pp. 399–415, June 1990.

[179] P. Blaha, P. Dufek, K. Schwarz, and H. Haas, "Calculation of electric hyperfine interaction parameters in solids", *Hyperfine Interactions*, vol. 97, 1996.

[180] John P. Perdew, Kieron Burke, and Matthias Ernzerhof, "Generalized Gradient Approximation Made Simple", *Physical Review Letters*, vol. 77, no. 18, pp. 3865–3868, October 1996.

[181] P. Ravindran, A. Kjekshus, H. Fjellvåg, A. Delin, and O. Eriksson, "Ground-state and excited-state properties of $LaMnO_3$ from full-potential calculations", *Physical Review B*, vol. 65, no. 6, pp. 064445, January 2002.

[182] Bayer H., "Zur Theorie der Spin-Gitterrelaxation in Molekiilkristallen", *Zeitschrift für Physik*, vol. 30, pp. 227–238, 1951.

[183] T. Kushida, "The Influence of Lattice Vibration on the Pure Quadrupole Line", *Journal of Science of the Hiroshima University. Series A*, vol. 19, pp. 327, November 1955.

[184] T. Kushida, G. B. Benedek, and N. Bloembergen, "Dependence of the pure quadrupole resonance frequency on pressure and temperature", *Physical Review*, vol. 104, no. 5, pp. 1364–1377, December 1956.

[185] Tien-Chuan Wang, "Pure nuclear quadrupole spectra of chlorine and antimony isotopes in solids", *Physical Review*, vol. 99, no. 2, pp. 566–577, July 1955.

[186] Z. Jirák, C. Martin, M. Hervieu, and J. Hejtmánek, "Charge and spin configurations in $Pr_{1-x}Ca_xMnO_3$ (x=0.5-0.75)", *Applied Physics A: Materials Science & Processing*, vol. 74, pp. 1755–1757, 2002.

[187] Q. Zhou and B. J. Kennedy, "Thermal expansion and structure of orthorhombic $CaMnO_3$", *Journal of Physics and Chemistry of Solids*, vol. 67, pp. 1595–1598, 2006.

[188] J. Christiansen, P. Heubes, R. Keitel, W. Klinger, W. Loeffler, W. Sandner, and W. witthuhn, "Temperature-dependence of electric-field gradient in noncubic metals", *Zeitschrift fur Physik B-Condensed matter*, vol. 24, no. 2, pp. 177–187.

[189] P. Jena, "Temperature Dependence of Electric Field Gradients in Noncubic Metals", *Physical Review Letters*, vol. 36, no. 8, pp. 418–421, February 1976.

[190] Pattnaik P. C. Thompson, M. D, , and T. P. Das, "Theory of antishielding effects and temperature dependence of field-gradients in metals ", *Hyperfine Interactions*, vol. 4, no. 1-2, pp. 515–522, January 1978.

[191] P. Jena and J. Rath, "Ab initio calculation of the temperature dependence of the electric field gradient in Be", *Physical Review B*, vol. 23, no. 8, pp. 3823–3827, April 1981.

[192] A. C. Junqueira, A. W. Carbonari, Mestnik J., and R. N. Saxena, "Electric field gradient at Nb site in the intermetallic compounds Nb_3X (X = Al, In, Si, Ge, Sn) measured by PAC", *Zeitschrift fur naturforschung-section A*, vol. 55, no. 1-2, pp. 41–44, Jan-Feb 2000.

[193] G. L. Catchen, Wukitch. S. J., E. M. Saylor, W. Huebner, and M. Blaszkiewicz, "Investigating phase-transitions in ABO_3 perovskites using perturbed angular-correlation spectroscopy", *Ferroelectrics*, vol. 117, no. 1-4, pp. 175–195, January 1993.

[194] G. L. Catchen, Stephen J. Wukitch, David M. Spaar, and M. Blaszkiewicz, "Temperature dependence of the nuclear quadrupole interactions at Ti sites in ferroelectric $PbTiO_3$ and in ilmenite and perovskite $CdTiO_3$: Evidence for order-disorder phenomena", *Physical Review B*, vol. 42, no. 4, pp. 1885–1894, August 1990.

[195] J. A. Alonso, M. J. Martínez-Lope, M. T. Casais, de Silva P. S. I. P. N. MacManus-Driscoll, J. L., L. F. Cohen, and M. T. Fernandez-Diaz, "Non-stoichiometry, structural defects and properties of $LaMnO_{3+\delta}$ with high δ values ($0.11 \leq \delta \leq 0.29$)", *Journal of materials chemistry*, vol. 7, pp. 2139–2144, October 1997.

[196] B. Dabrowski, R. Dybzinski, Z. Bukowski, O. Chmaissem, and J. D. Jorgensen, "Oxygen Content and Structures of $La_{1-x}Ca_xMnO_{3+\delta}$ as a Function of Synthesis Conditions", *Journal of Solid State Chemistry*, vol. 146, pp. 448–457, September 1999.

[197] L. Martín-Carrón, A. de Andrés, M. J. Martínez-Lope, M. T. Casais, and J. A. Alonso, "Raman phonons as a probe of disorder, fluctuations, and local structure in doped and undoped orthorhombic and rhombohedral manganites", *Physical Review B*, vol. 66, no. 17, pp. 174303, November 2002.

[198] J. A. M. van Roosmalen and E. H. P. Cordfunke, "The Defect Chemistry of $LaMnO_{3\pm\delta}$. 4. Defect Model for $LaMnO_{3+\delta}$", *Journal of Solid State Chemistry France*, vol. 110, pp. 109–112, May 1994.

[199] J. Rodríguez-Carvajal, "Recent advances in magnetic structure determination by neutron powder diffraction", *Physica B: Condensed Matter*, vol. 192, pp. 55–69, 1993.

[200] I. Maurin, P. Barboux, Y. Lassailly, J.-P. Boilot, F. Villain, and P. Dordor, "Charge-Carrier Localization on Mn Surface Sites in Granular $LaMnO_{3\pm\delta}$ Samples", *Journal of Solid State Chemistry*, vol. 160, pp. 123–133, August 2001.

[201] Th. Proffen, R. G. DiFrancesco, S. J. L. Billinge, E. L. Brosha, and G. H. Kwei, "Measurement of the local Jahn-Teller distortion in $LaMnO_{3.006}$ ", *Physical Review B*, vol. 60, no. 14, pp. 9973–9977, October 1999.

[202] D. Louca, T. Egami, W. Dmowski, and J. F. Mitchell, "Structural effect on colossal magnetoresistivity in manganites: Bond versus band", *Physical Review B*, vol. 64, no. 18, pp. 180403, October 2001.

[203] D. Louca, E. L. Brosha, and T. Egami, "Structure and lattice defects in $LaMnO_{3+\delta}$ and $La_{0.96}Sr_{0.04}MnO_{3+\delta}$ ", *Physical Review B*, vol. 61, no. 2, pp. 1351–1356, January 2000.

[204] S. Blundell , *Magnetism in Condensed Matter* , Oxford university press, Oxford, 2001.

[205] V. S. Amaral, J. P. Araújo, Y. G. Pogorelov, J. B. Sousa, P. B. Tavares, J. M. Vieira, J. M. B. Lopes Dos Santos, A. A. C. S. Lourenço, and P. A. Algarabel, "Anomalous low-field magnetization in $La_{2/3}Ca_{1/3}MnO_3$ near the critical point: Stable clusters?", *Journal of Applied Physics*, vol. 83, pp. 7154–7156, June 1998.

[206] V. S. Amaral, J. P. Araújo, Y. G. Pogorelov, J. M. B. Lopes dos Santos, P. B. Tavares, A. A. C. S. Lourenço, J. B. Sousa, and J. M. Vieira, "Anomalous magnetic behavior in $La_{2/3}Ca_{1/3}MnO_3$ near the critical point: stable clusters and crossover to uniform ferromagnetism", *Journal of Magnetism and Magnetic Materials*, vol. 226, pp. 837–839, May 2001.

[207] D. Talbayev, L. Mihaly, and J. Zhou, "Antiferromagnetic Resonance in $LaMnO_3$ at Low Temperature", *Physical Review Letters*, vol. 93, no. 1, pp. 017202, July 2004.

[208] L. Mihaly, D. Talbayev, Laszlo F. Kiss, J. Zhou, T. Feher, and A. Janossy, "Field-frequency mapping of the electron spin resonance in the paramagnetic and antiferromagnetic states of $LaMnO_3$", *Physical Review B*, vol. 69, no. 2, pp. 024414, January 2004.

[209] V. Skumryev, F. Ott, J. M. D. Coey, A. Anane, J.-P. Renard, L. Pinsard-Gaudart, and A. Revcolevschi, "Weak ferromagnetism in $LaMnO_3$", *European Physical Journal B*, vol. 11, pp. 401–406, 1999.

[210] R. Laiho, K. G. Lisunov, E. Lähderanta, V. S. Stamov, V. S. Zakhvalinskii, P. Colomban, P. A. Petrenko, and Y. P. Stepanov, "Lattice distortions, magnetoresistance and hopping conductivity in $LaMnO_{3+\delta}$", *Journal of Physics Condensed Matter*, vol. 17, pp. 105–118, January 2005.

[211] R. Mahendiran, S. K. Tiwary, A. K. Raychaudhuri, T. V. Ramakrishnan, R. Mahesh, N. Rangavittal, and C. N. R. Rao, "Structure, electron-transport properties, and giant magnetoresistance of hole-doped $LaMnO_3$ systems", *Physical Review B*, vol. 53, no. 6, pp. 3348–3358, February 1996.

[212] N. F. Mott, *Metal Insulator Transitions*, Taylor and Francis, London, 1990.

[213] A. V. Zalessky, M. K. Gubkin, T. A. Khimich, E. V. Kleparskaya, and T. M. Perekalina, "Magnetic and NMR studies of lanthanum perovskite manganites", *Journal of Magnetism and Magnetic Materials*, vol. 154, pp. 351–354, May 1996.

[214] D. Stauffer and A. Aharony, *Introduction to Percolation theory*, Taylor and Francis, London, 1992.

[215] M. M. Savosta and P. Novák, "Two-Phase Character of Metallic Ferromagnetism in Manganites", *Physical Review Letters*, vol. 87, no. 13, pp. 137204, September 2001.

[216] M. M. Savosta, V. D. Doroshev, V. I. Kamenev, V. A. Borodin, T. N. Tarasenko, A. S. Mazur, and M. Maryško, "Inhomogeneity of the ferromagnetic state of $(La_{1-x}Sr_x)_{1-\delta}MnO_3$ perovskites according to ^{1}39La and ^{5}5Mn NMR data", *Journal of Experimental and Theoretical Physics*, vol. 97, no. 3, pp. 573–586, 2003.

[217] J.-S. Zhou and J. B. Goodenough, "Orbital order-disorder transition in single-valent manganites", *Physical Review B*, vol. 68, no. 14, pp. 144406, July 2003.

[218] A. Weisse, J. Loos, and H. Fehske, "Mixed-phase description of colossal magnetoresistive manganites", *Physical Review B*, vol. 68, no. 2, pp. 024402, July 2003.

[219] K. Kumagai, A. Iwai, Y. Tomioka, H. Kuwahara, Y. Tokura, and A. Yakubovskii, "Microscopically homogeneous magnetic structure of $La_{1-x}Sr_xMnO_3$ beyond the range of $0 < x < 0.1$ observed by La NMR", *Physical Review B*, vol. 59, no. 1, pp. 97–99, January 1999.

[220] P. Ravindran, "Private Comunication", 2004.

[221] J. F. Mitchell, D. N. Argyriou, C. D. Potter, D. G. Hinks, J. D. Jorgensen, and S. D. Bader, "Structural phase diagram of $La_{1-x}Sr_xMnO_{3+\delta}$: Relationship to magnetic and transport properties", *Physical Review B*, vol. 54, no. 9, pp. 6172–6183, September 1996.

[222] L. Sheng and D. N. Sheng, "Effective Orbital Interaction:. Spin and Orbital Ordering in Undoped Manganites", *International Journal of Modern Physics B*, vol. 13, pp. 1397–1418, 1999.

[223] Satoshi Okamoto, Sumio Ishihara, and Sadamichi Maekawa, "Orbital ordering in $LaMnO_3$: Electron-electron and electron-lattice interactions", *Physical Review B*, vol. 65, no. 14, pp. 144403, March 2002.

[224] T. Hotta, S. Yunoki, M. Mayr, and E. Dagotto, "A-type antiferromagnetic and C-type orbital-ordered states in $LaMnO_3$ using cooperative Jahn-Teller phonons", *Physical Review B*, vol. 60, no. 22, pp. R15009–R15012, December 1999.

[225] P. B. Allen and V. Perebeinos, "Anti-Jahn-Teller polaron in $LaMnO_3$ ", *Physical Review B*, vol. 60, no. 15, pp. 10747–10753, October 1999.

[226] Z. Popovic and S. Satpathy, "Cooperative Jahn-Teller Coupling in the Manganites", *Physical Review Letters*, vol. 84, no. 7, pp. 1603–1606, February 2000.

[227] C. P. Adams, J. W. Lynn, Y. M. Mukovskii, A. A. Arsenov, and D. A. Shulyatev, "Charge Ordering and Polaron Formation in the Magnetoresistive Oxide $La_{0.7}Ca_{0.3}MnO_3$", *Physical Review Letters*, vol. 85, no. 18, pp. 3954–3957, October 2000.

[228] X. Qiu, Th. Proffen, J. F. Mitchell, and S. J. L. Billinge, "Orbital Correlations in the Pseudocubic O and Rhombohedral R Phases of $LaMnO_3$", *Physical Review Letters*, vol. 94, no. 17, pp. 177203, May 2005.

[229] P. G. Radaelli, R. M. Ibberson, D. N. Argyriou, H. Casalta, K. H. Andersen, S.-W. Cheong, and J. F. Mitchell, "Mesoscopic and microscopic phase segregation in manganese perovskites", *Physical Review B*, vol. 63, no. 17, pp. 172419, April 2001.

[230] G. Zheng and C. H. Patterson, "Ferromagnetic polarons in $La_{0.50}Ca_{0.50}MnO_3$ and $La_{0.33}Ca_{0.67}MnO_3$", *Physical Review B*, vol. 67, no. 22, pp. 220404, June 2003.

[231] R. J. Goff and J. P. Attfield, "Charge ordering in half-doped manganites", *Physical Review B*, vol. 70, no. 14, pp. 140404, October 2004.

[232] J. C. Loudon, S. Cox, A. J. Williams, J. P. Attfield, P. B. Littlewood, P. A. Midgley, and N. D. Mathur, "Weak Charge-Lattice Coupling Requires Reinterpretation of Stripes of Charge Order in $La_{1-x}Ca_xMnO_3$", *Physical Review Letters*, vol. 94, no. 9, pp. 097202, March 2005.

[233] G. C. Milward, M. J. Calderón, and P. B. Littlewood, "Electronically soft phases in manganites", *Nature*, vol. 433, pp. 607–610, February 2005.

[234] D. V. Efremov, J. van den Brink, and D. I. Khomskii, "Charge order versus Zener polarons: ferroelectricity in manganites", *ArXiv Condensed Matter e-prints*, June 2003.

[235] D. V. Efremov, J. Van den Brink, and D. I. Khomskii, "Bond-versus site-centred ordering and possible ferroelectricity in manganites", *Nature Materials*, vol. 3, pp. 853–856, December 2004.

[236] E. Pollert, S.. Krupicka, and E. Kuzmicova, "Structural study of $Pr_{1-x}Ca_xMnO_3$ and $Y_{1-x}Ca_xMnO_3$ perovskites", *Journal of Physics and Chemistry of Solids*, vol. 43, pp. 1137–1145, December 1982.

[237] Z. Jirák, S. Krupička, V. Nekvasil, E. Pollert, G. Villeneuve, and F. Zounová, "Structural and magnetization study of $Pr_{1-x}Ca_xMnO_3$", *Journal of Magnetism and Magnetic Materials*, vol. 15, pp. 519–520, January 1980.

[238] M. Hervieu, G. Van Tendeloo, V. Caignaert, A. Maignan, and B. Raveau, "Monoclinic microdomains and clustering in the colossal magnetoresistance manganites $Pr_{0.7}Ca_{0.25}Sr_{0.05}MnO_3$ and $Pr_{0.75}Sr_{0.25}MnO_3$", *Physical Review B*, vol. 53, no. 21, pp. 14274–14284, June 1996.

[239] Z. Jirák, J. Hejtmánek, E. Pollert, M. Maryško, M. Dlouhá, and S. Vratislav, "Canted structures in the Mn^{3+}/Mn^{4+} perovskites", *Journal of Applied Physics*, vol. 81, pp. 5790–5792, April 1997.

[240] Y. Tokura, Y. Tomioka, H. Kuwahara, A. Asamitsu, Y. Moritomo, and M. Kasai, "Origins of colossal magnetoresistance in perovskite-type manganese oxides", *Journal of Applied Physics*, vol. 79, pp. 5288–5291, April 1996.

[241] J.-P. Renard and A. Anane, "Experimental studies of colossal magnetoresistance manganites: effects of oxygen non-stoichiometry, ^{55}Mn nuclear magnetic resonance, slow relaxation near the metal-insulator phase transition", *Materials Science and Engineering B*, vol. 63, pp. 22–29, August.

[242] H. Yoshizawa, H. Kawano, Y. Tomioka, and Y. Tokura, "Neutron-diffraction study of the magnetic-field-induced metal-insulator transition in $Pr_{0.7}Ca_{0.3}MnO_3$", *Physical Review B*, vol. 52, no. 18, pp. R13145–R13148, November 1995.

[243] M. R. Lees, J. Barratt, G. Balakrishnan, D. McK. Paul, and C. Ritter, "Neutron-powder-diffraction study of the magnetic and structural properties of $Pr_{0.6}(Ca_{1-x}Sr_x)_{0.4}MnO_3$ $(0 < x < 1)$ ", *Physical Review B*, vol. 58, no. 13, pp. 8694–8703, October 1998.

[244] M. R. Lees, J. Barratt, G. Balakrishnan, D. McK. Paul, and M. Yethiraj, "Influence of charge and magnetic ordering on the insulator-metal transition in $Pr_{1-x}Ca_xMnO_3$", *Physical Review B*, vol. 52, no. 20, pp. R14303–R14307, November 1995.

[245] A. M. Gomes, F. García, A. P. Guimarães, M. S. Reis, and V. S. Amaral, "Field-tuned magnetocaloric effect in metamagnetic manganite system", *Applied Physics Letters*, vol. 85, pp. 4974–+, November 2004.

[246] M. S. Reis, V. S. Amaral, P. B. Tavares, A. M. Gomes, A. Y. Takeuchi, A. P. Guimarães, I. S. Oliveira, and P. Panissod, "NMR evidence for an inhomogeneous transition between the ferromagnetic and antiferromagnetic ground states in $Pr_{1-x}Ca_xMnO_3$ manganites", *ArXiv Condensed Matter e-prints*, November 2002.

[247] J. Dho, E. O. Chi, N. H. Hur, K. W. Lee, H. S. Oh, and Y. N. Choi, "Two ferromagnetic transitions in $Pr_{0.8}Ca_{0.2}MnO_3$", *Solid State Communications*, vol. 123, pp. 441–444, August 2002.

[248] D. E. Cox, P. G. Radaelli, M. Marezio, and S.-W. Cheong, "Structural changes, clustering, and photoinduced phase segregation in $Pr_{0.7}Ca_{0.3}MnO_3$ ", *Physical Review B*, vol. 57, pp. 3305–3314, February 1998.

[249] J. Blasco, C. Ritter, J. García, J. M. de Teresa, J. Pérez-Cacho, and M. R. Ibarra, "Structural and magnetic study of $Tb_{1-x}Ca_xMnO_3$ perovskites", *Physical Review B*, vol. 62, no. 9, pp. 5609–5618, September 2000.

[250] M. M. Savosta, P. Novák, M. Maryško, Z. Jirák, J. Hejtmánek, J. Englich, J. Kohout, C. Martin, and B. Raveau, "Coexistence of antiferromagnetism and ferromagnetism in $Ca_{1-x}Pr_xMnO_3$ ($x <\sim 0.1$) manganites", *Physical Review B*, vol. 62, no. 14, pp. 9532–9537, October 2000.

[251] P. G. Radaelli, D. E. Cox, L. Capogna, S.-W. Cheong, and M. Marezio, "Wigner-crystal and bi-stripe models for the magnetic and crystallographic superstructures of $La_{0.333}Ca_{0.667}MnO_3$ ", *Physical Review B*, vol. 59, no. 22, pp. 14440–14450, June 1999.

[252] Renhui Wang, Jianian Gui, Yimei Zhu, and A. R. Moodenbaugh, "Distinguishing between the bi-stripe and Wigner-crystal model: A crystallographic study of charge-ordered $La_{0.33}Ca_{0.67}MnO_3$ ", *Physical Review B*, vol. 61, no. 18, pp. 11946–11955, May 2000.

[253] J. M. Tranquada, B. J. Sternlieb, J. D. Axe, Y. Nakamura, and S. Uchida, "Evidence for stripe correlations of spins and holes in copper oxide superconductors", *Nature*, vol. 375, pp. 561–563, June 1995.

[254] T. Vogt, P. M. Woodward, P. Karen, B. A. Hunter, P. Henning, and A. R. Moodenbaugh, "Low to High Spin-State Transition Induced by Charge Ordering in Antiferromagnetic $YBaCo_2O_5$", *Physical Review Letters*, vol. 84, no. 13, pp. 2969–2972, March 2000.

[255] J. P. Wright, J. P. Attfield, and P. G. Radaelli, "Long Range Charge Ordering in Magnetite Below the Verwey Transition", *Physical Review Letters*, vol. 87, no. 26, pp. 266401, December 2001.

[256] Z. Jirák, F. Damay, M. Hervieu, C. Martin, B. Raveau, G. André, and F. Bourée, "Magnetism and charge ordering in $Pr_{0.5}Ca_xSr_{0.5-x}MnO_3$ (x=0.09 and 0.5)", *Physical Review B*, vol. 61, no. 2, pp. 1181–1188, January 2000.

[257] Hirofumi Hazama, Terutaka Goto, Yuichi Nemoto, Yasuhide Tomioka, Atsushi Asamitsu, and Yoshinori Tokura, "Lattice effects of orbital and charge orderings in the perovskite manganite $Pr_{1-x}Ca_xMnO_3$", *Physical Review B*, vol. 69, no. 6, pp. 064406, November 2004.

[258] M. Braden, L. Pintschovius, T. Uefuji, and K. Yamada, "Dispersion of the high-energy phonon modes in $Nd_{1.85}Ce_{0.15}CuO_4$", *Physical Review B*, vol. 72, no. 18, pp. 184517, November 2005.

[259] L. Pintschovius, "Electron-phonon coupling effects explored by inelastic neutron scattering", *Physica Status Solidi B Basic Research*, vol. 242, pp. 30–50, January 2005.

[260] D. Reznik, L. Pintschovius, M. Ito, S. Iikubo, M. Sato, H. Goka, M. Fujita, K. Yamada, G. D. Gu, and J. M. Tranquada, "Electron-phonon coupling reflecting dynamic charge inhomogeneity in copper oxide superconductors", *Nature*, vol. 440, pp. 1170–1173, April 2006.

[261] W. J. Lu, Y. P. Sun, B. C. Zhao, X. B. Zhu, and W. H. Song, "Inhomogeneous strain and phase coexistence in $Bi_{0.4}Ca_{0.6}MnO_3$", *Physical Review B*, vol. 73, no. 21, pp. 214409, 2006.

[262] C. X. Chen, T. Qian, R. K. Zheng, F. Wang, and X. G. Li, "Charge-ordering correlated elastic anomalies in $Pr_{1-x}Ca_xMnO_3$ perovskite", *Physica Status Solidi B Basic Research*, vol. 241, pp. 1827–1831, July 2004.

[263] T. P. Das and P. C. Schmidt, "Current status of theory of nuclear-quadrupole interaction in metallic systems", *Zeitschrift Fur Naturforschung Section A*, vol. 41, pp. 47–77, January 1986.

[264] A. K. Raychaudhuri, A. Guha, I. Das, R. Rawat, and C. N. R. Rao, "Specific heat of single-crystalline $Pr_{0.63}Ca_{0.37}MnO_3$ in the presence of a magnetic field", *Physical Review B*, vol. 64, no. 16, pp. 165111, October 2001.

[265] Y. Yeshurun, Y. Schlesinger, and S. Havlin, "Temperature-dependence of the electric quadrupole interaction in $PbHfO_3$ ", *Journal of physics and chemistry of solids*, vol. 40, pp. 231–237, March 1979.

[266] S. Cox, E. Rosten, J. C. Chapman, S. Kos, M. J. Calderon, D.-J. Kang, P. B. Littlewood, P. A. Midgley, and N. D. Mathur, "Strain control of superlattice implies weak charge-lattice coupling in $La_{0.50}Ca_{0.50}MnO_3$", *Physical Review B*, vol. 73, no. 13, pp. 132401, April 2006.

[267] S. Grenier, J. P. Hill, Doon Gibbs, K. J. Thomas, M. v. Zimmermann, C. S. Nelson, V. Kiryukhin, Y. Tokura, Y. Tomioka, D. Casa, T. Gog, and C. Venkataraman, "Resonant x-ray diffraction of the magnetoresistant perovskite $Pr_{0.6}Ca_{0.4}MnO_3$", *Physical Review B*, vol. 69, no. 13, pp. 134419, April 2004.

[268] J. Herrero-Martin, J. Garcia, G. Subias, J. Blasco, and M. C. Sánchez, "Structural origin of dipole x-ray resonant scattering in the low-temperature phase of $Nd_{0.50}Sr_{0.50}MnO_3$", *Physical Review B*, vol. 70, no. 2, pp. 024408, July 2004.

[269] F. Rivadulla, M. A. López-Quintela, L. E. Hueso, C. Jardon, A. Fondado, J. Rivas, M. T. Causa, and R. D. Sánchez, "Strong ferro-antiferromagnetic competition and charge ordering in $Pr_{0.67}Ca_{0.33}MnO_3$", *Solid State Communications*, vol. 110, pp. 179–183, March 199.

[270] C. Jardón, F. Rivadulla, L. E. Hueso, A. Fondado, M. A. López-Quintela, J. Rivas, R. Zysler, M. T. Causa, and R. D. Sánchez, "Experimental study of charge ordering transition in $Pr_{0.67}Ca_{0.33}MnO_3$", *Journal of Magnetism and Magnetic Materials*, vol. 196, pp. 475–476, May 1999.

[271] S. Mercone, A. Wahl, A. Pautrat, M. Pollet, and C. Simon, "Anomaly in the dielectric response at the charge-orbital-ordering transition of $Pr_{0.67}Ca_{0.33}MnO_3$", *Physical Review B*, vol. 69, no. 17, pp. 174433, May 2004.

[272] N. Biskup, A. de Andres, J. L. Martínez, and C. Perca, "Origin of the colossal dielectric response of $Pr_{0.6}Ca_{0.4}MnO_3$", *Physical Review B*, vol. 72, no. 2, pp. 024115, July 2005.

[273] Y. Yeshurun, S. Havlin, and Y. Schlesinger, "Static and dynamic aspects of perturbed angular correlation measurements in perovskite crystals", *Solid State Communications*, vol. 27, pp. 181–184, 1978.

[274] L. D. Landau and E. M Lifshitz, *Statistical Physics*, Pergramon press, London, 1959.

[275] B. Zalar, A. Lebar, J. Seliger, R. Blinc, V. V. Laguta, and M. Itoh, "NMR study of disorder in $BaTiO_3$ and $SrTiO_3$", *Physical Review B*, vol. 71, no. 6, pp. 064107, February 2005.

[276] B. Zalar, V. V. Laguta, and R. Blinc, "NMR Evidence for the Coexistence of Order-Disorder and Displacive Components in Barium Titanate", *Physical Review Letters*, vol. 90, no. 3, pp. 037601, January 2003.

[277] Wei-Guo Yin, Dmitri Volja, and Wei Ku, "Orbital Ordering in $LaMnO_3$: Electron-Electron versus Electron-Lattice Interactions", *Physical Review Letters*, vol. 96, no. 11, pp. 116405, 2006.

[278] W. Eerenstein, N. D. Mathur, and J. F. Scott, "Multiferroic and magnetoelectric materials", *Nature*, vol. 442, pp. 759–765, August 2006.

List of Figures

List of Tables

List of Articles

List of all scientific articles published in international journals during this thesis. The articles based on the research material exposed in this work are assigned with *.

*A. M. L. Lopes, J. P. Araújo, J.J Ramasco, V. S. Amaral, R. Suryanarayanan, and J. G. Correia, "Percolative transition on ferromagnetic insulator manganites: Uncorrelated to correlated polaron clusters", *Physical Review B - Rapid Communication*, vol. 73, pp. R100408-RR100412, March 2006.

*A. M. L. Lopes, J. P. Araújo, A. M. Gomes, T. M. Mendonça, P. B. Tavares, J. G. Correia, and V. S. Amaral, "Cd-doped $LaMnO_3$ manganites prepared by the sol-gel technique", *Materials Science Forum*, vol. 514-516 pp. 289-293, February 2006.

*J. P. Araújo, A. M. L. Lopes, E. Rita , J. G. Correia, and V. S. Amaral, and U. Wahl, "Local probe studies on oxides using radioactive isotopes", *Materials Science Forum*, vol. 514-516, pp. 1593-1597, February 2006.

J. G. Correia, H. Haas, V. S. Amaral, A. M. L. Lopes, J. P. Araújo, S. Le Floch, P. Bordet, E. Rita, J. C. Soares, and W. Tröger, "Atomic ordering of the fluorine dopant in the $HgBa_2CuO_{4+\delta}$ high-Tc superconductor", *Physical Review B*, vol. 72, pp. 144523-144533, October 2005.

*J. P. Araújo, A. M. L. Lopes, T. M. Mendonça, E. Rita, J. G. Correia, and V. S. Amaral, "Electrical Field Gradient Studies on $La_{1-x}Cd_xMnO_{3+\delta}$", *Hyperfine Interactions*, vol. 158, pp. 347-351, September 2004.

E. Rita, J. G. Correia, U. Wahl, E. Alves, A. M. L. Lopes, and J. C. Soares, "PAC studies of implanted Ag-111 in single-crystalline ZnO", *Hyperfine Interactions*, vol. 158, pp. 395-400, September 2004.

*A. M. L. Lopes, J. P. Araújo, A. M. Gomes, M. S. Reis, V. S. Amaral, and P. B. Tavares, "Cadmium doping at Mn site in $Pr_{0.5}Ca_{0.5}MnO_3$", *Journal of Magnetism and Magnetic Materials*, vol. 272, pp. 1767-1768, May 2004.

*A. M. L. Lopes, J. P. Araújo, E. Rita, J. G. Correia, V. S. Amaral, R. Suryanarayanan, and ISOLDE Collaboration, "Local probe studies on $LaMnO_{3+\delta}$ using the Perturbed Angular Correlation Technique", *Journal of Magnetism and Magnetic Materials*, vol. 272, pp. E1671-E1673, May 2004.

*A. M. L. Lopes, J. P. Araújo, E. Rita, J. G. Correia, V. S. Amaral, Y. Tomioka, Y. Tokura, and R. Suryanarayanan, "Perturbed angular correlation study of $Pr_{1-x}Ca_xMnO_3$", *Journal of Magnetism and Magnetic Materials*, vol. 272, pp. E1667-E1668, May 2004.

B. De Vries, V. Matias, A. Vantomme, U. Wahl, E. Rita , E. Alves, A. M. L. Lopes, and J.G. Correia, "Influence of O and C co-implantation on the lattice site of Er in GaN", *Applied Physics Letters*, vol. 84, pp. 4304–4306, May 2004.

E. Rita, U. Wahl, A. M. L. Lopes, J. P. Araújo, J. G. Correia, E. Alves, J. C. Soares, and ISOLDE Collaboration, "Lattice site and stability of implanted Ag in ZnO", *Physica B-Condensed Matter*, vol. 240, pp. 240-244, December 2003.

G.N. Kakazei, A.M.L. Lopes, Yu.G. Pogorelov, M.A. Salgueiro da Silva, J.A.M. Santos, J.B. Sousa, S. Cardoso, P.P. Freitas, E. Snoeck, "Current-in-plane transport in granular single layers and multilayers of CoFe in Al_2O_3", *Journal of Magnetism and Magnetic Materials*, vol. 266, pp. 62-67, October 2003.